# DESIGN AND SYNTHESIS OF FLUORESCENCE TURN-ON CHEMOSENSORS FOR SOME METAL IONS

**Ph.D. THESIS**

*by*

**MERGU NAVEEN**

**DEPARTMENT OF CHEMISTRY**
**INDIAN INSTITUTE OF TECHNOLOGY ROORKEE**
**ROORKEE - 247 667 (INDIA)**
**OCTOBER, 2015**

# DESIGN AND SYNTHESIS OF FLUORESCENCE TURN-ON CHEMOSENSORS FOR SOME METAL IONS

**A THESIS**

*Submitted in partial fulfilment of the requirements for the award of the degree*

*of*

**DOCTOR OF PHILOSOPHY**

*in*

**CHEMISTRY**

*by*

**MERGU NAVEEN**

**DEPARTMENT OF CHEMISTRY**
**INDIAN INSTITUTE OF TECHNOLOGY ROORKEE**
**ROORKEE-247 667 (INDIA)**
**OCTOBER, 2015**

# INDIAN INSTITUTE OF TECHNOLOGY ROORKEE
# ROORKEE

## CANDIDATE'S DECLARATION

I hereby certify that the work which is being presented in this thesis entitled **"DESIGN AND SYNTHESIS OF FLUORESCENCE TURN-ON CHEMOSENSORS FOR SOME METAL IONS"** in partial fulfilment of the requirements for the award of the Degree of Doctor of Philosophy and submitted in the Department of Chemistry of the Indian Institute of Technology Roorkee is an authentic record of my own work carried out during a period from December, 2010 to October, 2015 under the supervision of **Dr. V. K. Gupta**, Professor and **Dr. A. K. Singh**, Professor, Department of Chemistry, Indian Institute of Technology Roorkee, Roorkee.

The matter presented in this thesis has not been submitted by me for the award of any other degree of this or any other Institute.

**(MERGU NAVEEN)**

This is to certify that the above statement made by the candidate is correct to the best of our knowledge.

(V. K. Gupta)
Supervisor

(A. K. Singh)
Supervisor

Date: 14.10.2015

The Ph.D. Viva-Voce Examination of **Mr. Mergu Naveen**, Research Scholar, has been held on .....

Chairman, SRC

Signature of External Examiner

This is to certify that the student has made all the corrections in the thesis.

Signature of Supervisors

Head of the Department

# Abstract

Over the past few years, high sensitive and selective fluorescent chemosensors towards various transition and other toxic metal ions are particularly attractive to current researchers due to its potential applications in the medicinal, clinical and environmental research areas. At present, many techniques are available for qualitative and quantitative analysis of metal ions and found their applications in various food, biological, geological and industrial effluents such as atomic absorption spectroscopy, inductively coupled plasma-mass spectroscopy, inductively coupled plasma emission spectrometry, neutron activation analysis, chromatography and voltammetry. Nevertheless, most of these methods involve tedious sample preparation procedures, sophisticated instruments and high maintenance expenditure. In recent years there has been a growing need for constructing chemical sensors for fast, on-time and cost-effective monitoring of environmental samples. The research and development (R&D) in the sensors area has expanded exponentially in terms of financial investment, numbers of paper published, and the number of active researchers worldwide. Compared with the traditional analysis instruments, chemical sensors are portable, simple to use, in-situ and miniature in size. These features are ideal for real-time on field measurements, thus the errors caused by the sample transportation and storage can be largely reduced. On the other hand, fluorescent chemosensors have drawn attention and offer considerable advantages over other techniques *via* their simplicity, convenience, low-cost, sensitivity, immediate response, and naked-eye visualization.

The thesis is divided into six chapters. General introduction and a survey of fluorescence-based optical sensors reported in the literature are presented in **Chapter 1**. These chemosensors are typically derived from a core group of well-known fluorophores, such as coumarin, bipyridine, indole, quinoline, calixarene, porphyrin, crown ether, fluorescein, rhodamine, BODIPY and nanoparticle, each emitting in different regions of the electromagnetic spectrum.

**Chapter 2** describes the theory which involves during the sensing process. Details related to the photoluminescence process will be discussed in the different subsections. The properties of excited states as well as their relaxation processes are explained with the help of Jablonski diagram. Classification of chemosensors according to the nature of the signal

emitted by the active unit and the different possible mechanisms such as PET, ICT and ET for signal transduction upon analyte binding to chemosensors, and the terms used in the study of fluorescence sensing have also been discussed in this chapter.

In **Chapter 3**, the fluorescent sensors **C1** and **C2** with 4-aminoantipyrine unit have been prepared and characterized. Their complexation behaviour and binding mode towards $Al^{3+}$ and other metal ions have been studied by UV–Vis, fluorescence spectrometric and HRMS methods. The free ligands **C1** and **C2** exhibited a main absorption band at about 345 nm and 380 nm, respectively. On the addition of metal ions to sensors, a new broad absorption band (mainly for $Cu^{2+}$, $Ni^{2+}$, $Co^{2+}$ and $Al^{3+}$ ions) was observed at 350–480 nm region. Receptor **C1** and **C2** alone displayed a very weak single fluorescence emission band at 498 nm and 484 nm respectively, with an excitation of 360 nm. On addition of $Al^{3+}$, receptors **C1** and **C2** exhibited a prominent fluorescence enhancement accompanied by a blue shift of 32 nm from 498 to 466 nm and 18 nm from 484 to 466 nm, respectively. Indicating that the receptors **C1** and **C2** exhibit "off-on" mode with high sensitivity towards $Al^{3+}$ over other metal ions which are used. The $^1H$ NMR titrations were carried out to explore the nature of interaction between receptor and aluminum ion. These sensors are successfully applied in highly acidic and neutral pH medium with the fastest response time (<5 sec). The fluorescence color change could be easily detected by the naked eye under a UV lamp. Fluorescence quenching of complex is observed in the presence of $Cu^{2+}$, $Ni^{2+}$ and $Co^{2+}$ ions due to dissociation of $Al^{3+}$ complex of receptor.

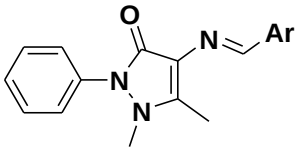


**C1**: Ar = 2-hydroxyphenyl
**C2**: Ar = 2-hydroxynaphthyl

**Chart 1.** Structures of the antipyrine based sensors.

In **Chapter 4**, new fluorescence chemosensors, **CS1** and **CS2** based on flavonol derivatives were synthesized and characterized. Complexation behaviour of sensors towards zinc and other tested metals have been studied using UV–Vis and fluorescence spectrometric methods. The free ligands **CS1** and **CS2** exhibited a main absorption band centred at 343 nm

and 356 nm, respectively. On the addition of metal ions to sensors, the absorption band of free receptors **CS1** and **CS2** is shifted to low intensity, while a new broad absorption band (mainly for $Cu^{2+}$, $Ni^{2+}$, $Zn^{2+}$, $Pb^{2+}$, $Al^{3+}$, $Co^{2+}$, $Cd^{2+}$, $Mn^{2+}$ and $Mg^{2+}$ ions) was observed at about 350–480 nm region. Chemosensors **CS1** and **CS2** alone displayed a weak single fluorescence emission band at 530 nm and a couple of emission bands at 425 and 530 nm, respectively, with an excitation of 340 nm. On addition of $Zn^{2+}$, receptors **CS1** and **CS2** exhibited a prominent fluorescence enhancement accompanied by a blue shift of 54 nm from 530 to 476 nm and 52 nm from 530 to 478 nm, respectively. These reveal selective detection towards $Zn^{2+}$ ion, along with fluorometric response. Also, those serve as a highly selective chemodosimeter for $Zn^{2+}$ at neutral pH with naked-eye detection and successfully examined the reversibility of Chemosensor–Zn(II) complexation.

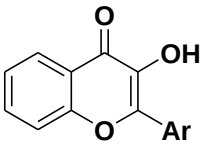


**CS1**: Ar = Phenyl
**CS2**: Ar = 2-furyl

**Chart 2.** Structures of the flavonol based sensors.

In **Chapter 5**, a simple 4-Methyl-7-hydroxy-8-formyl Coumarin serves as a selective chemosensor for $Mg^{2+}$ in the presence of alkali and alkaline earth metal ions. The free ligand **CS** exhibited a single absorption band at about 343 nm, hyperchromic shift was observed when added to $Co^{2+}$, $Cu^{2+}$, $Gd^{3+}$, $Mg^{2+}$, $Mn^{2+}$, $Nd^{3+}$, $Ni^{2+}$ and $Zn^{2+}$ ions. It showed a blue shift accompanied by a hyperchromic shift in the presence of $Cr^{3+}$ and $Al^{3+}$ metal ions. Chemosensor alone showed a single emission band at 473 nm with an excitation of 350 nm. **CS** showed a chelation enhanced fluorescence (CHEF) only with $Mg^{2+}$, even though there was a relatively chelation enhanced fluorescent quenching (CHEQ) effect with $Al^{3+}$, $Co^{2+}$, $Cr^{3+}$,

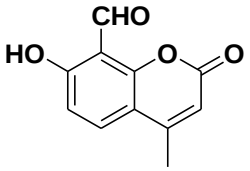


4-Methyl-7-hydroxy-8-formyl Coumarin

**Chart 3.** Structure of the Coumarin based sensor.

$Cu^{2+}$, $Fe^{2+}$, $Gd^{3+}$, $Mn^{2+}$, $Nd^{3+}$, $Ni^{2+}$ and $Zn^{2+}$. It showed a significant fluorescence enhancement and provides naked-eye detection towards $Mg^{2+}$. The receptor exhibited a good binding constant and lowest detection limit for $Mg^{2+}$. The variation of emission signal exists via of reversible chelation enhanced fluorescence (CHEF) with this inherent quenching metal ion.

In **Chapter 6**, a series of rhodamine derivatives have been prepared and characterized by FT-IR, $^{1}H$ NMR, $^{13}C$ NMR and ESI-MS, and their colorimetric and fluorescence responses toward various metal ions were explored. Ligand **L1–L4** shows fluorescence response to $Al^{3+}$ in the presence of other competing metal ions in methanol. The detection limit of Al(III) was estimated based on the fluorescence titration profile as $6.0\times10^{-7}$ M (for **L1**), $5.8\times10^{-7}$ M (for **L2**), $5.0\times10^{-7}$ M (for **L3**) and $1.4\times10^{-7}$ M (for **L4**). The resultant $Al^{3+}$ complex of the sensor **L4** is evaluated for anion recognition properties. The metal complex is highly selective for the determination of $AcO^{-}$ and $F^{-}$ with a detection limit of 0.4 μM in same solvent. The sensors, **RS1** and **RS2** exhibited highly selective and sensitive "turn-ON" fluorescent and colorimetric response toward $Cr^{3+}$. The detection limit of Cr(III) was calculated for **RS1** and **RS2** as $4.9\times10^{-8}$ M and $2.4\times10^{-7}$ M, respectively. Receptor **RH** exhibited strong colorimetric response toward Cu(II), Al(III) and Fe(III) and specific fluorometric response to Fe(III) in semi aqueous medium. The formation of **RH**–$Al^{3+}$ complex is fully reversible and can sense to $AcO^{-}$ and $F^{-}$ *via* dissociation. Thus, the sensor **RH** provides fluorescence "off-on-off" strategy for the sequential detection of $Al^{3+}$ and $AcO^{-}/F^{-}$. All these rhodamine-derived sensors works on the basis of structure change from spirocyclic form (fluorescence "OFF") to ring-opened amide form (fluorescence "ON") induced by a specific chemical species such as ionic metal at room temperature. Upon the addition of metal ion, the spiro ring was opened and the complex was formed in a 1 : 1 stoichiometry, and it was further confirmed by ESI-MS spectra.

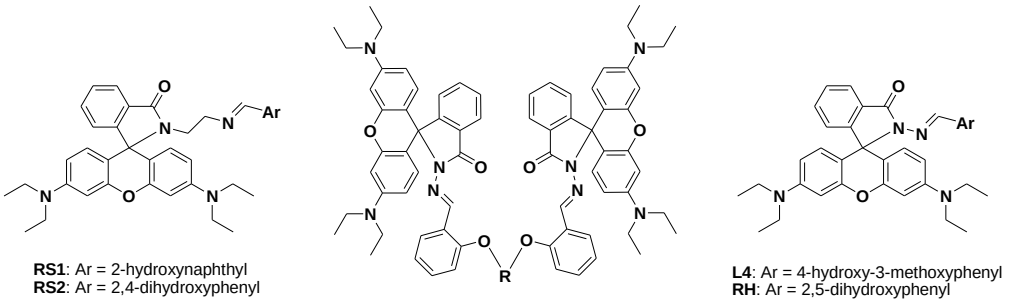


**Chart 4.** Structures of the rhodamine based chemosensors.

# ACKNOWLEDGEMENTS

*I would never have been able to finish my thesis without the guidance of my supervisors, help from lab mates, friends, and support from my family.*

*I would like to express my deepest gratitude to my supervisors,* ***Prof. V. K. Gupta*** *and* ***Prof. A. K. Singh****, for their excellent guidance, caring, patience, and providing me with an excellent atmosphere for doing research. They have been supportive since the day I began working in the lab and they teach me how to build research ability on my own, literature survey, writing, analyzing results critically, synthetic skills and what not. They are the only persons who want me to see as perfectionist in both education and life. It is an honor to be a student of you in doctoral program. Though, I made several mistakes while pursuing my doctoral program, you both corrected and put me in a good path with lot of patience. I tried to learn all the qualities from you sir, but still I have to develop and learn so many things from you because you are library of reference to me in all aspects. They helped a lot for making this thesis via number of times correction and giving suggestions to improve the language skills and output of the thesis. Not only research skills they build up caliber to create better future on my own.*

*I am thankful to* ***Prof. Anil Kumar****, Head, Department of Chemistry, IIT Roorkee for all the necessary official support and for all the facilities in the department.*

*I thank my SRC (Student Research Committee) members,* ***Dr. R. N. Goel*** *(Professor, Department of Chemistry, IIT Roorkee),* ***Dr. Bina Gupta*** *(Professor, Department of Chemistry, IIT Roorkee) and* ***Dr. Sashi*** *(Associate Professor, Department of Chemical Engineering, IIT Roorkee) for their helpful suggestions and constant support and encouragement.*

*I expend my thanks to* ***Dr. Ritu Barthwal*** *(Professor, Department of Biotechnology, IIT Roorkee) for extending the NMR facility. I am thankful to the entire faculty and the staff members who have helped me in some way or the other during my association with the institute and provided a good environment to develop my skill as a good researcher.*

*I gratefully acknowledge the funding source that made my Ph.D. work possible. I highly thankful to Ministry of Human Resource Development (MHRD) for providing financial*

*assistance that made my research work smooth and prompt. I would not have imagined the situation without their help and assistantship.*

*My gratitude is also extended to my seniors who taught me research skills such as synthetic and analytical techniques, and their selfless help and moral support all through my research work and guidance me as a guardian in many difficult moments:* ***Dr. Arunima Nayak****,* ***Dr. Arvind Kumar Bharti*** *and* ***Dr. Koteshwara Rao Bandi****. I cannot forget my friends and colleagues,* ***Lokesh Kumar Kumawat****,* ***Sudhir Kumar Shoora, Manoj Kumar Sharma*** *and* ***Inderjeet Tyagi****, who went through hard times together, cheered me on, and celebrated each accomplishment. Thank you for their support and help for completing my thesis. Finally, I thank all my lab members.*

*I would like to express special thanks to* ***Dr. Naveen Kumar****,* ***Dr. Ram Tilak*** *and* ***Dr. Venkat*** *for their constant encouragement, support and guidance. They provided me all possible help which I needed in the lab from the beginning till the end of the work. With their inspiration and great efforts to explain things clearly and simply, they helped to make my research easier for me.*

*I wish to extend a word of acknowledgement to my closely friends* ***Santosh****,* ***Naresh****,* ***Syam****,* ***Venkateshwarlu****,* ***Suresh****,* ***Murthy****,* ***Govardhan****,* ***Balu****,* ***Vijay****,* ***Srinivas*** *and* ***Krishnaiah****. Thank you for your encouragement, support and most of all your humor. You all kept things light and me smiling. Some more friends I must mention for their support and help:* ***Ambika****,* ***Ujjawal*** *and* ***Arun****.*

*I would not have contemplated this road if not for my parents,* ***Bharatamma*** *and* ***Anjaiah****, who instilled within me a love of creative pursuits, science and language, all of which finds a place in this thesis. My deepest gratitude goes to my other family members* ***Navita****,* ***Vedashri****,* ***Srikanth****,* ***Ravindar****,* ***Raju****,* ***Chiru****,* ***Soni****,* ***Rajavva****,* ***Muthyam****,* ***Laxmi Narsamma****,* ***Srinivas****,* ***Purushottam****,* ***Venu****,* ***Nagaraju****,* ***Meghana****,* ***Nagalaxmi*** *and* ***Naresh*** *for their love, affection, care and concern. This thesis is simply impossible without them. They have always support and encouraged me to do my best in all matters of life.*

*My heartfelt thanks to everybody who have helped me for successful realization of this thesis. My sincere apologies if I have missed someone, but I am grateful for their support. Finally, I*

*would also like to thank all the readers of this work, since any piece of academia is useful if it is read and understood by other so that it can become a bridge for further research.*

***Mergu Naveen***

# Table of Contents

# List of Figures

## List of Tables



## List of Schemes

## List of Publications

1. V.K. Gupta, A.K. Singh, **N. Mergu**, A new beryllium ion-selective membrane electrode based on dibenzo(perhydrotriazino)aza-14-crown-4 ether, *Anal. Chim. Acta*, 2012, **749**, 44–50.
2. V.K. Gupta, A.K. Singh, M.R. Ganjali, P. Norouzi, F. Faridbod, **N. Mergu**, Comparative study of colorimetric sensors based on newly synthesized schiff bases, *Sens. Actuators B*, 2013, **182**, 642–651.
3. V.K. Gupta, A.K. Singh, **N. Mergu**, Antipyrine based schiff bases as turn-on fluorescent sensors for Al(III) ion, *Electrochim. Acta*, 2014, **117**, 405–412.
4. V.K. Gupta, **N. Mergu**, A.K. Singh, Fluorescent chemosensors for $Zn^{2+}$ ions based on flavonol derivatives, *Sens. Actuators B*, 2014, **202**, 674–682.
5. V.K. Gupta, **N. Mergu**, L.K. Kumawat, A.K. Singh, Selective naked-eye detection of magnesium (II) ions using a coumarin-derived fluorescent probe, *Sens. Actuators B*, 2015, **207**, 216–223.
6. **N. Mergu**, V.K. Gupta, A novel colorimetric detection probe for copper(II) ions based on a Schiff base, *Sens. Actuators B*, 2015, **210**, 408–417.
7. L.K. Kumawat, **N. Mergu**, A.K. Singh, V.K. Gupta, A novel optical sensor for copper ions based on phthalocyanine tetrasulfonic acid, *Sens. Actuators B*, 2015, **212**, 389–394.
8. **N. Mergu**, A.K. Singh, V.K. Gupta, Highly sensitive and selective colorimetric and off-on fluorescent reversible chemosensors for $Al^{3+}$ based on the rhodamine fluorophore, *Sensors*, 2015, **15**, 9097–9111.
9. V.K. Gupta, **N. Mergu**, L.K. Kumawat, A.K. Singh, A reversible fluorescence "off–on–off" sensor for sequential detection of aluminum and acetate/fluoride ions, *Talanta*, 2015, **144**, 80–89.
10. V.K. Gupta, **N. Mergu**, A.K. Singh, Rhodamine-derived highly sensitive and selective colorimetric and off-on optical chemosensors for $Cr^{3+}$, *Sens. Actuators B*, 2015, **220**, 420–432.
11. V.K. Gupta, A.K. Singh, L.K. Kumawat, **N. Mergu**, An easily accessible switch-on optical chemosensor for the detection of noxious metal ions Ni(II), Zn(II), Fe(III) and $UO_2$(II), *Sens. Actuators B*, 2016, **222**, 468–482.

12. V.K. Gupta, **N. Mergu**, L.K. Kumawat, A new multifunctional rhodamine-derived probe for colorimetric sensing of Cu(II) and Al(III) and fluorometric sensing of Fe(III) in aqueous media, *Sens. Actuators B*, 2016, **223**, 101–113.

# CHAPTER 1
# Introduction

A Chemical sensor, defined by the IUPAC, "is a device that transforms chemical information, ranging from the concentration of a specific sample component to total composition analysis, into an analytically useful signal" [1].

### 1.1. General introduction

This work deals with detection/determination of toxins that may be accidentally or maliciously introduced into the environment. A few decades ago, there was a general feeling among many people that nature could effectively handle hazardous substances. Although, nowadays human beings are more concerned of their sensitive natural environment, pollution is still a problem. Experts estimate that industrial processes introduce up to a million different pollutants into the atmosphere and the aquatic ecosystem [2]. Heavy metals are one group of these substances, although not all of them are considered harmful to humans.

### 1.2. Historical review

In 1565 the first recorded fluorescence observation by Nicolas Monardes who was the Spanish physician and botanist, they observed a strange blue glimmer from water contained in a specific wooden cup made from *Ligirium nephiticiem*. This phenomenon was more widely illustrated in the 17th century by Isaac Newton and Robert Boyle. The first crude fluorescence emission spectrum was found by John Herschel for quinine in 1845. Good progress was made by George Stokes in the late 19th century toward the understanding of fluorescence. He launched the technique of observing fluorescence by using two different colored filters, one for the excitation, and one through which to observe the emission. Stokes was the first to find out and report that the emission wavelength was longer than the excitation wavelength (in 1852). This characteristic of fluorescence is now known as Stokes' Law. Association of Concentration with fluorescence intensity was also explained by Stokes. He defined the fluorescence quenching at high concentration and in the presence of foreign substances and used this information to suggest the use of fluorescence for the detection of organic substances. The first fluorescence based analysis was developed for the determination of Al(III) by forming a strongly fluorescent morin chelate by F. Goppelsroder in 1867. Roger Y. Tsien reported a fluorescent probe for $Ca^{2+}$ in 1980 [3].

### 1.3. Heavy metals in the environment

Heavy metals are considered as metals of a density higher than 5 $g/cm^3$. They obtained as pure elements, ions and complexes. Heavy metals include chromium (Cr), copper (Cu), iron (Fe), zinc (Zn), lead (Pb), mercury (Hg), silver (Ag), cadmium (Cd),

arsenic (As) and the platinum group elements [2]. Human activities started with metal mining more than 4000 years ago. Record pollution came up with the industrialization and its utilization of energy. A large amount of heavy metals are introduced into the aquatic environment and the atmosphere by the fossil fuels combustion. For example, the firing of coal causes the worldwide emission of $2.4 \times 10^4$ times of lead per year and crude oil contains 3.4 ppm mercury [2]. In addition, heavy metals are released to the ecosystem with the exponential growth of metal mining, the following processes and their industrial use.

Through polluted water supplies containing toxic metal ion is a potentially dangerous causing cancer and neurological dysfunction [2]. Metal ions are the second most rich water contaminant in the United States with the most common ion being mercury [2]. As reported by the Environmental Protections Agency (EPA) to Congress in 2007, 47% of considered reservoirs, ponds and lakes. In the US, approximately seven million acres are spoiled with different metal pollutants.

The EPA refers that mercury is a primary contaminant in US water, but chromium, lead and arsenic are also in abundant supply in America and abroad. Arsenic is one of the toxic metal present in the earth's crust. Arsenic in 3$^{rd}$ oxidation state is the most toxic and has a high occurrence in fish [4]. Although the EPA sets a limit of 50 μg/l, 13 million Americans mainly in western region are exposed to drinking water with twice this level, at 0.1 mg/l [4]. Arsenic contaminated water has been connected to risk of liver, bladder, lung and kidney cancers [5]. The US Toxicology Program and International Agency for the Research on Cancer refer to Cr(VI) as a lung carcinogen [6]. Highly toxic Cr(VI) and less toxic Cr(III) are present in US drinking water at levels of 1.8 μg/l [6]. Cr(VI) is most common metal in shallow groundwater with pH 6–8. The human body can reduce low levels of Cr(VI) to the less toxic Cr(III), but at higher levels (> 0.012 μg/l) of haxavalent chromium have shown allergic reactions in the lungs and skin, and an increased risk of lung cancer [6, 7].

The National Institute of Environmental Health Sciences (NIEHS) refers that lead toxicity is one of the most continual metal contamination issues. It occurs in low income homes where aging paint exists and eroding lead pipes are carrying the household's water supply [7]. These contaminants are difficult to locate since there is not a single contained source, but many individual sources. Lead poisoning is known to cause damage in reproductive and nervous system and is especially harmful to young children and fetuses. Due to these reasons it is particularly important to design a sensor system to detect hazardous metals in drinking water throughout the world.

### 1.4. Biochemistry and bio-toxicity of heavy metals

Recently, the term "heavy metals" has become widely used in biology and environmental studies related to their potential toxicity and ecotoxicity [8]. Human exposure to heavy metals is through the air, water chain, food chain, industry products and also occupational exposure. Due to their interference with the normal body biochemistry in the normal metabolic processes, they are considered as poisonous metals. When ingested, in the acid medium of the stomach, toxic metal ions (e.g., $Zn^{2+}$, $Pb^{2+}$, $Cd^{2+}$, $As^{2+}$, $As^{3+}$, $Hg^{2+}$ and $Cu^{2+}$) are converted to their stable oxidation states and form strong and stable chemical bonds when combine with the body's biomolecules (e.g., enzymes and proteins). These metals can replace the hydrogen atoms or the metal groups in the bio-molecules and the enzyme is thus inhibited from functioning [9, 10].

The toxicity of heavy metal ions depends on the type of metal, its biological role and the type of organisms that are exposed to it. Some heavy metals are essential to maintain the metabolism of the human body at trace concentrations, such as Cu, Fe, Mg, Mn and Zn, though they can be toxic in excess [11]. Some are considered to be both very toxic above recommended allowable levels and also relatively accessible, such as As, Cd, Hg, Pb and Sn [12]. Inhalation of heavy metals inhaled in vapour form can cause humans to exhibit the following symptoms: gastrointestinal (GI) disorders, diarrhoea, tremor, paralysis, ataxia, vomiting, depression, convulsion and pneumonia [11, 12].

Heavy metals are having a high tendency to form complexes, especially with oxygen nitrogen and sulphur-containing ligands of biological matter [13]. The toxicological effects can be explained by this interaction. As a result, breaking of hydrogen bonds, changes in the proteins molecular structure or enzymes inhibition can occur. Repeated exposure over long periods of time can cause chronic toxicity. Carcinogenic, teratogenic or mutagenic effects have been described for some heavy metals.

Besides the fact that arsenic, cadmium and mercury are highly toxic, and some heavy metals like as copper, cobalt, zinc, iron, nickel, manganese, selenium and tin are necessary to many organisms. These metals, along with amino acids, fatty acids and vitamins are essential for normal biochemical processes such as metabolism, biosynthesis and respiration [13]. An undersupply of these so called trace metals leads to deficiency, while oversupply results in toxic effects [13].

### 1.5. Conventional methods for the determination of metal ions

Accurate detection of metal ions is becoming increasingly important to the regulatory agencies, the regulated community and the general public. The development of

very sensitive and precise instruments is a big challenge. A variety of analytical methods fulfilling these demands are available. Recommended techniques for the detection of metal ions in water samples include inductively coupled plasma mass spectrometry (ICP-MS) [14], hydride-generation (HG) or cold vapour (CV) atomic absorption spectrometry (AAS) [15, 16], flame atomic absorption spectrometry (FAAS) [17], electrothermal atomic absorption spectrometry (ETAAS) [18], electrochemical [19–31] and other [32–50] methods. These methods are sensitive to metal ions which can provide a wide linear range and low detection limits of metal ions. However, these instruments are large in size and expensive in price and they are suitable for use in the laboratory only. Therefore, the samples have to be collected on site and transported by the labours. During these processes, contamination of samples may occur. The high cost and slow measurement times typically associated with the conventional measurements of regulated metals indicate requirements for novel analytical technologies that are fast, portable and cost effective.

### 1.6. Chemical sensors for the determination of metal ions

In recent years there has been a growing need for constructing chemical sensors for fast, on-time and cost-effective monitoring of environmental samples. The research and development (R&D) in the sensors area has expanded exponentially in terms of financial investment, numbers of paper published, and the number of active researchers worldwide [51]. Compared with the traditional analysis instruments, chemical sensors are portable, simple to use, in-situ and miniature in size. These features are ideal for real-time on field measurements, thus the errors caused by the sample transportation and storage can be largely reduced [52–54]. An appropriate definition of a “chemical sensor” has been described as the “Cambridge definition”, whereby a ‘‘chemical sensor’’ is that of a miniaturised device/material, that can deliver real time and on-line information on the presence of specific compounds or ions in complex samples [55].

### 1.7. The role of supramolecules in the field of chemical sensing

In 1987, the Nobel Prize for chemistry was awarded to triad of scientists – Donald J. Cram, Charles J. Pedersen and Jean-Marie Lehn in recognition of their brilliant work in the field of Supramolecular Chemistry. That day, this field has proved to be a well-established branch of modern chemistry. Since it lays on the crossroads between chemistry, biochemistry, physics and technology, it is highly interdisciplinary field, and has developed very rapidly in the last three decades [56, 57]. Since the field is expanding as it advances, numerous definitions describing it were reported in the literature. Phrases like ‘chemistry

beyond the molecule', 'the chemistry of the non-covalent bond', or 'non-molecular chemistry' are some of them, to name a few. The modern concept of supramolecular chemistry was introduced by Jean-Marie Lehn, which he defined as the ''chemistry of molecular assemblies and of the intermolecular bond'' [58]. From these descriptions, it can be easily inferred that, contrary to the traditional chemistry, supramolecular chemistry focuses on the weaker and reversible non-covalent interactions between molecular species. These interactions could be in the form of Van der Waals forces, hydrogen bonding, electrostatic forces, metal coordination, π–π interactions and hydrophobic forces.

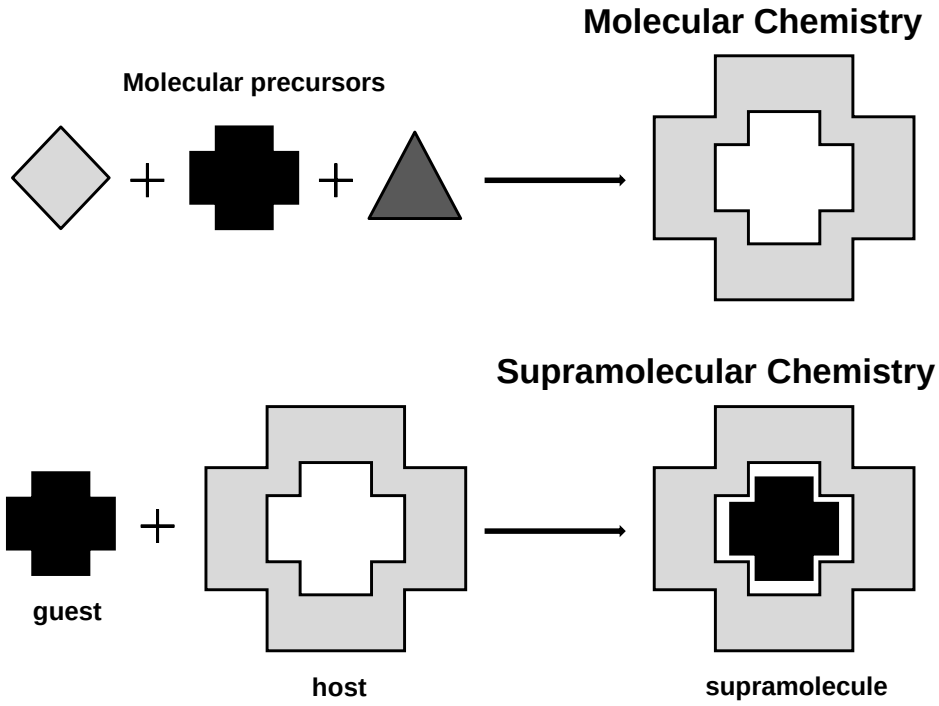


**Figure 1.1.** Comparison between molecular and supramolecular chemistry.

During the early days of this field, supramolecules mainly comprised two components, a host and a guest species (Figure 1.1), which interact with one another in a non-covalent manner. However, dramatic developments have occurred since then, such that past decade has seen its expansion into some interesting areas of materials chemistry and nanoscience with various potential and real applications.

A wide range of chromophores, fluorophores, and redox-active chemical species have been successfully incorporated into supramolecular frameworks. Utilizing the rich host-guest chemistry, they become ideal candidates for sensing applications. Moreover, contributions of supramolecular methods in the design and manufacture of molecular scale functional devices are significantly important. Developing molecular scale logic devices, designing and synthesizing artificial biological agents, and developing new therapeutic

agents, are some of the very hot and novel application areas of this field. No doubt that, as human needs are increasing, supramolecular chemistry concepts are going to be more involved in our daily life to facilitate it.

### 1.8. Literature survey

The most developed class of chemosensors is that of sensors which recognize metal ions. Metal ions are extremely important in fields such as biology, chemistry, medicine and environment. Metal cation roles in biological processes range from maintaining potentials across cell membranes to triggering muscle contraction, among other functions. They also have catalytic functions at the active sites of many enzymes. On the other hand, pollutant metals like lead, mercury or cadmium show the undesirable side of the coin, in environmental terms. Due to their importance in so many areas, the chemistry of cation complexation has played an important role in the origin of the field of molecular recognition.

These chemosensors are typically derived from a core group of well-known fluorophores, such as coumarin [59–82], bipyridine [83–87], indole [88–93], quinoline [94–107], calixarene [108–122], porphyrin [123–130], crown ether [131–138], fluorescein [139–141], rhodamine [142–149], BODIPY [150–166] and nanoparticle [167–185] (Figure 1.2), each emitting in different regions of the electromagnetic spectrum [186].

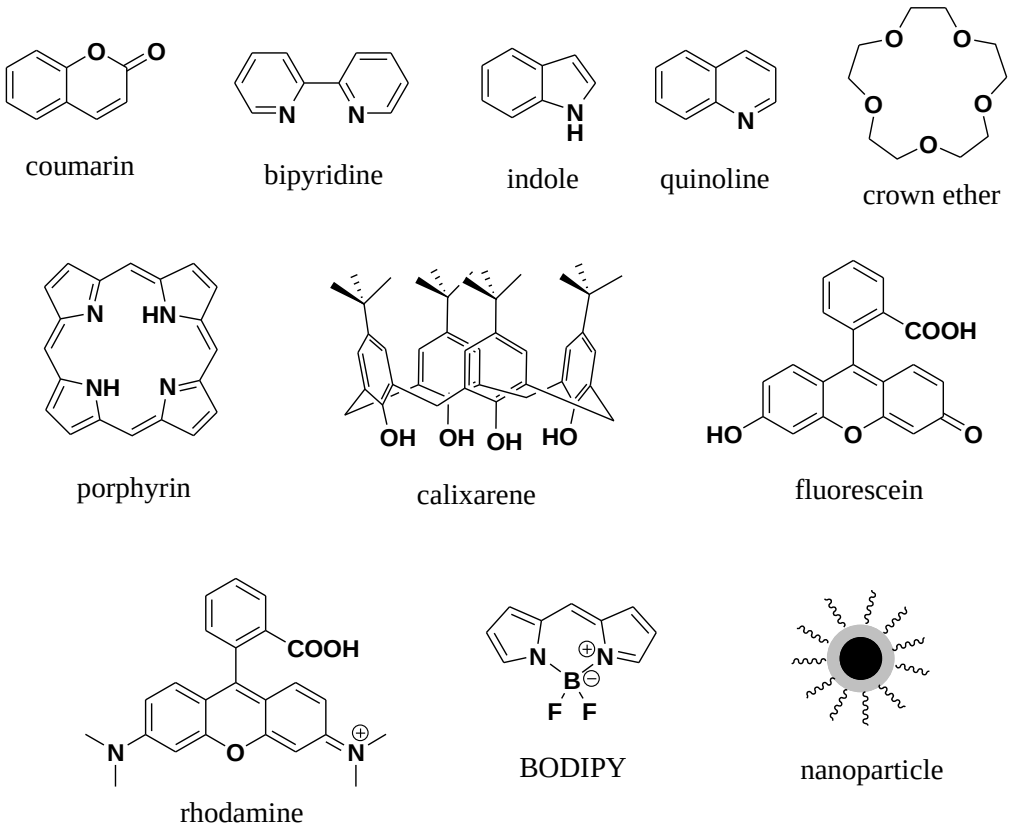


**Figure 1.2.** Well-known small molecule fluorophores.

### 1.8.1. Coumarin based fluorophores

X.F. Yang and co-workers designed and synthesized a coumarin-based chemosensor for $Zn^{2+}$, it exhibited lower background fluorescence due to ICT [62]. Upon addition of zinc ions to probe, a turn-on fluorescence emission is observed. Fluorescence emission increased with concentration of $Zn^{2+}$ with a detection limit of 0.29 μmol $L^{-1}$, formed 1:1 complexation between probe and zinc ion. The signalling of zinc by probe is significantly interfered by $Cu^{2+}$, $Co^{2+}$, $Ni^{2+}$. The neutral pH conditions are suitable for this sensor. Z. Li et al synthesized a new coumarin based $Fe^{3+}$-selective chemosensor, exhibited high selectivity toward $Fe^{3+}$ over other metal ions ($K^+$, $Li^+$, $Al^{3+}$, $Ca^{2+}$, $Mg^{2+}$, $Co^{2+}$, $Mn^{2+}$, $Cu^{2+}$, $Ni^{2+}$, $Cd^{2+}$, $Ag^+$, $Hg^{2+}$, $Pb^{2+}$, $Ba^{2+}$, $Sr^{2+}$ and $Zn^{2+}$) [64]. The binding ratio was determined for probe-$Fe^{3+}$ complex as 1:1. Association constant and detection limits were calculated to be $2.5\times10^3$ $M^{-1}$ and 0.388 μM, respectively.

An efficient coumarin based chemosensor has been synthesized for the detection of $Al^{3+}$ by T.K. Mondal and co-workers [65]. This receptor shows about 21-fold enhancement in fluorescence intensity upon $Al^{3+}$ addition. It is efficient in detection of $Al^{3+}$ in the intracellular region of human cervical cancer cells. The detection limit is calculated as low as 0.39 μM. Theoretical calculations are also studied to interpret the sensing mechanism. R. Sheng et al proposed a coumarin azine derivative as a colorimetric chemosensor for $Hg^{2+}$ [67]. Upon addition of $Hg^{2+}$, the ligand absorption maximum shows a large red shift. The color change is very easily observed by the naked eye, while alkali and alkaline earth metal ions do not induce such a change.

A highly sensitive and selective coumarin based chemosensor for $Ag^+$ was developed by S. Huang et al [68]. 4-fold fluorescent enhancement was observed due to inhibiting a PET quenching pathway through binding with $Ag^+$, limit of detection was found as low as 0.01 μM. D. Maity and T. Govindaraju introduced a highly selective coumarin-conjugated thiocarbanohydrazone based colorimetric chemosensor for $Co^{2+}$ [69]. It shown color change on the addition of $Co^{2+}$ from light yellow to deep pink and successfully applied in microorganisms. For $Cu^{2+}$ ion, a novel coumarin derived fluorogenic probe was developed by H.S. Jung et al [78]. To the monitoring of $Cu^{2+}$, the probe was applied successfully in the pH range 4–10. They also employed it for the detection of $Cu^{2+}$ in the cultured cells.

### 1.8.2. Bipyridine based fluorophores

A multi-substituted phenol-ruthenium(II) tris(bipyridine) complex was designed and prepared by C.Y. Li et al [83]. In this complex, Ru(II) tris(bipyridine) unit chosen as a fluorophore and the multi-substituted phenol moiety selected as receptor. It shows

fluorometrically selective towards $Co^{2+}$ ion and from 1:1 complex with a binding constant of $2.5\times10^{5}$ $M^{-1}$ and a detection limit of $5\times10^{-8}$ M. the response behaviour of probe was successfully carried out in a wide pH range of 4.5–9.5. A. Reynal et al prepared a series of 2,2′-bipyridine-3,3′-diols with different substituents [84]. The fluorescence of ligands is quenched in the presence of $Cu^{2+}$ ions. Working range and detection limit were calculated as 0.7–30 μM and 0.04 ppm.

A.A.G. Al Abdel Hamid and co-workers proposed a selective chemosensor based on ruthenium(II) complex for Mercuric ions [86]. The sensitivity of probe was measured by using FTIR and UV-Vis spectroscopy. Limit of detection for Hg(II) ions was estimated to be 0.4 ppm. For copper(II) ions, a novel ruthenium tris(bipyridine)-based chemosensor was prepared by M. Li et al [87]. It displayed "ON-OFF" fluorescence change with $Cu^{2+}$ amongst 16 various metal ions, and further fluorescence recovered in the presence of $S^{2-}$, indicating OFF-ON sensing process. The sensing mechanism is confirmed by emission, NMR and mass spectrometry.

### 1.8.3. Indole based fluorophores

H.H. Wu et al introduced a novel indole-derived fluorescent chemosensor and its sensing properties towards metal ions were investigated [88]. It exhibited high selective and sensitive response towards $Hg^{2+}$ among several metal ions. It forms 1:1 complex with association constant of $9.57\times10^{3}$ $M^{-1}$, and the limit of detection of Hg(II) was calculated to be $2.25\times10^{-5}$ M. Computational results suggested that a central tetrahedron-coordination was formed between probe and $Hg^{2+}$. Two new fluorescent chemosensors based on indole were prepared and investigated its response with various transition metal ions by A.T. Wu and co-workers [89]. The results shown that sensors were selective for $Hg^{2+}$ ion, formed 1:1 complex with a central, sandwich-coordination. Sandwich-coordinated Hg(II) ion center was confirmed by the computational calculations.

P. Kaur et al designed and synthesized a new indole based "ratiometric" and "turn-off" fluorescent chemosensor towards $Hg^{2+}$ and $Cu^{2+}$ ions [92]. It exhibited NOR and YES logic gates, and in cervix cancer (HeLa) cell, intracellular $Hg^{2+}$ was also imaged (see the publication for more information). It is successfully carried out in a wide pH range of 2–12. D.T. Shi et al prepared a new series of chemosensors that respond to $Cu^{2+}$ and $F^{-}$ [93]. Due to NH-proton of indole, shows high-affinity binding towards fluoride ion. In these probes, the bis-triazolyl part serves as a receptor for metal ions and the indole moiety serves as a fluorophore for fluoride ion exerts specific and reversible emission changes along with colorimetric alternations upon the recognitions.

### 1.8.4. Quinoline based fluorophores

As Z.J. Jiang et al reported, a new quinoline-based fluorescent chemosensor selectively responded toward $Cu^{2+}$ over other metal ions [94]. The stoichiometric ratio was determined as 1:1 according to Job method. Both of intramolecular charge transfer and photo-induced electron transfer mechanisms were considered to be operational for fluorescence enhancement. Copper detection limit was determined as 1.16 μM. A highly sensitive and selective chemosensor was developed for the $Zn^{2+}$ ion by D. Sarkar et al [97]. The prepared chemosensor showed highly efficient in detecting zinc ion over other metal ions. It exhibited 'turn-on' response with about 50 fold enhancement of fluorescence intensity on addition of $Zn^{2+}$. The lowest detection limit of Zn(II) was established as low as 5 nM. Sensing mechanism and electronic structure have been understood by DFT and TDDFT calculations.

A quinoline-derived fluorescent chemosensor was reported by Y. Ma et al for the simultaneous detection of $Zn^{2+}$ and $Cd^{2+}$ in aqueous medium [98]. The internal charge transfer mechanism was proposed and this effect induced by binding with $Zn^{2+}$ or $Cd^{2+}$ produced the emission changes. The formed complex of probe and $Cd^{2+}$ was dissociated in the presence of cysteine, so it is considered as reversible chemosensor. Furthermore, it can provide real-time detection for intracellular ionic zinc and cadmium. Y.J. Jang et al developed a chemosensor based on quinoline and naphthol moieties and it showed a colorimetric and fluorescent response to $Cr^{3+}$ and $Al^{3+}$ [99]. Probe could selectively and sensitively detect $Cr^{3+}$ ion through a visible color change, while sense $Al^{3+}$ ion through a fluorescence enhancement.

K. Ghosh and D. Tarafdar designed and synthesised a new quinoline-based chemosensor, which recognised $Hg^{2+}$ ions by exhibiting ratiometric change in emission [103]. It also detected both $Zn^{2+}$ and $Cd^{2+}$ by significant non-ratiometric increase in fluorescence accompanied by red shift. The effectiveness of complexation between probe and $Hg^{2+}$ was further proved by $^{1}H$ NMR analysis. As results shown, "N" of quinoline ring and "O" of ether link involved in the formation of complex. A.T. Wu and co-workers utilized a quinoline-based Schiff base as a fluorescent chemosensor for the selective detection of Al(III) [106]. It exhibited a high binding constant with a good detection limit as 0.18 ppm. Fluorescence enhancement of probe upon addition of $Al^{3+}$ attributed to the chelation enhanced fluorescence (CHEF) effect.

### 1.8.5. Calixarene based fluorophores

X. Hu et al prepared a novel ON-OFF fluorescent chemosensor for $Cu^{2+}$ [112]. The proposed thiacalix[4]arene-based fluorescent chemosensor can sense $Cu^{2+}$ ions in aqueous solution. Fluorescence quenching takes place upon addition of cupric ions, which is attributed to intramicellar energy transfer effect. $Cu^{2+}$ can be detected selectively in the submicromolar concentration level. Manoj Kumar and co-workers have developed a selective chemosensor for $Ni^{2+}$ based on calix[4]arene [113]. They synthesized the calix[4]arene diamine of partial cone conformation, which undergoes fluorescence enhancement in the presence of nickel ions. The formation of a new band is attributed to the ICT effect.

Calixarene-derived fluorescent chemosensor was prepared by J.M. Liu et al [115]. It possesses two 3-alkoxy-2-naphthoic acid units and fluorescent intensity was quenched upon addition of $Cu^{2+}$ or $Fe^{3+}$. M.A. Qazi et al described synthesis and characterization of calix[4]arene based chemosensor, and studied detailed complexation of probe toward $Cd^{2+}$ and $Cu^{2+}$ [116]. Clearly stated the changes in FTIR spectra of chemosensor upon addition of metal ions, according that results two phenolic OH and nitrogen atoms of azo moiety are participating in complexation. A novel calix[4]arene-derived chemosensor have been developed for $Hg^{2+}$ ion, which works based on fluorescence resonance energy transfer (FRET). Energy transfer occurs from pyrenyl excimer to rhodamine upon addition of $Hg^{2+}$ (fluorescence-On). In the absence of $Hg^{2+}$ ion, it consists of a form of spirolactam, at this stage the energy transfer cannot take place (fluorescence-OFF) [117].

N.J. Wang et al prepared a highly selective calixarene with lower-rim proximal triazolylpyrenes based fluorescent chemosensor was prepared for $Ag^{+}$ ion [118]. The binding ratio was determined to be 1:1 for probe-$Ag^{+}$ and the binding constant was found to be $7.0\times10^{3}$ $M^{-1}$. The complexation behaviour also studied by $^{1}H$ NMR titration experiment. A new photochromic Schiff base derivative based on calix[4]arene has been synthesized [121], and it showed the color change on the addition of $Dy^{3+}$ or $Er^{3+}$ ions. Upon complexation with those ions, 'N' of imine group donates its lone pair to $Dy^{3+}$ or $Er^{3+}$, and a CHEF is observed due to chelation abrogates the PET process. G.G. Talanova and co-workers prepared a fluorogenic and dansyl group-containing calix[4]arene derivative, and provided fluorometric detection of $Tl^{+}$ [122].

### 1.8.6. Porphyrin based fluorophores

Y.Q. Weng et al synthesized a new fluorescent chemosensor based on porphyrin-zinc complex [123]. It exhibited high selectivity towards $Cu^{2+}$ ions and its fluorescence was

quenched upon binding with copper ion. Its fluorescence was regenerated by addition of EDTA solution. The stoichiometric ratio was determined by mole ratio method, and then it was further confirmed by ESI-MS. Two metal-free porphyrin derivatives were prepared by J. Jiang and co-worker [124]. This is the first example of porphyrin-based triple-signal fluorescent chemosensor for $Pb^{2+}$. Their dual-mode Cu(II) selective sensing properties by either the fluorescence ON-OFF mechanism or metal displacement from the $Pb^{2+}$ complex. Thus it is selective for both $Pb^{2+}$ and $Cu^{2+}$.

C.Y. Li et al designed and synthesized a chemosensor for recognition of $Zn^{2+}$ ions and exhibited unexpected ratiometric response to zinc ion [126]. The response of proposed chemosensor towards $Zn^{2+}$ was based on the metallation of porphyrin. The complex ratio was found as 1:1 between probe and metal ion with a good binding constant of $1.0\times10^{5}$ $M^{-1}$. The results shown that the sensitivity of probe to $Zn^{2+}$ is pH-independent and the probe was applied successfully in the pH range 4–8. Another chemosensor has been reported based on porphyrin for Ag(I) ions [127]. Performed with a linear range of Ag(I) from $1.0\times10^{-7}$ M to $5.0\times10^{-5}$ M with a detection limit of $2.5\times10^{-8}$ M.

H.Y. Luo et al designed a chemosensor based on porphyrin-appended terpyridine for cadmium ion [129]. Upon addition of cadmium ion, it showed a chelation-enhanced fluorescence effect via disruption of PET process. It exhibited a linear response to Cd(II) in the concentration range of $3.2\times10^{-6}$ M to $3.2\times10^{-4}$ M with a detection limit of $1.2\times10^{-6}$ M. It showed a good selectivity toward $Cd^{2+}$ ion over a huge number of alkali, alkali earth and transition metal ions. X. Zhou and co-workers provided a highly selective and sensitive chemosensor having β-functionalised porphyrin to detect $Hg^{2+}$ in aqueous solution [130]. It forms 1:1 stoichiometric complex with $Hg^{2+}$.

### 1.8.7. Crown ether based fluorophores

A.T. Wu and co-workers synthesized a sugar-aza-crown based chemosensor for $Cu^{2+}$ and its fluorescence response toward transition metal ions was examined [132]. It exhibited highly detection toward $Cu^{2+}$ ion amongst a series of metal ions. They used a Stern-Volmer plot to calculate the association constant and found to be $2.5\times10^{4}$ $M^{-1}$. H. Zhou et al synthesized two new diaminomaleonitrile derivatives containing aza-crown ether, which was selective for Cu(II) [133]. And also employed DFT theoretical calculations to understand the sensing behaviour of the receptor toward Cu(II) ions. A novel luminescent chemosensor was prepared based on the benzo crown ether terbium complex by Y. Tang and co-workers, which recognise $Hg^{2+}$ ion in methanol [134].

A new fluorescent chemosensor was prepared based on diaza-18-crown-6 ether by H. Li et al [136]. It exhibited high selectivity for $Fe^{3+}$ among biologically and environmentally relevant metal ions. Spectroscopic changes were observed upon addition of $Fe^{3+}$ via complexation with probe. The detection limit of $Fe^{3+}$ and the response time estimated as 0.31 μM and 10 s, respectively. Recently, the anthracene modified benzo-15-crown-5 ethers were introduced as a chemosensors for $Mg^{2+}$ and $Ca^{2+}$ ions by H. Nakamura and co-workers [138]. Their complexation behaviour was investigated through UV, fluorescence and $^1H$ NMR spectroscopy. All receptors which are used showed a very slight fluorescence emission because of PET process. Upon complexation with metal ions ($Mg^{2+}$ and $Ca^{2+}$) gave fluorescence emission by inhibiting the PET process.

### 1.8.8. Fluorescein based fluorophores

F.A. Abebe and E. Sinn designed two novel fluorescein-derived chemosensors to detection of $Cu^{2+}$ ions [139]. Their binding toward $Cu^{2+}$ is reversible, as indicated by the lightening of the color when copper ion is extracted with EDTA. The proposed sensors recognised the metal ion via the ring opened amide form. Recently, a another publication has been received on fluorescein-based 'turn-on' fluorescent chemosensor for $Co^{2+}$ and $Ni^{2+}$ from F.A. Abebe et al [140], which are highly selective and sensitive for those ions. The stoichiometry was confirmed as 1:1 ratio by Job's method. The electrochemical experiments were also conducted to know sensing behaviour of receptors.

X. Zeng and co-workers successfully synthesized two new fluorescein-based chemosensors for silver ions [141]. The fluorescent chemosensors displayed a high selective and sensitive response toward $Ag^+$ due to the high thiophility and selenophility of silver ions. The stoichiometric ratio of the complex between probe and silver ion is indicated as 1:2 by a Job's plot and the detection limit of $Ag^+$ found to be 0.01 μM.

### 1.8.9. Rhodamine based fluorophores

Y. Wang et al proposed a novel rhodamine based chemosensor for $Cu^{2+}$ by colorimetric and fluorometric detection [142]. The spirolactam ring of rhodamine derivative was opened and the color changes were observed from colorless to red. Probe showed a reversible absorption enhancement and fluorescence quenching response towards copper ion via a 1:1 stoichiometry. FRET process takes place during the complexation of probe with 1 eq. of $Cu^{2+}$ and FRET is inhibited when $Cu^{2+}$ is in excess (> 5 eq.). Another fluorescent chemosensor based on rhodamine was designed by Y. Zhou et al [143], and its sensing

behaviour was investigated toward metal ions by fluorescence spectroscopy. It exhibited high selective detection toward $Cr^{3+}$ with a detection limit of 0.023 μM.

A series of chemosensors based on rhodamine derivatives were synthesized by N.R. Chereddy et al for $Fe^{3+}$ ions [144]. The number and nature of coordinating moieties as well as size of cavity in rhodamine based fluorescent chemosensors were tuned to enhance the selectivity and sensitivity for ferric ions. The development of pink color indicated that the formation of complex between probe and metal ion at pH 7.4. Recently, W. Liu and co-workers reported two chemosensors to detection of Fe(III) and Cr(III) [145]. Upon complexation with metal ions, non-fluorescent spirocyclic form converted into fluorescent ring open form. The results showed that a probe form a complex with $Cr^{3+}$ ion with a 1:1 binding ratio and another one form 1:1 complex with $Fe^{3+}$.

P. Chattopadhyay and co-workers studied on substituents effect on FRET process in chemosensor selectivity for $Hg^{2+}$ ions [146]. They synthesized two novel rhodamine derivatives with different donor moieties (methoxy and nitro). Theoretical and experimental studies showed that the FRET mechanism is not operated in the probe which is having the nitro group (–R effect). H. Ju et al designed and prepared chemosensing monolayers on glass as a "turn-on" sensing film for $Pb^{2+}$ [148]. Immobilized chemosensors showed reversible transitions between the spirolactam (fluorescence-OFF) and open-ring (fluorescence-ON) structures, providing reversible fluorescent switches of the immobilized fluorescent chemosensors.

### 1.8.10. BODIPY based fluorophores

W. Dehaen and co-workers designed a colorimetric and near-IR fluorescent turn-on chemosensor based on BODIPY [154]. It displayed a highly selective and sensitive fluorescence response toward $Cu^{2+}$. They calculated the fluorescence quantum yields for probe and probe+$Cu^{2+}$ and results shown that the enhancement is occurred in quantum yield upon addition of copper ions. Recently, a novel phenol-based BODIPY chemosensor was prepared by L. Wang et al [155]. Probe is showing high sensitivity and selectivity toward $Fe^{3+}$ with small interference from $Cr^{3+}$ and $Al^{3+}$. Blue-shift takes place in the absorption spectra in the presence of $Fe^{3+}$ which indicated that the ICT process is operated in the sensing mechanism. The stoichiometry of ligand and $Fe^{3+}$ has been proved by Job's method, MALDI-TOF-MS and FT-IR experiments.

Two new off-on chemosensors based on BODIPY moiety were synthesized by A. Barba-Bon et al [157], they are highly sensitive for trivalent cations. Upon binding of metal ion to the probe, electron-donating ability of the N atom which is conjugated to the BODIPY

core was reduced. Forms 1:1 ligand to metal complexes and it also proved by Mass analysis. Another colorimetric and fluorometric sensor based on BODIPY was designed and prepared by S.P Wu and co-worker [161]. They showed high response toward $Hg^{2+}$ by color change and red emission. Upon binding with $Hg^{2+}$, the absorption band of probe is blue-shifted due to the inhibition of ICT effect from the N atom to BODIPY moiety. The sharp enrichment in the quantum yields indicate that the sensitivity of probe toward $Hg^{2+}$.

J.R. Lin et al proposed a BODIPY-based selective fluorescence probe for Zinc(II) [162]. The binding ratio of complex was determined to be 1:1 by Job's plot, the binding constant and detection limit were found to be $5.9\times10^4$ $M^{-1}$ and 0.59 μM, respectively. Furthermore, this complex was also used as a detector for pyrophosphate through fluorescence quenching. M. Baruah et al synthesized a BODIPY-based fluorescent chemosensor to detect $Pb^{2+}$ ion in living cells [165]. The fluorescence intensity was increased by 10-fold upon addition of $Pb^{2+}$. The dissociation constant of the complex was determined to be 18 μM.

### 1.8.11. Nanoparticle based fluorophores

P. Zhang et al reported on a fabrication of core-shell nanoparticle-based fluorescent chemosensors [171]. The core-shell nanoparticle sensor was obtained by a facile one-pot miniemulsion polymerization, which was used for detection of $Cu^{2+}$. Fluorescence resonance energy transfer takes place from the dye in the core to the Cu(II)-cyclam complexes on the nanoparticle surface. As observed, other metal ions did not interfere in the detection of $Cu^{2+}$ and successfully applied in a wide pH range 4–10. Organic nanoparticles were proposed as a fluorescent chemosensor by N. Singh and co-workers [172]. They prepared by using re-precipitation method and successfully detected $Ag^{+}$ ions in aqueous media. For this nanoparticle, the lowest detection limit was found to be 15.5 nM of $Ag^{+}$.

Another report on organic nanoparticles based on naphthalimide as a chemosensor for $Al^{3+}$ was received from A. Saini et al [173]. No interference was observed with the other metal ions in the detection of $Al^{3+}$. DFT calculations were also conducted to confirm the mechanism of fluorescence recognition. Another type luminescent chemosensor based on silica cross-linked micellar nanoparticles was designed by Q. Huo and co-workers, which is highly selective for $Fe^{3+}$ ions [174]. It showed no sensing ability of $Fe^{2+}$ because of the weak electron-accepting behaviour of $Fe^{2+}$. Due to their ultrasmall size, good water solubility, nontoxicity and biocompatibility, the used nanoparticles have potential applications in biological systems.

E. Delgado-Pinar et al prepared fluorescent chemosensors based on core-shell aluminosilicate nanoparticles for $Hg^{2+}$ [176]. The system functionalised with the monoamine chain shows high sensitive toward $Hg^{2+}$. The detection limit of Hg(II) was found as low as 0.2 ppb, and this system worked over a wide pH range 2–11. A novel fluorescent chemosensor based on magnetic core-shell silica nanoparticle for the detection of $Eu^{3+}$ ionic species was introduced by M.R. Ganjali et al [178]. The nano-chemosensor was prepared and characterized by FT-IR, TEM, SEM, UV-visible and fluorescence emission spectroscopy. The fluorescence enhancement of nano-chemosensor is due to the formation of strong covalent binding with $Eu^{3+}$ ion with a binding constant of $1.7\times10^{5}$ $M^{-1}$.

These types of chemosensors have attracted much interest during the last two decades. Despite the numerous studies that were reported and reviewed extensively in the literature, finding new strategies and mechanisms in the design of fluorescent chemosensors is still of continuing interest. Studies presented in the chapter 3–6 of this thesis, briefly summarizes our recent contributions to this field.

**References**


1. A. Hulanicki, S. Glab and F. Ingman, Chemical sensors: Definitions and classification, *Pure Appl. Chem.*, 1991, **63**, 1247−1250.
2. United States environmental protection Agency, Washington, DC, 2007.
3. R.Y. Tsien, New calcium indicators and buffers with high selectivity against magnesium and protons: design, synthesis, and properties of prototype structures, *Biochemistry*, 1980, **19**, 2396−2404.
4. B.A. Fowler, Topics in environmental health, Vol. 6: Biological and environmental effects of arsenic, *Elsevier*, Amsterdam, 1983, pp. 281.
5. D. Das, G. Basu, T.R. Chowdhury, D. Chakraborty, *in Proc. Intl. Conf. on Arsenic in Groundwater*, Calcutta, 1995, 44−45.
6. R.E. Jones, Hexavalent chrome: Threshold concept for carcinogenicity, *Biomed. Environ. Sci.*, 1990, **3**, 20−34.
7. R.L. Smith, Risk-based concentrations: Prioritizing environmental problems using limited data, *Toxicol.*, 1996, **106**, 243−266.
8. J.O. Duruibe, M.O.C. Ogwuegbu, J.N. Egwurugwu, Heavy metal pollution and human biotoxic effects, *Int. J. Phy. Sci.*, 2007, **2**, 112−118.
9. W.T.S. Lenntech, Water treatment solutions lenntech, 2010, http://www.lenntech.es/periodica/elementos/as.htm, http://www.lenntech.es/periodica/elementos/cu.htm, http://www.lenntech.es/periodica/elementos/fe.htm, http://www.lenntech.es/periodica/elementos/al.htm, http://www.lenntech.es/periodica/elementos/mn.htm, http://www.lenntech.es/periodica/elementos/ni.htm, http://www.lenntech.es/periodica/elementos/zn.htm.
10. V. Gopal, S. Parvathy, P.R. Balasubramanian, Effect of heavy metals on the blood protein biochemistry of the fish Cyprinus carpio and its use as a bioindicator of pollution stress, *Environ. Monit. Assess.*, 1997, **48**, 117−124.
11. E.S. Nielsen, S. Wium-Andersen, Copper ions as poison in the sea and in freshwater, *Mar. Biol.*, 1970, **6**, 93−97.
12. L. Mercier, T.J. Pinnavaia, Heavy metal ion adsorbents formed by the grafting of a thiol functionality to mesoporous silica molecular sieves: Factors affecting Hg(II) uptake, *Environ. Sci. Technol.*, 1998, **32**, 2749−2754.

13. International programme on chemical safety, Copper: Environmental health criteria 200, World health organization, Geneva, Switzerland, 1998.
14. K. Itoh, M. Chikuma, H. Tanaka, Determination of selenium in sediments by hydride generation atomic absorption spectrometry. Elimination of interferences, *Anal. Chem.*, 1988, **330**, 600−604.
15. M.H.M. Chan, I.H.S. Chan, A.P.S. Kong, R. Osaki, R.C.K. Cheung, C.S. Ho, G.W.K. Wong, P.C.Y. Tong, J.C.N. Chan, C.W.K. Lam, Cold-vapour atomic absorption spectrometry underestimates total mercury in blood and urine compared to inductively-coupled plasma mass spectrometry: An important factor for determining mercury reference intervals, *Pathology*, 2009, **41**, 467−472.
16. M. Ghaedi, K. Niknam, A. Shokrollahi, E. Niknam, H.R. Rajabi, M. Soylak, Flame atomic absorption spectrometric determination of trace amounts of heavy metal ions after solid phase extraction using modified sodium dodecyl sulphate coated on alumina, *J. Hazard. Mater.*, 2008, **155**, 121−127.
17. R.Q. Aucelio, A.J. Curtius, Evaluation of electrothermal atomic absorption spectrometry for trace determination of Sb, As and Se in gasoline and kerosene using microemulsion sample introduction and two approaches for chemical modification, *J. Anal. At. Spectrom.*, 2002, **17**, 242−247.
18. D. Diamond. Principles of chemical and biological sensors, *John Wiley & Sons*, New York, 1998, 45−60.
19. P.C. Pandey, B. Singh, R.C. Boro, C.R. Suri, Chemically sensitized ormosil-modified electrodes—Studies on the enhancement of selectivity in electrochemical oxidation of hydrogen peroxide, *Sens. Actuators B*, 2007, **122**, 30–41.
20. R.K. Mishra, P.C. Pandey, Study of s-polarized photonic bandgap structure in three component optical fibonacci multilayers composed of nanoscale materials, *Solid State Commun.*, 2009, **149**, 946–951.
21. P.C. Pandey, S. Upadhyay, A.K. Upadhyay, Electrochemical sensors based on functionalized ormosil-modified electrodes—role of ruthenium and palladium on the electrocatalysis of NADH and ascorbic acid, *Sens. Actuators B*, 2004, **102**, 126–131.
22. V. Singh, S. Mohan, G. Singh, P.C. Pandey, R. Prakash, Synthesis and characterization of polyaniline–carboxylated PVC composites: Application in development of ammonia sensor, *Sens. Actuators B*, 2008, **132**, 99–106.
23. H. Beitollahi, H.K. Maleh, H. Khabazzadeh, Nanomolar and selective determination of epinephrine in the presence of norepinephrine using carbon paste electrode modified

with carbon nanotubes and novel 2-(4-Oxo-3-phenyl-3,4-dihydroquinazolinyl)-N′-phenyl hydrazinecarbothioamide, *Anal. Chem.*, 2008, **80**, 9848–9851.

24. A.A. Ensafi, H.K. Maleh, S. Mallakpour, B. Rezaei, Highly sensitive voltammetric sensor based on catechol-derivative-multiwall carbon nanotubes for the catalytic determination of captopril in patient human urine samples, *Colloids Surf. B*, 2011, **87**, 480–488.
25. H.M. Moghaddam, H. Beitollahi, S. Tajik, M. Malakootian, H.K. Maleh, Simultaneous determination of hydroxylamine and phenol using a nanostructure-based electrochemical sensor, *Environ. Monit. Assess.*, 2014, **186**, 7431–7441.
26. H. Beitollahi, M. Hamzavi, M.T. Mahani, M. Shanesaz, H.K. Maleh, A novel strategy for simultaneous determination of dopamine and uric acid using a carbon paste electrode modified with CdTe quantum dots, *Electroanal.*, 2015, **27**, 524–533.
27. A. Jakob, C.C. Joubert, T. Rüffer, J.C. Swarts, H. Lang, Chemical and electrochemical oxidation studies on new copper(I) ferrocenyl-functionalised β-diketonates, *Inorg. Chim. Acta*, 2014, **411**, 48–55.
28. B.J. Sanghavi, P.K. Kalambate, S.P. Karna, A.K. Srivastava, Voltammetric determination of sumatriptan based on a graphene/gold nanoparticles/Nafion composite modified glassy carbon electrode, *Talanta*, 2014, **120**, 1–9.
29. B.J. Sanghavi, O.S. Wolfbeis, T.Hirsch, N.S. Swami, Nanomaterial-based electrochemical sensing of neurological drugs and neurotransmitters, *Microchim. Acta*, 2015, **182**, 1–41.
30. B.J. Sanghavi, S.Sitaula, M.H. Griep, S.P. Karna, M.F. Ali, N.S. Swami, Real-time electrochemical monitoring of adenosine triphosphate in the picomolar to micromolar range using graphene-modified electrodes, *Anal. Chem.*, 2013, **85**, 8158−8165.
31. B.J. Sanghavi, W. Varhue, J.L. Chavez, C.F. Chou, N.S. Swami, Electrokinetic preconcentration and detection of neuropeptides at patterned graphene-modified electrodes in a nanochannel, *Anal. Chem.*, 2014, **86**, 4120−4125.
32. I. Ali, W.A. Wani, K. Saleem, M.F. Hseih, Design and synthesis of thalidomide based dithiocarbamate Cu(II), Ni(II) and Ru(III) complexes as anticancer agents, *Polyhedron*, 2013, **56**, 134–143.
33. W.A. Wani, Z. Al-Othmanb, I. Ali, K. Saleem, M.F. Hsieh, Copper(II), nickel(II), and ruthenium(III) complexes of an oxopyrrolidine-based heterocyclic ligand as anticancer agents, *J. Coord. Chem.*, 2014, **67**, 2110–2130.

34. I. Ali, I. Hussain, M.M. Sanagi, W.A.W. Ibrahim, H.Y. Aboul-Enein, Analyses of biguanides and related compounds in biological and environmental samples by HPLC, *J. Liq. Chromatogr. Relat. Technol.*, 2015, **38**, 303–321.
35. I. Ali, A. Hussain, K. Saleem, H.Y. Aboul-Enein, Separation and identification of antidepressant drugs in human plasma by SPE-TLC method, *J. Appl. Biopharm. Pharmacokinet.*, 2013, **1**, 12–17.
36. A. Mittal, R.K. Soni, K. Dutt, S. Singh, Scanning electron microscopic study of hazardous waste flakes of polyethylene terephthalate (PET) by aminolysis and ammonolysis, *J. Hazard. Mater.*, 2010, **178**, 390–396.
37. V.K. Gupta, R. Jain, A. Mittal, M. Mathur, S. Sikarwar, Photochemical degradation of the hazardous dye Safranin-T using TiO2 catalyst, *J. Colloid Interface Sci.*, 2007, **309**, 464–469.
38. V.K. Gupta, R. Jain, A. Mittal, T.A. Saleh, A. Nayak, S. Agarwal, S. Sikarwar, Photo-catalytic degradation of toxic dye amaranth on TiO2/UV in aqueous suspensions, *Mater. Sci. Eng. C*, 2012, **32**, 12–17.
39. P. Kumar, S. Mishra, A. Malik, S. Satya, Preparation and characterization of PEG-Mentha oil nanoparticles for housefly control, *Colloids Surf. B*, 2014, **116**, 707–713.
40. S. Sharma, A. Malik, S. Satya, Application of response surface methodology (RSM) for optimization of nutrient supplementation for Cr (VI) removal by Aspergillus lentulus AML05, *J. Hazard. Mater.*, 2009, **164**, 1198–1204.
41. S.K. Prajapati, P. Kaushik, A. Malik, V.K. Vijay, Phycoremediation coupled production of algal biomass, harvesting and anaerobic digestion: Possibilities and challenges, *Biotechnol. Adv.*, 2013, **31**, 1408–1425.
42. S. Kaushik, A. Juwarkar, A. Malik, S. Satya, Biological removal of Cr (VI) by bacterial isolates obtained from metal contaminated sites, *J. Environ. Sci. Health A*, 2008, **43**, 419–423.
43. L. Smykalla, P. Shukrynau, C. Mende, H. Lang, M. Knupfer, M. Hietschold, Photoelectron spectroscopy investigation of the temperature-induced deprotonation and substrate-mediated hydrogen transfer in a hydroxyphenyl-substituted porphyrin, *Chem. Phys.*, 2015, **450–451**, 39–45.
44. S. Seifert, A. Seifert, G. Brunklaus, K. Hofmann, T. Rüffer, H. Lang, S. Spange, Probing the surface polarity of inorganic oxides using merocyanine-type dyes derived from barbituric acid, *New J. Chem.*, 2012, **36**, 674–684.

45. J.M. Speck, M. Korb, T. Rüffer, A. Hildebrandt, H. Lang, Substituent influence on charge transfer interactions in α,α′ - diferrocenylthiophenes, *Organometallics*, 2014, **33**, 4813−4823.
46. N. Lenghor, J. Jakmunee, M. Vilen, R. Sara, G.D. Christian, K. Grudpan, Sequential injection redox or acid–base titration for determination of ascorbic acid or acetic acid, *Talanta*, 2002, **58**, 1139–1144.
47. P. Ampan, J. Ruzicka, R. Atallah, G.D. Christian, J. Jakmunee, K. Grudpan, Exploiting sequential injection analysis with bead injection and lab-on-valve for determination of lead using electrothermal atomic absorption spectrometry, *Anal. Chim. Acta*, 2003, **499**, 167–172.
48. T. Settheeworrarit, S.K. Hartwell, S. Lapanatnoppakhun, J. Jakmunee, G.D. Christian, K. Grudpan, Exploiting guava leaf extract as an alternative natural reagent for flow injection determination of iron, *Talanta*, 2005, **68**, 262–267.
49. Y. Luo, S. Nakano, D.A. Holman, J. Ruzicka, G.D. Christian, Sequential injection wetting film extraction applied to the spectrophotometric determination of chromium(VI) and chromium(III) in water, *Talanta*, 1997, **44**, 1563–1571.
50. V.P. Andreev, N.B. Ilyina, D.A. Holman, L.D. Scampavia, G.D. Christian, Experimental study of kinematic focusing. Comparison of electroinjection and sequential injection determination of copper, *Talanta*, 1999, **48**, 485–490.
51. O.S. Wolfbeis, Optical Sensors: Industrial, *Springer*, Germany, 2004.
52. B.R. Eggins. Chemical sensors and biosensors, *John Wiley & Sons*, Chichester, 2002.
53. J. Janata, A. Bezegh, A. Pungor, Bibliography of chemical sensors 1985−1987, *IE Sensors*, Salt Lake City, Utah,1988.
54. G.G. Cammann, E.A. Guilbault, H.K.R. Hal, O.S. Wolfbeis, The Cambridge defination of chemical sensors, *Cambridge Workshop in Chemical Sensors and Biosensors*, Cambridge University Press, New York, 1996.
55. C. McDonagh; C.S. Burke, B.D. MacCraith, Optical chemical sensors, *Chem. Rev.*, 2008, **108**, 400−422.
56. J.M. Lehn, Supra molecular chemistry: Concepts and perspectives, *Wiley-VCH*, Weinheim, 1995.
57. F. Vögtle, Supramolecular chemistry: An introduction, *Wiley*, Chichester, 1991.
58. J.M. Lehn, Toward complex matter: Supramolecular chemistry and self-organization, *Proc. Natl. Acad. Sci.*, 2002, **99**, 4763−4768.

59. H. Li, S. Gao, Z. Xi, A colorimetric and ‘‘turn-on” fluorescent chemosensor for Zn(II) based on coumarin Shiff-base derivative, *Inorg. Chem. Commun.*, 2009, **12**, 300–303.
60. A. Helal, M.H.O. Rashid, C.H. Choi, H.S. Kim, Chromogenic and fluorogenic sensing of $Cu^{2+}$ based on coumarin, *Tetrahedron*, 2011, **67**, 2794–2802.
61. F. Chen, G. Liu, Y. Shi, P. Xi, J. Cheng, J. Hong, R. Shen, X. Yao, D. Bai, Z. Zeng, A coumarin-derived fluorescent chemosensor for selectively detecting $Cu^{2+}$: Synthesis, DFT calculations and cell imaging applications, *Talanta*, 2014, **124**, 139–145.
62. Z. Su, K. Chen, Y. Guo, H. Qi, X.F. Yang, M. Zhao, A coumarin-based fluorescent chemosensor for $Zn^{2+}$ in aqueous ethanol media, *J. Fluoresc.*, 2010, **20**, 851–856.
63. N. Chattopadhyay, A. Mallick, S. Sengupta, Photophysical studies of 7-hydroxy-4-methyl-8-(4′-methylpiperazin-1′-yl) methylcoumarin: A new fluorescent chemosensor for zinc and nickel ions in water, *J. Photochem. Photobiol. A*, 2006, **177**, 55–60.
64. Z. Li, Y. Zhou, K. Yin, Z. Yu, Y. Li, J. Ren, A new fluorescence “turn-on” type chemosensor for $Fe^{3+}$ based on naphthalimide and coumarin, *Dyes Pigm.*, 2014, **105**, 7–11.
65. D. Sarkar, A. Pramanik, S. Biswas, P. Karmakar, T.K. Mondal, $Al^{3+}$ selective coumarin based reversible chemosensor: Application in living cell imaging and as integrated molecular logic gate, *RSC Adv.*, 2014, **4**, 30666–30672.
66. D. En, Y. Guo, B.T. Chen, B. Dong, M.J. Peng, Coumarin-derived $Fe^{3+}$-selective fluorescent turn-off chemosensors: Synthesis, properties, and applications in living cells, *RSC Adv.*, 2014, **4**, 248–253.
67. R. Sheng, P. Wang, W. Liu, X. Wu, S. Wu, A new colorimetric chemosensor for $Hg^{2+}$ based on coumarin azine derivative, *Sens. Actuators B*, 2008, **128**, 507–511.
68. S. Huang, S. He, Y. Lu, F. Wei, X. Zeng, L. Zhao, Highly sensitive and selective fluorescent chemosensor for $Ag^{+}$ based on a coumarin–$Se_2N$ chelating conjugate, *Chem. Commun.*, 2011, **47**, 2408–2410.
69. D. Maity, T. Govindaraju, Highly selective colorimetric chemosensor for $Co^{2+}$, *Inorg. Chem.*, 2011, **50**, 11282–11284.
70. N.C. Lim, L. Yao, H.C. Freake, C. Bruckner, Synthesis of a fluorescent chemosensor suitable for the imaging of Zinc(II) in live cells, *Bioorg. Med. Chem. Lett.*, 2003, **13**, 2251–2254.
71. Q.H. You, A.W.M. Lee, W.H. Chan, X.M. Zhu, K.C.F. Leung, A coumarin-based fluorescent probe for recognition of $Cu^{2+}$ and fast detection of histidine in hard-to-

transfect cells by a sensing ensemble approach, *Chem. Commun.*, 2014, **50**, 6207–6210.

72. J. Yao, W. Dou, W. Qin, W. Liu, A new coumarin-based chemosensor for $Fe^{3+}$ in water, *Inorg. Chem. Commun.*, 2009, **12**, 116–118.
73. R. Sheng, P. Wang, Y. Gao, Y. Wu, W. Liu, J. Ma, H. Li, S. Wu, Colorimetric test kit for $Cu^{2+}$ detection, *Org. Lett.*, 2008, **10**, 5015–5018.
74. M.X. Wang, X.M. Meng, M.Z. Zhu, Q.X. Guo, A novel selective fluorescent chemosensor for Cu(II), *Chin. Chem. Lett.*, 2007, **18**, 1403–1406.
75. G.J. Park, H.Y. Jo, K.Y. Ryu, C. Kim, A new coumarin-based chromogenic chemosensor for the detection of dual analytes $Al^{3+}$ and $F^{-}$, *RSC Adv.*, 2014, **4**, 63882–63890.
76. D. Sarkar, A.K. Pramanik, T.K. Mondal, Coumarin based fluorescent 'turn-on' chemosensor for $Zn^{2+}$: An experimental and theoretical study, *J. Lumin.*, 2014, **146**, 480–485.
77. L. Huang, J. Cheng, K. Xie, P. Xi, F. Hou, Z. Li, G. Xie, Y. Shi, H. Liu, D. Bai, Z. Zeng, $Cu^{2+}$-selective fluorescent chemosensor based on coumarin and its application in bioimaging, *Dalton Trans.*, 2011, **40**, 10815–10817.
78. H.S. Jung, P.S. Kwon, J.W. Lee, J.I. Kim, C.S. Hong, J.W. Kim, S. Yan, J.Y. Lee, J.H. Lee, T. Joo, J.S. Kim, Coumarin-derived $Cu^{2+}$-selective fluorescence sensor: Synthesis, mechanisms, and applications in living cells, *J. Am. Chem. Soc.*, 2009, **131**, 2008–2012.
79. M.X. Wang, X.M. Meng, M.Z. Zhu, Q.X. Guo, Novel fluorescent chemosensor for Ag+ based on coumarin fluorophore, *Chin. Chem. Lett.*, 2008, **19**, 977–980.
80. D. Sarkar, A.K. Pramanik, T.K. Mondal, Coumarin based dual switching fluorescent 'turn-on' chemosensor for selective detection of $Zn^{2+}$ and $HSO_4^{-}$: An experimental and theoretical study, *RSC Adv.*, 2014, **4**, 25341–25347.
81. N.C. Lim, J.V. Schuster, M.C. Porto, M.A. Tanudra, L. Yao, H.C. Freake, C. Bruckner, Coumarin-based chemosensors for Zinc(II): Toward the determination of the design algorithm for CHEF-type and ratiometric probes, *Inorg. Chem.*, 2005, **44**, 2018–2030.
82. H.S. Jung, K.C. Ko, G.H. Kim, A.R. Lee, Y.C, Na, C. Kang, J.Y. Lee, J.S. Kim, Coumarin-based thiol chemosensor: Synthesis, turn-on mechanism, and its biological application, *Org. Lett.*, 2011, **13**, 1498–1501.

83. C.Y. Li, X.B. Zhang, Z. Jin, R. Han, G.L. Shen, R.Q. Yu, A fluorescent chemosensor for cobalt ions based on a multi-substituted phenol-ruthenium(II) tris(bipyridine) complex, *Anal. Chim. Acta*, 2006, **580**, 143–148.

84. A. Reynal, J. Etxebarria, N. Nieto, S. Serres, E. Palomares, A. Vidal-Ferran, A bipyridine-based "naked-eye" fluorimetric $Cu^{2+}$ chemosensor, *Eur. J. Inorg. Chem.*, 2010, 1360–1365.

85. C.L. He, F.L. Ren, X.B. Zhang, Y.Y. Dong, Y. Zhao, A fluorescent chemosensor for copper(II) based on a carboxylic acid-functionalized tris(2,2′-bipyridine)-ruthenium(II) complex, *Anal. Sci.*, 2006, **22**, 1547–1551.

86. A.A.G. Al Abdel Hamid, M. Al-Khateeb, Z.A. Tahat, M. Qudah, S.M. Obeidat, A.M. Rawashdeh, A selective chemosensor for mercuric ions based on 4-aminothiophenol-ruthenium(II) bis(bipyridine) complex, *Int. J. Inorg. Chem.*, 2011, 6 pp.

87. M. Li, Q. Liang, M. Zheng, C. Fang, S. Peng, M. Zhao, An efficient ruthenium tris(bipyridine)-based luminescent chemosensor for recognition of Cu(II) and sulfide anion in water, *Dalton Trans.*, 2013, **42**, 13509–13515.

88. H.H. Wu, Y.L. Sun, C.F. Wan, S.T. Yang, S.J. Chen, C.H. Hu, A.T. Wu, Highly selective and sensitive fluorescent chemosensor for $Hg^{2+}$ in aqueous solution, *Tetrahedron Lett.*, 2012, **53**, 1169–1172.

89. H.J. Huang, J.L. Chir, H.J. Cheng, S.J. Chen, C.H. Hu, A.T. Wu, Synthesis of highly selective indole-based sensors for mercuric ion, *J. Fluoresc.*, 2011, **21**, 1021–1026.

90. Y. Son, H. Kim, S.H. Kim, Synthesis and chemosensing properties of indole based donor–π–acceptor dye material, *J. Nanosci. Nanotechnol.*, 2014, **14**, 7976–7980.

91. Y.L. Sun, A.T. Wu, Indole-based fluorescent sensors for selective detection of $Hg^{2+}$, *J. Fluoresc.*, 2013, **23**, 629–634.

92. P. Kaur, S. Kaur, K. Singh, P.R. Sharma, T. Kaur, Indole-based chemosensor for $Hg^{2+}$ and $Cu^{2+}$ ions: Applications in molecular switches and live cell imaging, *Dalton Trans.*, 2011, **40**, 10818–10821.

93. D.T. Shi, B. Zhang, Y.X. Yang, C.C. Guan, X.P. He, Y.C. Li, G.R. Chen, K. Chen, Bis-triazolyl indoleamines as unique "off-approach-on" chemosensors for copper and fluorine, *Analyst*, 2013, **138**, 2808–2811.

94. Z.J. Jiang, H.S. Lv, J. Zhu, B.X. Zhao, New fluorescent chemosensor based on quinoline and coumarin for $Cu^{2+}$, *Synth. Met.*, 2012, **162**, 2112–2116.

95. K. Zhang, Z. Yang, B. Wang, S.B. Sun, Y.D. Li, T. Li, Z. Liu, J. An, A highly selective chemosensor for $Al^{3+}$ based on 2-oxo-quinoline-3-carbaldehyde Schiff-base, *Spectrochim. Acta A*, 2014, **124**, 59–63.
96. H. Kim, J. Kang, K.B. Kim, E.J. Song, C. Kim, A highly selective quinoline-based fluorescent sensor for Zn(II), *Spectrochim. Acta A*, 2014, **118**, 883–887.
97. D. Sarkar, A. Pramanik, S. Jana, P. Karmakar, T.K. Mondal, Quinoline based reversible fluorescent 'turn-on' chemosensor for the selective detection of $Zn^{2+}$: Application in living cell imaging and as INHIBIT logic gate, *Sens. Actuators B*, 2015, **209**, 138–146.
98. Y. Ma, F. Wang, S. Kambam, X. Chen, A quinoline-based fluorescent chemosensor for distinguishing cadmium from zinc ions using cysteine as an auxiliary reagent, *Sens. Actuators B*, 2013, **188**, 1116–1122.
99. Y.J. Jang, Y.H. Yeon, H.Y. Yang, J.Y. Noh, I.H. Hwang, C. Kim, A colorimetric and fluorescent chemosensor for selective detection of $Cr^{3+}$ and $Al^{3+}$, *Inorg. Chem. Commun.*, 2013, **33**, 48–51.
100. T. Liu, S. Liu, Responsive polymers-based dual fluorescent chemosensors for $Zn^{2+}$ ions and temperatures working in purely aqueous media, *Anal. Chem.*, 2011, **83**, 2775–2785.
101. I. Ravikumar, P. Ghosh, Zinc(II) and PPi selective fluorescence off-on-off functionality of a chemosensor in physiological conditions, *Inorg. Chem.*, 2011, **50**, 4229–4231.
102. H.M. Park, B.N. Oh, J.H. Kim, W. Qiong, I.H. Hwang, K.D. Jung, C. Kim, J. Kim, Fluorescent chemosensor based-on naphthol–quinoline for selective detection of aluminum ions, *Tetrahedron Lett.*, 2011, **52**, 5581–5584.
103. K. Ghosh, D. Tarafdar, A new quinoline-based chemosensor in ratiometric sensing of $Hg^{2+}$ ions, *Supramol. Chem.*, 2013, **25**, 127–132.
104. Y. Zhang, Y. Yan, S. Chen, Z. Gao, H. Xu, 'Naked-eye' quinoline-based 'reactive' sensor for recognition of $Hg^{2+}$ ion in aqueous solution, *Bioorg. Med. Chem. Lett.*, 2014, **24**, 5373–5376
105. X.B. Li, Z.G. Niu, L.L. Chang, M.X. Chen, E.J. Wang, Quinoline-based colorimetric chemosensor for $Cu^{2+}$: $Cu^{2+}$-induced deprotonation leading to color change, *Chin. Chem. Lett.*, 2014, **25**, 80–82.
106. C.Y. Huang, Y. Jhong, J.L. Chir, A.T. Wu, A Quinoline derivative as an efficient sensor to detect selectively $Al^{3+}$ ion, *J. Fluoresc.*, 2014, **24**, 991–994.

107. B.S. Kim, S.H. Kim, Y.S. Kim, S.H. Kim, Y.A. Son, Synthesis and characterization of quinoline-based dye sensor, *Mol. Cryst. Liq. Cryst.*, 2009, **504**, 173–180.
108. S. Elcin, H. Deligöz, A versatile approach toward chemosensor for $Hg^{2+}$ based on parasubstituted phenylazocalix[4]arene containing mono ethyl ester unit, *Dyes Pigm.*, 2014, **107**, 166–173.
109. S.K. Kim, J.H. Bok, R.A. Bartsch, J.Y. Lee, J.S. Kim, A fluoride-selective PCT chemosensor based on formation of a static pyrene excimer, *Org. Lett.*, 2005, **7**, 4839–4842.
110. S. Patra, R. Lo, A. Chakraborty, R. Gunupuru, D. Maity, B. Ganguly, P. Paul, Calix[4]arene based fluorescent chemosensor bearing coumarin as fluorogenic unit: Synthesis, characterization, ion-binding property and molecular modelling, *Polyhedron*, 2013, **50**, 592–601.
111. J.S. Kim, D.T. Quang, Calixarene-derived fluorescent probes, *Chem. Rev.*, 2007, **107**, 3780–3799.
112. X. Hu, C. Li, X. Song, D. Zhang, Y. Li, A new $Cu^{2+}$-selective self-assembled fluorescent chemosensor based on thiacalix[4]arene, *Inorg. Chem. Commun.*, 2011, **14**, 1632–1635.
113. M. Kumar, V. Bhalla, A. Dhir, J.N. Babu, A $Ni^{2+}$ selective chemosensor based on partial cone conformation of calix[4]arene, *Dalton Trans.*, 2010, **39**, 10116–10121.
114. E. Brunetti, J.F. Picron, K. Flidrova, G. Bruylants, K. Bartik, I. Jabin, Fluorescent chemosensors for anions and contact ion pairs with a cavity-based selectivity, *J. Org. Chem.*, 2014, **79**, 6179–6188.
115. J.M. Liu, Q.Y. Zheng, J.L. Yang, C.F. Chen, Z.T. Huang, A new fluorescent chemosensor for $Fe^{3+}$ and $Cu^{2+}$ based on calix[4]arene, *Tetrahedron Lett.*, 2002, **43**, 9209–9212.
116. M.A. Qazi, I. Qureshi, S. Memon, Calix[4]arene based chemosensor for selective complexation of Cd(II) and Cu(II), *J. Mol. Struct.*, 2010, **975**, 69–77.
117. A.B. Othman, J.W. Lee, J.S. Wu, J.S. Kim, R. Abidi, P. Thuery, J.M. Strub, A.V. Dorsselaer, J. Vicens, Calix[4]arene-based, $Hg^{2+}$-induced intramolecular fluorescence resonance energy transfer chemosensor, *J. Org. Chem.*, 2007, **72**, 7634–7640.
118. N.J. Wang, C.M. Sun, W.S. Chung, A highly selective fluorescent chemosensor for $Ag^{+}$ based on calix[4]arene with lower-rim proximal triazolylpyrenes, *Sens. Actuators B*, 2012, **171–172**, 984–993.

119. Y.H. Lee, M.H. Lee, J.un Feng Zhang, Jong Seung Kim, Pyrene excimer-based calix[4] arene FRET chemosensor for mercury(II), *J. Org. Chem.*, 2010, **75**, 7159–7165.
120. C. Fischer, M. Stapf, W. Seichter, E. Weber, Fluorescent chemosensors based on a new type of lower rim-dansylated and bridge-substituted calix[4]arenes, *Supramol. Chem.*, 2013, **25**, 371–383.
121. Z. Liang, Z. Liu, Y. Gao, A selective colorimetric chemosensor based on calixarene framework for lanthanide ions-$Dy^{3+}$ and $Er^{3+}$, *Tetrahedron Lett.*, 2007, **48**, 3587–3590.
122. G.G. Talanova, E.D. Roper, N.M. Buie, M.G. Gorbunova, R.A. Bartsch, V.S. Talanov, Novel fluorogenic calix[4]arene-bis(crown-6-ether) for selective recognition of thallium(I), *Chem. Commun.*, 2005, 5673–5675.
123. Y.Q. Weng, Y.L. Teng, F. Yue, Y.R. Zhong, B.H. Ye, A new selective fluorescent chemosensor for Cu(II) ion based on zinc porphyrin-dipyridylamino, *Inorg. Chem. Commun.*, 2007, **10**, 443–446.
124. Y. Chen, J. Jiang, Porphyrin-based multi-signal chemosensors for $Pb^{2+}$ and $Cu^{2+}$, *Org. Biomol. Chem.*, 2012, **10**, 4782–4787.
125. F. D'Souza, G.R. Deviprasad, Y.Y. Hsieh, A novel porphyrin based fluorescent chemosensor using a molecular recognition approach, *Chem. Commun.*, 1997, 533–534.
126. C.Y. Li, X.B. Zhang, Y.Y. Dong, Q.J. Ma, Z.X. Han, Y. Zhao, G.L. Shen, R.Q. Yu, A porphyrin derivative containing 2-(oxymethyl)pyridine units showing unexpected ratiometric fluorescent recognition of $Zn^{2+}$ with high selectivity, *Anal. Chim. Acta*, 2008, **616**, 214–221.
127. C.Y. Li, F. Xu, Y.F. Li, A fluorescent chemosensor for silver ions based on porphyrin compound with high selectivity, *Spectrochim. Acta A*, 2010, **76**, 197–201.
128. Z.X. Han, H.Y. Luo, X.B. Zhang, R.M. Kong, G.L. Shen, R.Q. Yu, A ratiometric chemosensor for fluorescent determination of $Hg^{2+}$ based on a new porphyrin-quinoline dyad, *Spectrochim. Acta A*, 2009, **72**, 1084–1088.
129. H.Y. Luo, J.H. Jiang, X.B. Zhang, C.Y. Li, G.L. Shen, R.Q. Yu, Synthesis of porphyrin-appended terpyridine as a chemosensor for cadmium based on fluorescent enhancement, *Talanta*, 2007, **72**, 575–581.
130. Q. Guo, Q. Zeng, X. Zhang, X. Zhou, Highly sensitive detection of mercury (II) in aqueous media by tetraphenylporphyrin with a metal ion receptor, *Supramol. Chem.*, 2014, **26**, 836–842.

131. J. Isaad, A.E. Achari, A water soluble fluorescent BODIPY dye with azathiacrown ether functionality for mercury chemosensing in environmental media, *Analyst*, 2013, **138**, 3809–3819.
132. Y.C. Hsieh, J.L. Chir, H.H. Wu, C.Q. Guo, A.T. Wu, Synthesis of a sugar-aza-crown ether-based cavitand as a selective fluorescent chemosensor for $Cu^{2+}$ ion, *Tetrahedron Lett.*, 2010, **51**, 109–111.
133. H. Zhou, J. Wang, Y. Chen, W. Xi, Z. Zheng, D. Xu, Y. Cao, G. Liu, W. Zhu, J. Wu, Y. Tian, New diaminomaleonitrile derivatives containing aza-crown ether: Selective, sensitive and colorimetric chemosensors for Cu(II), *Dyes Pigm.*, 2013, **98**, 1–10.
134. D. Liu, K. Tang, W. Liu, C. Su, X. Yan, M. Tan, Y. Tang, A novel luminescent chemosensor for detecting $Hg^{2+}$ based on the pendant benzo crown ether terbium complex, *Dalton Trans.*, 2010, **39**, 9763–9765.
135. W.S. Xia, R.H. Schmehl, C.J. Li, A fluorescent 18-crown-6 based luminescence sensor for lanthanide ions, *Tetrahedron*, 2000, **56**, 7045–7049.
136. H. Li, L. Li, B. Yin, Highly selective fluorescent chemosensor for $Fe^{3+}$ detection based on diaza-18-crown-6 ether appended with dual coumarins, *Inorg. Chem. Commun.*, 2014, **42**, 1–4.
137. B. Witulski, M. Weber, U. Bergstrasser, J.P. Desvergne, D.M. Bassani, H. Bouas-Laurent, Novel alkali cation chemosensors based on N-9-anthrylaza-crown ethers, *Org. Lett.*, 2001, **3**, 1467–1470.
138. J. Kim, Y. Oka, T. Morozumi, E.W. Choi, H. Nakamura, Steric effects on controlling of photoinduced electron transfer action of anthracene modified benzo-15-crown-5 by complexation with $Mg^{2+}$ and $Ca^{2+}$, *Tetrahedron*, 2011, **67**, 4814–4819.
139. F.A. Abebe, E.Sinn, Fluorescein-based fluorescent and colorimetric chemosensors for copper in aqueous media, *Tetrahedron Lett.*, 2011, **52**, 5234–5237.
140. F.A. Abebe, C.S. Eribal, G. Ramakrishna, E. Sinn, A 'turn-on' fluorescent sensor for the selective detection of cobalt and nickel ions in aqueous media, *Tetrahedron Lett.*, 2011, **52**, 5554–5558.
141. C. Liu, S. Huang, H. Yao, S. He, Y. Lu, L. Zhao, X. Zeng, Preparation of fluorescein-based chemosensors and their sensing behaviors toward silver ions, *RSC Adv.*, 2014, **4**, 16109–16114.
142. Y. Wang, H. Wu, J. Sun, X. Liu, J. Luo, M. Chen, A novel chemosensor based on rhodamine derivative for colorimetric and fluorometric detection of $Cu^{2+}$ in aqueous solution, *J. Fluoresc.*, 2012, **22**, 799–805.

143. Y. Zhou, J. Zhang, L. Zhang, Q. Zhang, T. Ma, J. Niu, A rhodamine-based fluorescent enhancement chemosensor for the detection of $Cr^{3+}$ in aqueous media, *Dyes Pigm.*, 2013, **97**, 148–154.
144. N.R. Chereddy, K. Suman, P.S. Korrapati, S. Thennarasu, A.B. Mandal, Design and synthesis of rhodamine based chemosensors for the detection of $Fe^{3+}$ ions, *Dyes Pigm.*, 2012, **95**, 606–613.
145. J. Mao, L. Wang, W. Dou, X. Tang, Y. Yan, W. Liu, Tuning the selectivity of two chemosensors to Fe(III) and Cr(III), *Organic Lett.*, 2007, **9**, 4567–4570.
146. S. Pal, B. Sen, M. Mukherjee, K. Dhara, E. Zangrando, S.K. Mandal, A.R. Khuda-Bukhsh, P. Chattopadhyay, Effect of substituents on FRET in rhodamine based chemosensors selective for $Hg^{2+}$ ions, *Analyst*, 2014, **139**, 1628–1631.
147. N.R. Chereddy, S. Thennarasu, A.B. Mandal, A new triazole appended rhodamine chemosensor for selective detection of $Cu^{2+}$ ions and live-cell imaging, *Sens. Actuators B*, 2012, **171–172**, 294–301.
148. H. Ju, M.H. Lee, J. Kim, J.S. Kim, J. Kim, Rhodamine-based chemosensing monolayers on glass as a facile fluorescent "turn-on" sensing film for selective detection of $Pb^{2+}$, *Talanta*, 2011, **83**, 1359–1363.
149. H. Yu, W. Sheng, Y.A Son, Synthesis and optical determination in rhodamine-based chemosensors toward $Hg^{2+}$, *Mol. Cryst. Liq. Cryst.*, 2012, **568**, 117–124.
150. H.Y. Lee, H. Son, J.M. Lim, J. Oh, D. Kang, W.S. Han, J.H. Jung, BODIPY-functionalized gold nanoparticles as a selective fluoro-chromogenic chemosensor for imaging $Cu^{2+}$ in living cells, *Analyst*, 2010, **135**, 2022–2027.
151. S. Yin, W. Yuan, J. Huang, D. Xie, B. Liu, K. Jiang, H. Qiu, A BODIPY derivative as a colorimetric, near-infrared and turn-on chemosensor for $Cu^{2+}$, *Spectrochim. Acta A*, 2012, **96**, 82–88.
152. M. Vedamalai, S.P. Wu, A BODIPY-based highly selective fluorescent chemosensor for $Hg^{2+}$ ions and its application in living cell imaging, *Eur. J. Org. Chem.*, 2012, 1158–1163.
153. X. Qi, E.J. Jun, L. Xu, S.J. Kim, J.S.J. Hong, Y.J. Yoon, J. Yoon, New BODIPY derivatives as off-on fluorescent chemosensor and fluorescent chemodosimeter for $Cu^{2+}$: Cooperative selectivity enhancement toward $Cu^{2+}$, *J. Org. Chem.*, 2006, **71**, 2881–2884.

154. S. Yin, V. Leen, S.V. Snick, N. Boens, W. Dehaen, A highly sensitive, selective, colorimetric and near-infrared fluorescent turn-on chemosensor for $Cu^{2+}$ based on BODIPY, *Chem. Commun.*, 2010, **46**, 6329–6331.
155. L. Wang, G. Fang, D. Cao, A novel phenol-based BODIPY chemosensor for selective detection $Fe^{3+}$ with colorimetric and fluorometric dual-mode, *Sens. Actuators B*, 2015, **207**, 849–857.
156. C.C. Zhao, Y. Chen, H.Y. Zhang, B.J. Zhou, X.J. Lv, W.F. Fu, A BODIPY-based fluorescent chemosensor for $Cu^{2+}$ and biological thiols, and its application as a $Cu^{2+}$ probe in live cell imaging, *J. Photochem. Photobiol. A*, 2014, **282**, 41–46.
157. A. Barba-Bon, L. Calabuig, A.M. Costero, S. Gil, R. Martinez-Manez, F. Sancenon, Off–on BODIPY-based chemosensors for selective detection of $Al^{3+}$ and $Cr^{3+}$ versus $Fe^{3+}$ in aqueous media, *RSC Adv.*, 2014, **4**, 8962–8965.
158. Q. Li, Y. Guo, S. Shao, A BODIPY based fluorescent chemosensor for Cu(II) ions and homocysteine/cysteine, *Sens. Actuators B*, 2012, **171–172**, 872–877.
159. J. Huang, X. Ma, B. Liu, L. Cai, Q. Li, Y. Zhang, K. Jiang, S. Yin, A colorimetric and ratiometric turn-on BODIPY-based fluorescent probe for double-channel detection of $Cu^{2+}$ and $Hg^{2+}$, *J. Lumin.*, 2013, **141**,130–136.
160. T. Keawwangchai, B. Wanno, N. Morakot, S. Keawwangchai, Optical chemosensors for Cu(II) ion based on BODIPY derivatives: An experimental and theoretical study, *J. Mol. Model.*, 2013, **19**, 4239–4249.
161. M. Vedamalai, S.P. Wu, A BODIPY-based colorimetric and fluorometric chemosensor for Hg(II) ions and its application to living cell imaging, *Org. Biomol. Chem.*, 2012, **10**, 5410–5416.
162. J.R. Lin, C.J. Chu, P. Venkatesan, S.P. Wu, Zinc(II) and pyrophosphate selective fluorescence probe and its application to living cell imaging, *Sens. Actuators B*, 2015, **207**, 563–570.
163. S. Atilgan, I. Kutuk, T. Ozdemir, A near IR di-styryl BODIPY-based ratiometric fluorescent chemosensor for Hg(II), *Tetrahedron Lett.*, 2010, **51**, 892–894.
164. M.J. Culzoni, A.M. de la Pena, A. Machuca, H.C. Goicoechea, R. Babiano, Rhodamine and BODIPY chemodosimeters and chemosensors for the detection of $Hg^{2+}$, based on fluorescence enhancement effects, *Anal. Methods*, 2013, **5**, 30–49.
165. M. Baruah, E.D. Huntimer, M.S. Ahmed, A.D. Hoppe, F.T. Halaweish, Selective BODIPY based fluorescent chemosensor for imaging $Pb^{2+}$ ion in living cells, *Tetrahedron Lett.*, 2012, **53**, 4273–4275.

166. M.J. Culzoni, A.M. de la Pena, A. Machuca, H.C. Goicoechea, R. Brasca, R. Babiano, Photoinduced electron transfer fluorometric Hg(II) chemosensor based on a BODIPY armed with a tetrapod receptor, *Talanta*, 2013, **117**, 288–296.
167. R. Azadbakht, J. Khanabadi, A novel aluminum-sensitive fluorescent nano-chemosensor based on naphthalene macrocyclic derivative, *Tetrahedron*, 2013, **69**, 3206–3211.
168. S. Jang, P. Thirupathi, L.N. Neupane, J. Seong, H. Lee, W.I. Lee, K.H. Lee, Highly sensitive ratiometric fluorescent chemosensor for silver ion and silver nanoparticles in aqueous solution, *Org. Lett.*, 2012, **14**, 4746–4749.
169. A. Singh, T. Raj, T. Aree, N. Singh, Fluorescent organic nanoparticles of biginelli-based molecules: Recognition of $Hg^{2+}$ and $Cl^{-}$ in an aqueous medium, *Inorg. Chem.*, 2013, **52**, 13830−13832.
170. N. Singh, R.C. Mulrooney, N. Kaur, J.F. Callan, A nanoparticle based chromogenic chemosensor for the simultaneous detection of multiple analytes, *Chem. Commun.*, 2008, 4900–4902.
171. P. Zhang, J. Chen, F. Huang, Z. Zeng, J. Hu, P. Yi, F. Zeng, S. Wu, One-pot fabrication of polymer nanoparticle-based chemosensors for $Cu^{2+}$ detection in aqueous media, *Polym. Chem.*, 2013, **4**, 2325–2332.
172. H. Sharma, V.K. Bhardwaj, N. Singh, Nanomolar detection of $Ag^{I}$ ions in aqueous medium by using naphthalimide-based imine-linked fluorescent organic nanoparticles-application in environmental Samples, *Eur. J. Inorg. Chem.*, 2014, 5424–5431.
173. A. Saini, J. Singh, R. Kaur, N. Singh, N. Kaur, Naphthalimide-based organic nanoparticles for aluminium recognition in acidic soil and aqueous media, *New J. Chem.*, 2014, **38**, 4580–4586.
174. F. Gai, X. Li, T. Zhou, X. Zhao, D. Lu, Y. Liu, Q. Huo, Silica cross-linked nanoparticles encapsulating a phenothiazine-derived Schiff base for selective detection of Fe(III) in aqueous media, *J. Mater. Chem. B*, 2014, **2**, 6306–6312.
175. V. Tharmaraj, K. Pitchumani, A highly selective ratiometric fluorescent chemosensor for Cu(II) based on dansyl-functionalized thiol stabilized silver nanoparticles, *J. Mater. Chem. B*, 2013, **1**, 1962–1967.
176. E. Delgado-Pinar, N. Montoya, M. Galiana, M.T. Albelda, J.C. Frias, H.R. Jimenez, E. Garcia-Espana, J. Alarcon, Preparation of $Hg^{2+}$ selective fluorescent chemosensors

based on surface modified core–shell aluminosilicate nanoparticles, *New J. Chem.*, 2010, **3**, 567–570.

177. N. Vasimalai, G. Sheeba, S. Abraham John, Ultrasensitive fluorescence-quenched chemosensor for Hg(II) in aqueous solution based on mercaptothiadiazole capped silver nanoparticles, *J. Hazard. Mater.*, 2012, **213–214**, 193–199.
178. M.R. Ganjali, M. Hosseini, M. Khobi, S. Farahani, M. Shaban, F. Faridbod, A. Shafiee, P. Norouzi, A novel europium-sensitive fluorescent nano-chemosensor based on new functionalized magnetic core–shell $Fe_3O_4$@$SiO_2$ nanoparticles, *Talanta*, 2013, **115**, 271–276.
179. R. Jain, D.C. Tiwari, P. Karolia, Highly sensitive and selective polyaniline–zinc oxide nanocomposite sensor for betahistine hydrochloride in solubilized system, *J. Mol. Liq.*, 2014, **196**, 308–313.
180. A. Sinha, Dhanjai, R. Jain, Electrocatalytic determination of α 2-adrenergic agonist tizanidine at graphene–silicon dioxide nanocomposite sensor, *Mater. Res. Bull.*, 2015, **65**, 307–314.
181. R. Jain, D.C. Tiwari, P. Pandey, Highly selective and sensitive graphene based electrochemical sensor for quantification of receptor agonist rizatriptan, *Electroanal.*, 2013, **25**, 1363–1367.
182. A. Sharma, V.K. Rao, D.V. Kamboj, R. Jain, Electrochemical immunosensor for Staphylococcal Enterotoxin B (SEB) based on platinum nanoparticles modified electrode using hydrogen evolution inhibition aproach, *Electroanal.*, 2014, **26**, 2320–2327.
183. A. Baghizadeh, S. Ranjbar, V.K. Gupta, M. Asif, S. Pourseyedi, M.J. Karimi, R. Mohammadinejad, Green synthesis of silver nanoparticles using seed extract of Calendula officinalis in liquid phase, *J. Mol. Liq.*, 2015, **207**, 159–163.
184. H.K. Maleh, A.L. Sanati, V.K. Gupta, M. Yoosefian, M. Asif, A. Bahari, A voltammetric biosensor based on ionic liquid/NiO nanoparticle modified carbon paste electrode for the determination of nicotinamide adenine dinucleotide (NADH), *Sens. Actuators B*, 2014, **204**, 647–654.
185. T. Sinha, M. Ahmaruzzaman, A. Bhattacharjee, M. Asif, V.K. Gupta, Lithium dodecyl sulphate assisted synthesis of Ag nanoparticles and its exploitation as a catalyst for the removal of toxic dyes, *J. Mol. Liq.*, 2015, **201**, 113–123.
186. L.D. Lavis, R.T. Raines, "Bright ideas for chemical biology", *ACS Chem. Biol.*, 2008, **3**, 142–155.

# CHAPTER 2
# Theory and Methodology

## 2.1. Photoluminescence

Most elementary particles are in their ground state at room temperature. The particles absorb photons with proper energy when these are exposed to an electromagnetic irradiation. The energy absorbed by the element leads to a rapid formation of an electronically excited state which is followed by dissipation of the excess energy in different forms (Figure 2.1). The term 'photoluminescence' can be defined as an optical property of a substance which absorbs photon upon irradiation and release them radiatively [1]. Depending on the nature of the excited state, mainly the emission light can be divided into two categories as fluorescence and phosphorescence. Details related to the photoluminescence process will be discussed in the following subsections.

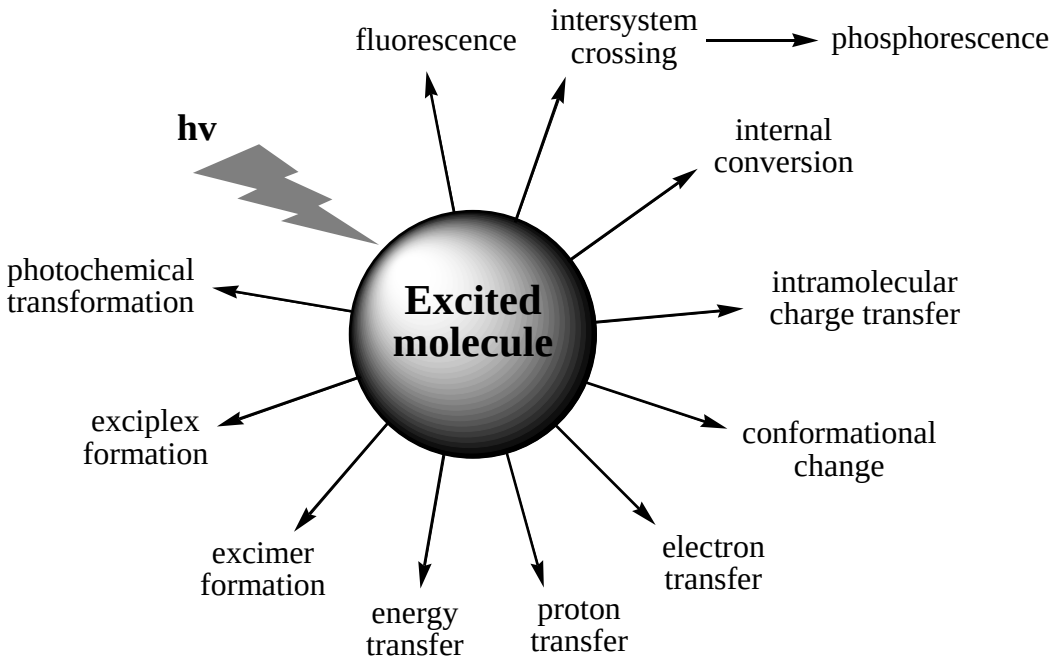


**Figure 2.1.** Possible de-excitation pathways of excited molecules.

### 2.1.1. Absorption of light and electronically-excited states

Once a molecule is irradiated by photons, absorption of photons and transition of an electron from highest occupied molecular orbital (HOMO, HOMO−1 etc.) to lowest unoccupied molecular orbital (LUMO, LUMO+1 etc.) of the molecule will happen very rapidly. In most cases, a photon of light of wavelength lying in the UV-Visible region of the electromagnetic spectrum is sufficient in energy for such electronic transitions. Because of this reason, the region of the UV-Visible spectrum covering 200–800 nm range. Besides, other regions of the electromagnetic spectrum may induce interesting changes on the molecule upon irradiation. They are roughly summarized in the table 2.1.

**Table 2.1.** Influence of the electromagnetic radiations on molecular structures

| Radiation | Wavelength | Photon Energy | Results of Absorption |
|---|---|---|---|
| Gamma rays | < 0.01 nm | > 1 MeV | Nuclear reactions |
| X rays | 0.01–10 nm | 124 eV–120 keV | Inner atomic electron transitions |
| UV | 10–400 nm | 3.1–124 eV | Outer atomic electron transitions |
| Visible | 400–750 nm | 1.7–3.1 eV | Outer atomic electron transitions |
| Infrared | 750 nm–15 μm | 80 meV–1.7 eV | Molecular vibrations |
| Far IR | 15 μm–1mm | 1.2 meV–80 meV | Molecular rotations |
| Radar | 1 mm–1 m | 1.2 μeV–1.2 meV | Oscillation of mobile electrons |

Optical radiation is subdivided into ultraviolet, visible light and near-infrared (NIR, 750–1000 nm). Near-infrared absorption can be achieved in extended conjugation [2] or mixed-valence system [3].

When matter is hit by radiation, the radiation might be absorbed, transmitted, scattered or reflected. Matter may absorb radiation of a distinct frequency; the energy of the frequency relates to the difference between two electron energy-levels. The relationship between absorbance, the concentration of the absorber and the path length is described by the Lambert-Beer Law:

$$\mathbf{A} = \boldsymbol{\varepsilon} \times \mathbf{c} \times \mathbf{l} = \log_{10} \frac{\mathbf{I_0}}{\mathbf{I}}$$

where A = Absorbance, ε = molar absorption coefficient, c = Concentration, l = absorption path length, $I_0$ = Incident light, I = Transmitted light

The absorption spectrum of a sample can be drawn by UV-Vis absorption spectroscopy. At a specific wavelength, the intensity of the absorption depends on the molar absorption coefficient (**ε**) of the molecule. It is the probability of an electronic transition at a specific wavelength of the particular molecule. In other words, its value gives us the information of how 'allowed' a transition is. 'Allowed' and 'forbidden' terms are beyond the classical physics, as they represent the results of quantum mechanical calculations.

As mentioned before, the value of absorption coefficient indicates the probability of an electronic transition from ground state to excited state of a molecule. The selection rules (a.k.a. selection rules) control the possible transitions and they are mainly based on two factors which are spin and symmetry. Spin component displays kind of a concrete property such that an electronic excitation is allowed if and only if the total spin remains unchanged during the transition. In other words, if a spin change is involved in the transition (e.g. singlet

to triplet), then the transition is said to be forbidden. In contrast, the symmetry component is related to the symmetry of the ground and excited states which determine the transitions to be allowed or forbidden. By just considering the symmetry it is very difficult to conclude that the transition is going to be forbidden. In idealized conditions, the symmetry calculations are done for the molecules, but for a real molecule the symmetry may be distorted by the presence of some environmental effects such as solvent or a heavy atom on the molecule. Keeping all these in mind and by analyzing the absorption coefficient value it can be concluded that how a transition is allowed or forbidden. When **ε** is measured to be greater than $10^5$ $M^{-1}$ $cm^{-1}$, the transition is said to be 'fully allowed'. If it is smaller than 100 $M^{-1}$ $cm^{-1}$, then the transition is 'forbidden', which means that the molecule does not absorb the photon well at this wavelength. The transitions are said to be 'partially allowed' when the **ε** value lying in between $10^2$–$10^4$ $M^{-1}$ $cm^{-1}$ and this condition is coming from the symmetry component. Therefore, if a transition is spin forbidden and symmetry allowed, then the probability of it is very low (**ε** < 100). On the other hand, if it is spin allowed but symmetry forbidden, then moderate absorption is observed and **ε** value is going to be between $10^2$–$10^4$ $M^{-1}$ $cm^{-1}$ and both spin and symmetry allowed, then strong absorption is taken place.

The shape of spectra which is related to the **ε** value at each wavelength is another important consequence regarding the light absorption. It is a well-known fact that an electronic transition and number of changes in both electronic and vibrational states occurs during the process of absorption of the light. Due to the overlap amount of the two vibrational wave functions in an individual electronic transition, It may be higher or lower than the others that the probability of a transition between vibrational levels of each orbital (i.e. HOMO and LUMO). For example, the greater overlap between wave functions of vibronic states occurred when the lower and upper electronic states have similar internuclear separations, resulting in the more intense transitions between the vibrational levels of the electronic states. Franck-Condon principle manages all these transitions, according to this principle: since the transition from one electronic state to another takes place very rapidly, nuclei of the vibrating molecule can be assumed to be fixed during the electronic transition. In other words, nuclei move much more slowly than the lighter electrons, so the nuclear geometry would remain very much the same (in terms of position and velocity) as it was before the electronic transition. As a consequence of this principle, an electronic transition is represented by a vertical arrow (Figure 2.2), indicating the electronic transitions within stationary nuclei [4].

A hypothetical Morse potential diagram of the ground and excited states and probable absorption fluorescence spectra was proposed by American physicist Philip M. Morse and are depicted in Figure 2.2. During the transition, it can be claimed that the internuclear distance has remained unchanged (Figure 2.2, left). However, there is a little shift between the nuclear coordinates of ground and excited states of the molecule which is represented as $\mathbf{r}_{01}$. There are many vibronic transitions those are allowed are also shown in the diagram.

Though, we can say that some of the transitions are more probable than others via qualitative analysis. It means that the intensities of each vibronic transitions are different. The most feasible transitions between the vibrational levels of HOMO and LUMO will be the one where the wave functions overlap the most along the vertical arrow. The best overlap in our case is between $\nu = 0$ and $\nu = 2$ in the ground state and excited state, respectively. Thus, these transitions are observed as the most intense absorption band in the absorption spectra. Generally organic molecules do not show those fine structures in solutions and solid phases because of the large number of vibrational levels in the electronic states and interactions between themselves and solvent molecules. Relatively, they appear as broad curves, like a line drawn over the peak maxima of the individual transition peaks. In addition, the Franck-Condon principle is equally applicable to both absorption and fluorescence phenomena. The red arrow in the diagrams (Figure 2.2) represents the decay to the ground state via photon emission. Details of this and other types of relaxation processes will be covered in the next section.

### 2.1.2. The physical deactivation of excited states

When the molecules expose to photons having particular energy, an electron can be promoted from lower-energy to higher-energy molecular orbitals in the molecule is called excitation. These types of excitations are typical for the photon energies which are in visible and/or ultraviolet range, and are producing electronically excited states. These excited states are unstable and lose their excess energy immediately via a variety of deactivation processes. For the convenience of the reader, the Perrin-Jablonski diagram is proposed to visualize the most typical processes that may happen after photon absorption in a simple way (Figure 2.3).

Jablonski diagram demonstrates the properties of excited states as well as their relaxation processes. The vibrational levels in the excited states will be crowded with electrons after the light absorption of molecules in ground states. Due to instability of this state, the electrons relax immediately to the lowest vibrational level of $S_1$ within picosecond or less via vibrational relaxation, and this process is called as the “internal conversion” (non-

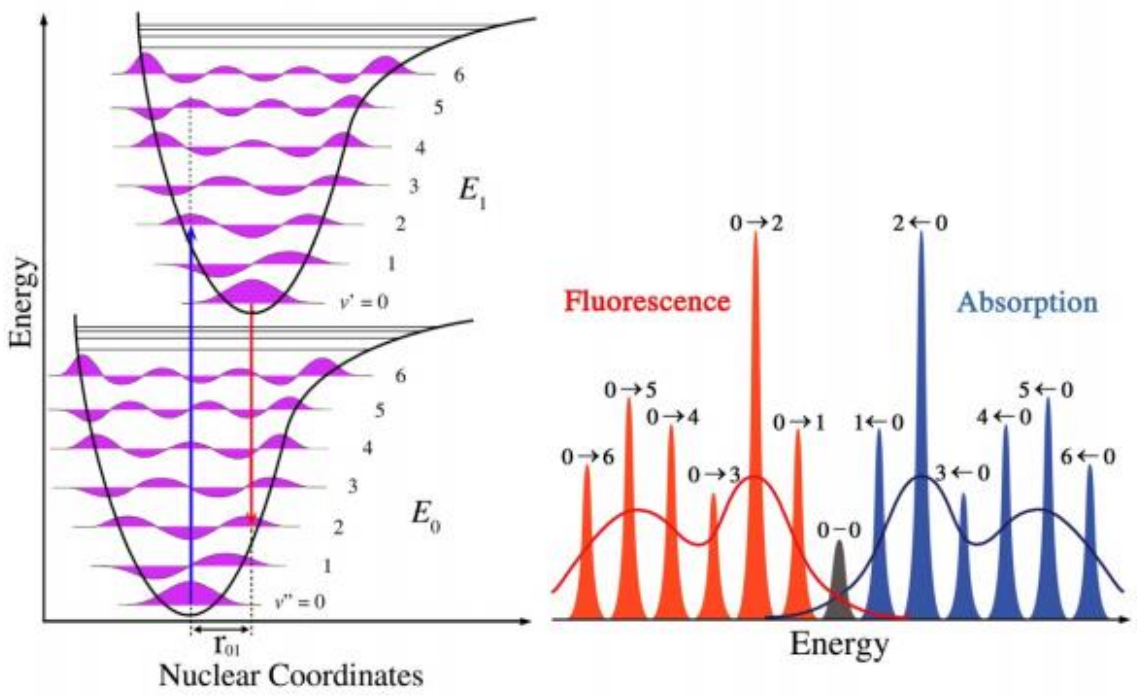


**Figure 2.2**. Morse potential diagram.

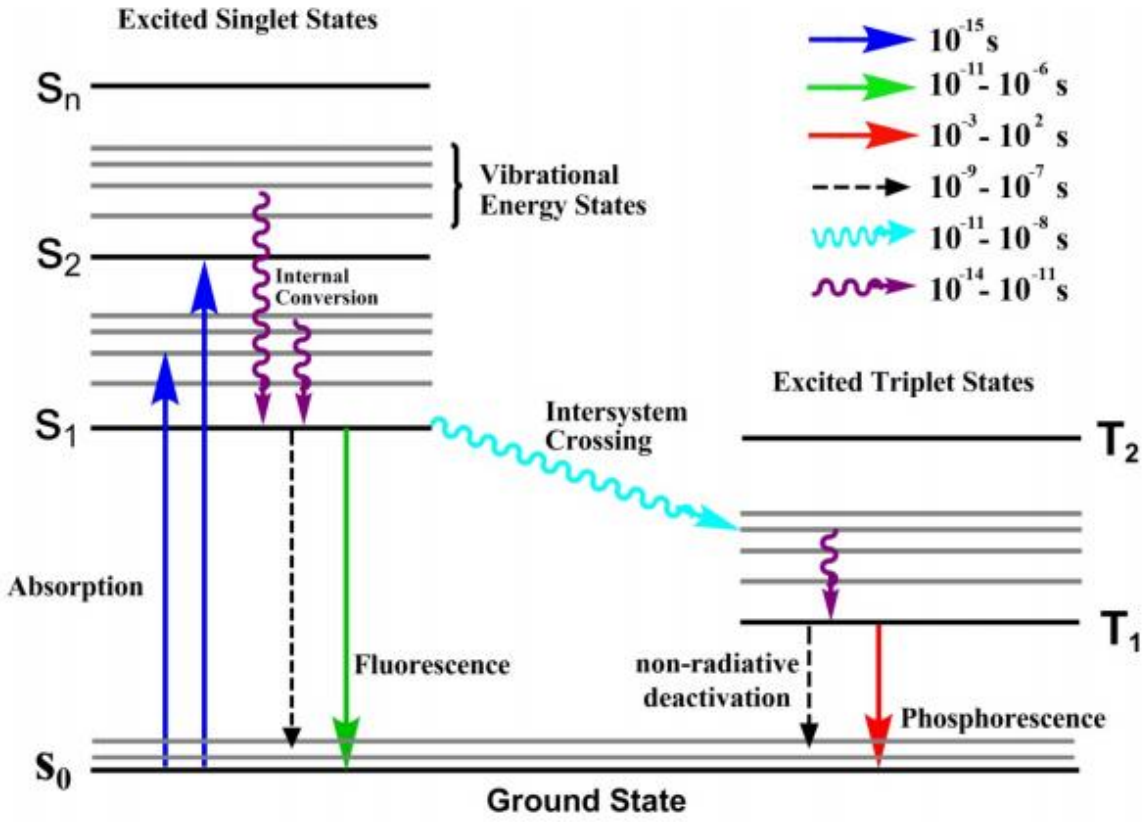


**Figure 2.3.** The Perrin-Jablonski diagram.

radiative loss of energy as heat to the surroundings). On the basis of Kasha's rule, the rest of photochemical processes such as fluorescence, quenching etc., are more likely to happen from the vibrational level of $S_1$ [5]. This rule states that all the photochemical reactions will always originate from the $\nu = 0$ of $S_1$ after excitation, since the relaxation rate to the lowest vibrational level of $S_1$ is the fastest deactivation process. The excited electron at $S_1$ of excited molecule now may undergo either fluorescence by emitting photons, or intersystem crossing to the triplet state or it may just relax to the ground singlet state $S_0$ via releasing the excess energy by internal conversion, as explained above.

Intersystem crossing from singlet state $S_1$ to the triplet state $T_1$ is a forbidden transition in the idealized conditions. It will happen when the electron in the $S_1$ state undergo a spin conversion. There are few conditions like presence of heavy atom and/or exciton coupling within a molecule favour such transitions. Relaxation of electron from $T_1$ state to $S_0$ state is a radiative process and termed as the "phosphorescence". Because of its spin multiplicity, the rate of radiative decay from $T_1$ to $S_0$ state is much slower than the fluorescence process and also it is a lower-energetic radiation. All the details of these processes including timescales are clearly shown in the Figure 2.3.

Due to the same spin multiplicity of the excited ($S_1$) and the ground ($S_0$) states, fluorescence is a spin-allowed radiative relaxation process. Hence, it happens in a very short period within the range of picoseconds to microseconds. As shown in the Jablonski diagram, emitted light always has a longer wavelength (less energetic) compared to absorbed light because of loss of limited energy by the molecule during this process. The difference between the $\lambda_{max}$ of spectral positions of the absorption and emission is called Stokes' shift (Figure 2.4) [6]. The main cause of Stokes' shift is that the rapid non-radiative decay to the lowest vibrational level of $S_1$. In addition to this effect, fluorescent molecules can display further Stokes' shift due to complex formation, energy transfer, excited-state reactions and solvent effects [1].

The fluorescence lifetime $\boldsymbol{\tau}$ and quantum yield $\boldsymbol{\Phi}$ are the essential photophysical parameters for a fluorescent molecule. Quantum yield is the ratio between the number of photons emitted by $S_1$ and the number of photons absorbed by $S_0$. It can be determined by using equation 1, where $\mathbf{k_r}$ and $\mathbf{k_{nr}}$ are the rates of radiative and non-radiative transitions, respectively. The fluorescence intensity increases with quantum yield of a molecule. Furthermore, the fluorescence quantum yield of a molecule may also be determined by comparing the area under its fluorescence spectrum with that of a known reference compound [7].

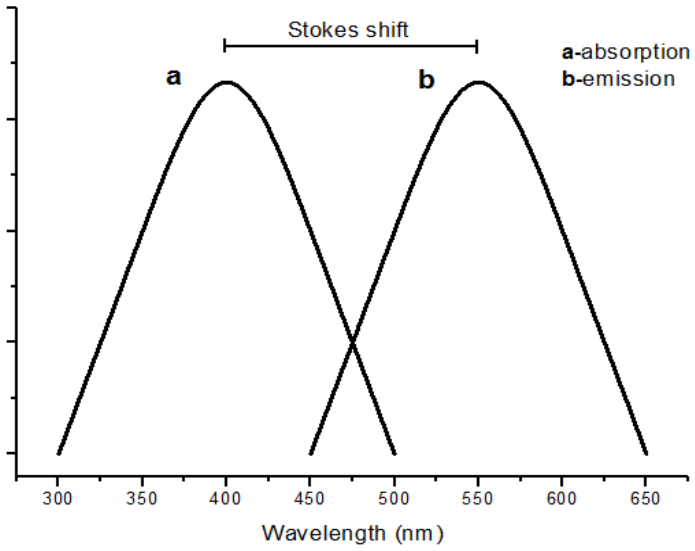


**Figure 2.4.** Stokes' shift.

$$\Phi = \frac{k_r}{k_r + k_{nr}} \quad \ldots\ldots\ldots\ldots\ldots\ldots\ldots\ldots \quad (1)$$

The average time of the electron of the molecule remains in its excited state is called the average lifetime of the excited states and it is numerically equivalent to the fluorescence lifetime which is determined by the time-resolved measurements. Fluorescence lifetime is a kinetic parameter which is inversely proportional to the sum of the rate constants and is represented as equation 2 [8].

$$\tau = \frac{1}{k_r + k_{nr}} \quad \ldots\ldots\ldots\ldots\ldots\ldots\ldots\ldots \quad (2)$$

## 2.2. Chemical sensors

It normally consists of a chemically selective sensing layer which is capable of chemically or physically responding to the presence of a particular chemical substance in the environment and can be used for the qualitative and quantitative determination of the substance. Figure 2.5 shows a schematic of a chemical sensing system, demonstrating the three main components: the sample (analyte), transduction platform and signal processing step.

Firstly, there is a region whereas selective chemical reaction takes place. Secondly, there is a transducer where the chemical reaction produces a signal, i.e. colour change or the emission of a fluorescent light and a change in the electrical potential at the surface, etc. Subsequently, the transducer responds to this signal and translates the magnitude of the signal into measure of the amount of the analytes [9].

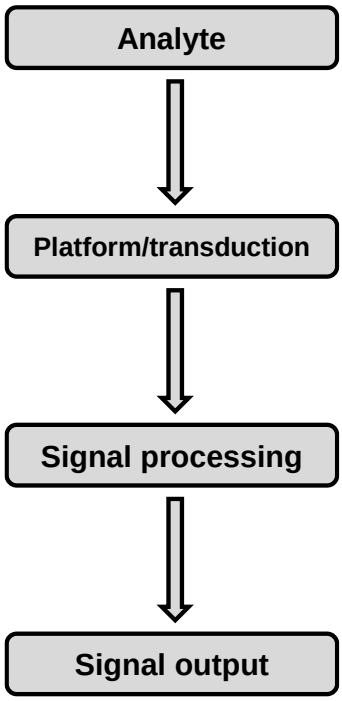


**Figure 2.5.** Basic schematic of a chemical sensing system.

### 2.2.1. Fluorescent chemosensors

The synthesis of signalling moieties and recognition of analyte are the most important things in the design of a chemosensor. In the case of fluorescent chemosensors, fluorophore act as a signalling part and the receptor unit recognizes the specific guest molecule (analyte). The analyte is covalently attached to the receptor during the recognition process. The importance of the receptor arises from its impact on binding and selectivity [10]. It means that a receptor should be sensitive, and should provide a strong and selective affinity towards the target analyte. The fluorophore part in the chemosensor acts as a signal transformer, so it can transform the information into useful optical signal. During binding of an analyte to the receptor, the significant changes arise in the photophysical properties of a fluorophore, the changes can be examined and processed in the right way to determine a given analyte. The variations in the fluorescence signal depend on the design of the chemosensor and this signal can be observed when complexed with the targeted analyte. The signal could be in the form of enhancement or quenching in the fluorescence, as well as the certain shift in the emission wavelength [11]. The fluorescent receptors or probes are two types to construct, they are integrated and spacer type fluorescent probes (Figure 2.6). In the first case, the signalling moiety and the receptor units (both having π-electron system) are conjugatively attached to each other (since the receptor, while in the latter case there is a spacer in between these two units that prevents the conjugation [12].

Chemosensors can be classified according to the nature of the signal emitted by the active unit. They can be, for example, electrochemical, optical or calorimetric. In optical sensors, a spectroscopic measurement is associated with the recognition process, e.g. absorbance, reflectance or luminescence measurements.

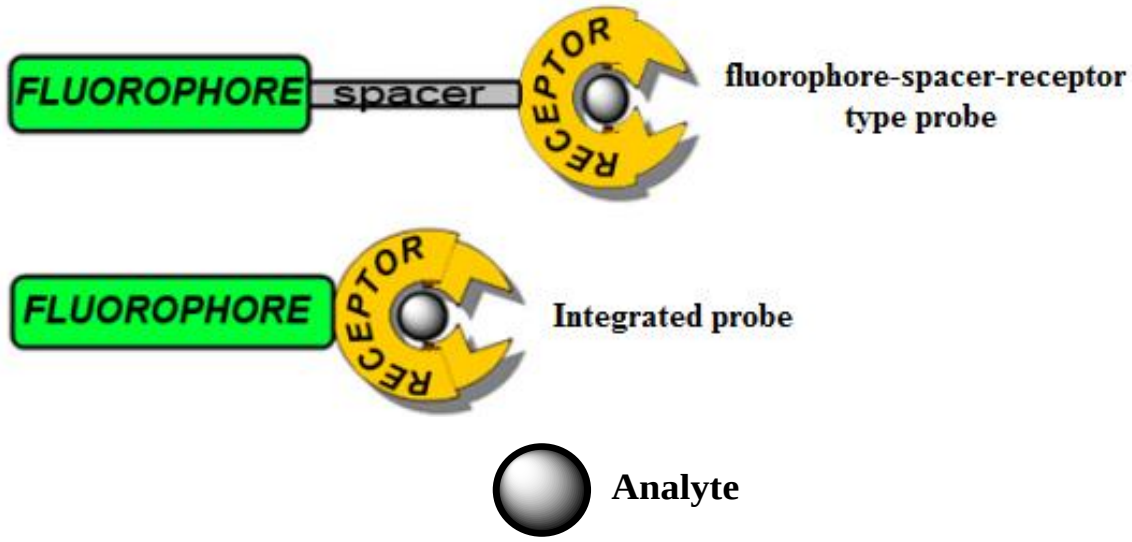


**Figure 2.6.** Schematic representation of a chemosensor.

### 2.2.1.1. Types of fluorescent chemosensors

The active unit in the case of fluorescent chemosensors is called a fluorophore, and it is responsible for converting the information (presence of an analyte) into an optical signal which is then expressed through changes in the photophysical properties of the fluorophore. Three types of fluorescent chemosensors can be distinguished (Figure 2.7).

**Type 1:** Fluorophores that experience fluorescence quenching motivated by collision with an analyte (e.g. $O_2$).

**Type 2:** Fluorophores able to bind the analyte in a reversible manner. In the case of the analyte being a proton, the term "fluorescent pH indicator" is employed. If it is an ion, the term "fluorescent chelating agent" is normally used. Two processes can occur upon analyte binding: Chelation Enhancement of Quenching (CHEQ), which means that the fluorescence emission is quenched, and Chelation Enhancement of Fluorescence (CHEF), where an increase in the emission intensity is observed. These compounds, in which the fluorophore is simultaneously responsible for binding and signalling, are usually called fluorogenic (in the case of CHEF).

**Type 3:** Fluorophores connected with or without spacer to a receptor unit. The bound analyte causes perturbations of photoinduced processes like electron transfer, charge transfer, energy transfer, excimer or exciplex formation or disappearance, etc. (see section 2.2.1.2), which

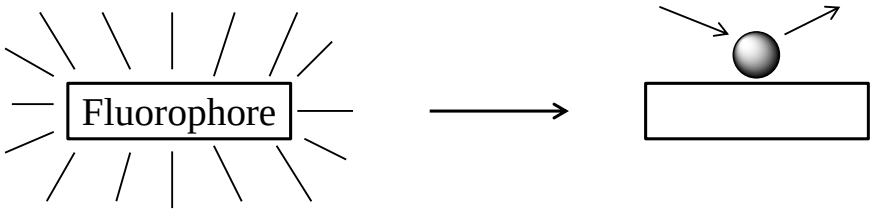


Type 1: No association. Quenching by collision with an analyte.

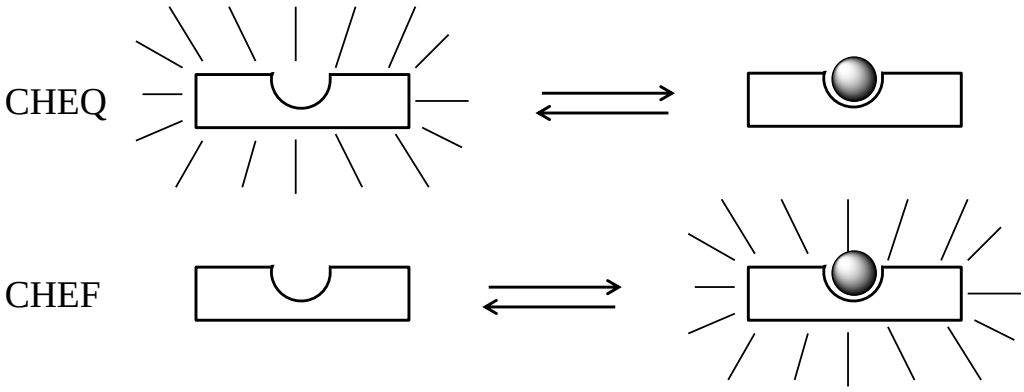


Type 2: Complexation fluorophores

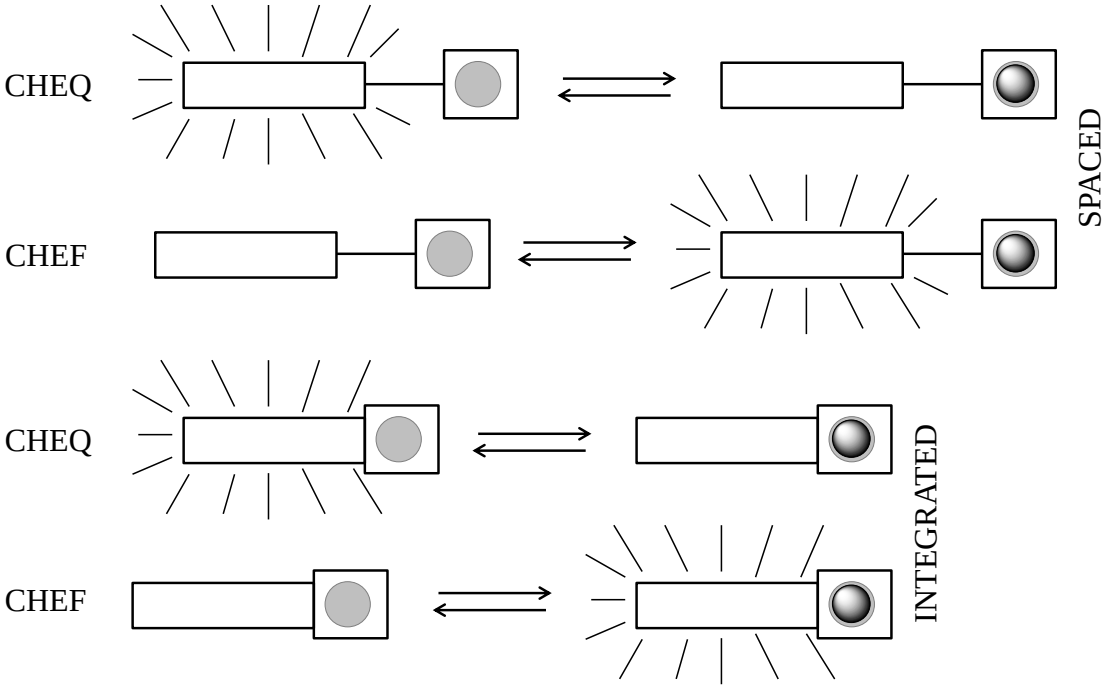


Type 3: Fluorophores linked to a receptor

**Figure 2.7.** Main types of fluorescent molecular sensors of ions or molecules.

bring about changes in the photophysical properties of the fluorophore. When the analyte is an ion, the receptor is called an ionophore, and the whole chemosensor is called a fluoroionophore. Also in this case, CHEQ and CHEF effects can be observed.

#### 2.2.1.2. Mechanisms of signal transduction

Fluorescence emission takes place from the electronic excited states of molecules. However, given the high reactivity of the electrons in these states, reactions that usually do not occur in the ground states are able to take place. From the point of view of chemical sensing, some of these reactions are found to be interesting, since they enable a one-step deactivation of the excited state (quenching) and, sometimes, formation of new emission bands corresponding to the products of these reactions. Upon analyte binding to chemosensors, it is possible to modulate some of these reactions (since they depend on the interaction of reaction sites with enhancers or quenchers of their emission), and thus take advantage of the different mechanisms for signal transduction.

##### 2.2.1.2.1. Photoinduced electron transfer (PET)

Fluorescent sensors provide simple, sensitive and naked-eye detection of a wide variety of analytes like cations, anions and neutral molecules. In some cases, the excited molecule before relaxation either can transfer an electron from potential donor unit to low-lying empty orbital or it may transfer to another system which is usually called a quencher. Moreover, the luminophore which absorbs the light after excitation process accept an electron into its unfulfilled ground state or it may donate an electron to vacant orbital of receptor from its excited state. Due to its significant role in photosynthesis, this process has been studied well [13]. After the absorption of light the electron is transferred, this process is called photo-induced electron transfer (PET). In the PET-type chemosensor both units, fluorophore and receptor exist in the same molecule and linked by a non-conjugated bridge and receptor accepts/donates an electron from/to the fluorophore.

The allowed and forbidden PET mechanisms in terms of frontier molecular orbitals shown in Figure 2.8. As shown in Figure, a model PET-type chemosensor is comprised of three units, those are fluorophore, spacer and receptor. Nature of the receptor unit determines the type of the response that fluorophore will give upon analyte binding. In this case, the receptor unit acts as the electron donating unit and the PET process is activated via the electron transfer to the semi vacant ground state orbital of the fluorophore from fulfilled HOMO of the receptor unit. This process blocks the usual relaxation pathway of excited fluorophore and quenches emission. This can also said to be reductive photo-induced

electron transfer. An off-on type fluorescence emission will be achieved when the donor orbital of receptor unit can be controlled or somehow stabilized. Moreover, weakly fluorescent sensor will become strongly fluorescent when bonded to the targeted analyte. Hence, probes that display this PET type mechanism are used extensively in chemosensing field [14–17].

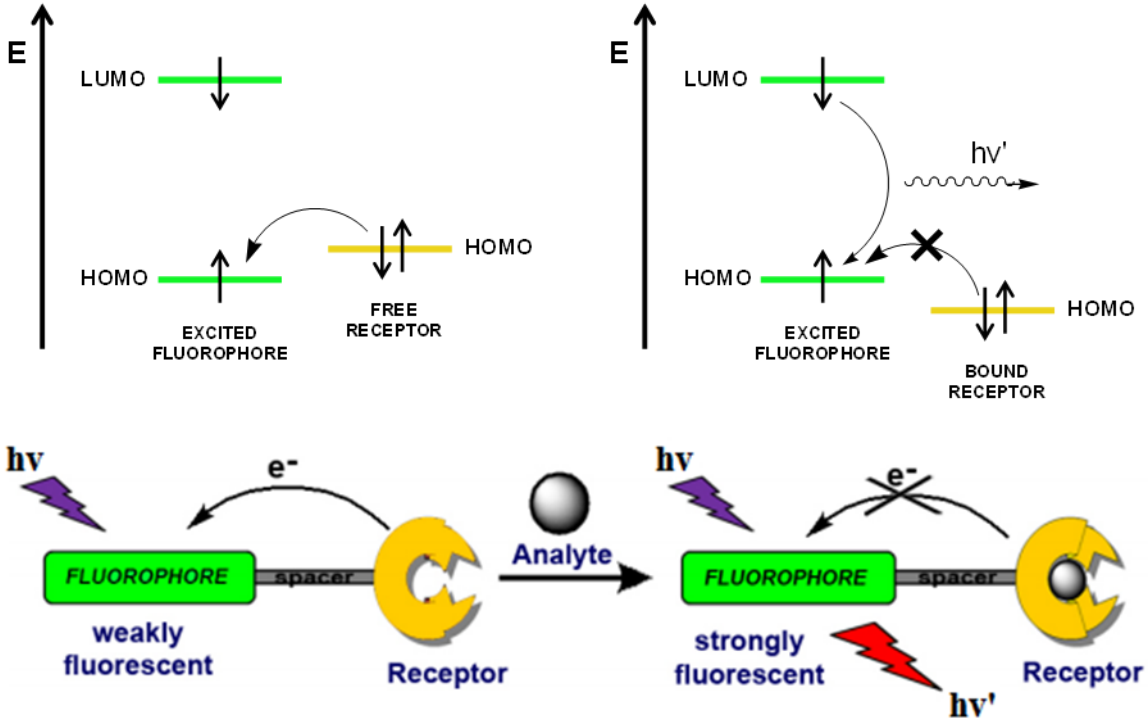


**Figure 2.8.** PET mechanism.

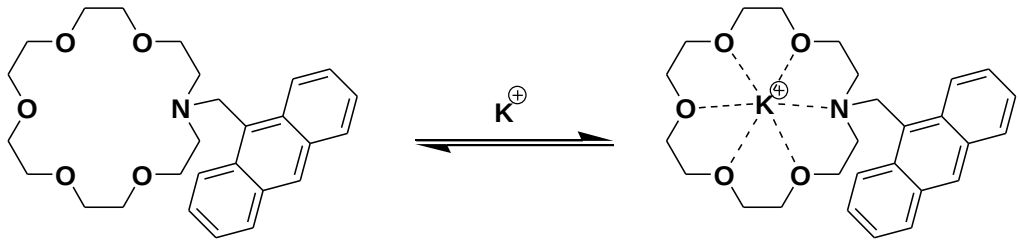


**1**

**Nonfluorescent** **Fluorescent**

**Scheme 2.1.** Azacrown ether based $K^+$ sensor displaying a PET fluorescence response.

In a practical sense, a PET switching mechanism is often achieved by the binding of a nitrogen lone pair of electrons as shown in Scheme 2.1. In the unbound azacrown ether **1** [18] the nitrogen lone pair can donate an electron to the excited state HOMO of the anthracene moiety. Upon binding, the same electron pair is complexed to the potassium

ion, and the electron is no longer available to quench fluorescence. PET systems can exhibit either ON-OFF or OFF-ON switching, but systems exhibiting OFF-ON behaviour are preferred for signalling binding events.

A molecule in the excited state is not only an electron acceptor also a better electron donor because of the promoted electron to a higher energy level. The working principle of a simple PET type chemosensor that contains electron accepting fluorophore from receptor is briefly discussed. What if the receptor moiety accepts electron from excited fluorophore?

Oxidative PET depends on the redox potentials of both the receptor and fluorophore units. Figure 2.9 demonstrates the possible Oxidative PET mechanism in terms of the molecular orbitals involved. Divergent to the previous mechanism, in this case the unbound form of the chemosensor exhibits strong fluorescence, while the fluorescence of the bound species is quenched and this is called an on-off system. The emission intensity of this system decreases significantly in the presence of an analyte.

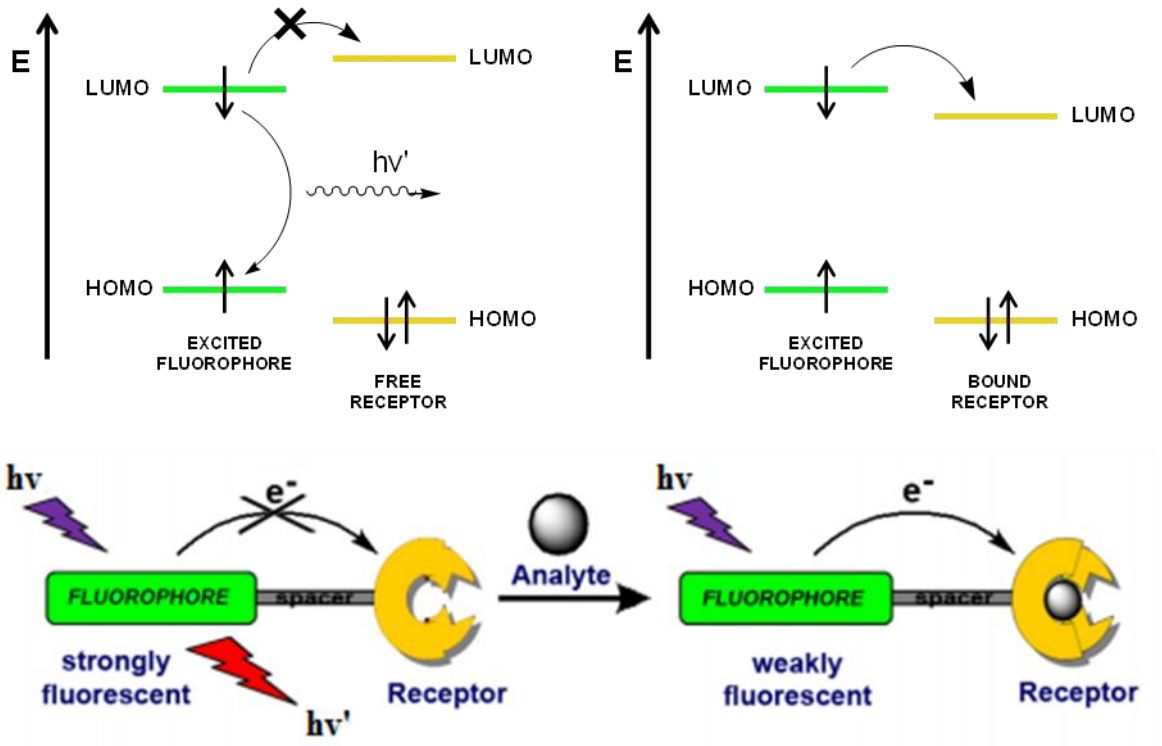


**Figure 2.9.** Oxidative PET mechanism.

Compound **2** [19] shows the oxidative PET mechanism in the presence of zinc cation. As depicted in Scheme 2.2, Bodipy dye and 2,2ˈ-bipyridine were chosen as the fluorophore and the receptor, respectively in the sensing probe. The fluorophore exhibits bright-green fluorescence in the absence of zinc cation, upon complexation with zinc ion quenches the fluorescence via oxidative PET mechanism.

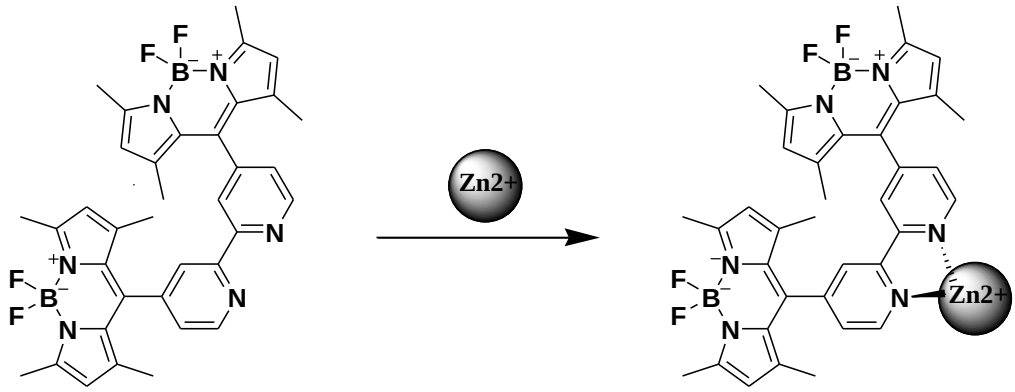


**2**

**bright-green fluorescence** **very weak fluorescence**

**Scheme 2.2.** Coordination of zinc triggers the oxidative PET mechanism.

Furthermore, another chemosensor for thiol based on this mechanism is reported by Nagano and co-workers. For this study, Bodipy derivative and maleimide moiety are utilized as the fluorophore and the receptor units, respectively (Figure 2.10) [20]. The sensor **3** alone exhibits oxidative PET mechanism and the probe is strongly quenched in the absence of thiol (Scheme 2.3). The oxidative PET mechanism is blocked after the reaction with thiol and the bright fluorescence of the Bodipy is restored back. Figure 2.10 illustrates the schematic representation of the oxidative PET to ground state maleimide unit from excited Bodipy unit in terms of molecular orbitals. Meta- and para-maleimide bound structures are also proposed in this paper to study the effect of distance between fluorophore and receptor on the PET efficiency.

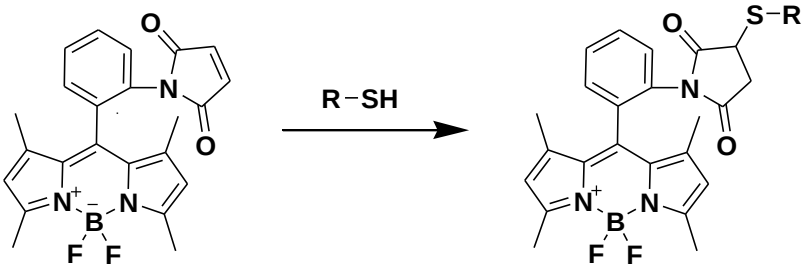


**3**

**Nonfluorescent** **Fluorescent**

**Scheme 2.3.** Binding of thiol prevents the oxidative PET mechanism.

The principles of various photo-induced electron transfer (PET) type mechanisms and its utilization in the field of development of molecular sensing have been discussed in this section. PET process and its proposed mechanisms were demonstrated schematically within the above figures. PET type chemosensors were examined with the help of examples

which are already proposed in the previous papers. No doubt that, PET has been the most widely applied mechanism among other conventional sensing mechanisms in the design of fluorescent chemosensors.

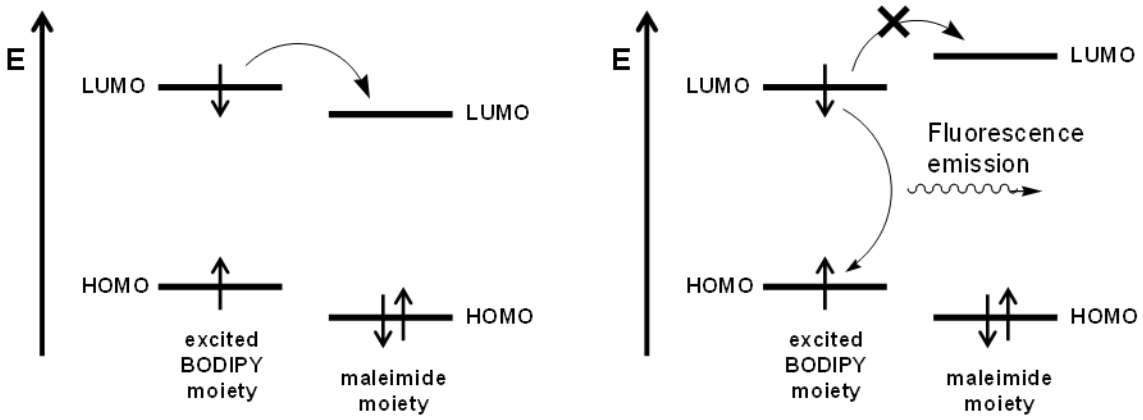


**Figure 2.10.** Reverse PET (d-PET) mechanism.

### 2.2.1.2.2. Intramolecular charge transfer (ICT)

In this system, the receptor is directly linked to the fluorophore and therefore is part of the fluorophore π–electron system such that one terminal is likely to be electron rich (electron donor) whereas the other one is electron poor (electron acceptor). This process is, in principle, also an electron transfer. The two (PET and ICT) phenomena are easily distinguished by their absorption and emission spectra [21]. In PET, strong quenching takes place and no spectral shifts are observed. On the other hand, binding of a cation to the receptor not only changes the fluorescence intensity and lifetime, but typically induces a spectral shift of the absorption and emission bands.

In terms of cation sensing, it is predictable that a complexed cation will diminish the electron-donating character of the electron donor (such as amino group), causing a reduction in conjugation and a consequent blue-shift of the absorption spectrum. Oppositely, if the acceptor group (e.g. a carbonyl group) interacts with a cation, its electron withdrawing character is enhanced, the conjugation is increased, and a red-shift in the absorption spectrum is observed. The fluorescence spectra are usually shifted in the same way as the absorption spectra [22].

Upon binding to cation, the changes in photophysical properties can also be explained by charge dipole interactions [23]. In the excited state, the electron donating group will be positively charged and upon binding with the cation, the excited state is destabilized than the ground state. As a result, the energy gap between the ground and excited states will

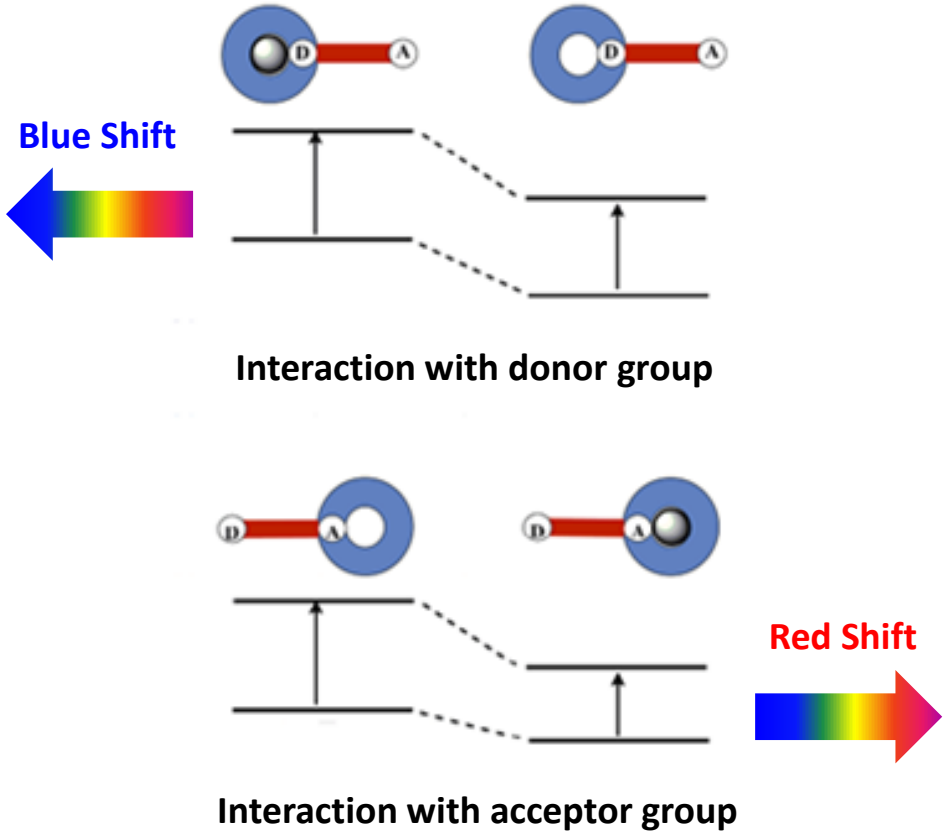


**Figure 2.11.** Spectral displacements of ICT type sensors.

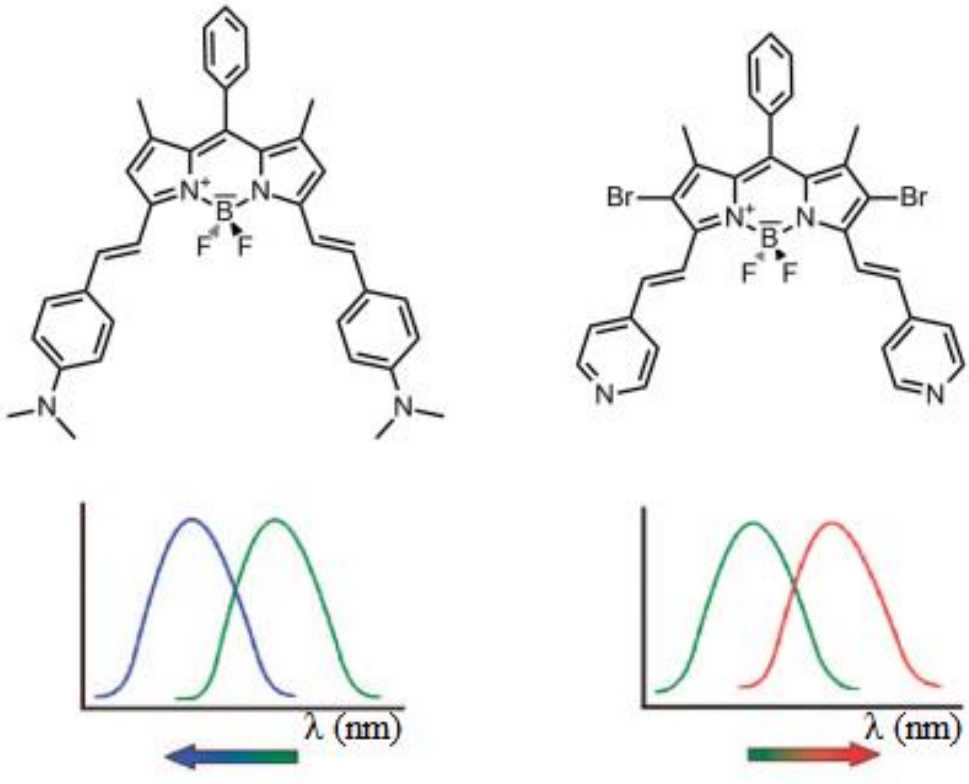


**Figure 2.12.** Bidirectional switching dyes related to ICT donor and acceptor characteristics.

increase and it cause a blue shift in the both absorption and emission spectra. On the other hand, in the presence of electron accepting group (like carbonyl group) on the receptor unit, the interaction towards cation will stabilize the excited state more than the ground state. Hence, the decreased energy gap between ground and excited states causes a red shift in the absorption and emission spectra. Therefore, the energy (ΔE) required to effect the electron promotion from ground state to excited state is less, and the wavelength that provides this energy is increased correspondingly and red-shift will be observed in the absorption as well as in the emission spectra (Figure 2.11).

Structurally similar compounds those varied in receptor unit can show different spectral shifts upon binding with the same analyte. For example, two Bodipy dyes alone show similar spectral properties and upon protonation exhibit opposite spectral shifts [24]. One of those dyes contains electron donating aniline moiety while other contains electron accepting pyridine moiety as receptor units (Figure 2.12). As a result, in their protonation form, these two compounds exhibit spectral shifts in the opposite directions because of the reasons as explained above.

To date, many fluorophores have been designed and reported according to the ICT mechanism. Compounds containing crown ether moiety **4** [25] and **5** [26] upon binding to the cation, show blue shift in both the absorption and emission spectra (Figure 2.13).

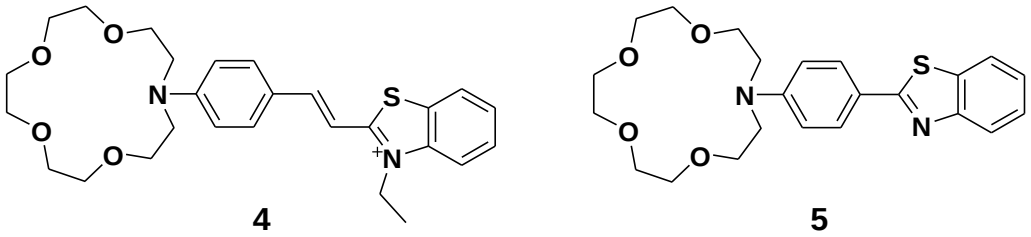


**4** **5**

**Figure 2.13.** Crown containing ICT sensors.

Conjugated compounds containing both electron donor (D) and electron accepting (A) groups that exhibit ICT mechanism through the π-conjugated link are also said to be 'Push-Pull' system (D-π-A system). Apart from the applications of chemosensing and analyte monitoring described above, this kind of systems has also been found in various optical-electrical applications including organic light emitting devices [27, 28], nonlinear optical devices [29] and solar cell materials [30, 31].

#### 2.2.1.2.3. Energy Transfer (ET)

Energy transfer is one more signalling mechanism, which can be classified as fluorescence resonance (FRET) and electronic energy transfer (EET) based on the

interaction distance between donor and acceptor moieties, and it is only possible when the system is multichromophoric. In this process, the energy of donor chromophore (D) is transferred to acceptor chromophore (A), always the donor unit absorbs light at relatively short wavelength and the acceptor unit fluoresces at longer wavelength. In other words, energy of the donor at its excited state is used to excite the acceptor through energy transfer.

As shown in Figure 2.14, the type of energy transfer is determined based on the interaction distance between donor and acceptor moieties. Electronic energy transfer (EET) is taking place when the distance remains within 10 Å range and is also known as Dexter electron transfer. In contrast, FRET is operated when the distance between donor and acceptor is in the range of 10–100 Å and this is not the only requirement also there should be a certain degree of overlap between the emission spectrum of donor and the absorption spectrum of acceptor units (Figure 2.14). Moreover, these mechanisms are also said to be Dexter and Förster type energy transfer and discussed briefly in the following subsections.

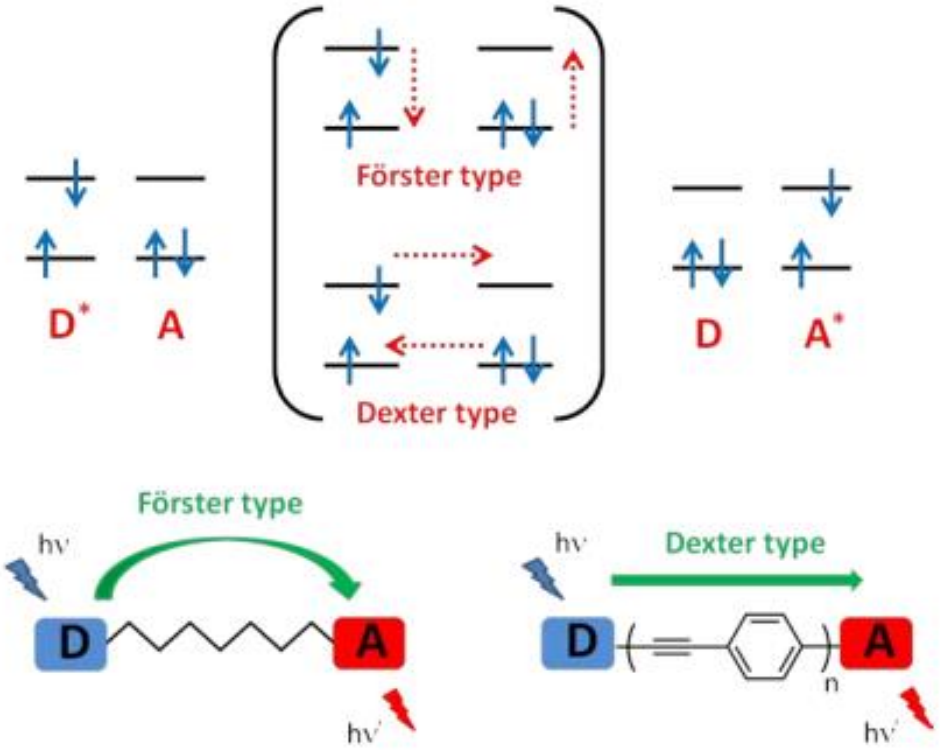


**Figure 2.14.** Förster type (through space) Dexter type (through bond) ET.

Types of energy transfer can be denoted based on various parameters like quantum yields, relative lifetimes, increase in the acceptor emission intensities and decrease in the donor emission intensities. Also, it is influenced with the rate of deactivation pathways of the excited state and thus, chromophores must be suitable to compete with these pathways.

In addition, life time of excited state of donor chromophore has to be longer than the time required for the energy transfer to acceptor chromophore [32].

#### 2.2.1.2.3.1. Förster type Energy Transfer

Fluorescent dyes, which emit light at wavelength distance from the excitation wavelength, have many applications in biotechnology. Generally, a very small Stokes' shift is observed for the simple fluorescent dye molecules. So, the simple and single dye molecules are not suitable for a particular application. For this, bi/multichromophoric systems which achieve through-space energy transfer between two chromophores (or dyes) are used. Förster type Energy Transfer is also called as fluorescence resonance energy transfer (FRET). In this process, the excited state donor transfers energy to a spatially close ground state acceptor, and the fluorescence of the latter is observed. Due to this reason, FRET is a non-radiative process (Figure 2.15).

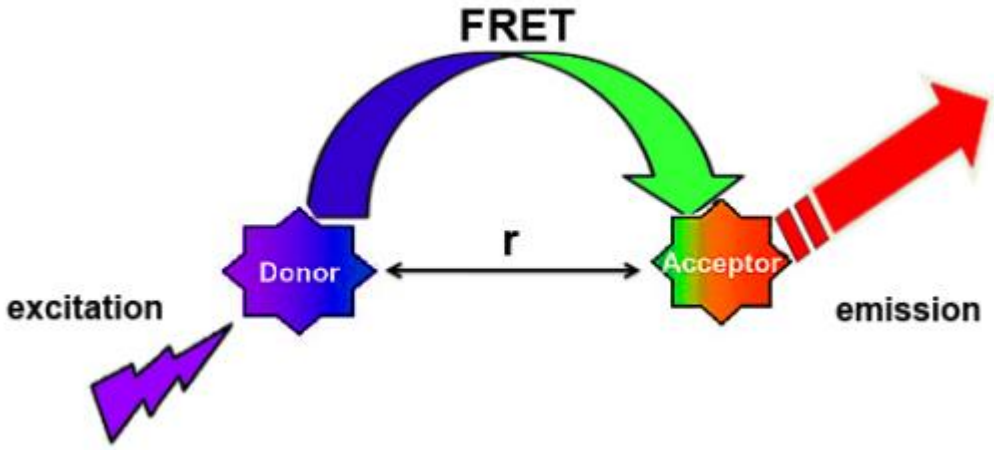


**Figure 2.15.** Schematic representation of the FRET process.

In other words, the energy released during the relaxation of an electron in the LUMO of the donor to its HOMO is used to excite an electron in the HOMO of the acceptor to its LUMO. Furthermore, the energy absorbed at a wavelength by the acceptor matches the emission wavelength of the donor.

Usually in FRET dyes, donor and acceptor units are connected through non-conjugated linker, and are not depend on the interaction of the orbital of these units. Therefore, this type of energy transfer is still operated although the distance between donor and acceptor units is large (10–100 Å). The distance between donor and acceptor groups, spectral overlap of donor emission and acceptor absorption and relative orientations of

transition dipoles of acceptor and donor units are significantly important parameters for an efficient FRET process [33, 34].

As shown in Scheme 2.4 exhibits FRET fluorescence when unbound; the phenanthrene group is excited, and emission from the pyrene is observed. The unbound sensor has free rotation through the hexyl spacer which allows the fluorophores to associate due to hydrophobic interactions. Binding of a carbohydrate forces the fluorophores apart by rigidifying the system and excitation of the phenanthrene yields phenanthrene emission.

Over the past three decades, the use of FRET has found applications in various fields such as artificial photosynthetic antenna, light frequency conversion, singlet oxygen generation, cascade systems and switching element in molecular machines.

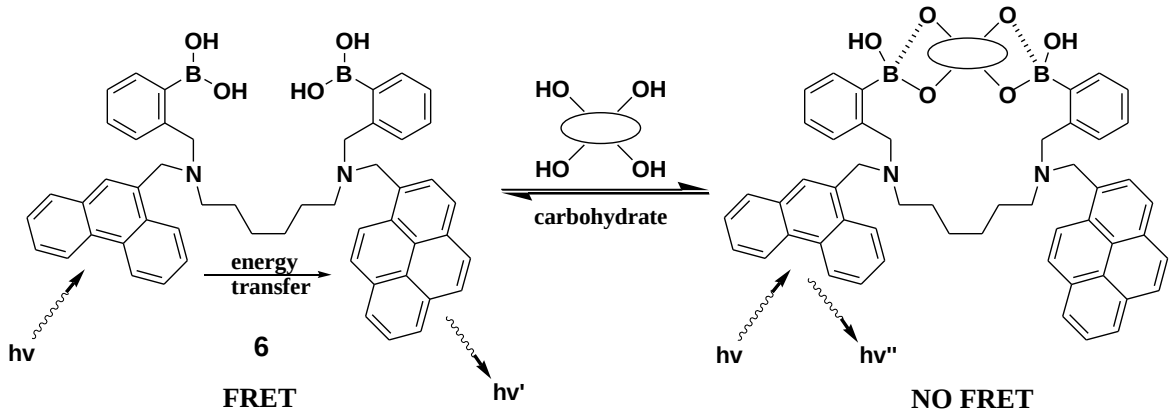


**Scheme 2.4.** FRET fluorescence response in a carbohydrate sensor.

### 2.2.1.2.3.2. Dexter type Energy Transfer

In contrast to the Förster type, Dexter type energy transfer requires interactions of donor-acceptor orbitals which can be provided either directly or by the bridge [35]. Usually, it happens when the donor and acceptor groups are connected to each other with a conjugated linker, therefore it is also known as 'through-bond' energy transfer. Due to the exchange of electrons between both HOMOs and LUMOs of donor and acceptor (Figure 2.14), it is also called as electronic energy transfer (EET). Short-range (< 10 Å) interaction favours the orbital overlap, which significantly affects the Dexter type energy transfer, the rate constant of energy transfer decreases exponentially with distance [32].

$$\mathbf{k_{ET} = K\,J\,exp(-\frac{2R_{DA}}{L})}$$

where $\mathbf{k_{ET}}$ is the rate constant of energy transfer, **J** represents the overlap integral between donor emission and acceptor absorbance, **L** is the Van der Waals radii, **K** is the orbital interaction and $\mathbf{R_{DA}}$ is the donor acceptor separation.

For example, this type energy transfer is operated in the Anthracene-BODIPY based ionophores (Figure 2.16) [36]. When anthracene is excited, a very fast energy transfer is observed (~200 fs) to BODIPY moiety from anthracene unit in compound **8**. It happens because of parallel alignment of $S_1$-$S_0$ transition dipole moments of donor and acceptor respectively. In contrast, compound **7** contains both anthracene and BODIPY and are directly connected to each other. Steric interactions prevent the planarity of the structure which makes it a true cassette.

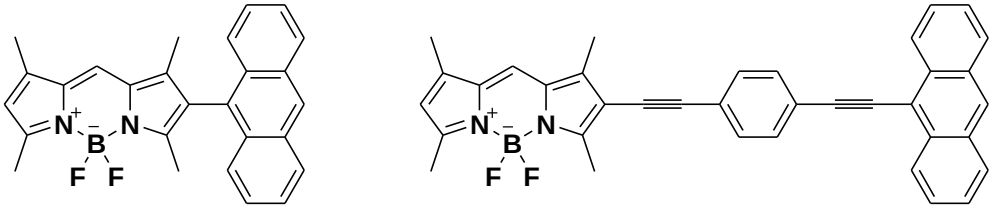


**Figure 2.16.** Through-bond (Dexter type) energy transfer probes.

### 2.2.1.2.4. Excimer and exciplex formation

A molecule in the excited state can associate (overlap) with an unexcited molecule like itself, giving rise to a dimer in the excited state [21, 38], which is called excimer (from "excited dimer"). The excimer emission spectrum differs substantially from that of monomers; it is normally broad, shifted to longer wavelengths and does not show vibrational resolution.

If the collision takes place between molecules that differ in structure (e.g. an electron donor and an acceptor), an excited state complex is formed, and is named exciplex (from "excited complex").

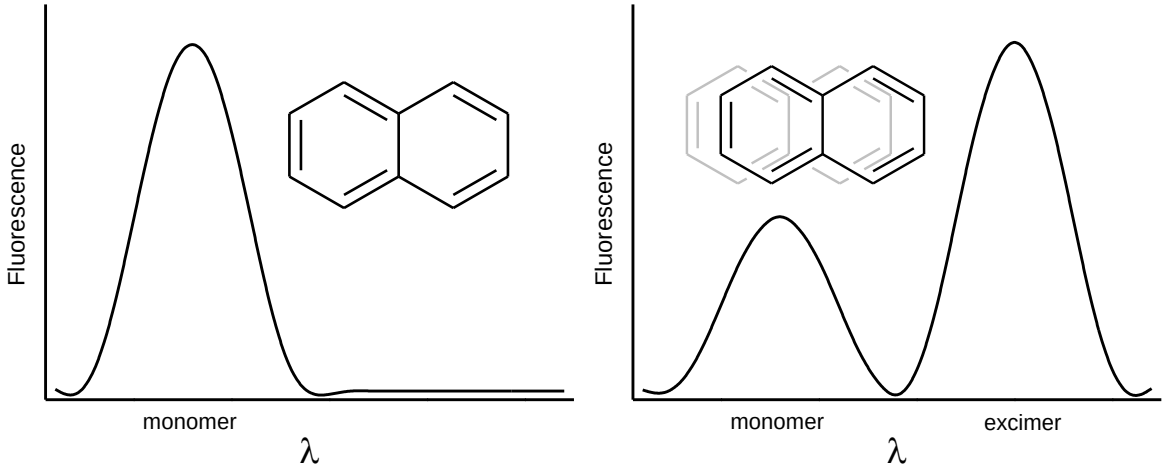


**Figure 2.17.** Excimer fluorescence of naphthalene.

The formation of excimers and exciplexes is reversible (after emission they separate and are free to form again upon excitation), and requires close location and adequate orientation of the two molecules involved (in the case of excimers, usually two heterocycles rich in π-electrons are required, which form two parallel planes through π-π stacking).

On the left in Figure 2.17, a band representing the monomer fluorescence of naphthalene is shown. At high concentrations of naphthalene, the fluorescence emission changes (right of Figure 2.17) and a new, red-shifted band is evident. The new band is the result of a lower energy complex that forms when an excited naphthalene moiety transfers energy to a nearby cofacially stacked naphthalene molecule to form an excited state complex (exciplex).

### 2.2.2. Solvatochromism

The term solvatochromism describes the influence of a solvent on the colour of a dye molecule. Depending on the nature of the dye and the resulting behaviour it is commonly distinguished between positive and negative solvatochromism.

In the case of positive solvatochromism the dye-molecule is present in a non-polar structure in its ground state. Upon addition of a polar solvent the ground state is destabilised, resulting in a higher energy level and thus an absorption maximum located at a longer wavelength. Due to the fact that the energy difference between the ground state and the excited state is diminished, the absorption process needs less energy. The wavelength is antiproportional to the energy content and thus a barthochromic shift in the absorption spectrum is observed (shift to longer wavelengths, red shift).

In the case of negative solvatochromism the dye molecule is mainly present in a polar structure in its ground state. Addition of a polar solvent stabilises the polar structure and the energy level is lowered. Due to the fact that the excited state is not influenced by the polar solvent and the energy gap between the ground state and the excited state is growing. Thus, the absorption process needs more energy. More energy corresponds to shorter wavelength, resulting in a hypsochromic shift (shift to shorter wavelengths, blue shift).

### 2.2.3. Association constant (K)

A mathematical constant that describes the bonding affinity between two molecules at equilibrium. The association constant for a fluorescence enhancement process is calculated by using Benesi-Hildebrand equation [38]:

$$\frac{\mathbf{1}}{\mathbf{F}-\mathbf{F_0}} = \frac{\mathbf{1}}{\mathbf{F_{MAX}}-\mathbf{F_0}} + \frac{\mathbf{1}}{\mathbf{F_{MAX}}-\mathbf{F_0}} \times \frac{\mathbf{1}}{\mathbf{K}[\mathbf{M^{n+}}]}$$

where $\mathbf{F_0}$, **F**, $\mathbf{F_{MAX}}$, and **K** are the intensities of fluorescence of the fluorophore without analyte, intensity with varying concentrations of analyte, intensity with the maximum concentration of analyte, and the association constant, respectively, $\mathbf{[M^{n+}]}$ is the analyte concentration.

From the fluorescence titration linear relationship was obtained for the plot measured $\mathbf{[1/(F-F_0)]}$ as a function of $\mathbf{1/[M^{n+}]}$, and a slope is equal to $\mathbf{[1/(F-F_0)K]}$.

For a fluorescence quenching process, the association constant is described by Stern-Volmer equation [1] which is given by

$$\frac{\mathbf{F_0}}{\mathbf{F}} = \mathbf{1} + \mathbf{K}[\mathbf{M^{n+}}]$$

where $\mathbf{F_0}$ and **F** are the observed fluorescence intensity of fluorophore in the absence and presence of analyte, respectively, $\mathbf{[M^{n+}]}$ is the concentration of analyte, and **K** is the association constant.

A plot of $\mathbf{F_0/F}$ versus $\mathbf{[M^{n+}]}$ is known as a Stern-Volmer (SV) plot, which yields a straight line with a slope equal to **K**.

### 2.2.4. Limit of detection (LOD)

Limit of detection, or detection limit, is the lowest concentration of an analyte that can be reliably detected or measured, was calculated based on Signal-to-Noise ratio = 3. Signal to Noise ratio (S/N) is a dimensionless measure of the relative strength of an analytical signal (S) to the average strength of the background instrumental noise (N) for a particular sample and is closely related to the detection level. The ratio is useful for determining the effect of the noise on the relative error of a measurement. The common formula of limit of detection is

$$\mathbf{LOD} = \frac{\mathbf{3\ SD}}{\mathbf{m}}$$

where **SD** is the standard deviation from the blank measurement (fluorophore without analyte), **m** is the slope from the calibration curve of the fluorophore with varying concentrations of analyte

The detection limit is estimated from the standard deviation of the blank. Sample Standard Deviation is a measure of the degree of agreement, or precision, among replicate analyses of a sample. The standard deviation is defined as:

$$\mathbf{SD} = \sqrt{\frac{\sum(\mathbf{x} - \mathbf{x}')^2}{\mathbf{n}}}$$

where **x** is the emission intensity of the blank solution, **x'** is the mean of the intensity of all blank solutions and **n** is the number of measurements.

**References**


1. J.R. Lakowicz, Principles of fluorescence spectroscopy, *Plenum Press*, New York, 1999.
2. M. Adachi, Y. Nagao, Design of near-infrared dyes based on π-conjugation system extension 2. Theoretical elucidation of framework extended derivatives of perylene chromophore, *Chem. Mater.*, 2001, **13**, 662–669.
3. M.F. Rastegar, E.K. Todd, H. Tang, Z.Y. Wang, A new class of near-infrared electrochromic oxamide-based dinuclear ruthenium complexes, *Org. Lett.*, 2004, **6**, 4519–4522.
4. B. Wardle, Principles and applications of photochemistry, *John Wiley & Sons*, Chichester, 2009.
5. M. Kasha, Characterization of electronic transitions in complex molecules, *Discuss. Faraday Soc.*, 1950, **9**, 14–19.
6. G.G. Stokes, On the change of refrangibility of Light, *Phil. Trans. R. Soc. Lond.*, 1852, **142**, 463–562.
7. G. Weber, F.W.J. Teale, Determination of the absolute quantum yield of fluorescent solutions, *Trans. Faraday Soc.*, 1957, **53**, 646–655.
8. M.Y. Berezin, S. Achilefu, Fluorescence lifetime measurements and biological imaging, *Chem. Rev.*, 2010, **110**, 2641–2684.
9. O.S. Wolfbeis. Materials for fluorescence-based optical chemical sensors. *J. Mater. Chem.*, 2005, **15**, 2657–2669.
10. Z. Xu, J. Yoon, D.R. Spring, Fluorescent chemosensors for $Zn^{2+}$, *Chem. Soc. Rev.*, 2010, **39**, 1996–2006.
11. B. Valeur, Molecular Fluorescence, *Wiley-VCH*, Weinheim, 2002.
12. K. Rurack, U. Resch-Genger, Rigidization, preorientation and electronic decoupling—the 'magic triangle' for the design of highly efficient fluorescent sensors and switches, *Chem. Soc. Rev.*, 2002, **31**, 116–127.
13. M. Wasielewski, J.M. Fenton, Govindjee, The rate of formation of $P_{700}^{+}$-$A_0^{-}$ in photosystem I particles from spinach as measured by picosecond transient absorption spectroscopy, *Photosynth. Res.*, 1987, **12**, 181–189.
14. A.W. Czarnik, Fluorescent chemosensors for ion and molecule recognition, *American Chemical Society*, Washington, DC, 1993.
15. C.N. Baki, E.U. Akkaya, Boradiazaindacene-appended calix[4]arene: Fluorescence sensing of pH near neutrality, *J. Org. Chem.*, 2001, **66**, 1512–1513.

16. L. Fabbrizzi, A. Poggi, Sensors and switches form supramolecular chemistry, *Chem. Soc. Rev.*, 1995, **24**, 197–202.
17. A.P. de Silva, T.S. Moody, G.D. Wright, Fluorescent PET (Photoinduced Electron Transfer) sensors as potent analytical tools, *Analyst*, 2009, **134**, 2385–2393.
18. A.P. de Silva, S.A. de Silva, Fluorescent signaling crown ethers: Switching on of fluorescence by alkali metal ion recognition and binding *in situ*, *J. Chem. Soc. Chem. Commun.*, 1986, 1709–1710.
19. B. Turfan, E.U. Akkaya, Modulation of boradiazaindacene emission by cation-mediated oxidative PET, *Org. Lett.*, 2002, **4**, 2857–2859.
20. T. Matsumoto, Y. Urano, T. Shoda, H. Kojima, T. Nagano, A thiol-reactive fluorescence probe based on donor-excited photoinduced electron transfer: Key role of ortho substitution, *Org. Lett.*, 2007, **9**, 3375–3377.
21. B. Valeur, Molecular fluorescence: Principles and applications, *Wiley-VCH*, Weinheim, 2001.
22. B. Valeur, F. Badaoui, E. Bardez, J. Bourson, P. Boutin, A. Chatelain, I. Devol, B. Larrey, J.P. Lefevre, A. Soulet, in: J.P. Desvergne, A.W. Czarnik, (Eds.), Chemosensors of ion and molecule recognition, *NATO ASI Series*, Kluwer, Dordrecht, 1997.
23. H.G. Lohr, F. Voegtle, Chromo- and fluoroionophores. A new class of dye reagents, *Acc. Chem. Res.*, 1985, **18**, 65–72.
24. E. Deniz, G.C. Isbasar, O.A. Bozdemir, L.T. Yildirim, A. Siemiarczuk, E.U. Akkaya, Bidirectional switching of near IR emitting boradiazaindacene fluorophores, *Org. Lett.*, 2008, **10**, 3401–3403.
25. N. Mateeva, V. Enchev, L. Antonv, T. Deligeorgiev, M. Mitewa, Spectroscopic study of the complexation of an aza-15-crown-5 containing chromofluoroionophore with $Ba^{2+}$ and $Ca^{2+}$ cations, *J. Incl. Phenom.*, 1995, **93**, 323–333.
26. M.M. Martin, P. Plaza, Y.H. Meyer, L. Begin, J. Bourson, B. Valeur, A new concept of photogeneration of cations: Evidence for photoejection of $Ca^{2+}$ and $Li^{+}$ from complexes with a crown-ether-linked merocyanine by picosecond spectroscopy, *J. Fluoresc.*, 1994, **4**, 271–273.
27. Y. Zhou, Y. Xiao, S. Chi, X. Qian, Isomeric boron-fluorine complexes with donor-acceptor architecture: Strong solid/liquid fluorescence and large Stokes shift, *Org. Lett.*, 2008, **10**, 633–636.

28. Y. Dong, A. Bolduc, N. McGregor, W.G. Shene, Push-pull aminobithiophenes: Highly fluorescent stable fluorophores, *Org. Lett.*, 2011, **13**, 1844–1847.
29. S.R. Marder, B. Kippelen, A.K.Y. Jen, N. Peyghambarian, Design and synthesis of chromophores and polymers for electro-optic and photorefractive applications, *Nature* (London), 1997, **388**, 845–851.
30. H. Burckstummer, N.M. Kronenberg, K. Meerholz, F. Wurthner, Near-infrared absorbing merocyanine dyes for bulk heterojunction solar cells, *Org. Lett.*, 2010, **12**, 3666–3669.
31. S. Erten-Ela, M.D. Yilmaz, B. Icli, Y. Dede, S. Icli, E.U. Akkaya, A panchromatic boradiazaindacene (BODIPY) sensitizer for dye-sensitized solar cells, *Org. Lett.*, 2008, **10**, 3299–3302.
32. N.J. Turro, Modern molecular photochemistry, *University Science Books*, Sausalito, CA, 1991.
33. T. Forster, Intermolecular energy migration and fluorescence, *Ann. Phys.*, 1948, **2**, 55–75.
34. A. Sharma, S.G. Schulman, Introduction to fluorescence spectroscopy, *John Wiley & Sons*, Chichester, 1999.
35. D.L. Dexter, A theory of sensitized luminescence in solids, *J. Chem. Phys.*, 1953, **21**, 836–850.
36. C.W. Wan, A. Burghart, J. Chen, F. Bergstrom, L.B.A. Johansson, M.F. Wolford, T.G. Kim, M.R. Topp, R.M. Hochstrasser, K. Burgess, Anthracene-BODIPY cassettes: Syntheses and energy transfer, *Chem. Eur. J.*, 2003, **9**, 4430–4441.
37. A.P. Demchenko, Introduction to fluorescence Sensing, *Springer*, New York, 2009.
38. H.A. Benesi, J.H. Hildebrand, A spectrophotometric investigation of the interaction of iodine with aromatic hydrocarbons, *J. Am. Chem. Soc.*, 1949, **71**, 2703–2707.
39. D. Magde, G.E. Rojas, P.G. Seybold, Solvent dependence of the fluorescence lifetimes of xanthene dyes, *Photochem. Photobiol.*, 1999, **70**, 737–744.
40. R.B. Mujumdar, L.A. Ernst, S.R. Mujumdar, C.J. Lewis, A.S. Waggoner, Cyanine dye labeling reagents: Sulfoindocyanine succinimidyl esters, *Bioconjugate Chem.*, 1993, **4**, 105–111.

# CHAPTER 3
# Antipyrine Based Turn-On Fluorescent Sensors for Al(III) Ion

## 3.1. Introduction

Aluminum is the one of the most abundant metal in the earth's crust and is the second most widely used metal after iron for the manufacture of electrical equipments, automobiles, packaging materials, water purification, clinical drug and building construction etc. [1, 2]. Recent studies are shown that the deposition of aluminum in bone and the nervous system in human body can cause neurotoxicity [3]. It plays an important role in the pathology of Alzheimer's, Parkinson's and dialysis diseases [4–7]. In plants, higher concentration of aluminum affects the growth of root and seed [8, 9]. Thus, the monitoring of aluminum is essential in environment, medicine, foodstuff, etc.

In recent years, many analytical methods have played a role in the detection of $Al^{3+}$ and other ions, including ion selective electrodes [10–12] and colorimetric sensors [13–17]. Lately, the fluorescent sensing method has become trendy due to its operational simplicity, high selectivity, sensitivity, real-time response and naked eye detection [18–27]. Due to its poor coordination ability compared to transition metals [28], only a few fluorescent sensors have been reported and on the other hand, most of the $Al^{3+}$ sensors are difficult to synthesis and insoluble in aqueous solvents. Some of the antipyrine derivatives are detected as a fluorescent chemosensor towards ions [29].

In this paper, we designed and synthesized 4-aminoantipyrine based compounds (**C1** and **C2**) in a simple approach as fluorescent sensors for $Al^{3+}$ ion. The fluorescence intensities of the two sensors **C1** and **C2** are enhanced by mixing $Al^{3+}$, and show bright blue and bright green color respectively, which can be easily observed by the naked eye under UV lamp. The results indicated that the prepared 4-aminoantipyrine based sensors can show high sensitivity and selectivity towards $Al^{3+}$ over other metal ions.

## 3.2. Experimental

### *3.2.1. Reagents and apparatus*

4-aminoantipyrine, salicylaldehyde, 2-hydroxy-1-naphthaldehyde and metal salts (from Merck and Aldrich, India). The IR spectra were recorded on a Nexus FT-IR (Illinois, USA) spectrometer in the range 4000–400 $cm^{-1}$ with KBr. The NMR spectra were recorded on a Bruker 500 MHz (USA), TMS as an internal standard, $CDCl_3$ and $CD_3OD$ are taken as solvents. The mass spectra were recorded using Bruker-micrOTOF II (USA). The UV-Vis absorption spectra were measured on a Shimadzu UV-2450 spectrophotometer (Japan) and the Fluorescent spectra were recorded on a Shimadzu RF-5301PC spectrofluorophotometer (Japan) instruments.

*3.2.2. Synthesis and characterization*

The Schiff base ligands (**C1** and **C2**) were synthesized by the reported method [30, 31] with some modifications (Scheme 3.1). The ethanol containing the mixture of 4-aminoantipyrine (10 mmol) and aldehyde (10 mmol) was stirred about 2–3 hours at room temperature; the obtained solid was filtered, washed with cold ethanol and dried under vacuum.

**1-phenyl-2,3-dimethyl-4-(N-2-hydroxybenzylidene)-3-pyrazolin-5-one (C1):** Yield: 2.76 g (90%); Color: Light yellow solid; Mp: 218–220 °C; FT-IR (KBr), *v*, $cm^{-1}$: 3448 (O−H), 2929, 759 (C−H), 1653 (C=O), 1593 (C=N), 1490 (C=C), 1139 (N−N); $^1$H NMR ($CDCl_3$), *δ*, ppm (*J*, Hz): 2.42 (s, 3H), 3.18 (s, 3H), 6.89 (t, *J* = 7.5, 1H), 6.96 (d, *J* = 8.5, 1H), 7.29 (dt, *J* = 1.5, 7.5, 1H), 7.33–7.37 (m, 2H), 7.39 (d, *J* = 2.5, 2H), 7.49 (t, *J* = 8.0, 2H), 9.82 (s, 1H); $^{13}$C NMR ($CDCl_3$), *δ*, ppm: 10.3, 35.7, 116.3, 116.7, 119.1, 120.2, 124.7, 127.3, 129.3, 131.9, 132.0, 134.4, 149.9, 160.3, 160.5, 160.7; HRMS *m/z*: Calcd for $C_{18}H_{17}N_3O_2$ $(M+Na)^+$: 330.1218, found: 330.1211.

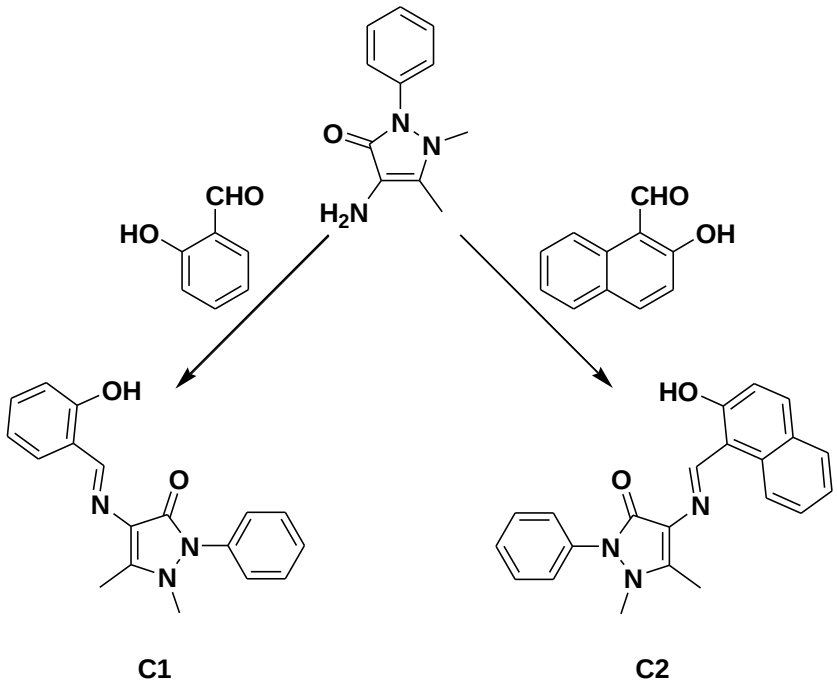


**Scheme 3.1.** Synthetic routes to **C1** and **C2**.

**1-phenyl-2,3-dimethyl-4-(N-2-hydroxynaphthylidene)-3-pyrazolin-5-one (C2):** Yield: 3.11 g (80%); Color: Yellow solid; Mp: 210–212 °C; FT-IR (KBr), *v*, $cm^{-1}$: 3427 (O−H), 3018, 2925, 746 (C−H), 1638 (C=O), 1588 (C=N), 1479 (C=C), 1145 (N−N); $^1$H NMR ($CHCl_3$), *δ*, ppm (*J*, Hz): 2.46 (s, 3H), 3.20 (s, 3H), 7.17 (d, *J* = 9.0, 1H), 7.34 (m, 2H), 7.43

(d, *J* = 7.5, 2H), 7.47 (dt, *J* = 1.0, 7.5, 1H), 7.51 (t, *J* = 8.0, 2H), 7.74 (d, *J* = 8.0, 1H), 7.79 (d, *J* = 9.0, 1H), 8.25 (d, *J* = 8.5, 1H), 10.84 (s, 1H); $^{13}$C NMR ($CDCl_3$), *δ*, ppm: 10.3, 35.7, 110.6, 116.4, 119.5, 120.6, 123.4, 124.7, 127.4, 127.6, 127.9, 128.8, 129.4, 132.9, 133.8, 134.4, 149.0, 156.8, 160.5, 162.2; HRMS *m/z*: Calcd for $C_{22}H_{19}N_3O_2$ $(M+Na)^+$: 380.1375, found: 380.1375.

*3.2.3. UV-Vis and fluorescent measurements*

UV-Vis absorption and fluorescence emission spectra of sensors were measured in 1.0 cm path length quartz cuvettes using a Shimadzu UV-2450 spectrophotometer and a Shimadzu RF-5301PC spectrofluorophotometer. Absorption and emission spectra of the sensor (**C1** and **C2**) in the presence of various metal ions ($Al^{3+}$, $Cd^{2+}$, $Ba^{2+}$, $Co^{2+}$, $Pb^{2+}$, $Ca^{2+}$, $Fe^{2+}$, $Fe^{3+}$, $Cs^{+}$, $Hg^{2+}$, $Cr^{3+}$, $Cu^{2+}$, $Mn^{2+}$, $Li^{+}$, $K^{+}$, $Mg^{2+}$, $Na^{+}$, $Nd^{3+}$, $Ni^{2+}$, $Zn^{2+}$ and $Sr^{2+}$) were measured in methanol solvent in the concentration of 50 µM and 20 µM, respectively.

**3.3. Results and discussion**

The binding ability and mode of sensors (**C1** and **C2**) towards $Al^{3+}$ and other metal ions was measured through UV-Vis, fluorescent spectrometry, naked-eye observation, HRMS and $^1$H NMR experiments.

*3.3.1. UV-Vis spectral studies*

The chemosensors (**C1** and **C2**) were investigated by UV-Vis absorption spectral behaviour in the presence of different metal ions in the 50 µM concentration of each component in methanol solvent. The free ligands, **C1** and **C2** exhibited a main absorption band at about 345 nm and 380 nm, respectively. Upon addition of metal ions to sensors, a new broad absorption band (mainly for $Cu^{2+}$, $Ni^{2+}$, $Co^{2+}$ and $Al^{3+}$ ions) was observed at region 350–480 nm (Figure 3.1). At the same time the absorption band at 300–390 nm and 340–430 nm of receptors **C1** and **C2** respectively, have also been shifted to low intensity. It means these two sensors are responding to the above mentioned metal ions, there is no significant changes were observed when mixed with other metal ions such as $Na^{+}$, $Ba^{2+}$, $Cd^{2+}$, $Fe^{2+}$, $Fe^{3+}$, $Cr^{3+}$, $Mn^{2+}$, $Cs^{+}$, $Hg^{2+}$, $Mg^{2+}$, $Ca^{2+}$, $Li^{+}$, $K^{+}$, $Nd^{3+}$, $Pb^{2+}$, $Zn^{2+}$ and $Sr^{2+}$.

*3.3.2. Fluorescence emission studies*

The fluorescence response of sensors **C1** and **C2** (20 µM) upon addition of metal ions (20 µM) have been investigated in methanol. Receptor **C1** and **C2** alone exhibited a single emission band at 498 nm and 484 nm respectively, with an excitation of 360 nm. Upon addition of various metals ($Ba^{2+}$, $Cd^{2+}$, $Na^{+}$, $K^{+}$, $Ca^{2+}$, $Mg^{2+}$, $Cs^{+}$, $Cu^{2+}$, $Cr^{3+}$, $Hg^{2+}$, $Li^{+}$, $Mn^{2+}$,

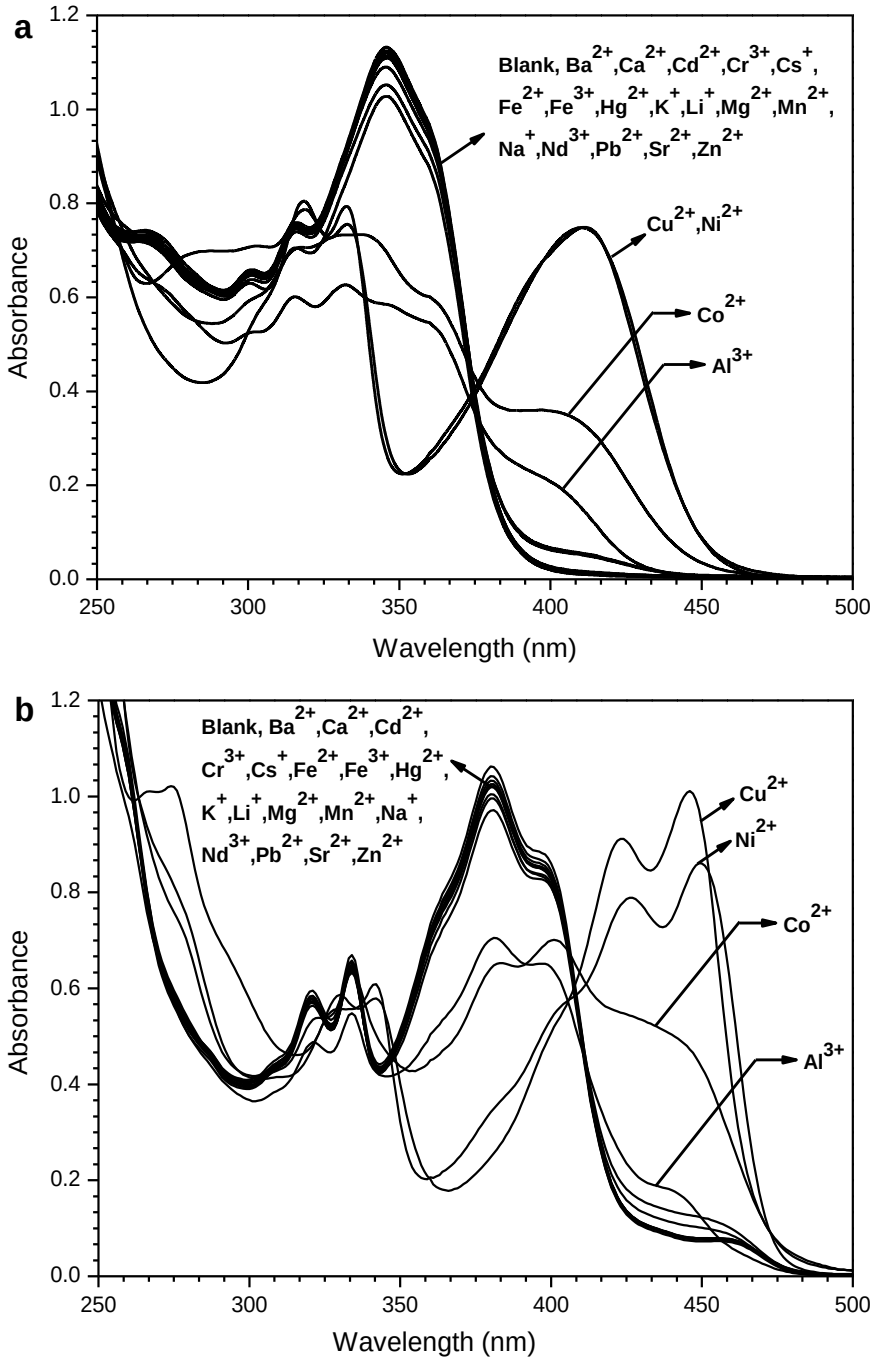


**Figure 3.1.** UV-Vis absorbance spectra of **C1** (50 µM) (a) and **C2** (50 µM) (b) in the presence of different metal ions ($Al^{3+}$, $Co^{2+}$, $Mg^{2+}$, $Na^{+}$, $Ca^{2+}$, $Li^{+}$, $Ba^{2+}$, $Cs^{+}$, $Hg^{2+}$, $Cu^{2+}$, $Ni^{2+}$, $Fe^{2+}$, $Fe^{3+}$, $K^{+}$, $Cr^{3+}$, $Mn^{2+}$, $Cd^{2+}$, $Nd^{3+}$, $Pb^{2+}$, $Zn^{2+}$ and $Sr^{2+}$) (50 µM) in methanol solvent.

$Nd^{3+}$, $Fe^{2+}$, $Fe^{3+}$, $Ni^{2+}$, $Co^{2+}$, $Pb^{2+}$, $Sr^{2+}$ and $Zn^{2+}$) no significant changes were observed (Figure 3.2). But on addition of $Al^{3+}$, receptors **C1** and **C2** exhibited a major fluorescence enrichment accompanied by a blue shift of 32 nm from 498 to 466 nm and 18 nm from 484 to 466 nm, respectively. Showing that the receptors **C1** and **C2** can exhibit "off-on" mode with high sensitivity towards $Al^{3+}$ over other metal ions. The receptors **C1** and **C2** in the presence of $Al^{3+}$ exhibited a spectacular color changes from colorless to bright blue and

bright green respectively, within 5 seconds, which could easily be detected by the naked-eye under UV lamp. While did not show any significant color changes with other metal ions.

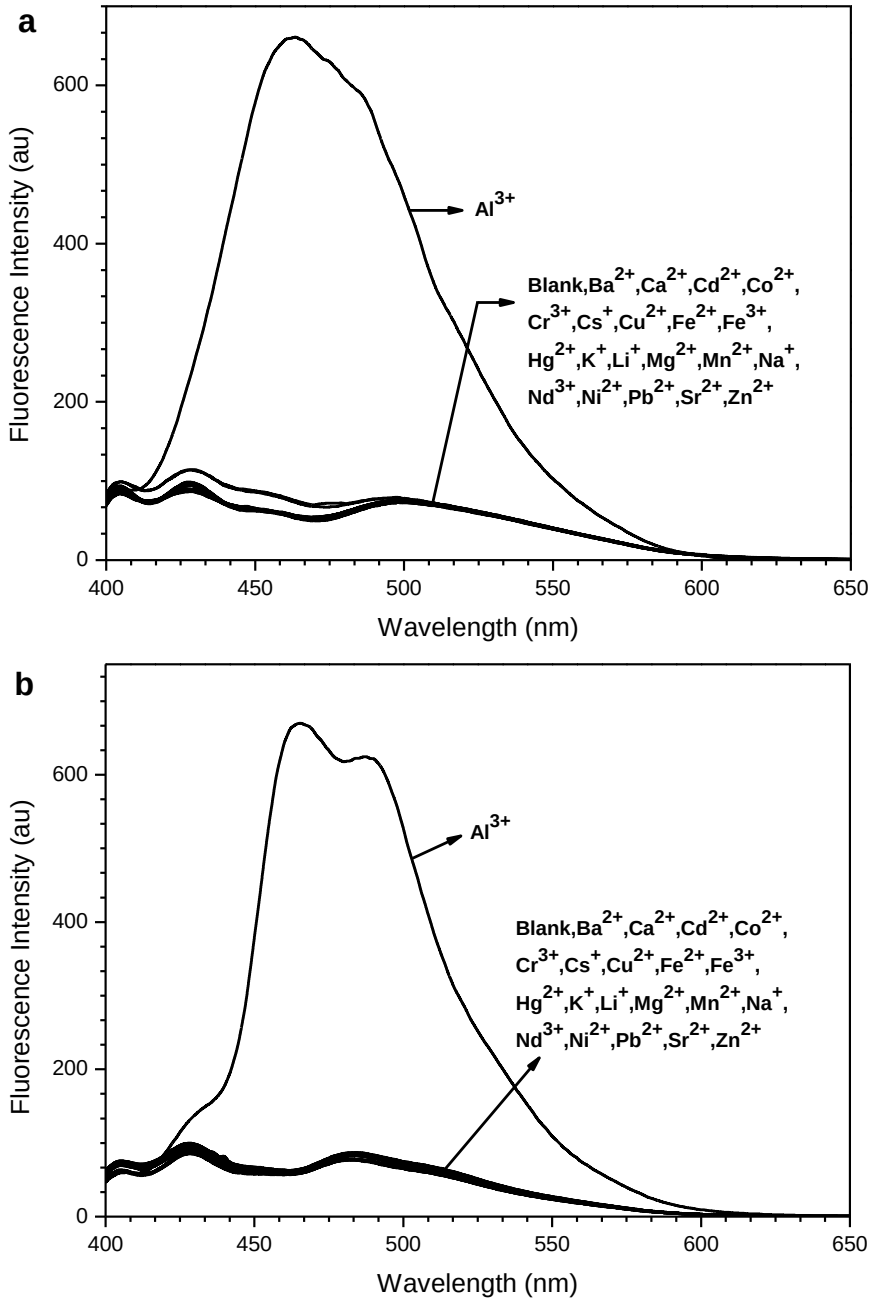


**Figure 3.2.** Fluorescence emission spectra of **C1** (20 µM) (a) and **C2** (20 µM) (b) in the presence of different metal ions ($Al^{3+}$, $Co^{2+}$, $Mg^{2+}$, $Na^{+}$, $Ca^{2+}$, $Li^{+}$, $Ba^{2+}$, $Cs^{+}$, $Hg^{2+}$, $Cu^{2+}$, $Ni^{2+}$, $Fe^{2+}$, $Fe^{3+}$, $K^{+}$, $Cr^{3+}$, $Mn^{2+}$, $Cd^{2+}$, $Nd^{3+}$, $Pb^{2+}$, $Zn^{2+}$ and $Sr^{2+}$) (20 µM) in methanol solvent.

The interaction between receptor (**C1** and **C2**) and $Al^{3+}$ ion was investigated at a pH range from 2.0 to 10.0. This experiment was carried out at a fixed concentration of receptor-$Al^{3+}$ is 20 µM in methanol. As shown in Figure 3.3, the fluorescence intensity at 466 nm almost did not change with the pH value at acidic and neutral conditions (pH < 7.0).

However, the fluorescence intensity decreased gradually from pH 7.0–10.0, due to the formation of salt. For further studies, the pH of solvent kept constant at 6.5.

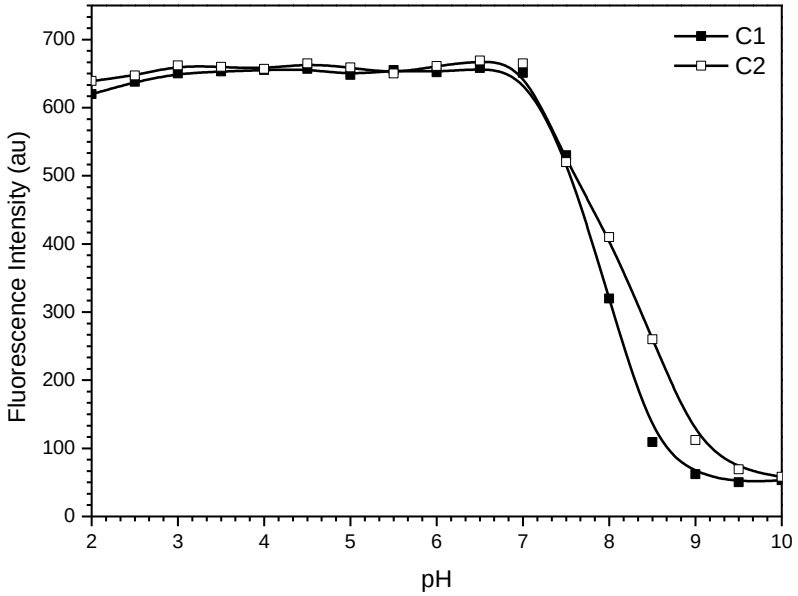


**Figure 3.3.** The variation in fluorescence intensity with the pH of receptor (**C1** and **C2**) (20 μM) in the presence of $Al^{3+}$ (1.0 equiv.) at 466 nm.

Furthermore, the fluorescence response of receptors (**C1** and **C2**) to various concentrations of $Al^{3+}$ (0–10 equiv.) was investigated. Upon addition of $Al^{3+}$, the fluorescence intensity centred at 466 nm of receptor slowly increased and remained stable when 1.0 equiv. $Al^{3+}$ was added, demonstrating the 1:1 stoichiometry between chemosensor and $Al^{3+}$ (Figure 3.4). The complex stability constants (*K*) through Benesi-Hildebrand

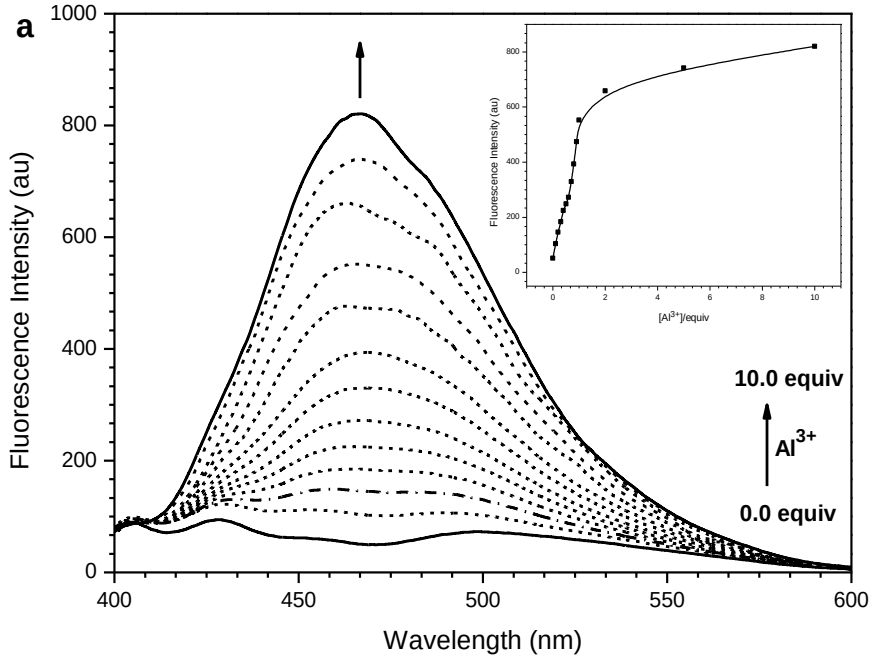

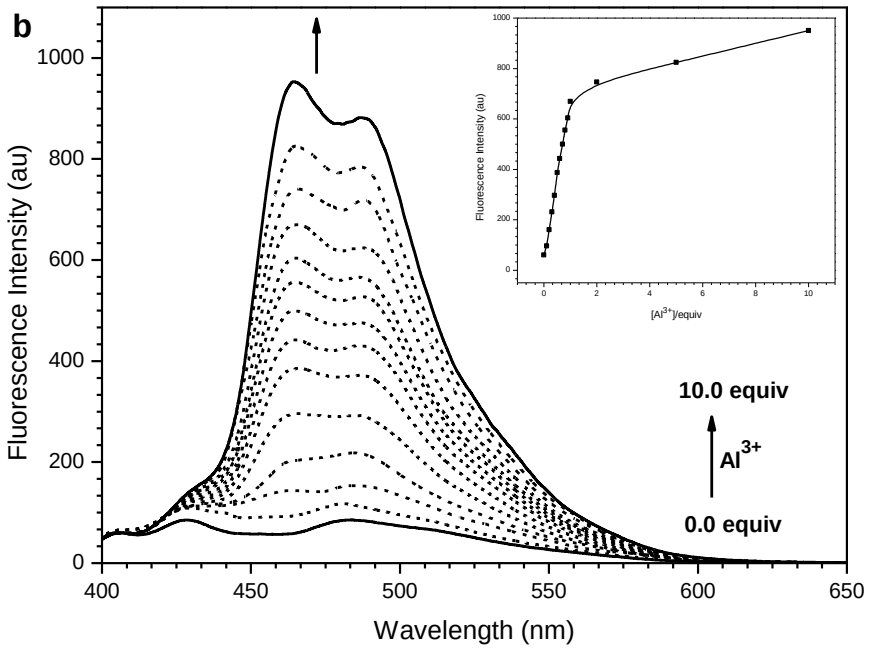


**Figure 3.4.** Fluorescence emission spectra of (a) **C1** (20 µM) and (b) **C2** (20 µM) upon addition of $Al^{3+}$ ion (0.0–1.0, 2.0, 5.0 and 10.0 equiv.) with an excitation of 360 nm. Inset shows the fluorescence change at 466 nm as a function of the amount of $Al^{3+}$ ions.

method for Al(III) with **C1** and **C2** were found to be $1.0\times10^{6}$ $M^{-1}$ and $9.7\times10^{5}$ $M^{-1}$, respectively (Figure 3.5). The detection limit of Al(III) was estimated based on the fluorescence titration profile as $2.1\times10^{-7}$ M (for **C1**) and $1.9\times10^{-7}$ M (for **C2**) based on S/N = 3 (Figure 3.6). In addition, a Job plot obtained from the emission data confirmed the 1:1 stoichiometry for probe–$Al^{3+}$ complex (Figure 3.7) and it is further proved from HRMS results (Figure 3.8).

The selectivity of **C1** and **C2** (20 µM) for $Al^{3+}$ over other metal ions (1.0 equiv.) was investigated by the competition experiments. As shown in Figure 3.9, the fluorescence response of **C1** and **C2** toward $Al^{3+}$ in the presence of various metal ions was investigated, and the results indicated that $Cu^{2+}$, $Ni^{2+}$ and $Co^{2+}$ could interfere in the interaction between receptor (**C1** and **C2**) and $Al^{3+}$. Indicating that the binding abilities of $Cu^{2+}$, $Ni^{2+}$and $Co^{2+}$ are stronger than that of $Al^{3+}$ toward receptors. Upon addition of 1.0 equiv. of $Al^{3+}$ in the presence of other metal ions ($Ca^{2+}$, $Li^{+}$, $Na^{+}$, $Cs^{+}$, $Ba^{2+}$, $K^{+}$, $Cr^{3+}$, $Mn^{2+}$, $Fe^{2+}$, $Fe^{3+}$, $Cd^{2+}$, $Hg^{2+}$, $Mg^{2+}$, $Nd^{3+}$, $Pb^{2+}$, $Sr^{2+}$ and $Zn^{2+}$), 11-fold enhancement of the fluorescence intensity was observed, which is large enough to determine $Al^{3+}$ from other metal ions. We could also directly observe the fluorescence changes of receptors (**C1** and **C2**) before and after addition of $Al^{3+}$, with and without other sensed metal ions under UV lamp. As depicted in Figure 3.10, by the addition of other metal ions ($Cu^{2+}$, $Co^{2+}$ and $Ni^{2+}$) quenches the fluorescence of the receptor–$Al^{3+}$ complex, due to the more binding ability towards $Cu^{2+}$, $Ni^{2+}$ and $Co^{2+}$ ions.

It means, the reported sensors provide simultaneous detection of $Al^{3+}$ and other metal ions ($Cu^{2+}$, $Ni^{2+}$ and $Co^{2+}$).

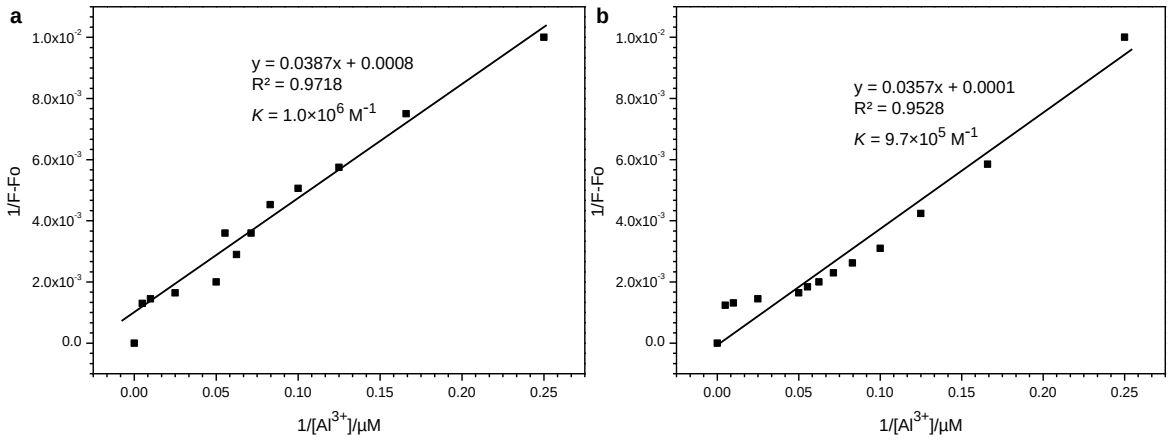


**Figure 3.5.** Linear regression plot of fluorescence intensity change $1/(F\text{-}F_0)$ as a function of concentration $1/[Al^{3+}]$.

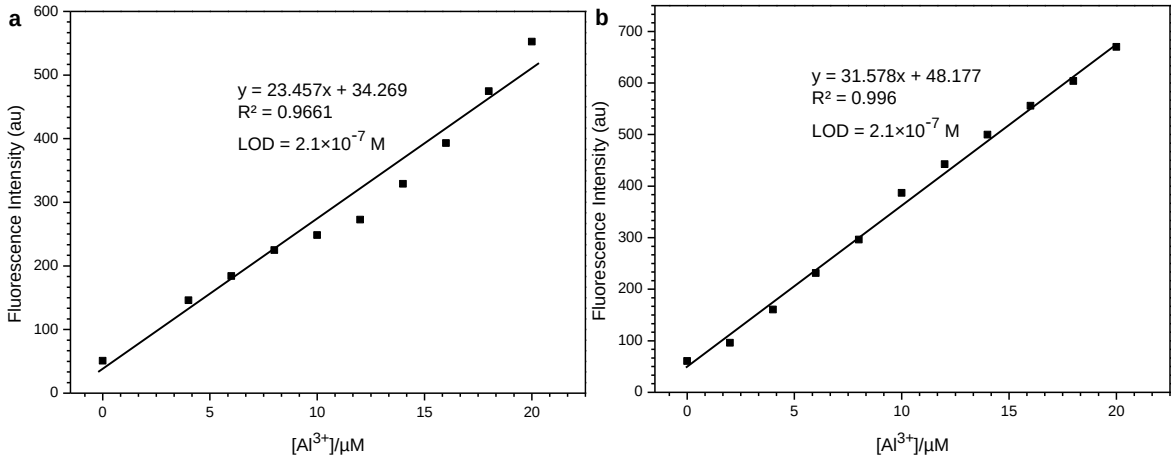


**Figure 3.6.** The fluorescence enhancement change as a function of concentration of Al(III) added.

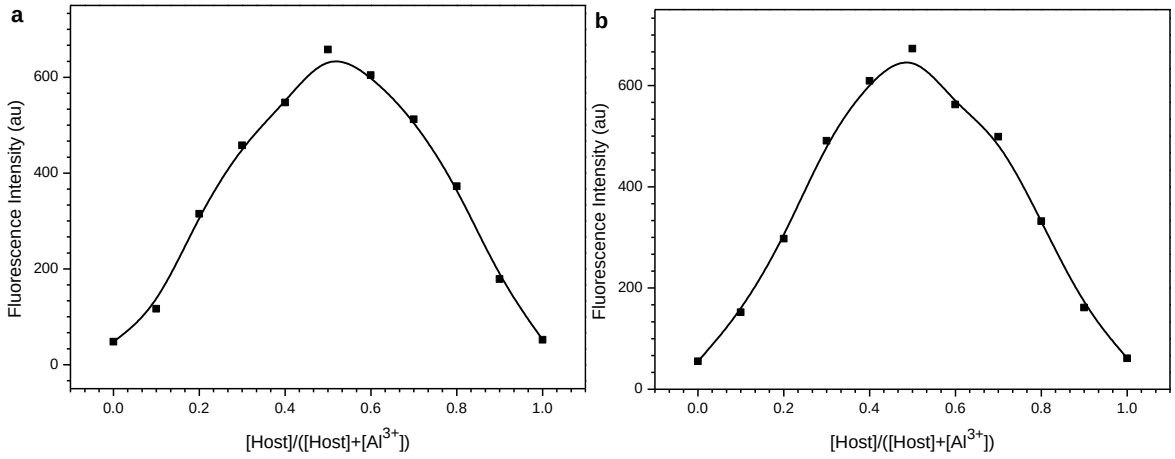


**Figure 3.7.** Job's plot for **C1** (a) and **C2** (b) by fluorescence method. Total concentration of receptor and metal is 20 μM.

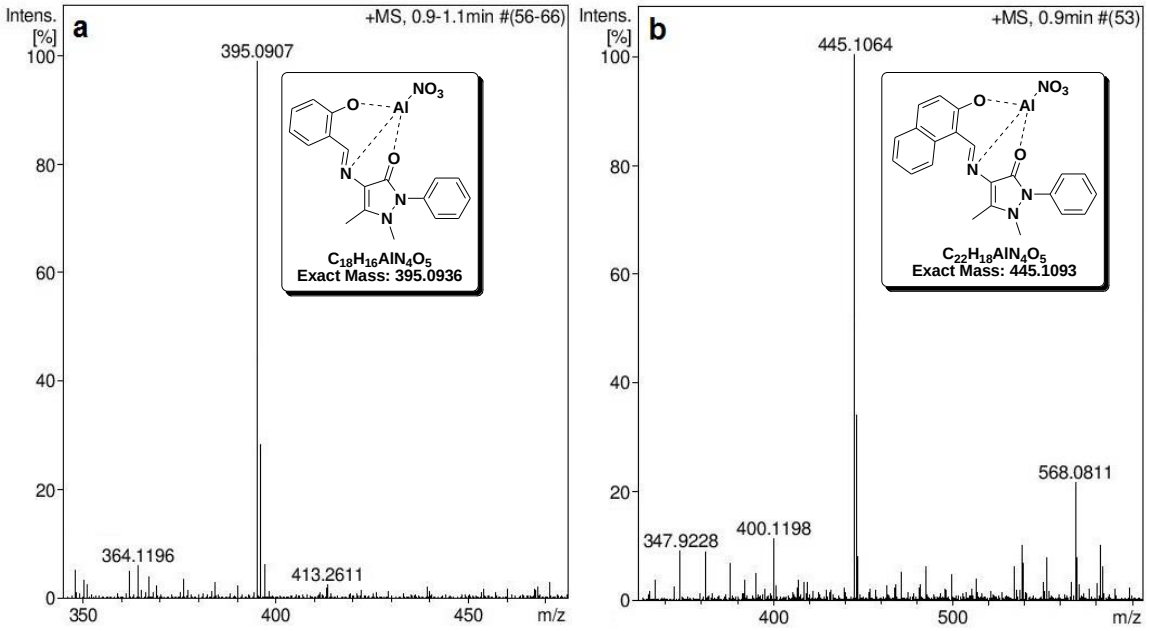


**Figure 3.8.** HRMS spectrum of (a) **C1** and (b) **C2** upon addition of $Al(N0_3)_3.9H_2O$ (1.0 equiv.) in MeOH.

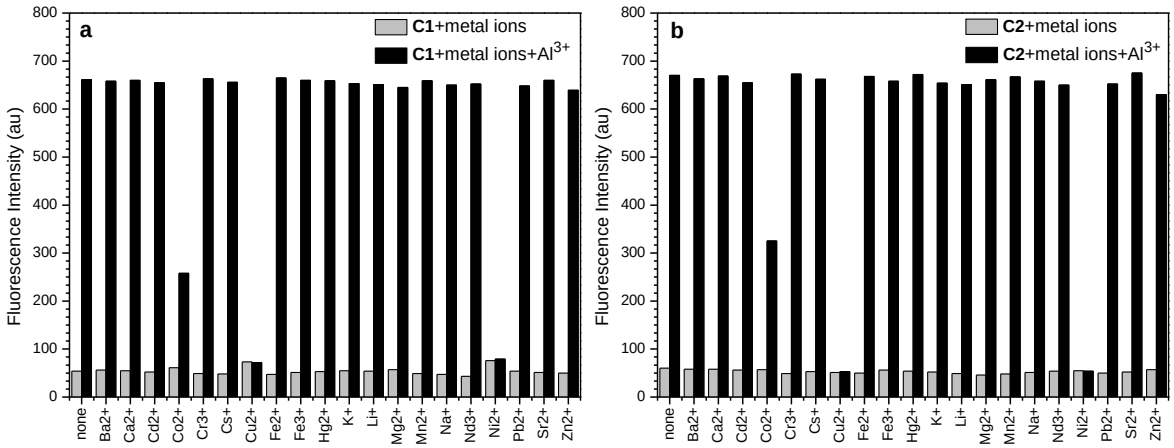


**Figure 3.9.** Selectivity of the **C1** (a) and **C2** (b) toward $Al^{3+}$ and other metal ions. In these experiments, the fluorescence measurement was taken for 20 μM concentration of **C1** (a) and **C2** (b) at $\lambda_{ex}$ = 360 nm in methanol at room temperature with various metal ions (1.0 equiv.) and in the absence (gray bars) and presence (black bars) of 1.0 equiv. $Al^{3+}$ ion.

### *3.3.3. $^1$H NMR titration*

The binding mode of receptor (**C1** and **C2**) towards $Al^{3+}$ was confirmed by the $^1$H NMR titrations using $CD_3OD$ as a solvent. As depicted in Figure 3.11, the proton of imine moiety at about 9.68 ppm (for **C1**) and 10.62 ppm (for **C2**) was shifted upfield to 8.87 ppm and 9.67 ppm, respectively, followed the addition of $Al^{3+}$. Due to interrupt the intramolecular hydrogen bonding between the phenolic hydroxyl group and nitrogen of the imine moiety by the addition of $Al^{3+}$. The imine proton signal at $\delta$ 10.62 almost completely disappeared,

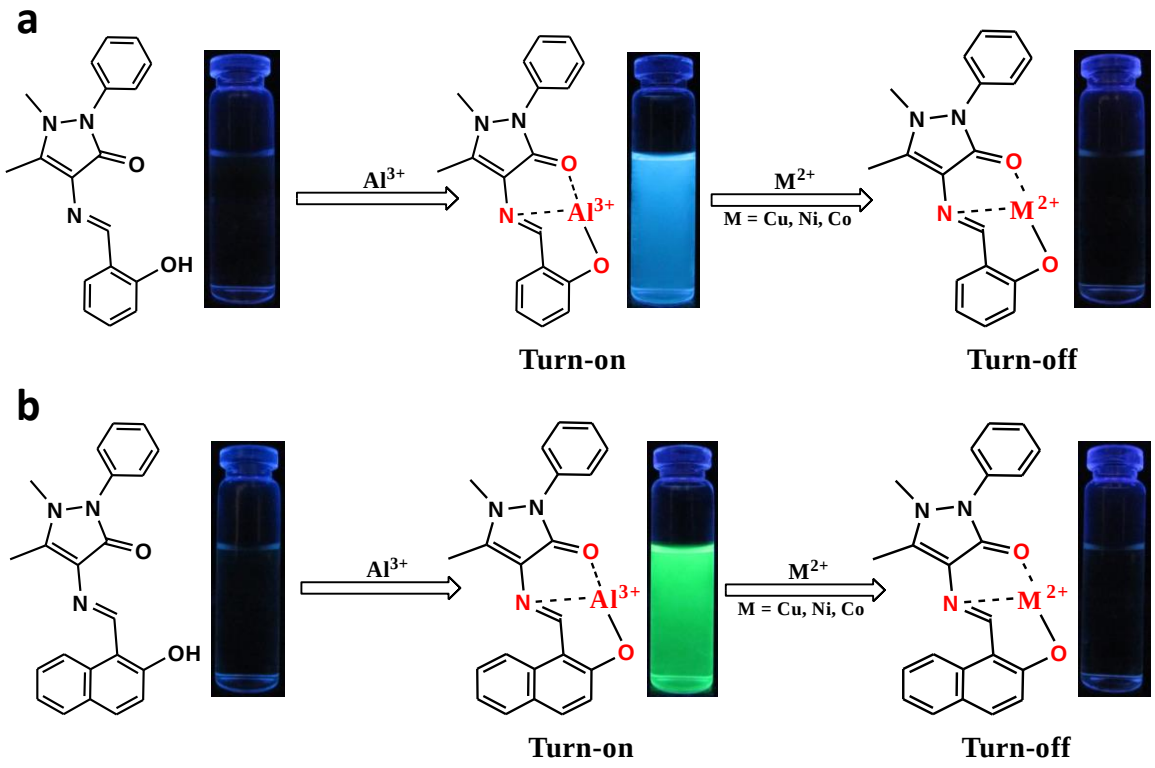


**Figure 3.10.** The fluorescence emission changes of sensors **C1** (a) and **C2** (b) (20 μM) with 1.0 equiv. of $Al^{3+}$, and in the presence of other metal ions ($Cu^{2+}$, $Co^{2+}$ and $Ni^{2+}$) excited by a commercially available UV lamp ($\lambda_{ex}$ = 365 nm).

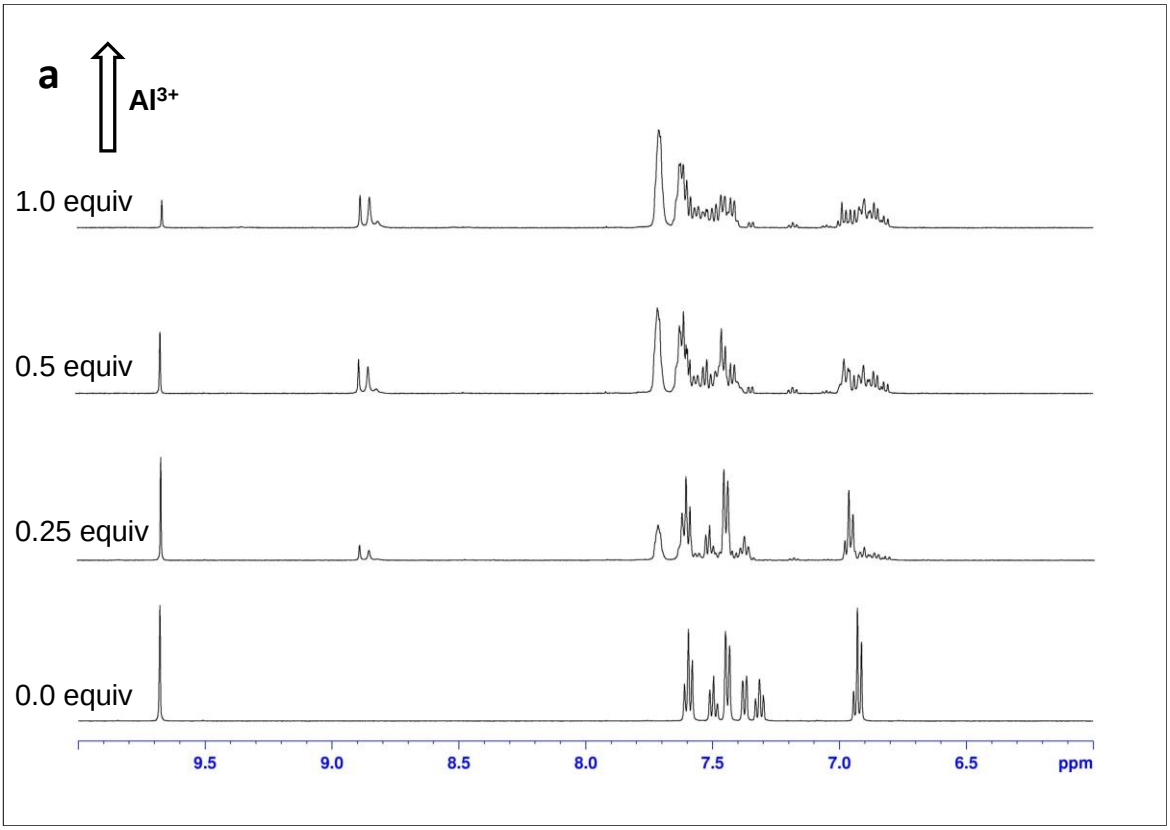

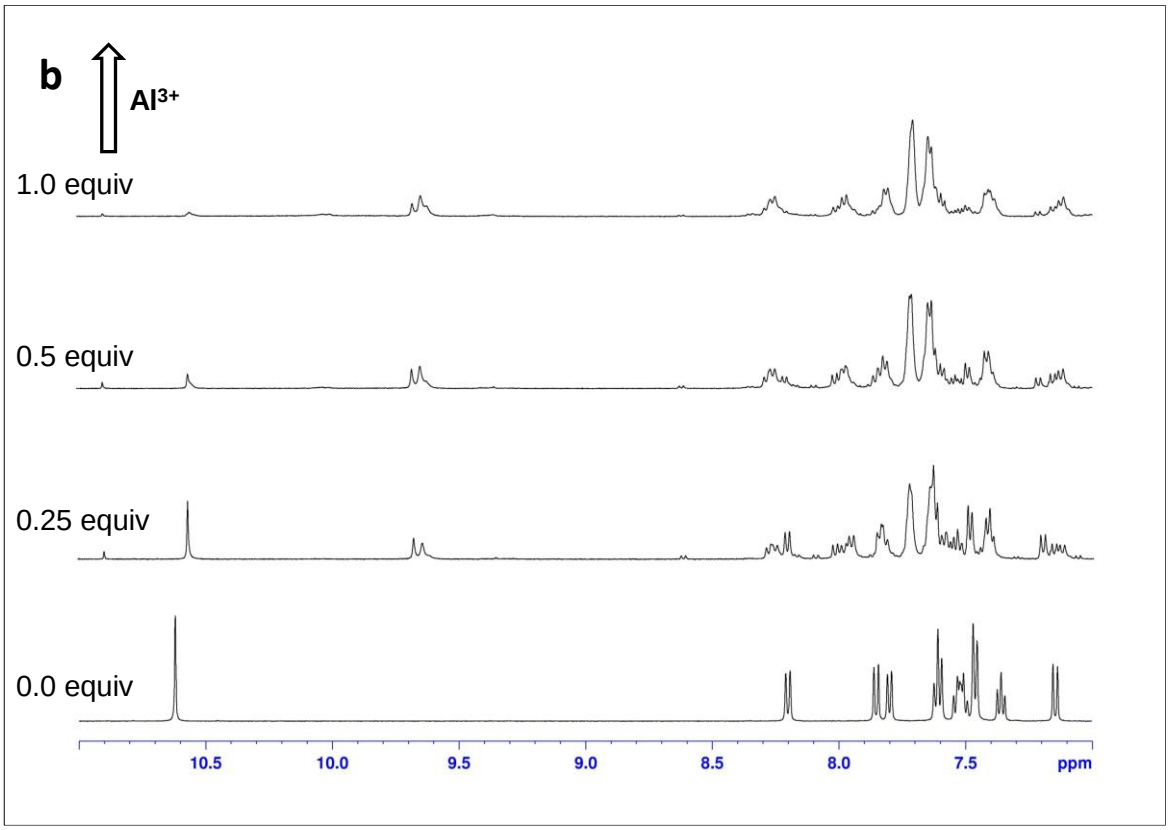


**Figure 3.11.** $^{1}$H NMR (500 MHz) spectra of receptor (a) **C1** and (b) **C2** with $Al^{3+}$ (0.0–1.0 equiv.) in $CD_3OD$.

when 1.0 equiv. of $Al^{3+}$ was added to receptor **C2**, indicating that the receptor interacts with $Al^{3+}$ and form stable complex with 1:1 stoichiometry. On the other hand, the protons of phenylene were shifted downfield upon addition of $Al^{3+}$, which indicated that the structure of receptors became more rigid after coordination with $Al^{3+}$. It indicated that the phenolic hydroxyl group and nitrogen atom of the imine moiety participated in complexation with $Al^{3+}$ ion.

### 3.4. Conclusion

In summary, the proposed sensors (**C1** and **C2**) exhibited a very good selective and sensitive toward $Al^{3+}$ ion over other tested metal ions. Moreover, the sensory system in methanol as well as in water shows bright blue (for **C1**) and bright green (**C2**) color with $Al^{3+}$ under a UV lamp, which can be easily identified by the naked eye. Thus, the reported sensors have the facility to provide as a practical sensor for detection of $Al^{3+}$ ion in both environment and biological samples.

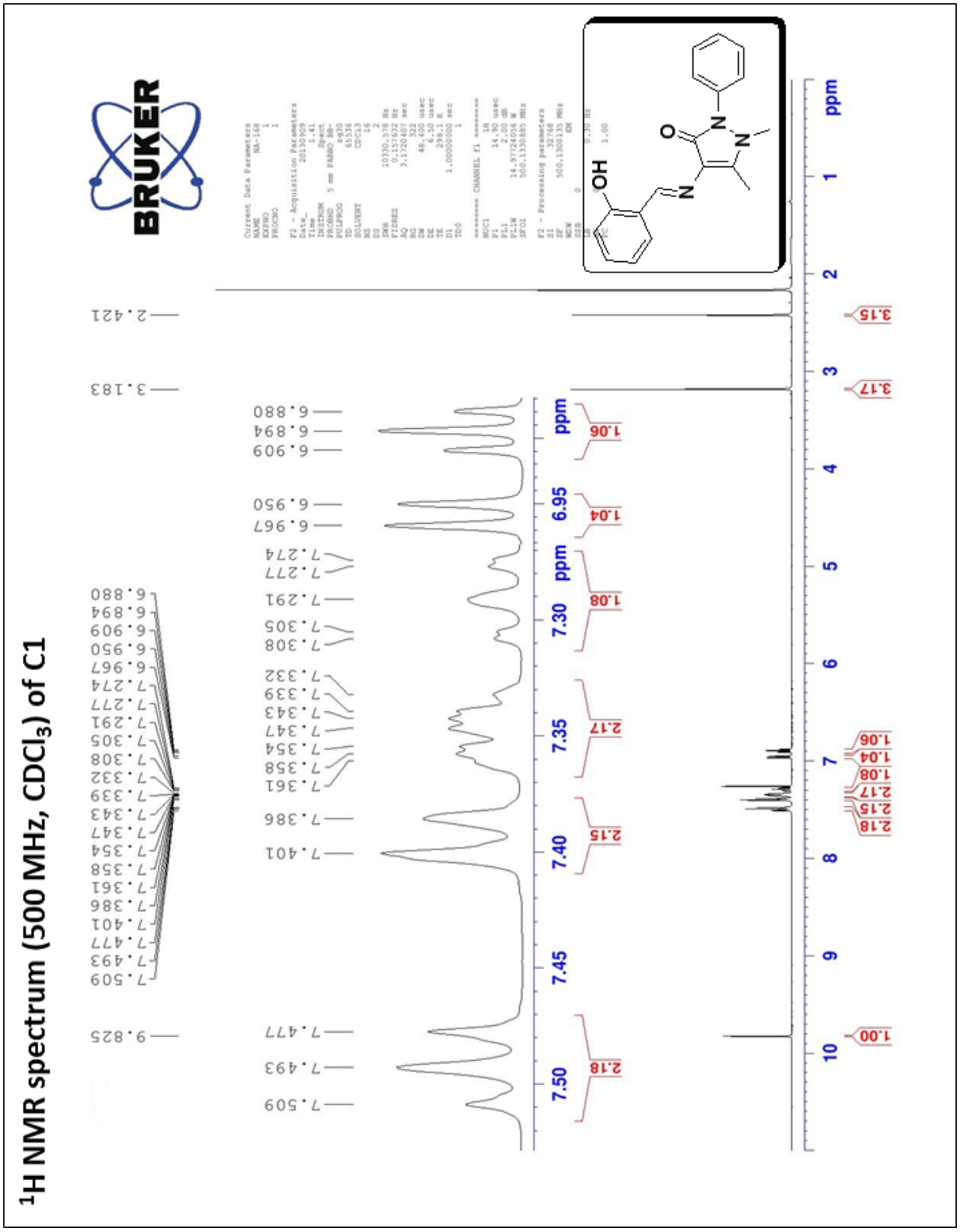
$^1$H NMR spectrum (500 MHz, $CDCl_3$) of C1
BRUKER
OH
N
N
O
ppm

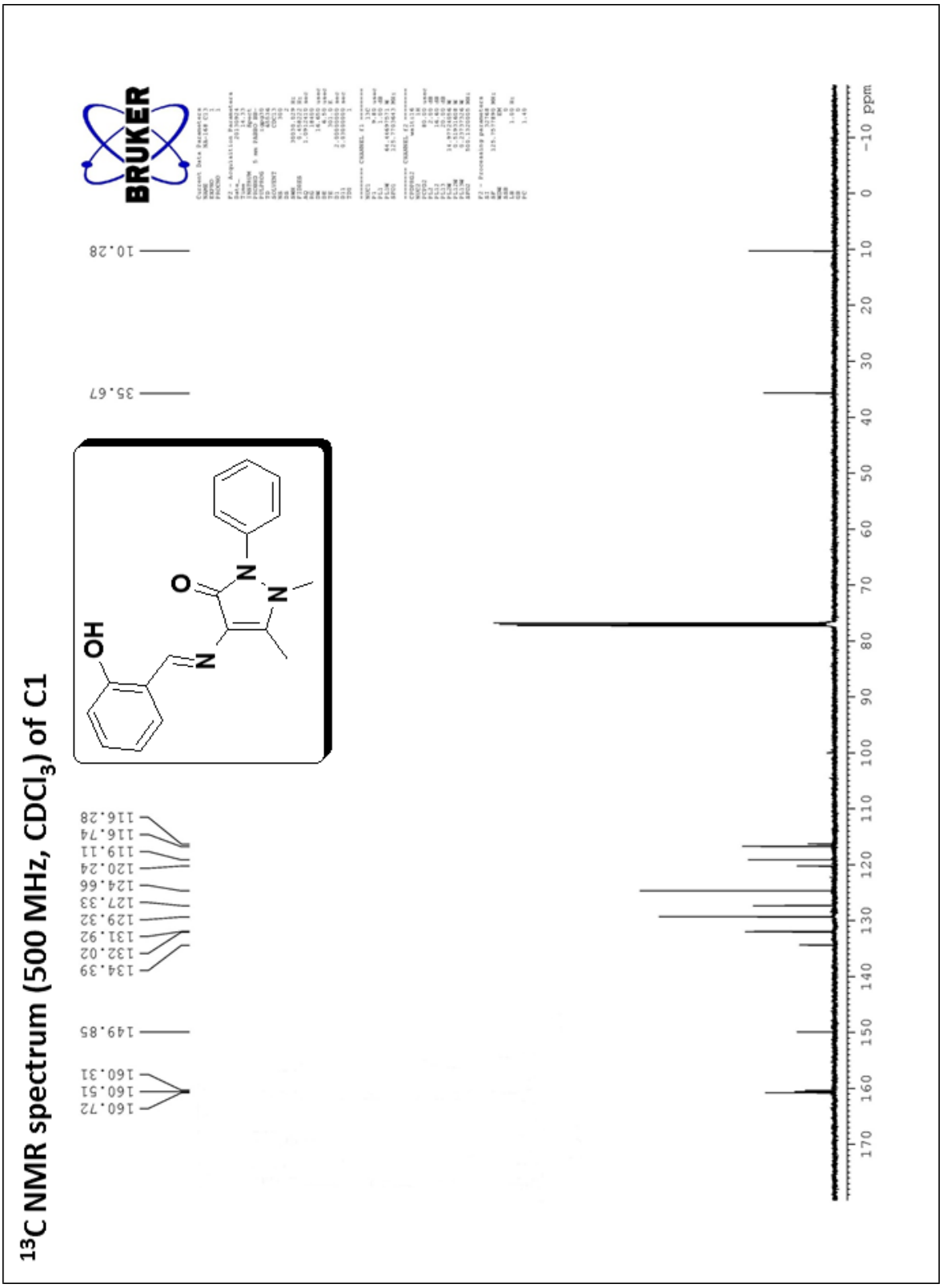
13C NMR spectrum (500 MHz, CDCl3) of C1
BRUKER
OH
N
N
O
10.28
35.67
116.28
116.74
119.11
120.24
124.66
127.33
129.32
131.92
132.02
134.39
149.85
160.31
160.51
160.72
ppm

## HRMS spectrum of C1

**Acquisition Parameter**

| | | | | | |
|---|---|---|---|---|---|
| Source Type | ESI | Ion Polarity | Positive | Set Nebulizer | 0.4 Bar |
| Focus | Not active | Set Capillary | 4500 V | Set Dry Heater | 180 °C |
| Scan Begin | 50 m/z | Set End Plate Offset | -500 V | Set Dry Gas | 4.0 l/min |
| Scan End | 3000 m/z | Set Collision Cell RF | 650.0 Vpp | Set Divert Valve | Source |

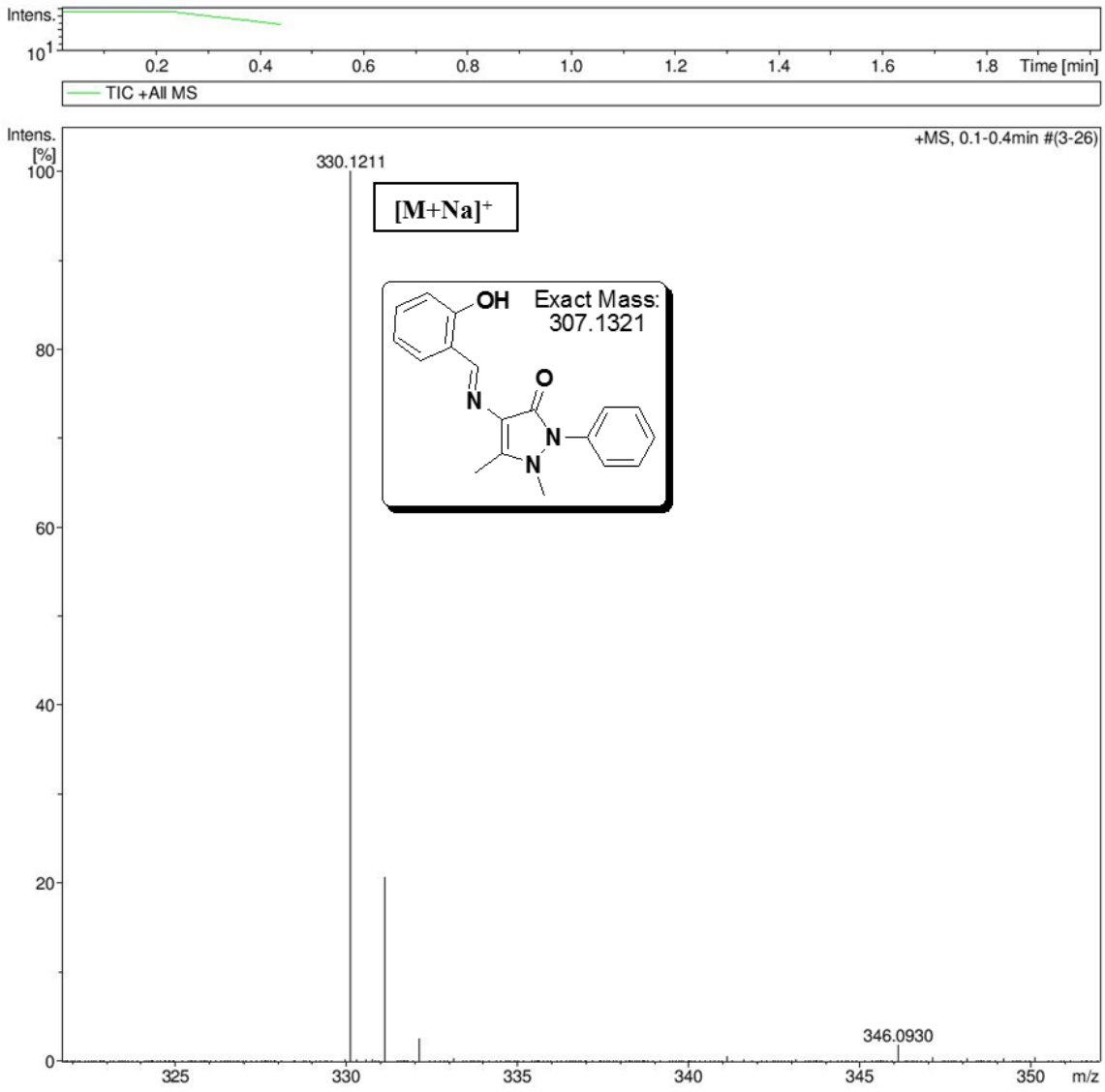

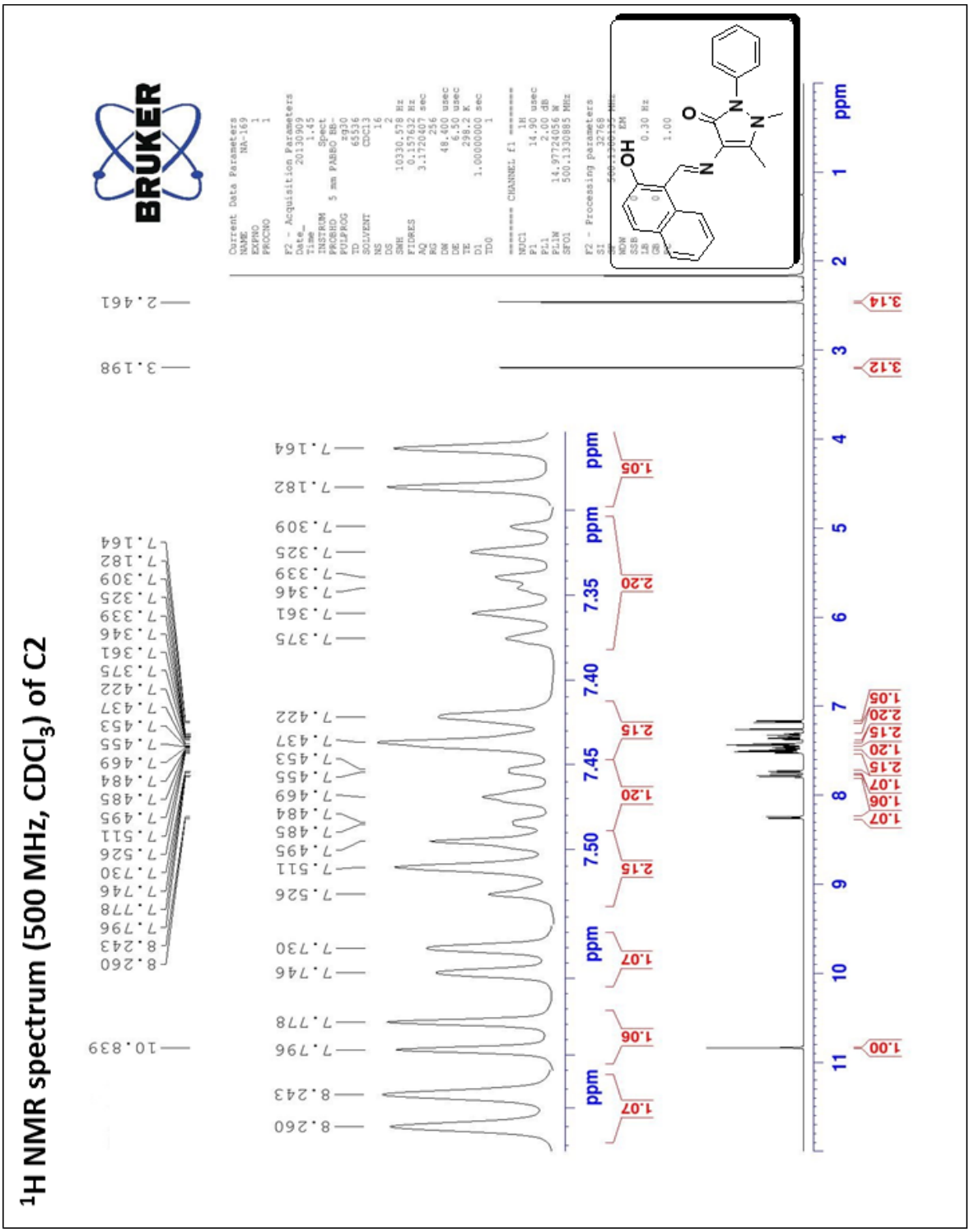
$^1$H NMR spectrum (500 MHz, $CDCl_3$) of C2
BRUKER
OH
N
O
ppm

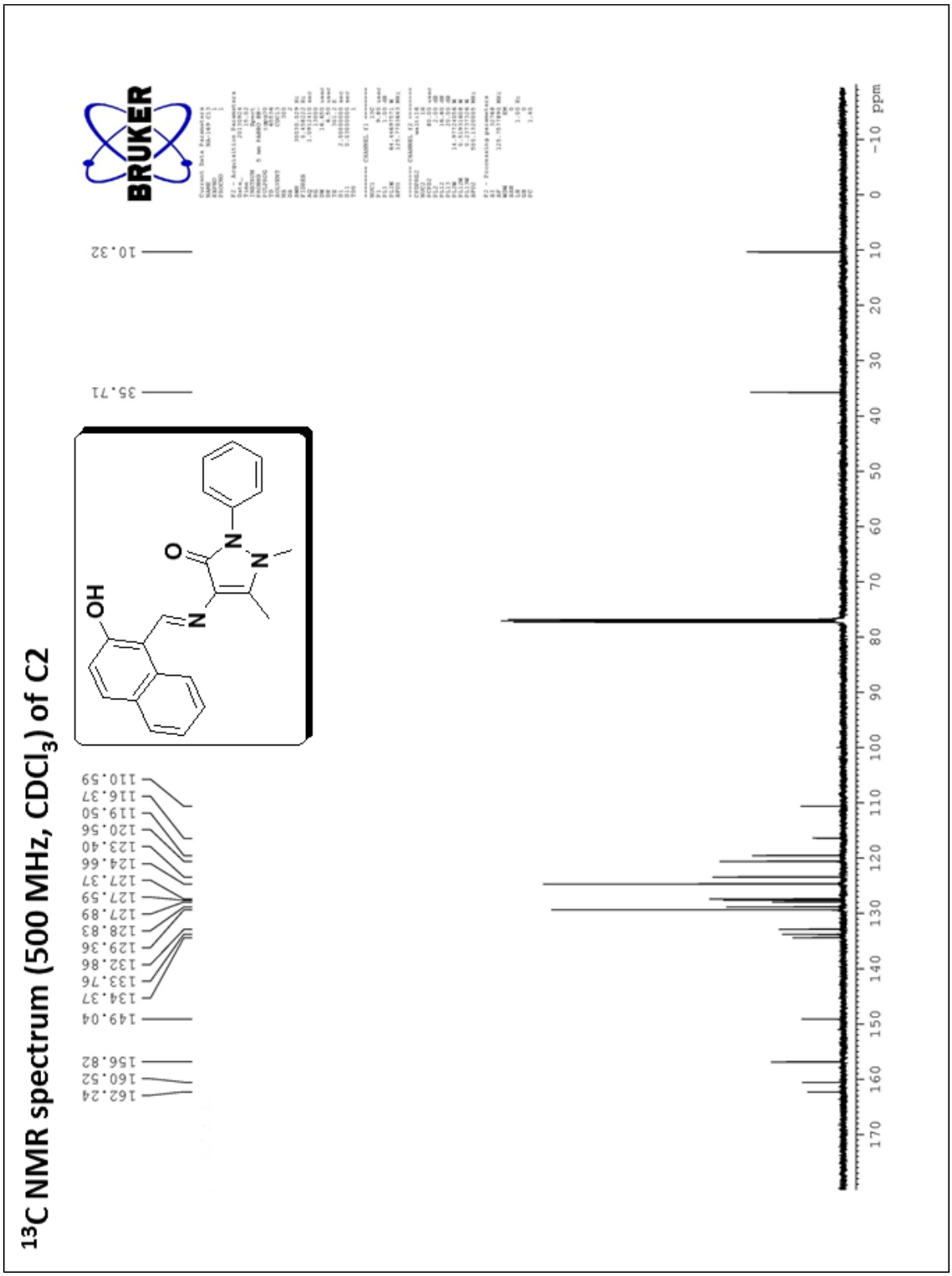
13C NMR spectrum (500 MHz, CDCl3) of C2
BRUKER
OH
O
N
N
N
10.32
35.71
110.59
116.37
119.50
120.56
123.40
124.66
127.37
127.59
127.89
128.83
129.36
132.86
133.76
134.37
149.04
156.82
160.52
162.24
ppm

## HRMS spectrum of C2

**Acquisition Parameter**

| | | | | | |
|---|---|---|---|---|---|
| Source Type | ESI | Ion Polarity | Positive | Set Nebulizer | 0.4 Bar |
| Focus | Not active | Set Capillary | 4500 V | Set Dry Heater | 180 ℃ |
| Scan Begin | 50 m/z | Set End Plate Offset | -500 V | Set Dry Gas | 4.0 l/min |
| Scan End | 3000 m/z | Set Collision Cell RF | 650.0 Vpp | Set Divert Valve | Source |

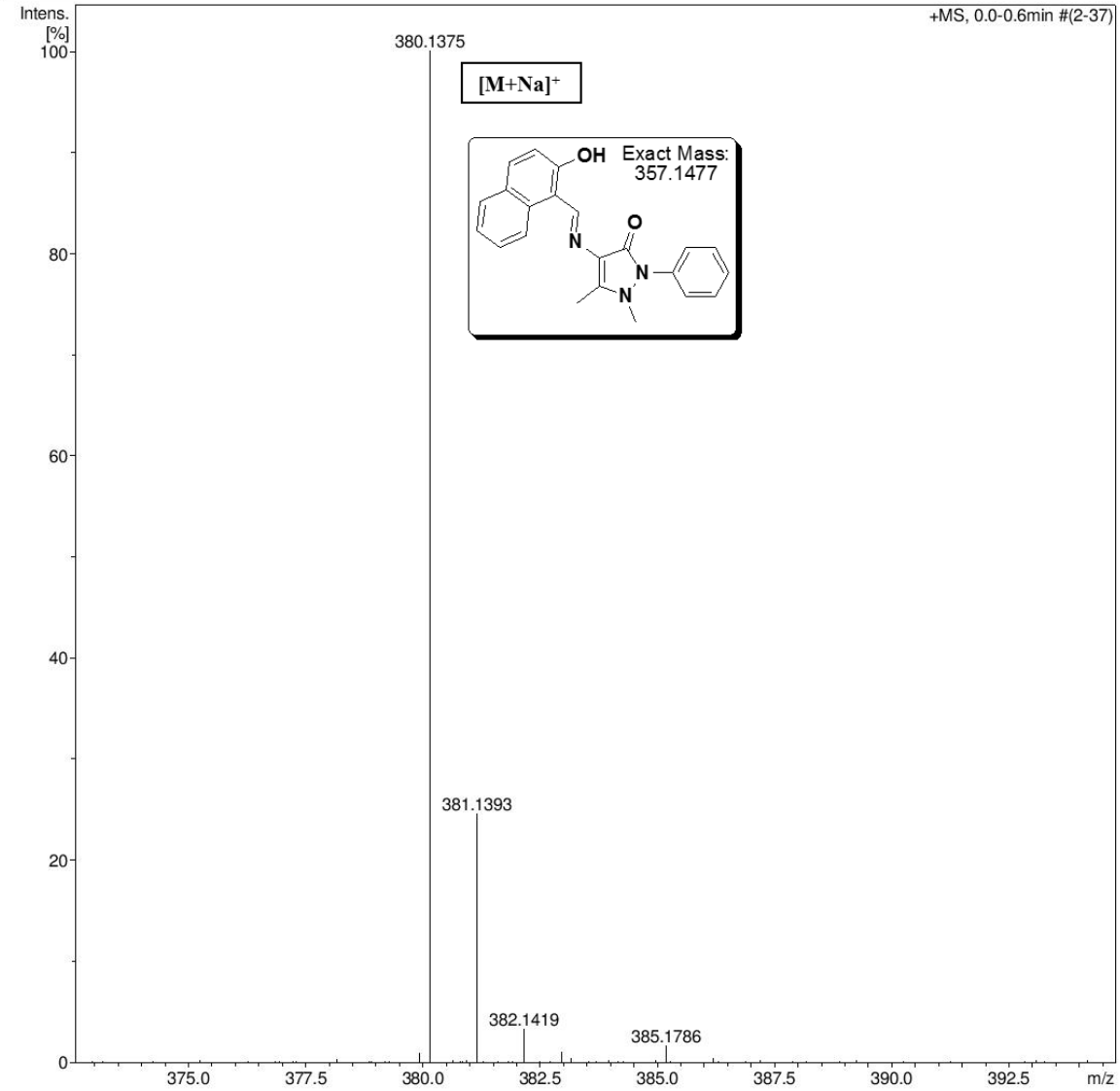

**References**


1. N.W. Baylor, W. Egan, P. Richman, Aluminum salts in vaccines—US perspective, *Vaccine*, 2002, **20**, S18–S23.
2. M.G. Soni, S.M. White, W.G. Flamm, G.A. Burdock, Safety evaluation of dietary aluminum, *Regul. Toxicol. Pharm.*, 2001, **33**, 66–79.
3. W.A. Banks, A.J. Kastin, Aluminum-induced neurotoxicity: alterations in membrane function at the blood-brain barrier, *Neurosci. Biobehav. Rev.*, 1989, **13**, 47–53.
4. M. Kawahara, K. Muramoto, K. Kobayashi, H. Mori, Y. Kuroda, Aluminum promotes the aggregation of Alzheimer′s amyloid β-protein in vitro, *Biochem. Biophys. Res. Commun.*, 1994, **198**, 531–535.
5. P.F. Good, C.W. Olanow, D.P. Perl, Neuromelanin-containing neurons of the substantia nigra accumulate iron and aluminum in Parkinson's disease: a LAMMA study, *Brain Res.*, 1992, **593**, 343–346.
6. J.L. Lin, M.T. Kou, M.L. Leu, Effect of long-term low-dose aluminum-containing agents on hemoglobin synthesis in patients with chronic renal insufficiency, *Nephron*, 1996, **74**, 33–38.
7. S.R. Paik, J.H. Lee, D.H. Kim, C.S. Chang, J. Kim, Aluminum-induced structural alterations of the precursor of the non-Aβ component of Alzheimer's disease amyloid, *Arch. Biochem. Biophys.*, 1997, **344**, 325–334.
8. M.N. Alvim, F.T. Ramos, D.C. Oliveira, R.M.S. Isaias, M.G.C. Franca, Aluminium localization and toxicity symptoms related to root growth inhibition in rice (Oryza sativa L.) seedlings, *J. Biosci.*, 2012, **37**, 1079–1088.
9. A.N.M. Alamgir, S. Akhter, Effects of aluminium ($Al^{3+}$) on seed germination and seedling growth of wheat (*Triticum aestivum L.*), *Bangladesh J. Bot.*, 2009, **38**, 1–6.
10. V.K. Gupta, A.K. Jain, G. Maheshwari, Aluminum(III) selective potentiometric sensor based on morin in poly(vinyl chloride) matrix, *Talanta*, 2007, **72**, 1469–1473.
11. V.K. Gupta, R.N. Goyal, A.K. Jain, R.A. Sharma, Aluminium (III)-selective PVC membrane sensor based on a Schiff base complex of N,N'-bis (salicylidene)-1,2-cyclohexanediamine, *Electrochim. Acta*, 2009, **54**, 3218–3224.
12. V.K. Gupta, A.K. Jain, M.A. Khayat, S.K. Bhargava, J.R. Raisoni, Electroanalytical studies on cobalt(II) selective potentiometric sensor based on bridge modified calixarene in poly(vinyl chloride), *Electrochim. Acta*, 2008, **53**, 5409–5414.
13. Y.S. Jang, B. Yoon, J.M. Kim, Colorimetric detection of aluminium ion based on conjugated polydiacetylene supramolecules, *Macromol. Res.*, 2011, **19**, 97–99.

14. S. Chen, Y.M. Fang, Q. Xiao, J. Li, S.B. Li, H.J. Chen, J.J. Sun, H.H. Yang, Rapid visual detection of aluminium ion using citrate capped gold nanoparticles, *Analyst*, 2012, **137** 2021–2023.
15. V.K. Gupta, A.K. Singh, M.R. Ganjali, P. Norouzi, F. Faridbod, N. Mergu, Comparative study of colorimetric sensors based on newly synthesized Schiff bases, *Sens. Actuators B*, 2013, **182**, 642–651.
16. L. Wang, D. Ye, D. Cao, A novel coumarin Schiff-base as a Ni(II) ion colorimetric sensor, *Spectrochim. Acta A*, 2012, **90**, 40–44.
17. K. Farhadi, M. Forough, R. Molaei, S. Hajizadeh, A. Rafipour, Highly selective $Hg^{2+}$ colorimetric sensor using green synthesized and unmodified silver nanoparticles, *Sens. Actuators B*, 2012, **161**, 880–885.
18. Y.P. Li, X.M. Liu, Y.H. Zhang, Z. Chang, A fluorescent and colorimetric sensor for $Al^{3+}$ based on a dibenzo-18-crown-6 derivative, *Inorg. Chem. Commun.*, 2013, **33**, 6–9.
19. C.H. Chen, D.J. Liao, C.F. Wan, A.T. Wu, A turn-on and reversible Schiff base fluorescence sensor for $Al^{3+}$ ion, *Analyst*, 2013, **138**, 2527–2530.
20. S. Guha, S. Lohar, A. Sahana, A. Banerjee, D.A. Safin, M.G. Babashkina, M.P. Mitoraj, M. Bolte, Y. Garcia, S.K. Mukhopadhyay, D. Das, A coumarin-based "turn-on" fluorescent sensor for the determination of $Al^{3+}$: single crystal X-ray structure and cell staining properties, *Dalton Trans.*, 2013, **42**, 10198–10207.
21. S. Kim, J.Y. Noh, K.Y. Kim, J.H. Kim, H.K. Kang, S.W. Nam, S.H. Kim, S. Park, C. Kim, J. Kim, Salicylimine-based fluorescent chemosensor for aluminum ions and application to bioimaging, *Inorg. Chem.*, 2012, **51**, 3597–3602.
22. M. Yan, T. Li, Z. Yang, A novel coumarin Schiff-base as a Zn(II) ion fluorescent sensor, *Inorg. Chem. Commun.*, 2011, **14**, 463–465.
23. K. Viswanathan, Utilizing a tripeptide conjugated fluorescent hybrid nanoparticles as a fluorescence sensor for the determination of copper ions, *Sens. Actuators A*, 2012, **175**, 15–18.
24. Y.J. Jang, Y.H. Yeon, H.Y. Yang, J.Y. Noh, I.H. Hwang, C. Kim, A colorimetric and fluorescent chemosensor for selective detection of $Cr^{3+}$ and $Al^{3+}$, *Inorg. Chem. Commun.*, 2013, **33**, 48–51.
25. Y. Dong, X. Mao, X. Jiang, J. Hou, Y. Cheng, C. Zhu, L-Proline promoted fluorescent sensor for $Mg^{2+}$ detection in a multicomponent sensory system, *Chem. Commun.*, 2011, **47**, 9450–9452.

26. Z. Chen, C. Xue, W. Shi, F.-T. Luo, S. Green, J. Chen, H. Liu, Selective and sensitive fluorescent sensors for metal ions based on manipulation of side-chain compositions of poly(p-phenyleneethynylene)s, *Anal. Chem.*, 2004, **76**, 6513–518.
27. J.Y. Kwon, Y.J. Jang, Y.J. Lee, K.M. Kim, M.S. Seo, W. Nam, J. Yoon, A highly selective fluorescent chemosensor for $Pb^{2+}$, *J. Am. Chem. Soc.*, 2005, **127**, 10107–10111.
28. K. Soroka, R.S. Vithanage, D.A. Phillips, B. Walker, P.K. Dasgupta, Fluorescence properties of metal complexes of 8-hydroxyquinoline-5-sulfonic acid and chromatographic applications, *Anal. Chem.*, 1987, **59**, 629–636.
29. Q.H. You, P.S. Chan, W.H. Chan, S.C.K. Hau, A.W.M. Lee, N.K. Mak, T.C.W. Mak, R.N.S. Wong, A quinolinyl antipyrine based fluorescence sensor for $Zn^{2+}$ and its application in bioimaging, *RSC Adv.*, 2012, **2**, 11078–11083.
30. T. Rosu, S. Pasculescu, V. Lazar, C. Chifiriuc, R. Cernat, Copper(II) complexes with ligands derived from 4-amino-2,3-dimethyl-1-phenyl-3-pyrazolin-5-one: synthesis and biological activity, *Molecules*, 2006, **11**, 904–914.
31. B. Caifeng, F. Yuhua, Synthesis and thermodecomposition kinetics of the $UO_2$ (II) complex with 4-(2-hydroxy-naphthalen-1-ylmethyleneamino)-antipyrin, *J. Radioanal. Nucl. Chem.*, 2004, **262**, 497–500.

# CHAPTER 4
# Flavonol Based Fluorescent Chemosensors for Zn(II) Ion

## 4.1. Introduction

Zinc is the second most abundant transition element after iron in the human body and essential with concentration ranging from sub-nM to 0.3 mM [1, 2]. It is a very important ion species in many biological activities such as cellular metabolism, gene expression, neural signal transmission, DNA binding or recognition, pathology, cell apoptosis and mammalian reproduction [3–9]. The disorder of zinc metabolism in biological systems is associated with diabetes, epilepsy and Alzheimer's diseases [10–16].

Therefore, there is a large demand for exploring novel development of $Zn^{2+}$ chemosensors over other techniques. The growth of chemosensors for active metal ions with high sensitivity and selectivity is an active field in analytical chemistry. Fluorescent chemosensors have attracted particular attention due to its non-destructive, high selective and sensitive, quick and naked eye detection [17–21].

Up to now, several fluorescent chemosensors for zinc have been developed using indole [22], coumarin [23, 24], quinoline [25, 26], BODIPY [27–29], bipyridine [30, 31], nanoparticles [32, 33] and other fluorophores [34–37], which showed excellent selectivity and sensitivity towards zinc and some of them are used for biological imaging in a physiological environment. However, most of them need complicated synthesis process, work in toxic organic-containing solution such as acetonitrile. Furthermore, many reported fluorescent chemosensors encountered difficulty in distinguishing zinc from other transition metal ions such as $Cu^{2+}$, $Ni^{2+}$, $Co^{2+}$ and $Cd^{2+}$, because $Cu^{2+}$, $Ni^{2+}$ and $Co^{2+}$ are in the same period and $Cd^{2+}$ is in the same group of the periodic table and illustrates alike properties to $Zn^{2+}$ [38–41]. Flavonol derivatives are also detected as a fluorescent chemosensor for some ions [42].

In this chapter, an elaborately prepared $Zn^{2+}$ chemosensor with functionalized flavonol derivatives (**CS1** and **CS2**) was elucidated. On the addition of zinc metal ions to methanol solution of chemosensor, fluorescence emission enhancement accompanied by a blue shift was detected, allowing fluorescence "turn-on" naked-eye detection of Zn(II) under a UV lamp. Both UV-Vis and fluorescence spectroscopic studies show that the prepared chemosensors (**CS1** and **CS2**) are highly sensitive and selective towards zinc over other metal ions in methanol. Thus compounds **CS1** and **CS2** are suitable for selective detection of $Zn^{2+}$ as fluorescence "turn-on" sensors.

## 4.2. Experimental

### *4.2.1. Reagents and apparatus*

All the commercially available chemicals were purchased from Merck and Aldrich and used without further purification. The IR spectra were recorded on a Nexus FT-IR (Illinois, USA) spectrometer in the range 4000–400 $cm^{-1}$ with KBr. The NMR spectra were recorded on a Bruker 500 MHz (USA), TMS as an internal standard, $CDCl_3$ taken as solvent. The mass spectra were recorded using Bruker-micrOTOF II (USA). The UV-Vis absorption spectra were measured on a Shimadzu UV-2450 spectrophotometer (Japan) and the Fluorescent spectra were recorded on a Shimadzu RF-5301PC spectrofluorophotometer (Japan). The pH was measured by use of a Eutech CyberScan pH 510 (Singapore).

### *4.2.2. Synthesis and characterization*

The chemosensors (**CS1** and **CS2**) were prepared by the reported method [43, 44] with some modifications (Scheme 4.1). NaOH (4 equiv.) was added to a solution of 2′-hydroxyacetophenone (10 mmol) and aldehyde (10 mmol) in methanol and the mixture was stirred for 18 h at room temperature. The reaction mixture was acidified with HCl (30%) and the 2′-hydroxychalcone was isolated by filtration. To the methanolic solution of 2′-hydroxychalcone (5 mmol) NaOH (4 equiv.) and $H_2O_2$ (30%, 10 equiv.) were added at 0–4 °C. The mixture was stirred for 2–3 h at room temperature, then acidified with HCl (30%) and poured into water (400 mL). Collected the precipitate by filtration and the pure product was obtained by recrystallization from methanol. The structures of chemosensors were characterized by IR, $^1H$ NMR, $^{13}C$ NMR and HRMS spectra.

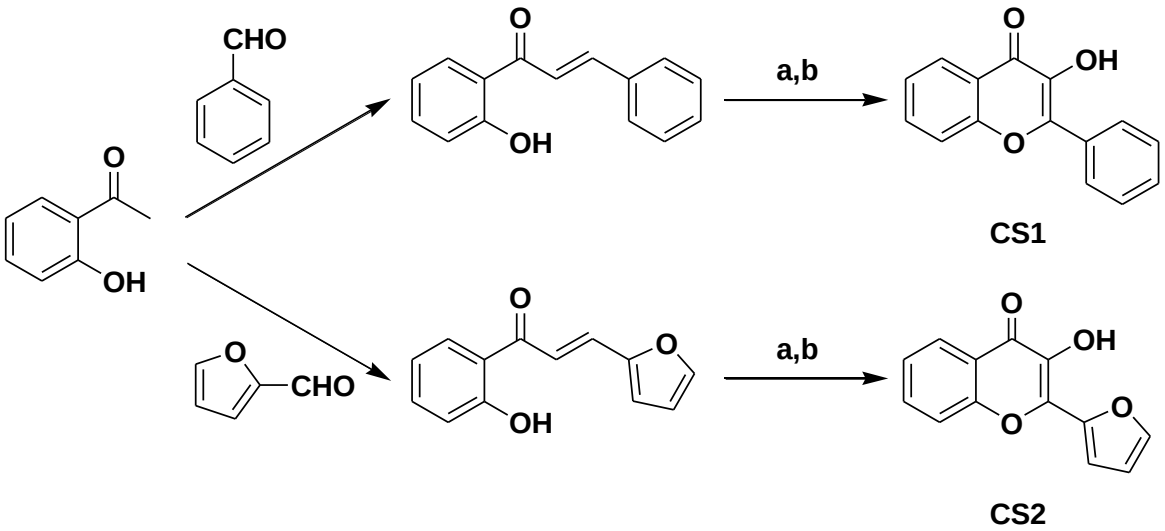


**Scheme 4.1.** Synthetic routes to chemosensors (**CS1** and **CS2**): (a) NaOH; (b) $H_2O_2$.

**3-Hydroxy-2-phenyl-4H-chromen-4-one (CS1):** Yield: 0.94 g (79%); Color: Yellow-white solid; Mp: 168–170 °C; FT-IR (KBr), *v*, $cm^{-1}$: 3236 (O−H), 1611 (C=O), 1480, 1415 (C=C), 1287, 1214, 1129 (C−O); $^{1}H$ NMR ($CDCl_3$), *δ*, ppm (*J*, Hz): 7.42 (t, *J* = 7.5, 1H), 7.48 (t, *J* = 7.5, 1H), 7.55 (t, *J* = 7.5, 2H), 7.60 (d, *J* = 8.5, 1H), 7.71 (dt, *J* = 1.5, 7.5, 1H), 8.26 (d, *J* = 7.5, 3H); $^{13}C$ NMR ($CDCl_3$), *δ*, ppm: 118.3, 120.7, 124.6, 125.5, 127.8, 128.6, 130.2, 131.1, 133.7, 138.5, 144.9, 155.5, 173.5; HRMS *m/z*: Calcd for $C_{15}H_{10}O_3$ $(M+Na)^+$: 261.0528, found: 261.0527.

**3-Hydroxy-2-(2-furyl)-4H-chromen-4-one (CS2):** Yield: 0.82 g (72%); Color: Pale yellow solid; Mp: 179–181 °C; FT-IR (KBr), *v*, $cm^{-1}$: 3258 (O−H), 1617 (C=O), 1482, 1418 (C=C), 1280, 1213, 1130 (C−O); $^{1}H$ NMR ($CDCl_3$), *δ*, ppm (*J*, Hz): 6.65 (q, *J* = 1.5, 1H), 7.36 (d, *J* = 3.5, 1H), 7.41 (t, *J* = 7.5, 1H), 7.60 (d, *J* = 8.5, 1H), 7.69 (t, *J* = 8.5, 2H), 8.24 (d, *J* = 8.0, 1H); $^{13}C$ NMR ($CDCl_3$), *δ*, ppm: 112.7, 115.8, 118.3, 121.2, 124.7, 125.4, 133.6, 136.4, 138.9, 144.4, 144.8, 155.0, 172.4; HRMS *m/z*: Calcd for $C_{13}H_8O_4$ $(M+Na)^+$: 251.032, found: 251.0339.

*4.2.3. UV-Vis and fluorescent studies*

UV-Vis absorption and fluorescence emission spectra were recorded in 1.0 cm path length quartz cuvettes in alcoholic medium (MeOH) using a Shimadzu UV-2450 spectrophotometer and a Shimadzu RF-5301PC spectrofluorophotometer. Absorption and emission spectra of the chemosensors in the presence of various metal ions ($Al^{3+}$, $Li^{+}$, $Ca^{2+}$, $Ba^{2+}$, $Na^{+}$, $Cs^{+}$, $Mn^{2+}$, $Co^{2+}$, $K^{+}$, $Cu^{2+}$, $Zn^{2+}$, $Ni^{2+}$, $Fe^{2+}$, $Fe^{3+}$, $Cd^{2+}$, $Mg^{2+}$, $Pb^{2+}$, $Cr^{3+}$, $Hg^{2+}$, $Nd^{3+}$ and $Sr^{2+}$) were recorded in the concentration of 5 µM (for **CS1** and **CS2**, absorption spectra), 5 µM (for **CS1**, emission spectra) and 2 µM (for **CS2**, emission spectra).

## 4.3. Results and discussion

The binding ability and mode of sensors (**CS1** and **CS2**) towards $Zn^{2+}$ and other metal ions was measured through UV-Vis, fluorescent spectrometry and naked-eye observation.

*4.3.1. UV-Vis spectral studies*

The chemosensors (**CS1** and **CS2**) were investigated by UV-Vis absorption spectral behaviour in the presence of various metal ions in the 50 µM concentration of each component in methanol solvent. The free ligands **CS1** and **CS2** exhibited a main absorption band centred at 343 nm and 356 nm, respectively. On the addition of metal ions to sensors, the absorption band of free receptors **CS1** and **CS2** is shifted to low intensity, while a new

broad absorption band (mainly for $Cu^{2+}$, $Ni^{2+}$, $Zn^{2+}$, $Pb^{2+}$, $Al^{3+}$, $Co^{2+}$, $Cd^{2+}$, $Mn^{2+}$ and $Mg^{2+}$ ions) was observed at about 350–480 nm region. As shown in Figure 4.1, both sensors are responding to the above mentioned metal ions and there is no significant changes were observed when mixed with other metal ions such as $Ca^{2+}$, $K^{+}$, $Na^{+}$, $Li^{+}$, $Cs^{+}$, $Ba^{2+}$, $Fe^{2+}$, $Fe^{3+}$, $Hg^{2+}$, $Cr^{3+}$, $Nd^{3+}$ and $Sr^{2+}$.

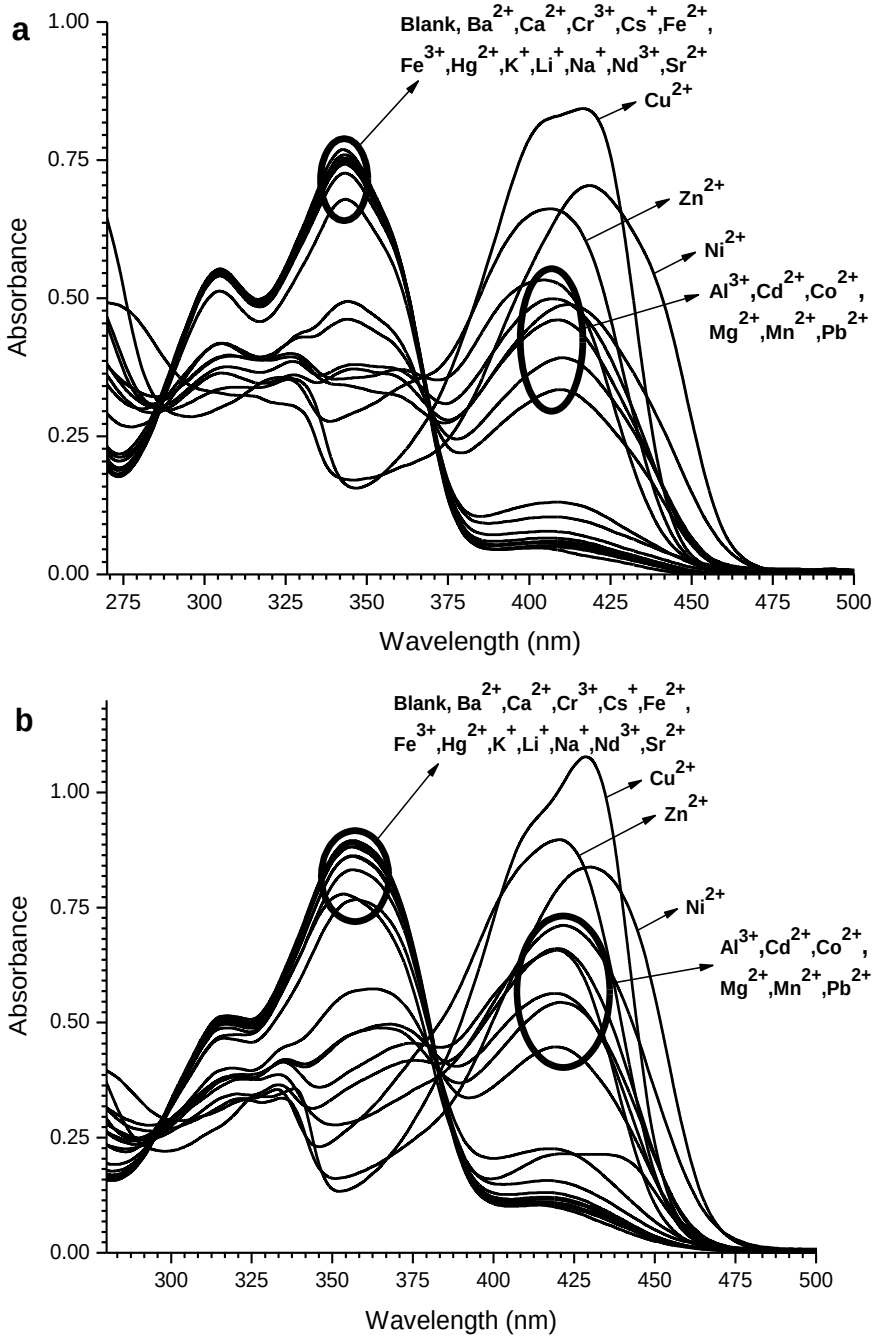


**Figure 4.1.** UV-Vis absorbance spectra of (a) **CS1** (50 μM) and (b) **CS2** (50 μM) in the presence of 1.0 equiv. of various metal ions in methanol.

*4.3.2. Fluorescence emission studies*

The fluorescence response of sensors **CS1** (5 μM) and **CS2** (2 μM) upon addition of various metal ions 5 μM (for **CS1**) and 2 μM (for **CS2**) have been investigated in methanol. Chemosensors **CS1** and **CS2** alone displayed a weak single fluorescence emission band at 530 nm and a couple of emission bands at 425 and 530 nm, respectively, with an excitation of 340 nm. Upon addition of various metals ($Na^+$, $Ca^{2+}$, $Li^+$, $Ba^{2+}$, $Cs^+$, $Mn^{2+}$, $Cr^{3+}$, $K^+$, $Co^{2+}$, $Fe^{2+}$, $Fe^{3+}$, $Hg^{2+}$, $Pb^{2+}$, $Ni^{2+}$, $Nd^{3+}$, $Cu^{2+}$, and $Sr^{2+}$) no significant changes (except $Zn^{2+}$, $Al^{3+}$,

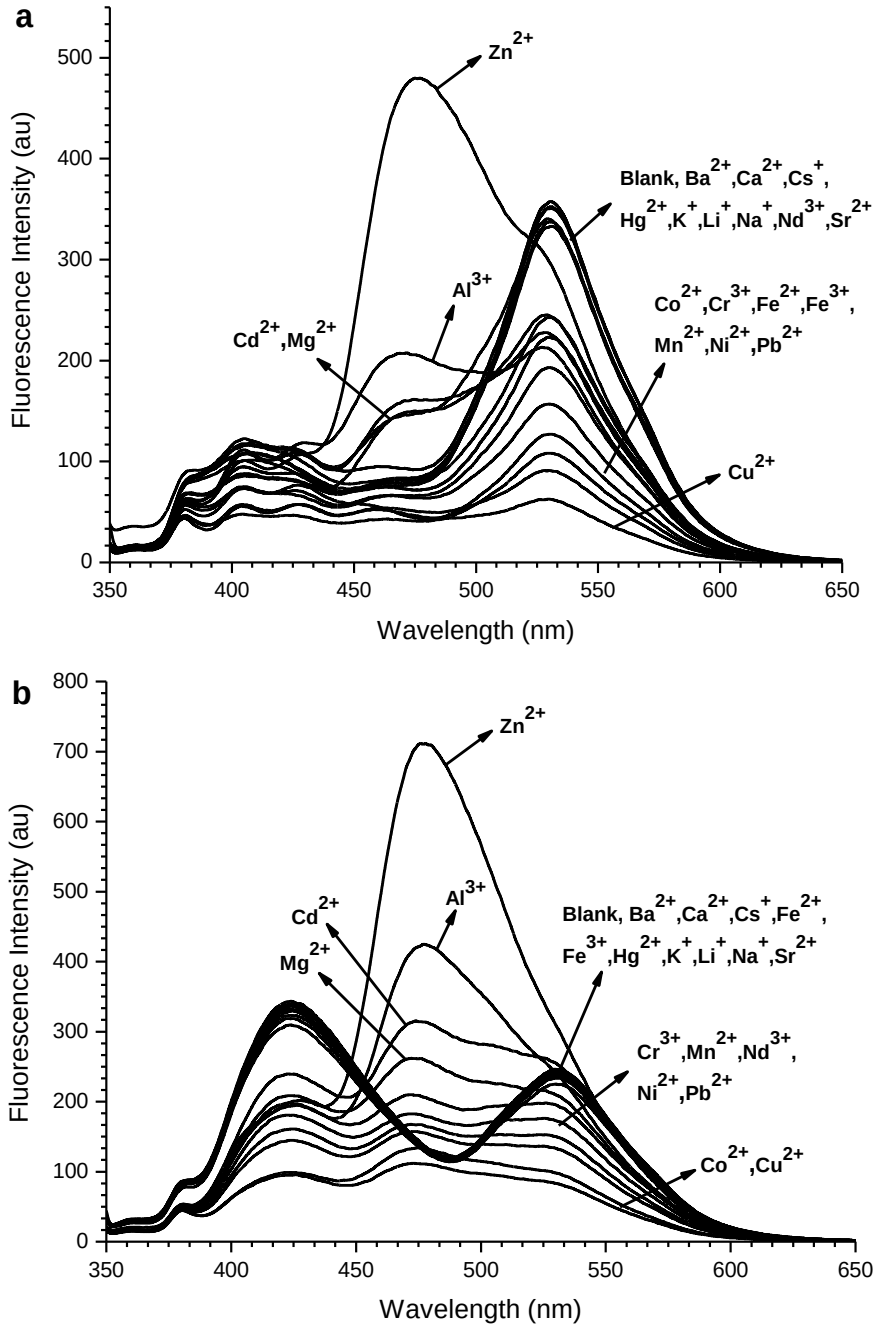


**Figure 4.2.** Fluorescence emission spectra ($\lambda_{ex}$ = 340 nm) of (a) **CS1** (5 μM) and (b) **CS2** (2 μM) in the presence of 1.0 equiv. of various metal ions in methanol.

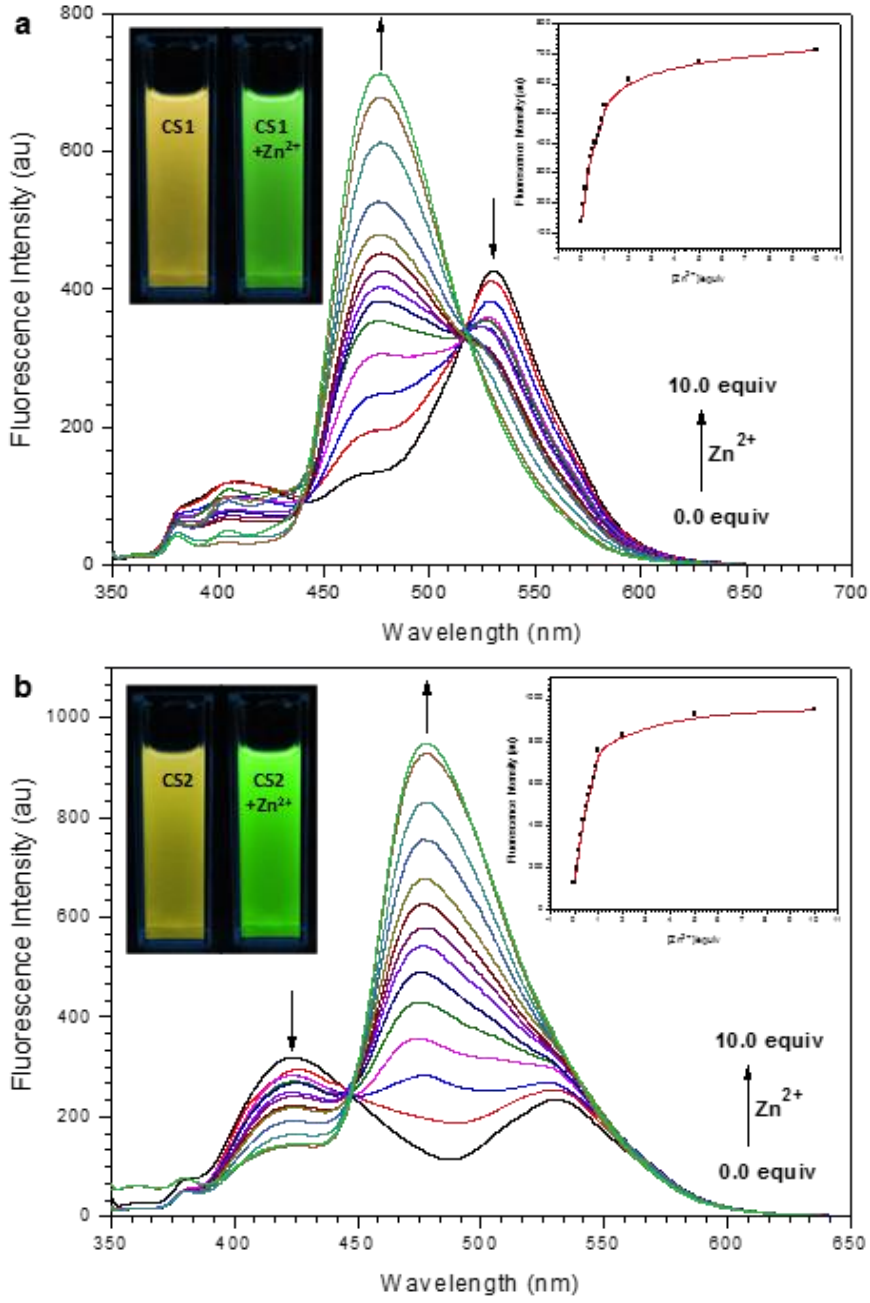


**Figure 4.3.** The variation in fluorescence emission spectra of (a) **CS1** (5 µM) and (b) **CS2** (2 µM) with increasing amounts of $Zn^{2+}$ ion (0.0, 0.1, 0.2, 0.3, 0.4, 0.5, 0.6, 0.7, 0.8, 0.9, 1.0, 2.0, 5.0 and 10.0 equiv.) in methanol. Inset, left: The fluorescence changes excited by UV lamp of (a) **CS1** (5 µM) and (b) **CS2** (2 µM) with 1.0 equiv. $Zn^{2+}$, right: The fluorescence change at 476 nm (for **CS1**) and 478 nm (for **CS2**) as a function of the amount of $Zn^{2+}$ ions.

$Cd^{2+}$ and $Mg^{2+}$) were observed (Figure 4.2). On addition of $Zn^{2+}$, receptors **CS1** and **CS2** exhibited a prominent fluorescence enhancement accompanied by a blue shift of 54 nm from 530 to 476 nm and 52 nm from 530 to 478 nm, respectively. Results are indicating that the sensors **CS1** and **CS2** exhibit "off-on" mode with high sensitivity towards $Zn^{2+}$ over other metal ions. Under a UV lamp, the chemosensors **CS1** and **CS2** in the presence of $Zn^{2+}$

showed a dramatic color changes from yellow-orange to bright green, which could easily be detected by the naked-eye (Figure 4.3, inset). At the same time, the addition of other metal ions did not show any significant color change.

In addition, the fluorescence response of **CS1** and **CS2** to various concentrations of $Zn^{2+}$ (0–1.0, 2.0, 5.0 and 10 equiv.) was investigated. Upon addition of $Zn^{2+}$, the fluorescence intensity centred at 476 nm (**CS1**) and 478 nm (**CS2**) gradually increased and remained steady when 1.0 equiv. $Zn^{2+}$ was added. The saturation behaviour of the fluorescence intensity after 1.0 equiv. of $Zn^{2+}$ reveals that the chemosensor–$Zn^{2+}$ has a 1:1 stoichiometry (Figure 4.3). The complex stability constants (*K*) through Benesi-Hildebrand method for Zn(II) with **CS1** and **CS2** were found to be $1.0\times10^{6}$ $M^{-1}$ and $9.6\times10^{5}$ $M^{-1}$, respectively (Figure 4.4). The limit of detection of Zn(II) was estimated based on the fluorescence titration profile as $1.7\times10^{-7}$ M (for **CS1**) and $2.8\times10^{-8}$ M (for **CS2**) based on S/N = 3 (Figure 4.5). In addition, a Job plot obtained from the emission data confirmed the 1:1 stoichiometry

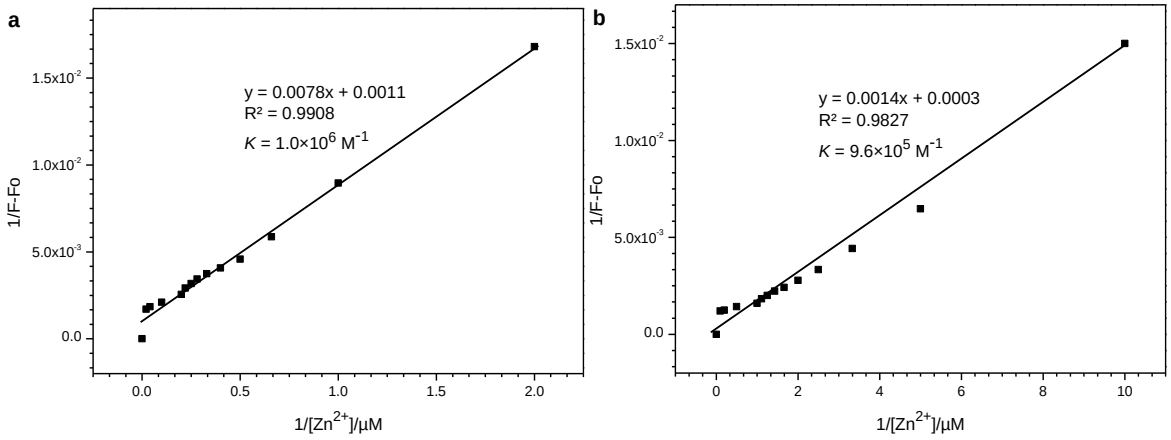


**Figure 4.4.** Linear regression plot of fluorescence intensity change $1/(F\text{-}F_0)$ as a function of concentration $1/[Zn^{2+}]$.

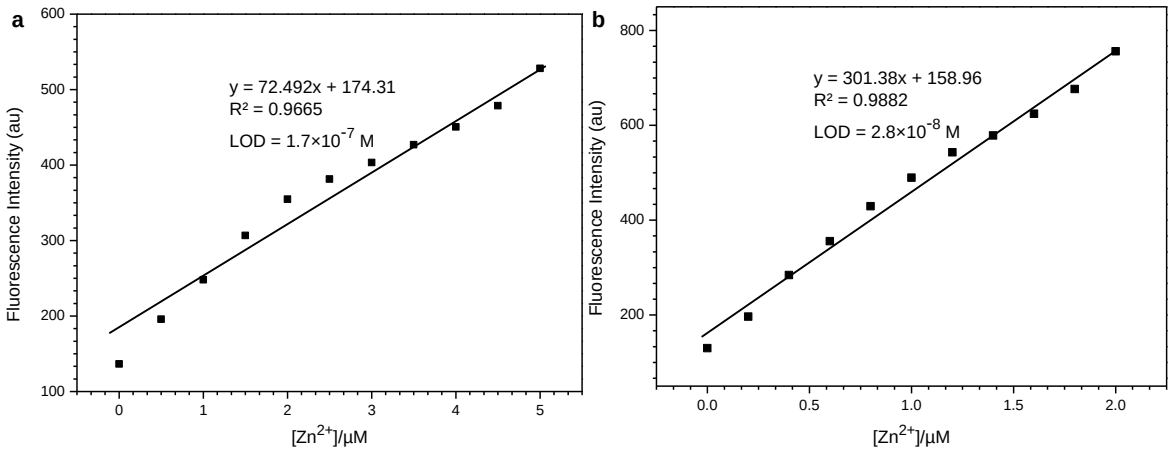


**Figure 4.5.** The fluorescence enhancement change as a function of concentration of Zn(II) ions added.

for chemosensor–$Zn^{2+}$ complex (Figure 4.6). When excited at $\lambda$ = 362 nm, receptor exhibited low fluorescence quantum yield, $\Phi$ = 0.0144 (**CS1**), 0.0498 (**CS2**) (standard: Coumarin 1 in ethyl acetate; $\Phi$ = 0.99). On the other hand, receptor–$Zn^{2+}$ exhibited strong fluorescence quantum yield, $\Phi$ = 0.0302 (**CS1**–$Zn^{2+}$), 0.1158 (**CS2**–$Zn^{2+}$). These data ensured that an enhancement in quantum yield can be achieved during the $Zn^{2+}$ sensing process by using chemosensor.

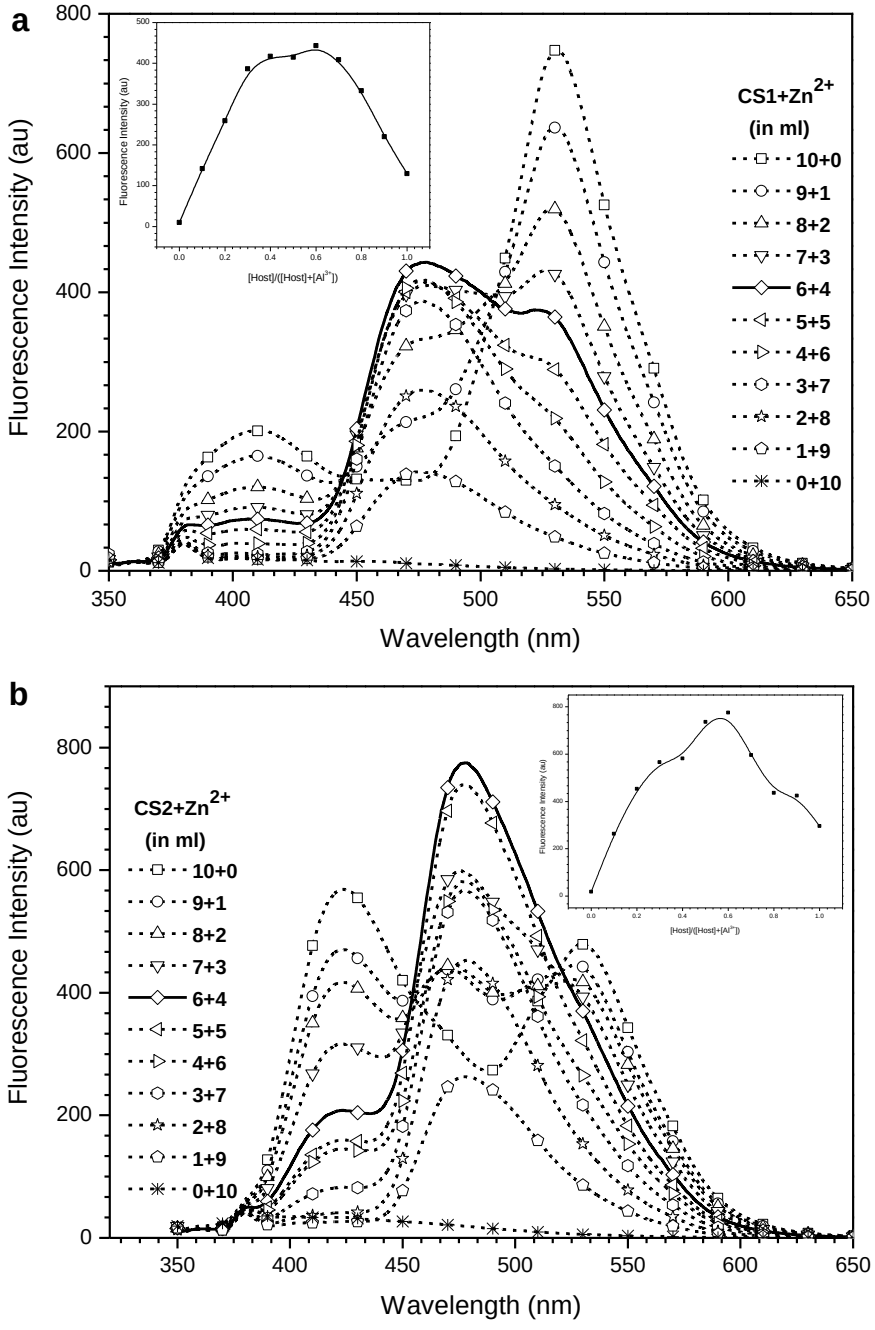


**Figure 4.6.** Job's plot for (a) **CS1** and (b) **CS2**–$Zn^{2+}$ complex. Inset: Fluorescence intensity at 476 nm (for **CS1**) and 478 nm (for **CS2**) was plotted as a function of the molar ratio of ligand.

The selectivity of **CS1** (5 μM) and **CS2** (2 μM) for $Zn^{2+}$ over other metal ions (1.0 equiv.) were examined by the competition experiments. As shown in Figure 4.7, the fluorescence response of **CS1** and **CS2** towards $Zn^{2+}$ in the presence of various metal ions was investigated, and the results show that $Cu^{2+}$ and $Ni^{2+}$ could interfere in the interaction between receptor (**CS1** and **CS2**) and $Zn^{2+}$ indicate that the binding ability of chemosensors toward $Cu^{2+}$ and $Ni^{2+}$ is stronger than $Zn^{2+}$. Upon addition of 1.0 equiv. $Zn^{2+}$ in the presence of other metal ions ($Li^{+}$, $Mg^{2+}$, $Ca^{2+}$, $Al^{3+}$, $Na^{+}$, $Ba^{2+}$, $K^{+}$, $Cs^{+}$, $Cr^{3+}$, $Fe^{2+}$, $Fe^{3+}$, $Hg^{2+}$, $Co^{2+}$, $Mn^{2+}$, $Cd^{2+}$, $Pb^{2+}$ $Nd^{3+}$, and $Sr^{2+}$), 4-fold enhancement of the fluorescence intensity was observed, which is large enough to determine $Zn^{2+}$ from other metal ions. By addition of other metal ions ($Cu^{2+}$ and $Ni^{2+}$) quenches the fluorescence of the receptor–$Zn^{2+}$ complex (Figure 4.8), due to the more binding ability towards $Cu^{2+}$ and $Ni^{2+}$ ions. It means, the reported sensors provide simultaneous detection of $Zn^{2+}$ and other metal ions ($Cu^{2+}$ and $Ni^{2+}$).

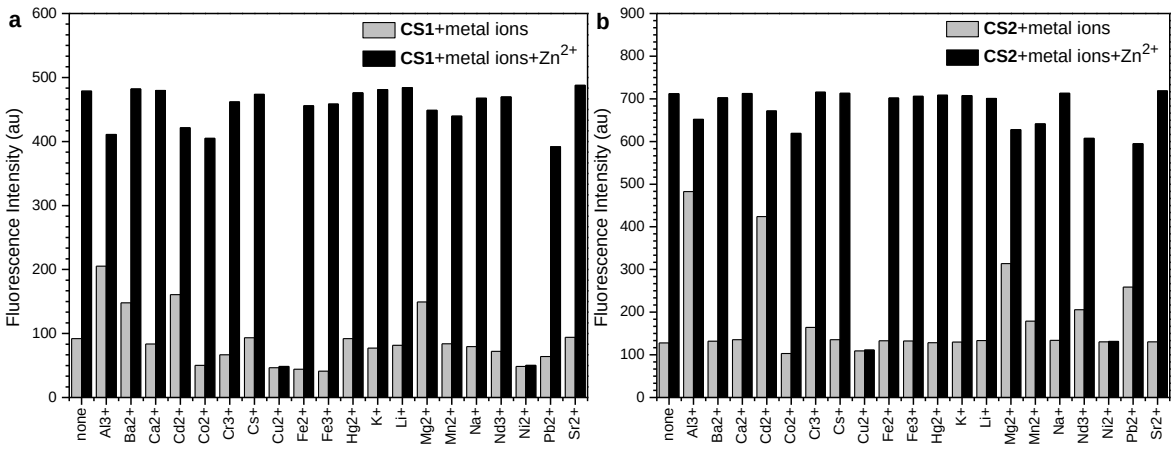


**Figure 4.7.** Competitive selectivity of **CS1** (a) and **CS2** (b) towards $Zn^{2+}$ in the presence of other metals (1.0 equiv.) with an excitation of 340 nm.

The interaction between receptor (**CS1** and **CS2**) and $Zn^{2+}$ ion was investigated at a pH range from 2.0 to 10.0. This experiment was carried out at a fixed concentration of receptor–$Zn^{2+}$ is 5 μM (for **CS1**) and 2 μM (for **CS2**) in methanol. As shown in Figure 4.9, the fluorescence intensity changes were observed at 476 nm (for **CS1**) and 478 nm (for **CS2**) with the pH value at acidic and basic conditions. The chemosensors **CS1** and **CS2** in the presence of $Zn^{2+}$ showed a dramatic color changes in different pH media, which could easily be detected by the naked-eye (Figure 4.9, inset) under a UV lamp. However, the fluorescence intensity decreased at acidic condition, due to receptor could be protonated and hence its binding ability reduced. Reduction in fluorescence intensity at basic condition could be due to the formation of salt.

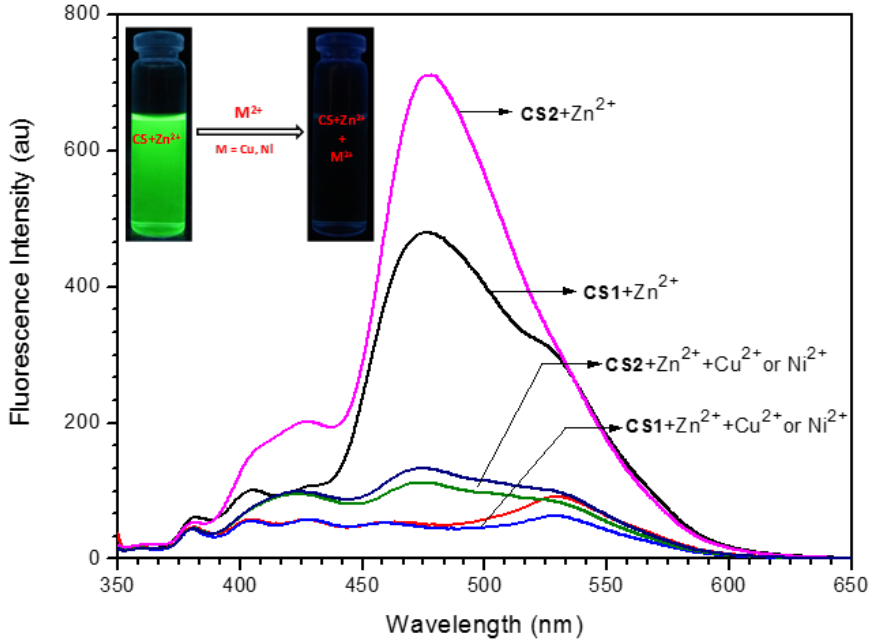


**Figure 4.8.** The variation in fluorescence emission spectra of chemosensor–$Zn^{2+}$ on addition of other metal ions ($Cu^{2+}$ and $Ni^{2+}$). Inset: Fluorescent color change of chemosensor upon addition of interfering metal ions.

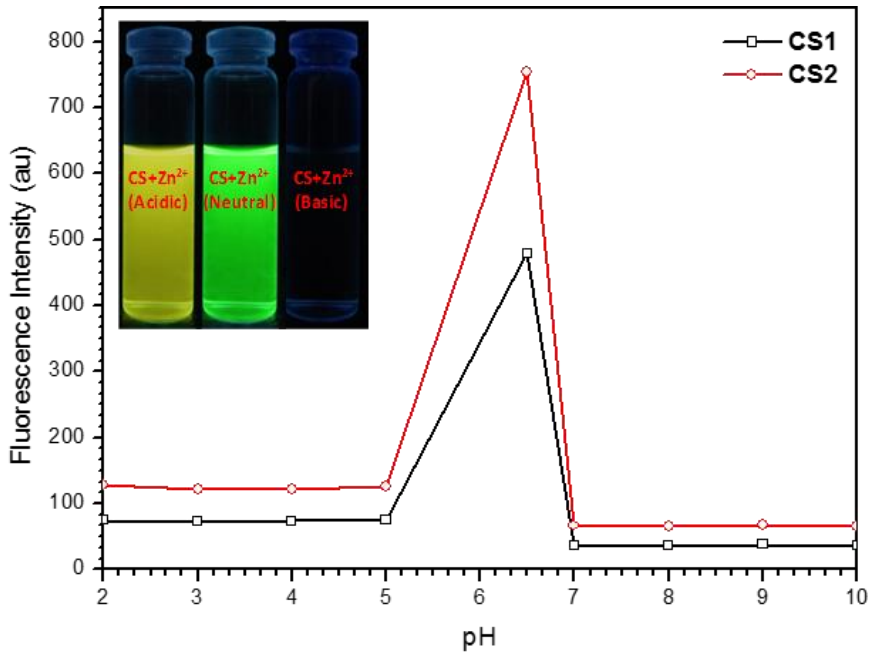


**Figure 4.9.** The variation in fluorescence intensity of probe–$Zn^{2+}$ complex as a function of pH. Inset: The color changes of chemosensor–$Zn^{2+}$ complex in different pH media.

### *4.3.3. Reversibility test of **CS1** and **CS2***

The reversibility of the chemosensor is an essential characteristic in practical applications. Thus EDTA titration was carried out to examine the reversibility of probe–Zn(II) complexation. The reversibility of the reaction of probe and Zn(II) was performed by

the titration of the mixture of receptor and Zn(II) (1:1) with EDTA (Figure 4.10). The enhancement in the fluorescence emission intensity at 530 nm (for **CS1,** Figure 4.10a) indicates the regeneration of free **CS1**. The fluorescence intensity was again quenched at 530 nm on addition of more Zn(II) to the same mixture. Upon addition of EDTA to the mixture of **CS2** and Zn(II), no significant changes were observed (Figure 4.10b).

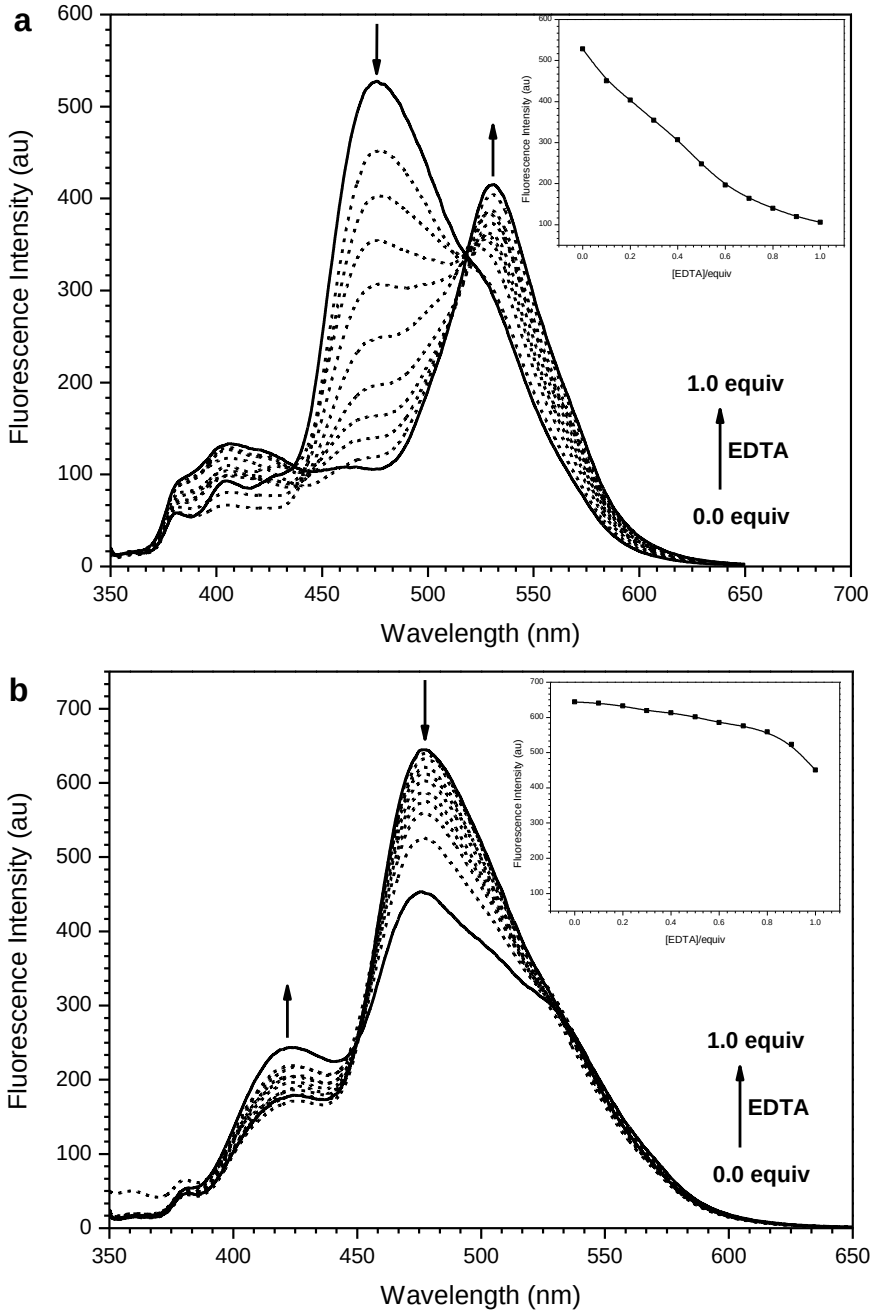


**Figure 4.10.** The variation in fluorescence emission spectra of (a) **CS1**+ $Zn^{2+}$ (5 μM) and (b) **CS2**+ $Zn^{2+}$ (2 μM) upon the addition of EDTA (0.0, 0.1, 0.2, 0.3, 0.4, 0.5, 0.6, 0.7, 0.8, 0.9 and 1.0 equiv.) in methanol. Inset shows the fluorescence change at 476 nm (for **CS1**) and 478 nm (for **CS2**) as a function of the amount of EDTA.

## 4.4. Conclusion

The reported chemosensors (**CS1** and **CS2**) show fluorometric response for $Zn^{2+}$ ions, exhibit high selective and sensitive towards zinc over other tested metal ions. Under a UV lamp, the detection process gives rise to a color change (from yellow-orange to bright green), which could easily be detected by the naked eye. Thus, the proposed sensors have a facility to serve as a practical sensor for detection of zinc ion in both environment and biological samples.

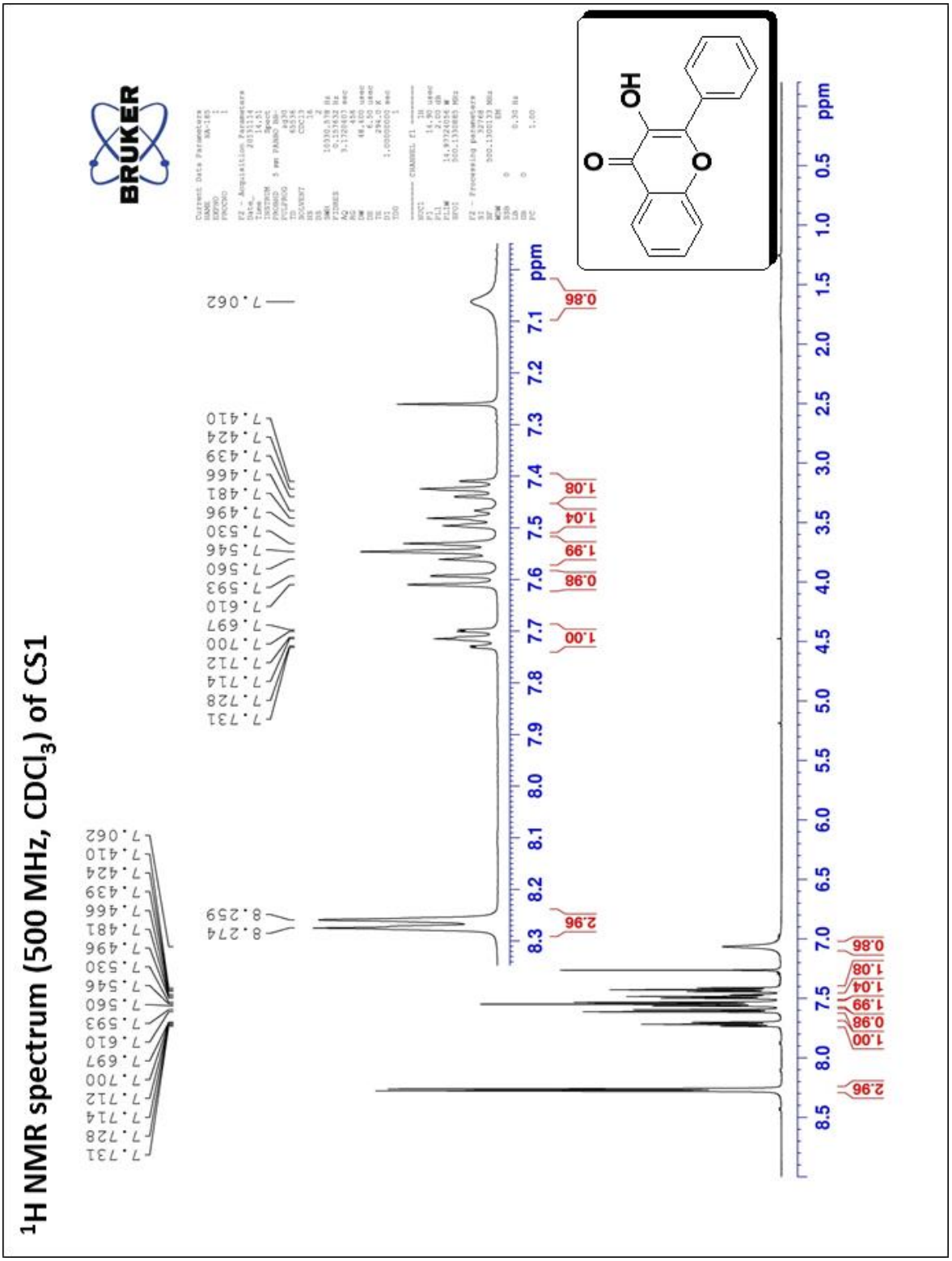
$^1$H NMR spectrum (500 MHz, $CDCl_3$) of CS1
BRUKER
OH
O
O
ppm
0.86
1.08
1.04
1.99
0.98
1.00
2.96
7.062
7.410
7.424
7.439
7.466
7.481
7.496
7.530
7.546
7.560
7.593
7.610
7.697
7.700
7.712
7.714
7.728
7.731
8.259
8.274

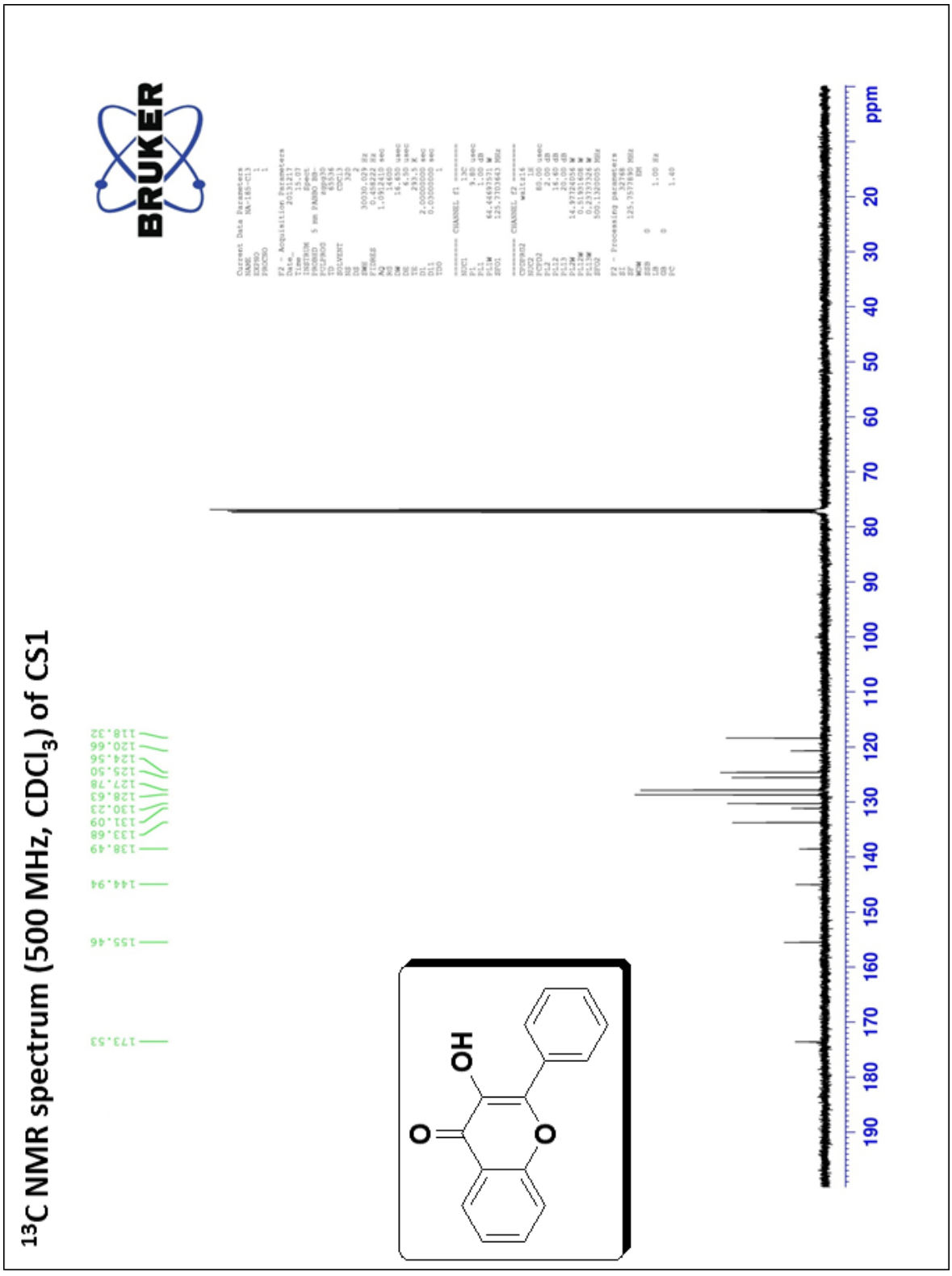
$^{13}$C NMR spectrum (500 MHz, $CDCl_3$) of CS1
BRUKER
OH
O
O
ppm

## HRMS spectrum of CS1

**Acquisition Parameter**

| | | | | | |
|---|---|---|---|---|---|
| Source Type | ESI | Ion Polarity | Positive | Set Nebulizer | 0.4 Bar |
| Focus | Not active | Set Capillary | 4500 V | Set Dry Heater | 180 °C |
| Scan Begin | 50 m/z | Set End Plate Offset | -500 V | Set Dry Gas | 4.0 l/min |
| Scan End | 3000 m/z | Set Collision Cell RF | 150.0 Vpp | Set Divert Valve | Source |

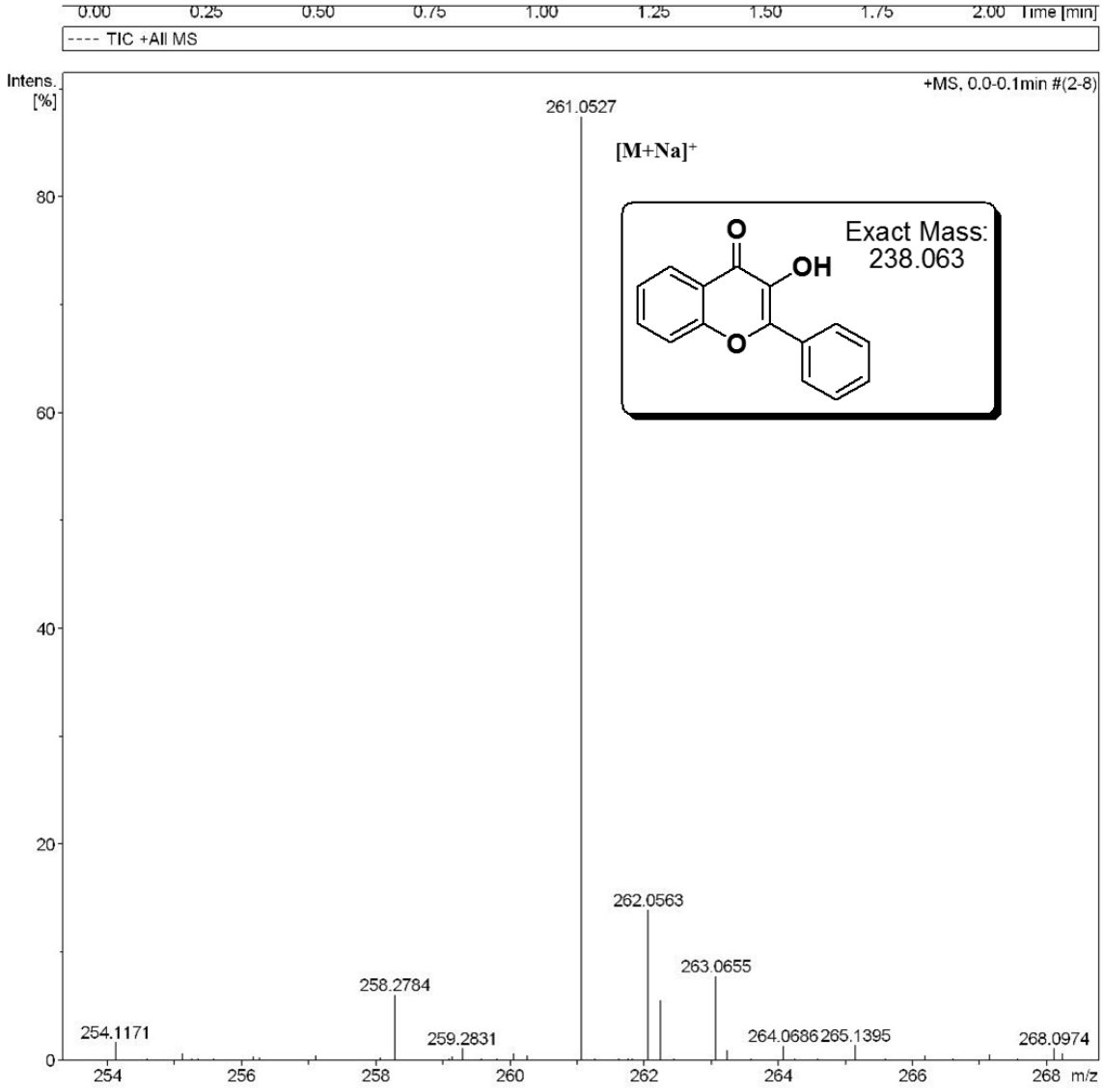

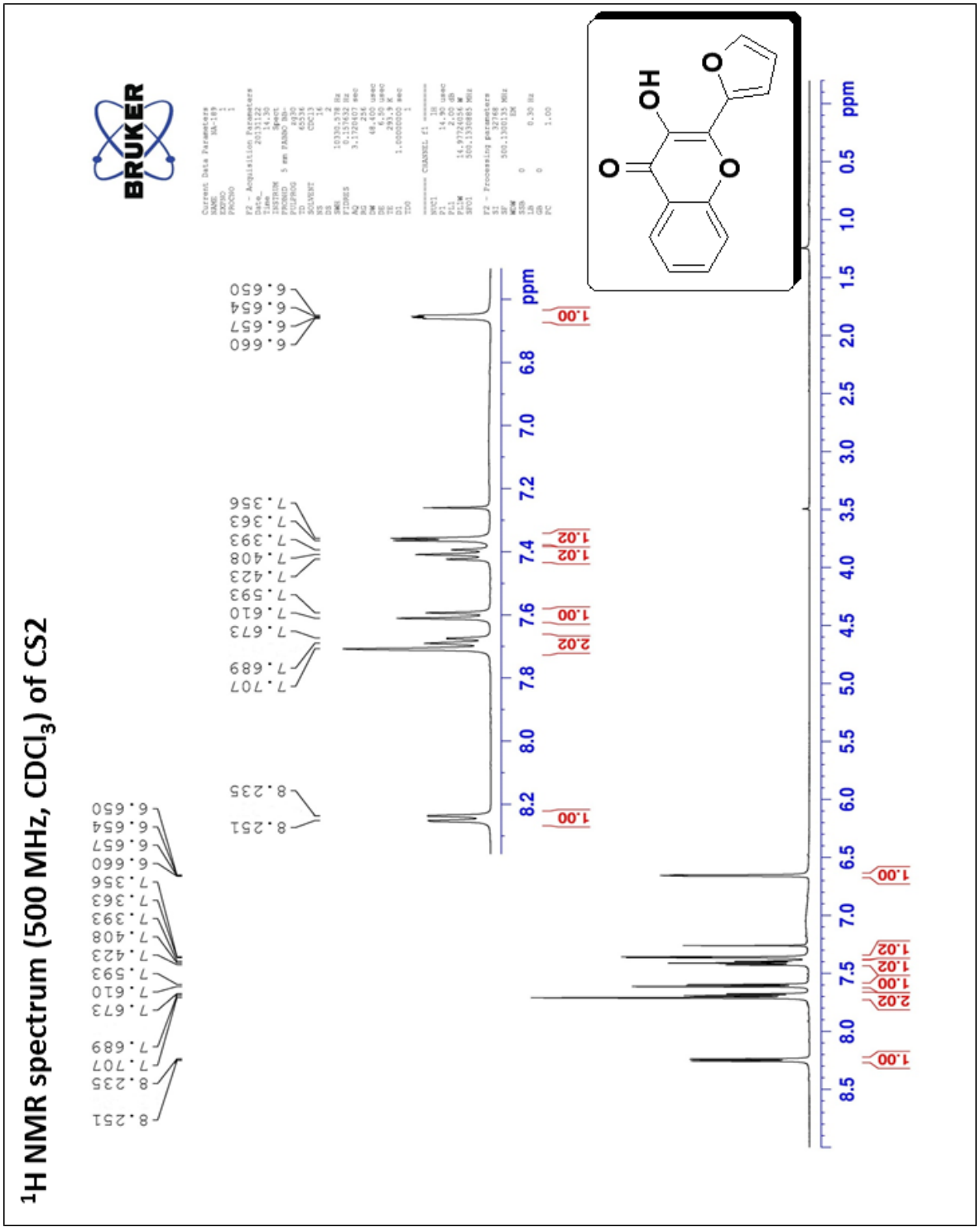
$^1$H NMR spectrum (500 MHz, $CDCl_3$) of CS2
BRUKER
OH
O
O
O
ppm

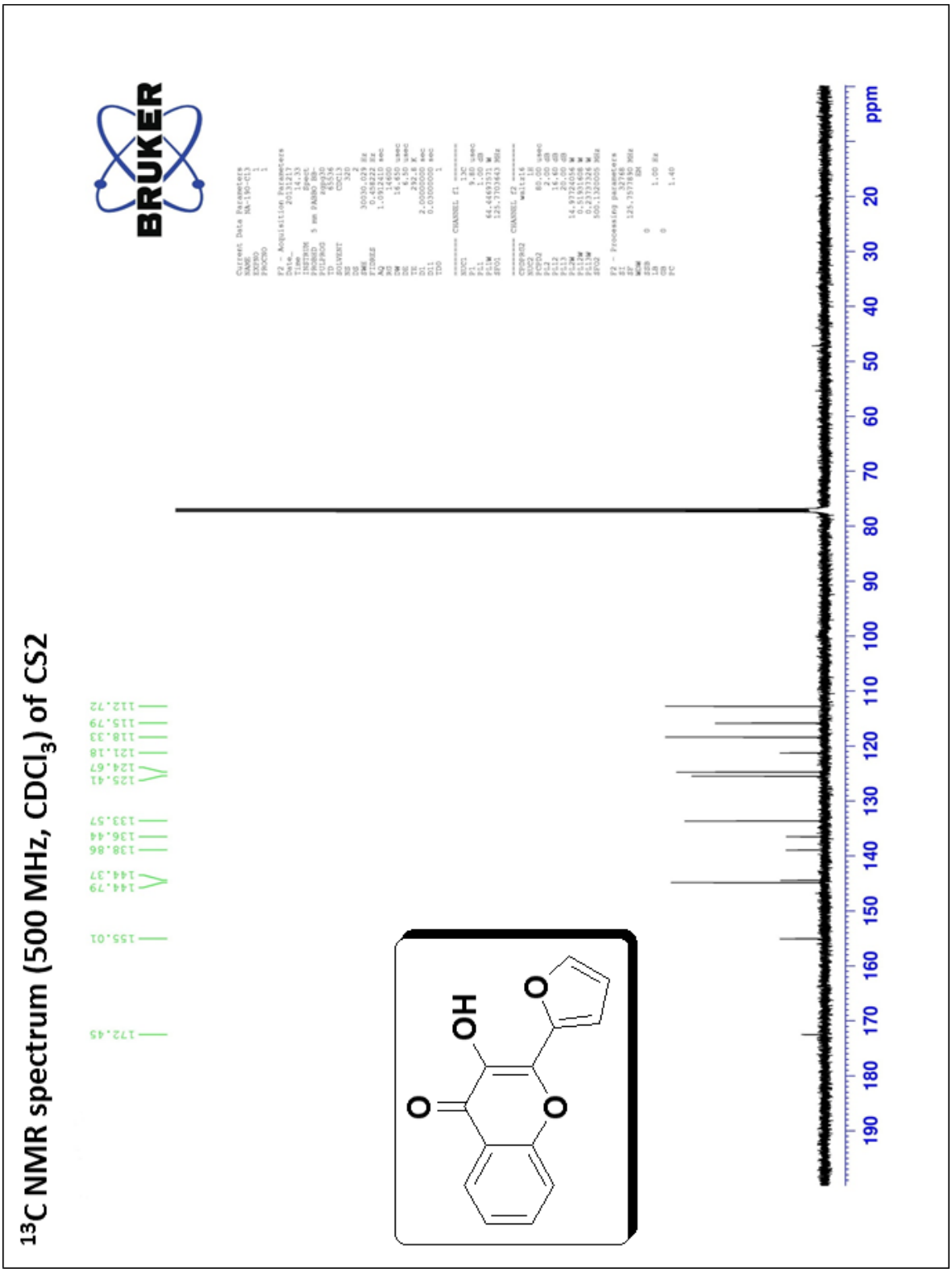
$^{13}$C NMR spectrum (500 MHz, $CDCl_3$) of CS2
BRUKER
OH
O
O
O
ppm

## HRMS spectrum of CS2

**Acquisition Parameter**

| | | | | | |
|---|---|---|---|---|---|
| Source Type | ESI | Ion Polarity | Positive | Set Nebulizer | 0.4 Bar |
| Focus | Not active | Set Capillary | 4500 V | Set Dry Heater | 180 °C |
| Scan Begin | 50 m/z | Set End Plate Offset | -500 V | Set Dry Gas | 4.0 l/min |
| Scan End | 3000 m/z | Set Collision Cell RF | 150.0 Vpp | Set Divert Valve | Source |

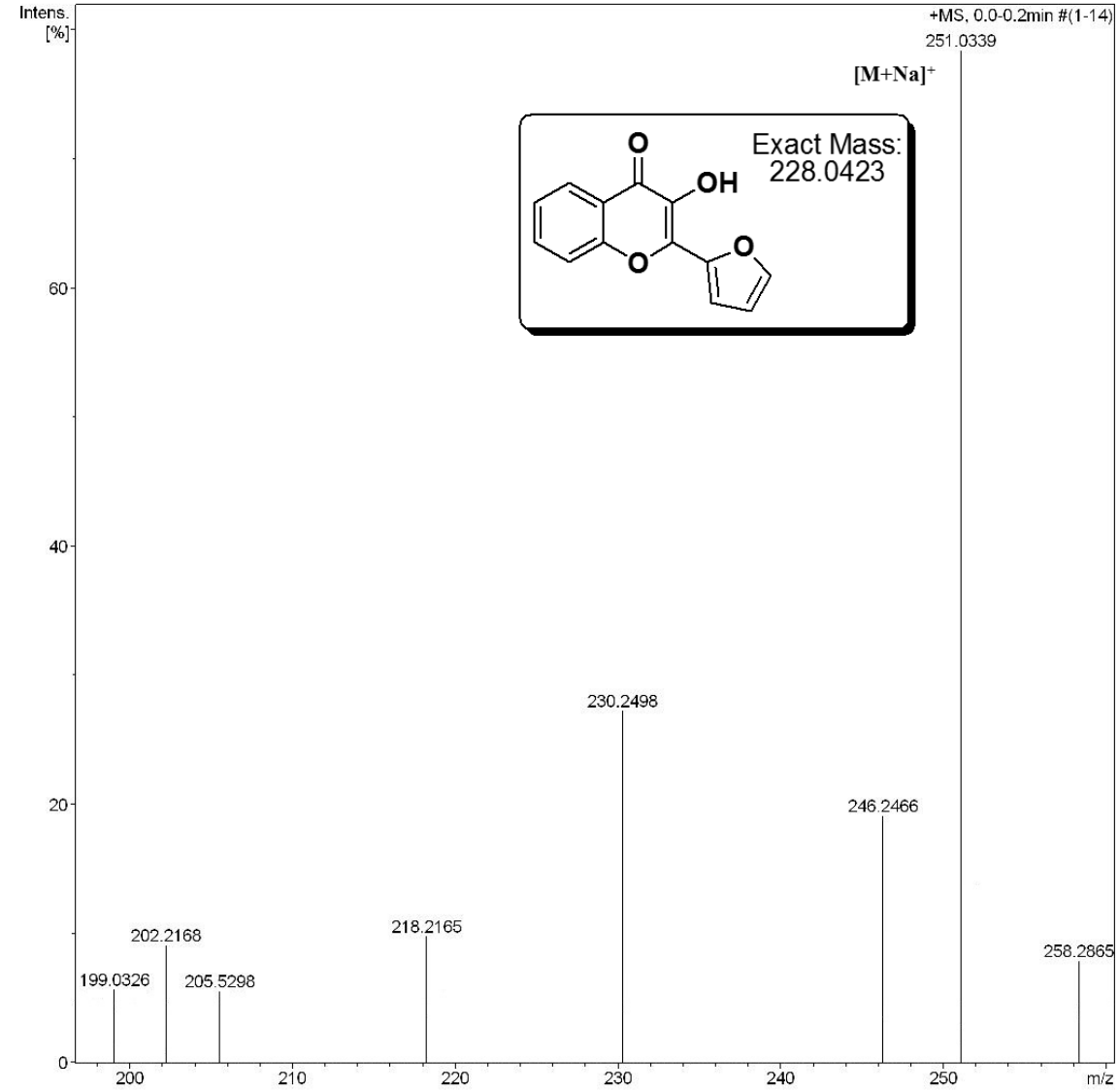

**References**


1. E.M. Nolan, S.J. Lippard, Small-molecule fluorescent sensors for investigating zinc metalloneurochemistry, *Acc. Chem. Res.*, 2009, **42**, 193–203.
2. S.J. Lippard, J.M. Berg, Principle of bioinorganic chemistry, University Science Book, CA, 1994, 78–183.
3. M.P. Cuajungco, G.J. Lees, Zinc metabolism in the brain: relevance to human neurodegenerative disorders, *Neurobiol. Dis.*, 1997, **4**, 137–169.
4. T.V. Ohalloran, Transition metals in control of gene expression, *Science*, 1993, **261**, 715–725.
5. K.H. Falchuk, The molecular basis for the role of zinc in developmental biology, *Mol. Cell. Biochem.*, 1998, **188**, 41–48.
6. J.M. Berg, Y.G. Shi, The galvanization of biology: a growing appreciation for the roles of zinc, *Science*, 1996, **271**, 1081–1085.
7. B.L. Vallee, K.H. Falchuk, The biochemical basis of zinc physiology, *Physiol. Rev.*, 1993, **73**, 79–118.
8. S.L. Sensi, P. Paoletti, A.I. Bus, I. Sekler, Zinc in the physiology and pathology of the CNS, *Nat. Rev. Neurosci.*, 2009, **10**, 780–791.
9. E. Tomat, S.J. Lippard, Imaging mobile zinc in biology, *Curr. Opin. Chem. Biol.*, 2010, **14**, 225–230.
10. A.I. Bush, The metallobiology of Alzheimer's disease, *Trends Neurosci.*, 2003, **26**, 207–214.
11. C.J. Frederickson, J.Y. Koh, A.I. Bush, The neurobiology of zinc in health and disease, *Nat. Rev. Neurosci.*, 2005, **6**, 449–462.
12. A.B. Chausmer, Zinc, insulin and diabetes, *J. Am. Coll. Nutr.*, 1998, **17**, 109–115.
13. J.L. Smith, S. Xiong, W.R. Markesbery, M.A. Lovell, Altered expression of zinc transporters-4 and -6 in mild cognitive impairment, early and late Alzheimer's disease brain, *Neuroscience*, 2006, **140**, 879–888.
14. E. Ho, Zinc deficiency, DNA damage and cancer risk, *J. Nutr. Biochem.*, 2004, **15**, 572–578.
15. R. Sladek, G. Rocheleau, J. Rung, C. Dina, L. Shen, D. Serre, P. Boutin, D. Vincent, A. Belisle, S. Hadjadj, A genome-wide association study identifies novel risk loci for type 2 diabetes, *Nature*, 2007, **445**, 881–885.
16. M. Lu, D. Fu, Structure of the zinc transporter YiiP, *Science*, 2007, **317**, 1746–1748.

17. A.P. de Silva, H.Q.N. Gunaratne, T. Gunnlaugsson, A.J.M. Huxley, C.P. McCoy, J.T. Rademacher, T.E. Rice, Signaling recognition events with fluorescent sensors and switches, *Chem. Rev.*, 1997, **97**, 1515–1566.
18. V. Amendola, L. Fabbrizzi, F. Foti, M. Licchelli, C. Mangano, P. Pallavicini, A. Poggi, D. Sacchi, A. Taglietti, Light-emitting molecular devices based on transition metals, *Coord. Chem. Rev.*, 2006, **250**, 273–299.
19. J.S. Kim, D.T. Quang, Calixarene-derived fluorescent probes, *Chem. Rev.*, 2007, **107**, 3780–3799.
20. V.K. Gupta, A.K. Singh, L.K. Kumawat, Thiazole Schiff base turn-on fluorescent chemosensor for $Al^{3+}$ ion, *Sens. Actuators B*, 2014, **195**, 98–108.
21. V.K. Gupta, A.K. Singh, N. Mergu, Antipyrine based Schiff bases as turn-on fluorescent sensors for Al(III) ion, *Electrochim. Acta*, 2014, **117**, 405–412.
22. M. Taki, Y. Watanabe, Y. Yamamoto, Development of ratiometric fluorescent probe for zinc ion based on indole fluorophore, *Tetrahedron Lett.*, 2009, **50**, 1345–1347.
23. H.Y. Li, S. Gao, Z. Xi, A colorimetric and "turn-on" fluorescent chemosensor for Zn(II) based on coumarin Shiff-base derivative, *Inorg. Chem. Commun.*, 2009, **12**, 300–303.
24. Z.C. Xu, X. Liu, J. Pan, D.R. Spring, Coumarin-derived transformable fluorescent sensor for $Zn^{2+}$, *Chem. Commun.*, 2012, **48**, 4764–4766.
25. J.J. Du, J.L. Fan, X.J. Peng, H.L. Li, S.G. Sun, The quinoline derivative of ratiometric and sensitive fluorescent zinc probe based on deprotonation, *Sens. Actuators B*, 2010, **144**, 337–341.
26. P.G. Sutariya, N.R. Modi, A. Pandya, B.K. Joshi, K.V. Joshi, S.K. Menon, An ICT based "turn on/off" quinoline armed calix[4]arene fluoroionophore: its sensing efficiency towards fluoride from waste water and $Zn^{2+}$ from blood serum, *Analyst*, 2012, **137**, 5491–5494.
27. J. Cao, C.C. Zhao, X.Z. Wang, Y.F. Zhang, W.H. Zhu, Target-triggered deprotonation of 6-hydroxyindole-based BODIPY: specially switch on NIR fluorescence upon selectively binding to $Zn^{2+}$, *Chem. Commun.*, 2012, **48**, 9897–9899.
28. A.N. Kursunlu, E. Guler, H.I. Ucan, R.W. Boyle, A novel bodipy-dipyrrin fluorescent probe: synthesis and recognition behaviour towards Fe (II) and Zn (II), *Dyes Pigm.*, 2012, **94**, 496–502.

29. S.L. Zhu, J.T. Zhang, J. Janjanam, G. Vegesna, F.T. Luo, A. Tiwari, H.Y. Liu, Highly water-soluble BODIPY-based fluorescent probes for sensitive fluorescent sensing of zinc(II), *J. Mater. Chem. B*, 2013, **1**, 1722–1728.

30. J.F. Zhang, S. Bhuniya, Y.H. Lee, C. Bae, J.H. Lee, J.S. Kim, Novel 2,2′-bipyridine-modified calix[4]arenes: ratiometric fluorescent chemosensors for $Zn^{2+}$ ion, *Tetrahedron Lett.*, 2010, **51**, 3719–3723.

31. L. Kong, Y. Chen, W.B. Ye, L. Zhao, B. Song, J.X. Yang, Y.P. Tian, X.T. Tao, Synthesis characterization, optical property of a bipyridine derivative and its application to determine trace $Zn^{2+}$ in water, *Sens. Actuators B*, 2013, **177**, 218–223.

32. G. Kang, H.J. Son, J.M. Lim, H.S. Kweon, I.S. Lee, D.M. Kang, J.H. Jung, Functionalized $Fe_3O_4$ nanoparticles for detecting zinc ions in living cells and their cytotoxicity, *Chem. Eur. J*., 2012, **18**, 5843–5847.

33. Y. Li, Z.Y. Yang, Z.C. Liu, B.D. Wang, S.L. Li, Highly selective and sensitive fluorescent nanosensor for zinc ions, *Sens. Actuators B*, 2011, **160**, 1504–1507.

34. S. Lee, J.H. Lee, T. Pradhan, C.S. Lim, B.R. Cho, S. Bhuniya, S. Kim, J.S. Kim, Fluorescent turn-on $Zn^{2+}$ sensing in aqueous and cellular media, *Sens. Actuators B*, 2011, **160**, 1489–1493.

35. A. Ciupa, M.F. Mahon, P.A.D. Bank, L. Caggiano, Simple pyrazoline and pyrazole turn on fluorescent sensors selective for $Cd^{2+}$ and $Zn^{2+}$ in MeCN, *Org. Biomol. Chem.*, 2012, **10**, 8753–8757.

36. T. Mistri, M. Dolai, D. Chakraborty, A.R. Khuda-Bukhsh, K.K. Das, M. Ali, A highly selective and sensitive in vivo fluorosensor for zinc(II) without cytotoxicity, *Org. Biomol. Chem.*, 2012, **10**, 2380–2384.

37. S.C. Yin, J. Zhang, H.K. Feng, Z.J. Zhao, L.W. Xu, H.Y. Qiu, B.Z. Tang, $Zn^{2+}$-selective fluorescent turn-on chemosensor based on terpyridine-substituted siloles, *Dyes Pigm.*, 2012, **95**, 174–179.

38. E.M. Nolan, S.J. Lippard, The zinspy family of fluorescent zinc sensors: syntheses and spectroscopic investigations, *Inorg. Chem.*, 2004, **43**, 8310–8317.

39. E.M. Nolan, S.C. Burdette, J.H. Hervey, S.A. Hilderbrand, S.J. Lippard, Synthesis and characterization of zinc sensors based on a monosubstituted fluorescein platform, *Inorg. Chem.*, 2004, **43**, 2624–2635.

40. S. Aoki, D. Kagata, M. Shiro, K. Takeda, E. Kimura, Metal chelation-controlled twisted intramolecular charge transfer and its application to fluorescent sensing of metal ions and anions, *J. Am. Chem. Soc.*, 2004, **126**, 13377–13390.

41. R. Parkesh, T.C. Lee, T. Gunnlaugsson, Highly selective 4-amino-1,8-naphthalimide based fluorescent photoinduced electron transfer (PET) chemosensors for Zn(II) under physiological pH conditions, *Org. Biomol. Chem.*, 2007, **5**, 310–317.
42. J.L. Fillaut, J. Andries , R.D. Marwaha, P.H. Lanoe, O. Lohio, L. Toupet, J.A.G. Williams, Flavonol based ruthenium acetylides as fluorescent chemosensors for lead ions, *J. Organomet. Chem.*, 2008, **693**, 228–234.
43. A. Kurzwernhart, W. Kandioller, C. Bartel, S. Bachler, R. Trondl, G. Muhlgassner, M.A. Jakupec, V.B. Arion, D. Marko, B.K. Keppler, C.G. Hartinger, Targeting the DNA-topoisomerase complex in a double-strike approach with a topoisomerase inhibiting moiety and covalent DNA binder, *Chem. Commun.*, 2012, **48**, 4839–4841.
44. M.P. Gharpure, V.N. Ingle, H.D. Juneja, R.G. Choudhary, Microwave assisted synthesis and biological evaluation of 2-aryl/heteryl-3-aryloxy/heteryloxy-4h-chromones (4-oxo-2-aryl/heteryl-4h-chromen-3-yl-carboxylate), *Int. J. Appl. Biol. Pharm. Technol.*, 2012, **3**, 287–296.

# CHAPTER 5
# Coumarin-derived Fluorescent Probe for Mg(II) Ion

## 5.1. Introduction

Magnesium is the fourth most abundant cation in the human body, most abundant divalent cation within cells and plays an important role in many physiological functions [1]. Also Magnesium found in the bone and plays an active role in bone remodelling and skeletal development [2, 3]. In addition, magnesium is the eighth most abundant element on earth crust [4]. Magnesium deficiency can causes hypokalaemia, gastrointestinal, cardiac, hypocalcaemia, renal losses and neurological manifestations. A number of chronic diseases, such as diabetes, osteoporosis, hypertension and coronary heart disease have been associated with chronic low magnesium [5, 6]. Detection of $Mg^{2+}$ in the presence of other alkali and alkaline earth metal ions, like as $Ca^{2+}$, $Na^{+}$ and $K^{+}$ is of particular significance. Serum magnesium and the magnesium tolerance test are the most widely used. There are no easy and readily available methods to assess magnesium status.

In this respect, the design of fluorescent chemosensors is an active field of research for analytical as well as environmental and biological problems [7–11]. In general, chemo sensing probes are small molecules and are capable to associate with analyte with a change in the sensing system property, such as absorption, emission and redox potentials, which may permit naked eye detection of analyte without resorting to the use of any costly instruments. The different types of chemosensors, especially fluorescent based sensors present many advantages. Fluorescence measurements are usually low cost, very sensitive, easily performed, capability of real-time detection and versatile [12–17].

Till now, various families of fluorescent probes for $Mg^{2+}$ have been developed. These probes have receptor groups based upon moieties including diaza-18-crown-6 [18], benzo-15-crown-5 [19], calix[4]arene [20], benzo chromene [21] and imidazo-1,10-phenanthroline [22]. Most of the reported fluorescent probes for $Mg^{2+}$ exhibit poor selectivity for $Mg^{2+}$ over $Ca^{2+}$ and are helpful only where the concentration of $Mg^{2+}$ ions is much higher than those of $Ca^{2+}$ ions.

In this chapter, the capacity of 4-Methyl-7-hydroxy-8-formyl Coumarin (**CS**) as a fluorescent probe to serve as a chemosensor for magnesium (II) ion in the presence of other alkali and alkaline earth metal ions was described. Our particular interest is to investigate how $Mg^{2+}$ affects the fluorescent behaviour of fluorophore upon complexation.

## 5.2. Experimental

### *5.2.1. Reagents and apparatus*

All the commercially available chemicals were purchased from Merck and Aldrich and used without further purification. The IR spectra were recorded on a Nexus FT-IR

(Illinois, USA) spectrometer in the range 4000–400 $cm^{-1}$ with KBr. The NMR spectra were measured by using Bruker 500 MHz (USA), TMS as an internal standard, DMSO-d6, $CDCl_3$ and $CD_3OD$ are taken as solvents. The mass spectra were recorded on a Bruker-micrOTOF II (USA). The UV-Vis absorption spectra were obtained on a Shimadzu UV-2450 spectrophotometer (Japan) and the Fluorescent spectra were recorded by using Shimadzu RF-5301PC spectrofluorophotometer (Japan). Differential Pulse Voltammetric experiments were performed using a CHI760E electrochemical workstation (USA) with a conventional three-electrode configuration consisting of a glassy carbon working electrode, a platinum wire counter electrode, and an aqueous $Ag/AgNO_3$ reference electrode. The pH was measured with a Eutech CyberScan pH 510 (Singapore).

*5.2.2. Synthesis and characterisation*

The synthetic route of Chemosensor (**CS**) was outlined in Scheme 5.1. Chemosensor was prepared by following the literature method [23, 24] and the structure was characterised by FT-IR, $^1H$ NMR and HRMS spectra.

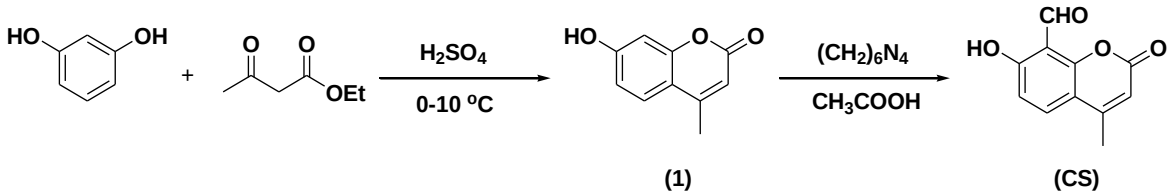


**Scheme 5.1.** Synthetic route for **CS**.

*5.2.2.1. Synthesis of 4-Methyl-7-hydroxy Coumarin (**1**):*

Concentrated sulphuric acid (20 mL) was cooled at 0–5 °C in an ice bath. A solution of resorcinol (20 mmol) in ethyl acetoacetate (30 mmol) was added to sulphuric acid under constant stirring at 0–5 °C. The reaction mass was stirred about 2–3 h under the same conditions and poured in to crushed ice under vigorous stirring. Obtained solid was filtered and recrystallised from methanol. Yield: 2.8 g (79%); Color: White crystals; Mp: 179–181 °C; FT-IR (KBr), *v*, $cm^{-1}$: 3158 (O−H), 1681 (C=O), 1594 (C=C), 1382, 1234 (C−O); $^1H$ NMR (DMSO-d6), $\delta$, ppm (*J*, Hz): 2.38 (s, 3H), 6.14 (s, 1H), 6.72 (s, 1H), 6.81 (d, $J$ = 8.5, 1H), 7.61 (d, $J$ = 8.5, 1H), 10.54 (s, 1H).

*5.2.2.2. Synthesis of 4-Methyl-7-hydroxy-8-formyl Coumarin (**CS**):*

The mixture of 7-hydroxy-4-methyl-coumarin (10 mmol), hexamethylene tetramine (30 mmol) in glacial acetic acid (20 mL) was refluxed for 4–5 h in a water bath. Then, 20% HCl (25 mL) was added and further heated for 30 min, cooled to room temperature and

extracted with diethyl ether. Solid was obtained on evaporation of solvent. Yield: 0.37 g (18%); Color: Pale yellow solid; Mp: 175–177 °C; FT-IR (KBr), *v*, $cm^{-1}$: 3433 (O−H), 2924 (OC−H), 1745 (HC=O), 1642 (C=O), 1589 (C=C), 1387, 1298 (C−O); $^1$H NMR ($CDCl_3$), *δ*, ppm (*J*, Hz): 2.43 (s, 3H), 6.20 (s,1H), 6.91 (d, *J* = 8.5, 1H), 7.73 (d, *J* = 9.0, 1H), 10.62 (s, 1H), 12.22 (s, 1H); HRMS *m/z*: Calcd for $C_{11}H_8O_4$ $(M+Na)^+$: 227.0320, found: 227.0356.

*5.2.3. UV-Vis and fluorescent studies*

All measurements of UV-Vis absorption and fluorescence emission studies were carried out in 1.0 cm path length quartz cuvettes in alcoholic medium (MeOH) at room temperature. Absorption and emission spectra of the chemosensor in the presence of various metal ions were measured in the concentration of 50 µM (for absorption spectra), 10 µM (for emission spectra). Stoichiometry, binding constant of sensing probe–$Mg^{2+}$ complex and limit of detection of $Mg^{2+}$ were calculated by using spectrofluorophotometer. For all the fluorescent measurements, excitation wavelength was 350 nm, and both the excitation and emission slit widths were 3 and 5 nm, respectively.

## 5.3. Results and discussion

The binding ability and mode of chemosensor towards $Mg^{2+}$ were investigated through absorption, emission, electrochemical and $^1$H NMR spectroscopic experiments.

*5.3.1. Absorption spectroscopic studies*

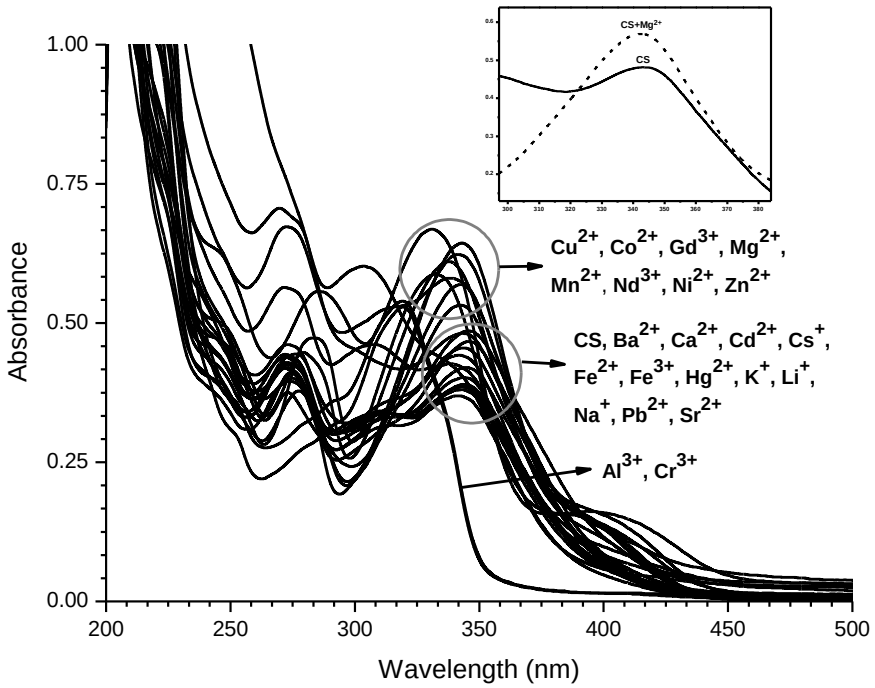


**Figure 5.1.** UV-Vis absorbance spectra of **CS** (50 µM) in the presence of 1.0 equiv. of various metal ions in MeOH.

The binding ability of probe (50 μM) against cations (50 μM), such as $Ca^{2+}$, $K^{+}$, $Co^{2+}$, $Li^{+}$, $Ba^{2+}$, $Cr^{3+}$, $Pb^{2+}$, $Cd^{2+}$, $Nd^{3+}$,$Mn^{2+}$, $Cs^{+}$, $Fe^{2+}$, $Fe^{3+}$, $Cu^{2+}$, $Gd^{3+}$, $Al^{3+}$, $Hg^{2+}$, $Mg^{2+}$, $Na^{+}$, $Ni^{2+}$, $Sr^{2+}$ and $Zn^{2+}$ was carried out by UV-Vis absorption spectroscopic studies in methanol. The free ligand **CS** exhibited a single absorption band at about 343 nm, hyperchromic shift was observed when added to $Cu^{2+}$, $Co^{2+}$, $Gd^{3+}$, $Mn^{2+}$, $Mg^{2+}$, $Ni^{2+}$, $Nd^{3+}$ and $Zn^{2+}$ ions (Figure 5.1). It showed a blue shift accompanied by a hyperchromic shift in the presence of $Cr^{3+}$ and $Al^{3+}$ metal ions. The other cations $Ba^{2+}$, $K^{+}$, $Hg^{2+}$, $Cd^{2+}$, $Cs^{+}$, $Ca^{2+}$, $Fe^{2+}$, $Fe^{3+}$, $Li^{+}$, $Na^{+}$, $Pb^{2+}$ and $Sr^{2+}$ did not show any considerable spectroscopic change even when added in excess (10 equiv.).

*5.3.2. Fluorescence emission studies*

The fluorescence emission spectral behaviour of sensor **CS** (10 μM) upon addition of various metal ions (10 μM) have been investigated in methanol. Chemosensor alone showed a single emission band at 473 nm with an excitation of 350 nm. **CS** showed a chelation enhanced fluorescence (CHEF) only with $Mg^{2+}$, even though there was a relatively chelation enhanced fluorescent quenching (CHEQ) effect with $Al^{3+}$, $Co^{2+}$, $Cu^{2+}$, $Cr^{3+}$, $Fe^{2+}$, $Mn^{2+}$, $Ni^{2+}$, $Gd^{3+}$, $Nd^{3+}$ and $Zn^{2+}$ (Figure 5.2).

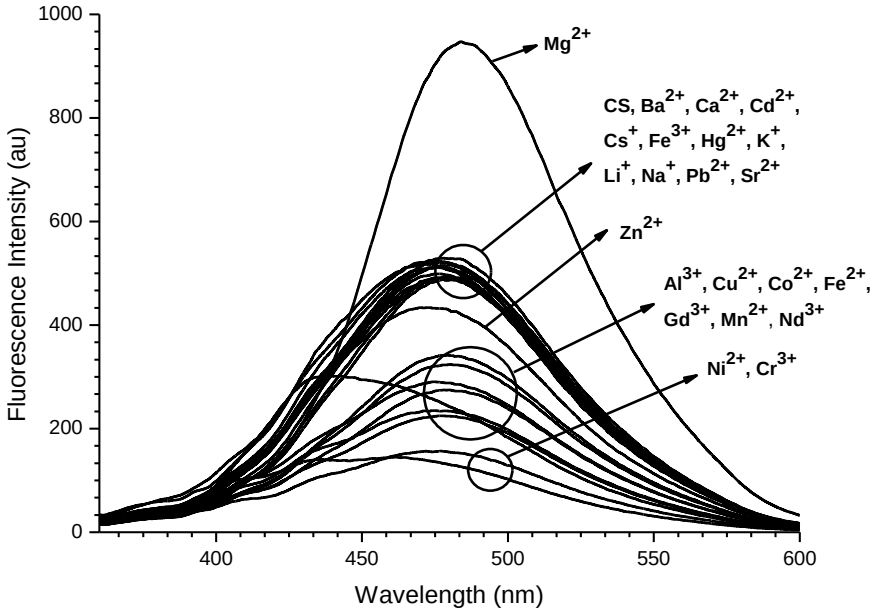


**Figure 5.2.** Fluorescence emission spectra ($\lambda_{ex}$ = 340 nm) of receptor **CS** (10 μM) in the presence of 1.0 equiv. of various metal ions in MeOH.

The sequential addition from 0.0 to 1.0 equiv. $Mg^{2+}$ ions to **CS** showed a gradual increase in emission accompanied by a small red shift of 12 nm from 473 to 485nm (Figure 5.3). Under a UV lamp, the solution of **CS** in the presence of $Mg^{2+}$ showed a spectacular color change

from dull fluorescent blue to bright fluorescent blue, which could simply be identified by the naked-eye (Figure 5.3, inset). Furthermore, to investigate the binding mechanism, the Job's plot of fluorescence emission titration of $Mg^{2+}$ was exposed in Figure 5.4. A maximum emission intensity was detected when the molar fraction of $Mg^{2+}$ reached 0.5, which indicates a 1:1 stoichiometry for the newly formed species of **CS**–$Mg^{2+}$.

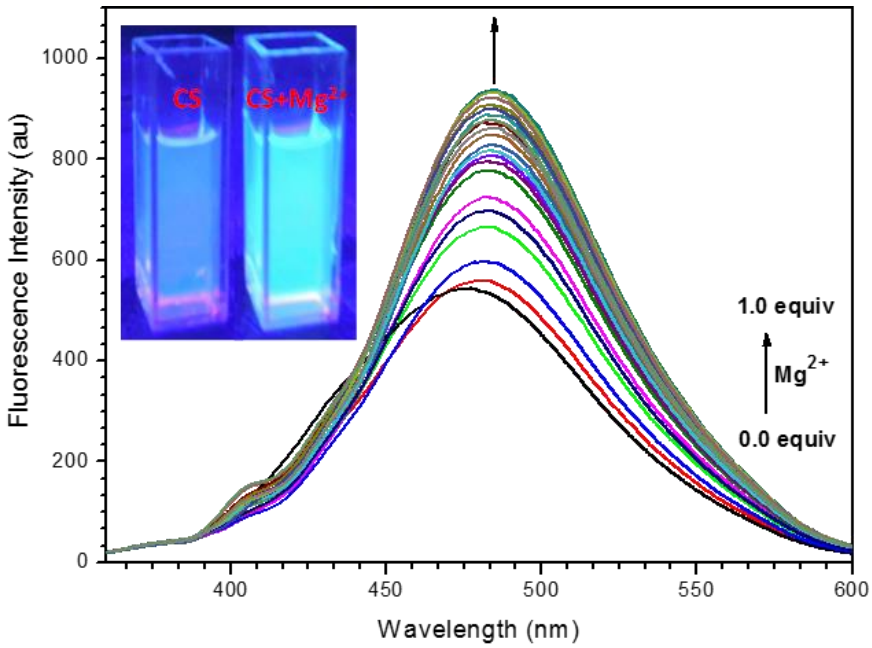


**Figure 5.3.** Fluorescent spectral changes of **CS** (10 μM) upon titration with $MgCl_2$ in MeOH. Inset: Changes in the fluorescence intensity of **CS** with $Mg^{2+}$ under 365 nm UV light.

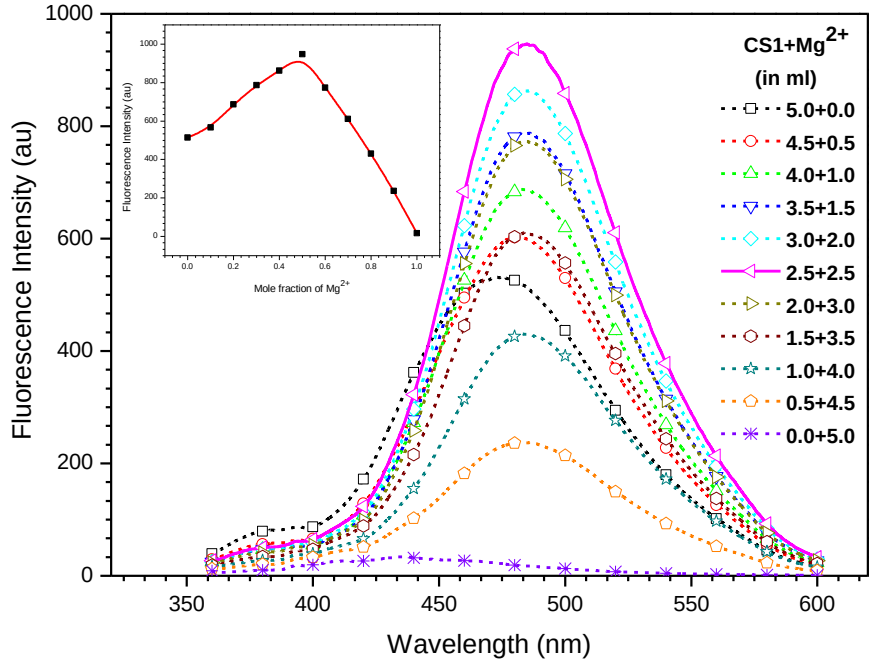


**Figure 5.4.** Job's plot, inset: Fluorescence intensity at 485 nm was plotted as a function of the molar ratio of $Zn^{2+}$.

From the Fluorescence titration profiles, linear relationship was obtained for the plot measured $1/(F-F_0)$ at 485 nm as a function of $1/[Mg^{2+}]$ using the well-known linear Benesi-Hildebrand expression [25]. The binding constant of the newly formed complex (**CS**–$Mg^{2+}$) was determined as $5.7\times10^5$ $M^{-1}$ (Figure 5.5). The detection limit was calculated based on the fluorescence titration of $Mg^{2+}$ as 0.43 μM based on S/N = 3 (Figure 5.6).

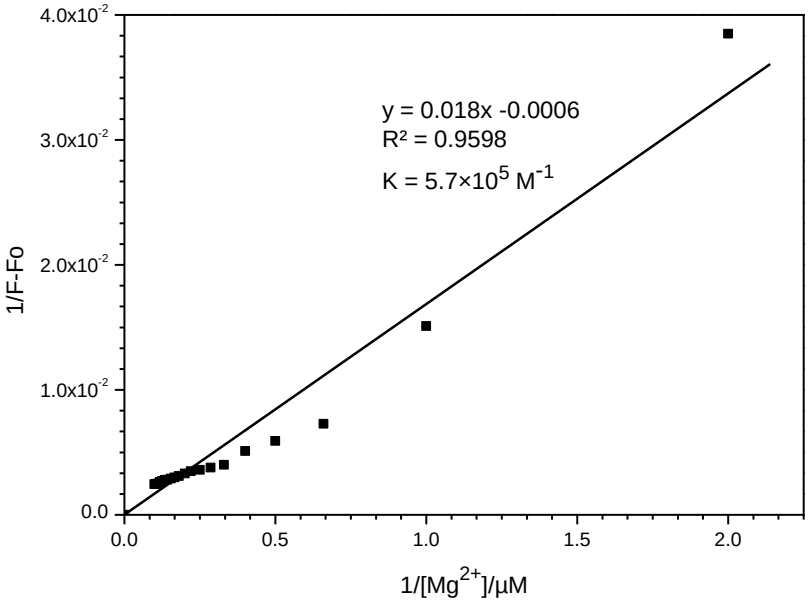


**Figure 5.5.** Benesi-Hildebrand plot, fluorescence intensity at 485 nm.

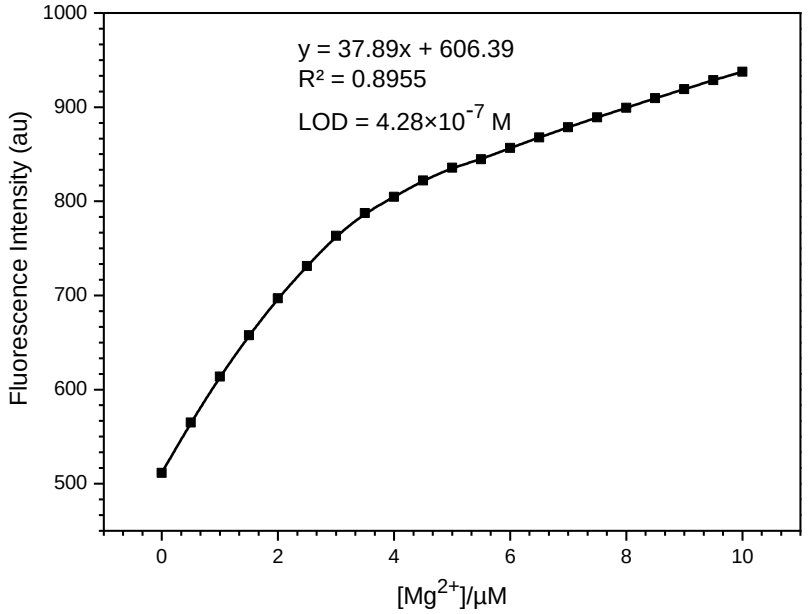


**Figure 5.6.** The linear relation for fluorescent intensity of **CS** (10 μM) toward $Mg^{2+}$ concentration in the range of 0–10 μM.

In addition, the selectivity of **CS** towards $Mg^{2+}$ over other metal ions was investigated by the competition experiment. As depicted in Figure 5.7, probe **CS** (10 μM) was treated

with 1.0 equiv. $Mg^{2+}$ in the presence of various metal ions in the same concentration. Comparatively low interference levels were monitored for the detection of $Mg^{2+}$ in the presence of alkali ($Na^+$, $Li^+$, $K^+$ and $Cs^+$), alkaline earth ($Ca^{2+}$, $Ba^{2+}$ and $Sr^{2+}$), p-block ($Pb^{2+}$) and d-block ($Fe^{3+}$, $Mn^{2+}$, $Zn^{2+}$, $Hg^{2+}$ and $Cd^{2+}$) metal ions. The receptor **CS** responses for $Mg^{2+}$ in the presence of $Al^{3+}$, $Cu^{2+}$, $Cr^{3+}$, $Co^{2+}$, $Fe^{2+}$, $Gd^{3+}$, $Nd^{3+}$ and $Ni^{2+}$ are relatively low. Thus probe **CS** can perform as a selective fluorescent chemosensor for $Mg^{2+}$ in the attendance of most challenging metal ions particularly alkali and alkaline earth metal ions.

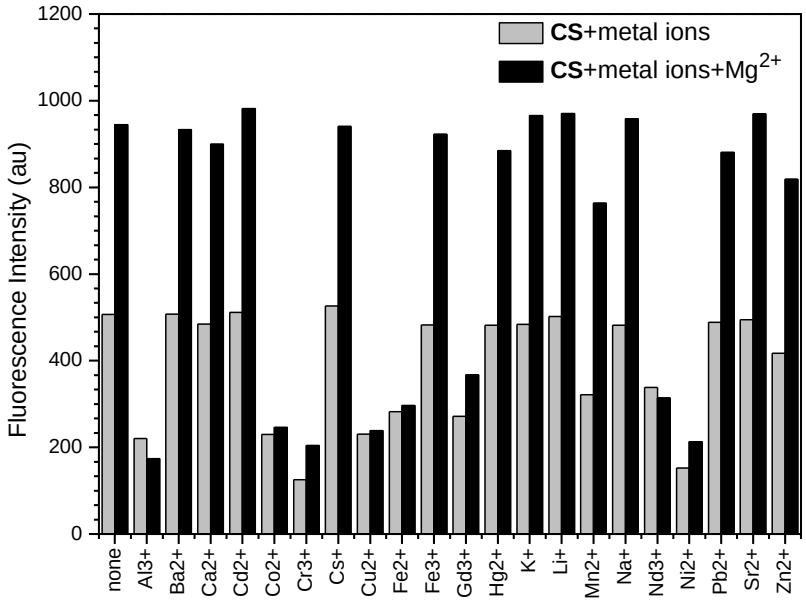


**Figure 5.7.** Selectivity of the probe **CS** toward various metal ions (1.0 equiv.) in the absence and presence of $Mg^{2+}$ (1.0 equiv.), fluorescence intensity at 485 nm.

*5.3.3. Electrochemical measurement*

As shown in Figure 5.8, the corresponding wavelength to the band gap energy can be calculated from the cross point of absorption and emission onset lines. The corresponding wavelength for **CS** is 396 nm and **CS**+$Mg^{2+}$ is 415 nm which are equal to 3.13 eV (for **CS**) and 2.99 eV (for **CS**+$Mg^{2+}$) band gap energy.

Figure 5.9 shows the current–voltage curve for **CS** and **CS**+$Mg^{2+}$ regarding to Differential Pulse Voltammetric (DPV) experiments. Based on results, **CS** shows $E_{ox}$= 0.656 V which is equal to $E_{HOMO}$= -5.46 eV and **CS**+$Mg^{2+}$ shows $E_{ox}$= 0.7 V which is equal to $E_{HOMO}$= -5.5 eV [26]. By addition of $Mg^{2+}$ ion increased the oxidation potential of **CS**, due to decrease in electron releasing nature of **CS**–$Mg^{2+}$ complex. LUMO energy levels (-2.33 eV for **CS** and -2.51 eV for CS+$Mg^{2+}$) were estimated from HOMO and band gap energies.

This experiment proves that, increase in oxidation potential and decrease in band gap due to the interaction between **CS** probe and magnesium ion. Figure 5.10 shows the energy diagram with HOMO/LUMO levels of **CS** and **CS**+$Mg^{2+}$.

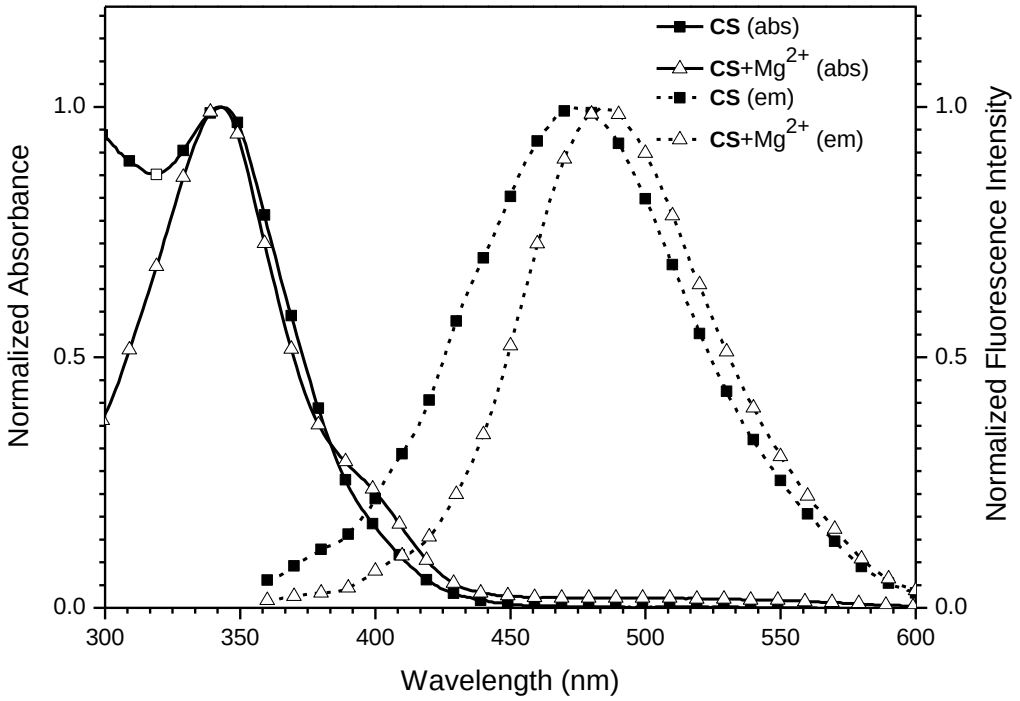


**Figure 5.8.** UV-Vis absorption and fluorescence emission spectra of **CS** and **CS**–$Mg^{2+}$.

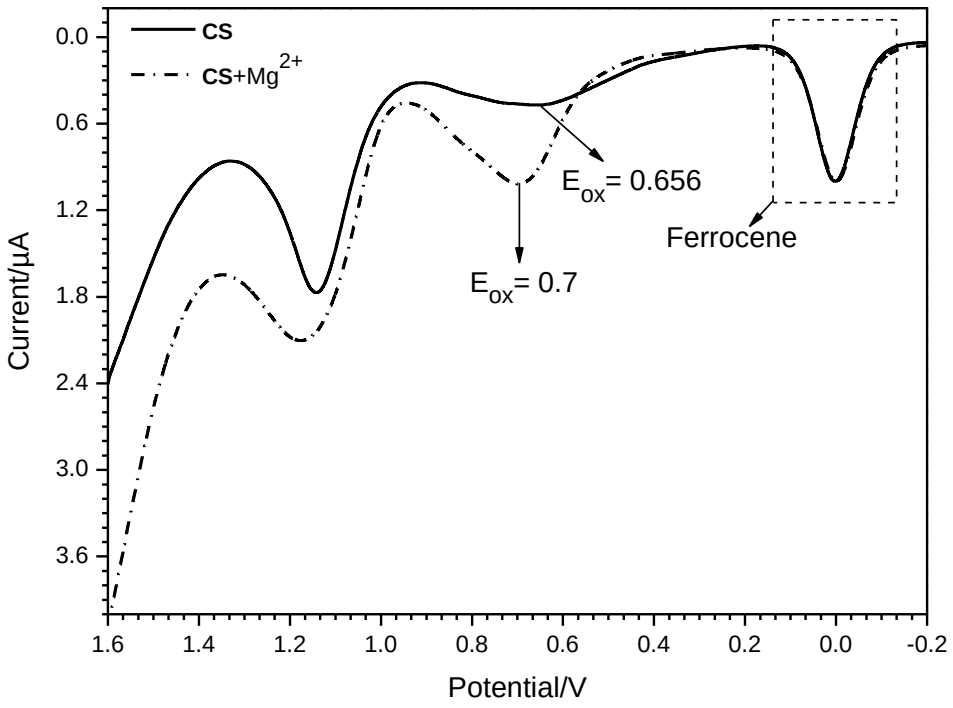


**Figure 5.9.** Differential pulse voltammograms recorded for the probe **CS** and the corresponding $Mg^{2+}$ addition product in methanol.

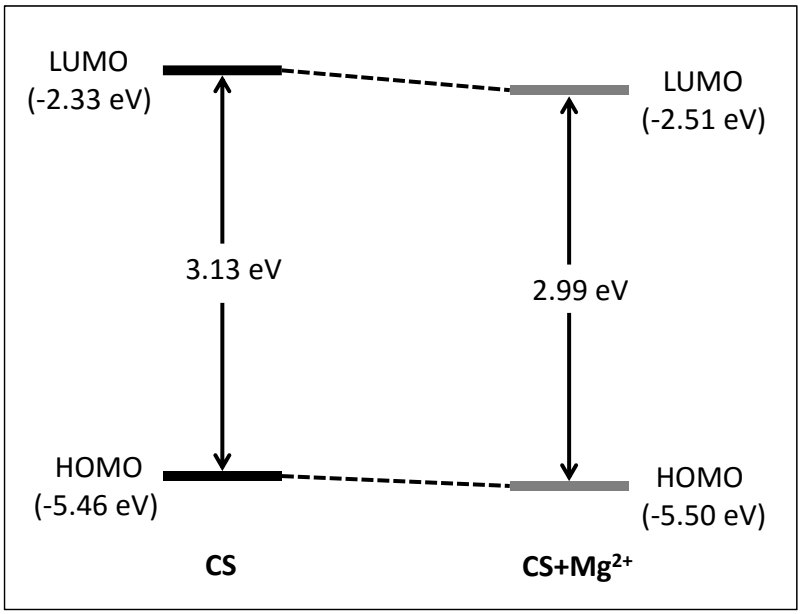


**Figure 5.10.** Energy level diagram of the probe **CS** and the corresponding $Mg^{2+}$ addition product.

*5.3.4. $^{1}H$ NMR titration*

To further clarify the bonding mode of sensing probe (**CS**) towards $Mg^{2+}$, $^{1}H$ NMR titration experiments were carried out in both absence and presence of magnesium ion in various concentrations in methanol-d4 at room temperature. As shown in Figure 5.11, on the addition of $Mg^{2+}$, aldehyde proton of **CS** at about 10.58 ppm was shifted downfield toward

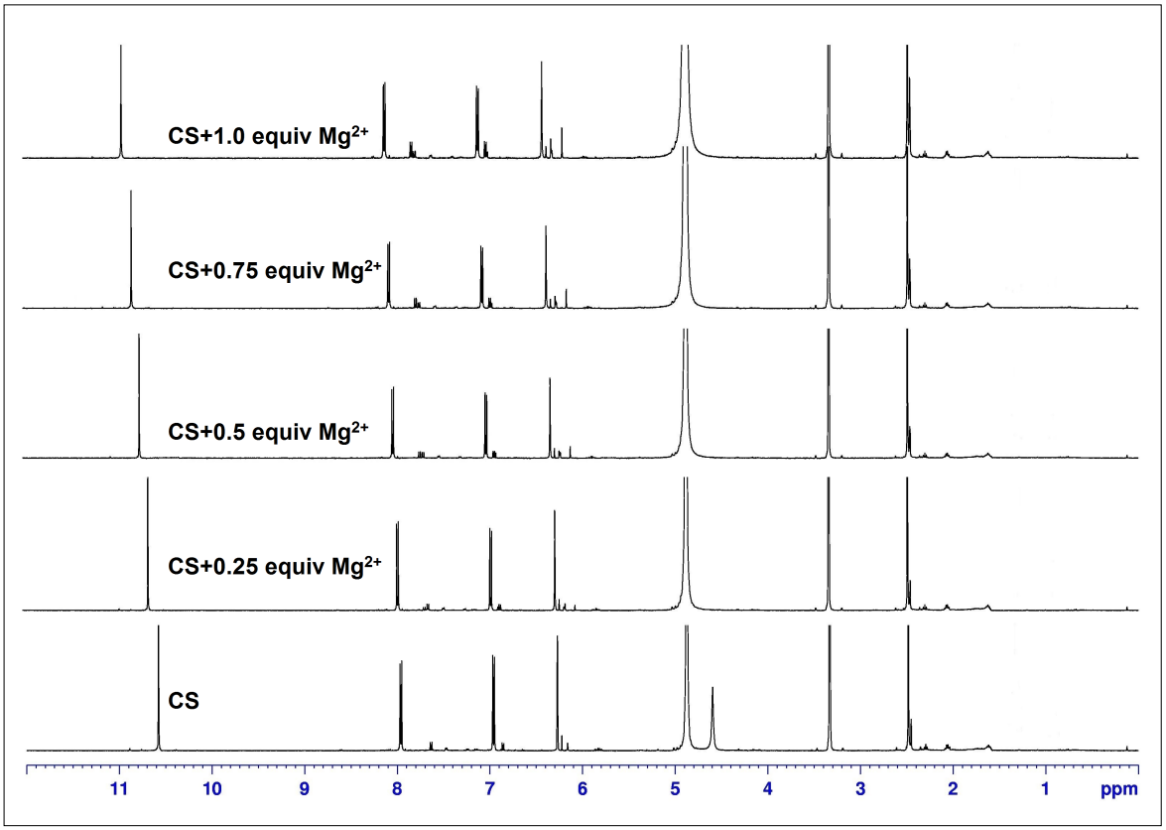


**Figure 5.11.** $^{1}H$ NMR titration plot of receptor **CS** with $Mg^{2+}$ in $CD_3OD$.

10.98 ppm. The hydroxyl proton was disappeared in $CD_3OD$ solvent. On the other hand, the aromatic protons were shifted downfield by 0.02–0.17 ppm followed the addition of $Mg^{2+}$. The results recommended that the binding of probe (**CS**) to $Mg^{2+}$ forms a rigid system by a chelation with the phenolic OH and the oxygen atom of carbonyl group (Scheme 5.2).

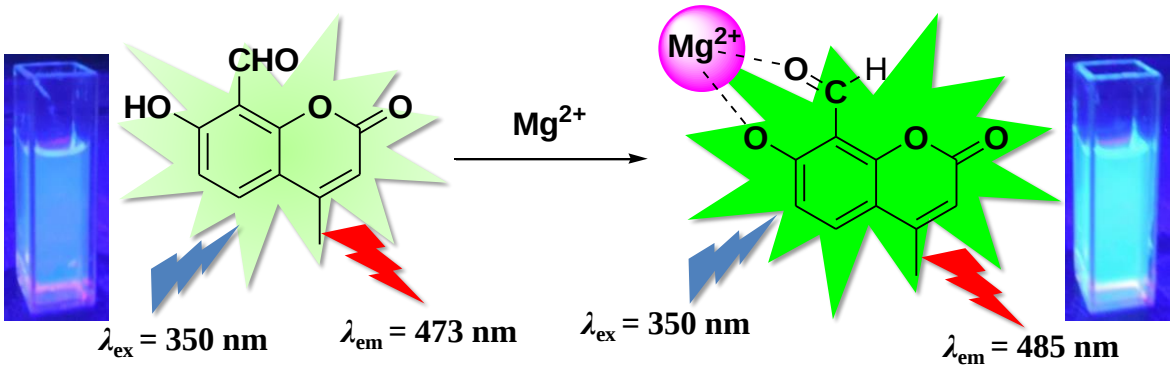


**Scheme 5.2.** Schematic representation of proposed binding mode of receptor with $Mg^{2+}$.

*5.3.5. pH effect*

The pH-dependent response of **CS** was carried out to investigate a suitable pH range for detection of $Mg^{2+}$. As depicted in Figure 5.12, the fluorescence emission changes were observed at 485 nm with pH variation. After mixing **CS** with $Mg^{2+}$ in the basic pH range, exhibited a rapid fluorescence enhancement accompanied by a blue shift of 37 nm from 485 to 448 nm. The emission intensity of **CS**–$Mg^{2+}$ complex was quenched in the acidic

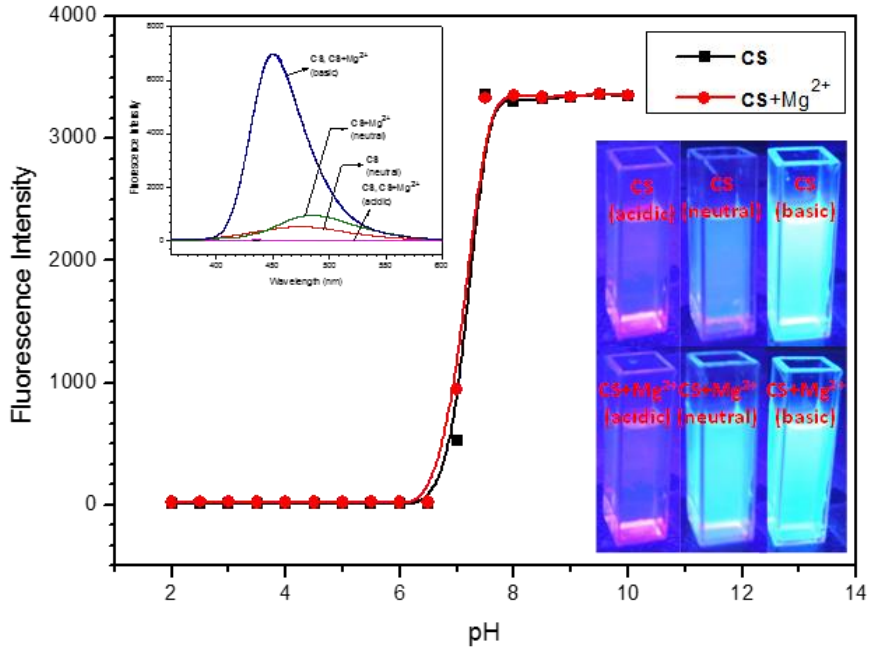


**Figure 5.12.** Fluorescence intensities of **CS** (10 µM) at 485 nm in the presence of $Mg^{2+}$ (10 µM) under different pH conditions. Inset: Spectral changes of **CS**–$Mg^{2+}$ as a function of pH (left), photographs of **CS** and **CS**–$Mg^{2+}$ in different pH media under a UV lamp (right).

conditions. For pH < 7, the decreased fluorescence intensity at 485 nm indicates that the protonation of Coumarin prevents the formation of **CS**–$Mg^{2+}$complexes in acidic condition. The chemosensors **CS** in the presence of $Mg^{2+}$ showed a dramatic color changes in the different pH conditions, which could simply be identified by the naked-eye (Figure 5.12, inset) under a UV lamp. The same fluorescence emission changes were observed for **CS** alone in acidic and basic conditions.

*5.3.6. Reversibility of complexation of probe–$Mg^{2+}$*

To establish the reversibility binding of **CS**–$Mg^{2+}$, EDTA titration was conducted. This experiment was performed by the addition of EDTA to the solution containing **CS** (1.0 equiv.) and Mg(II) (1.0 equiv.). Therefore, the addition of EDTA resulted in quenching of the fluorescence intensity at 485 nm, which showed the restoration of the free receptor **CS** (Figure 5.13). The fluorescence was improved by the addition of $Mg^{2+}$ again. These results show that **CS** is suitable to be used as a reversible fluorescent chemosensor to detect $Mg^{2+}$.

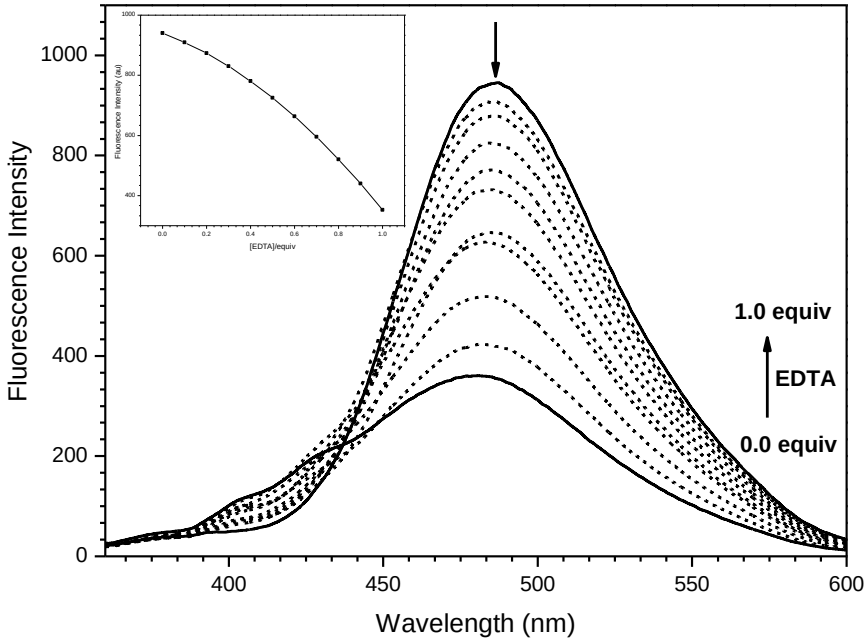


**Figure 5.13.** The variation in fluorescence emission spectra of **CS**–$Mg^{2+}$ (10 μM) upon addition of EDTA in methanol. Inset: Fluorescence spectral changes at 485 nm as a function of the amount of EDTA.

## 5.4. Conclusion

In summary, we have found a Coumarin based sensitive probe **CS** to $Mg^{2+}$ which fluorometrically selective with $Mg^{2+}$ ions and makes it a dual probe for naked eye detection of Mg(II) through change in color and fluorescence emission. The limit of detection of $Mg^{2+}$ was found to be much lower as 0.43 μM. The binding ability and mode of sensor **CS** towards

$Mg^{2+}$ were investigated through UV-Vis absorption, fluorescence emission, electrochemical and $^{1}H$ NMR spectroscopic techniques. Thus, our chemosensor can be used as a practical sensor for detection of Mg(II) in analytical as well as environmental and biological samples.

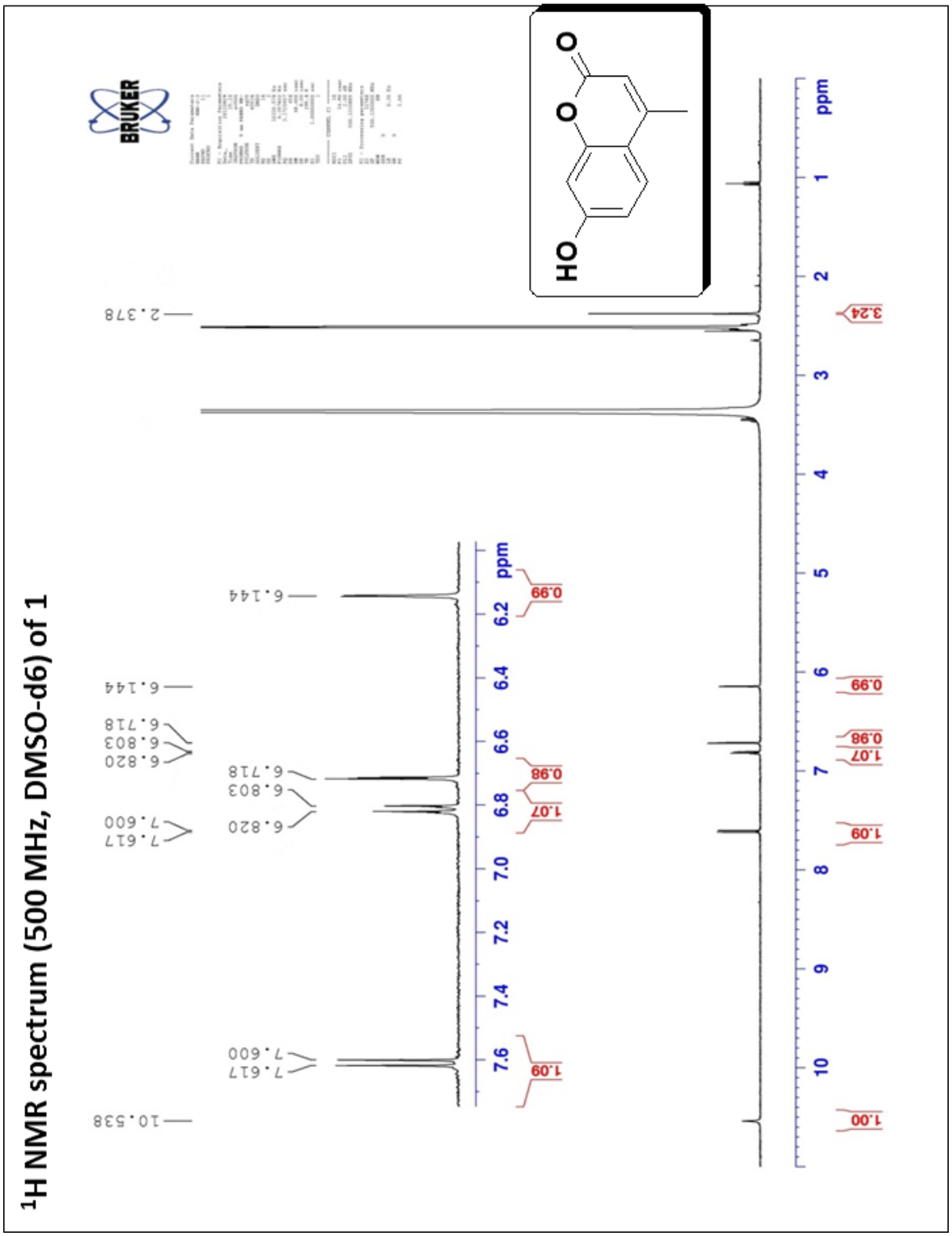
$^1$H NMR spectrum (500 MHz, DMSO-d6) of 1
BRUKER
HO
O
O
2.378
6.144
6.144
6.718
6.803
6.820
7.617
7.600
10.538
ppm
0.99
0.98
1.07
1.09
3.24
1.00

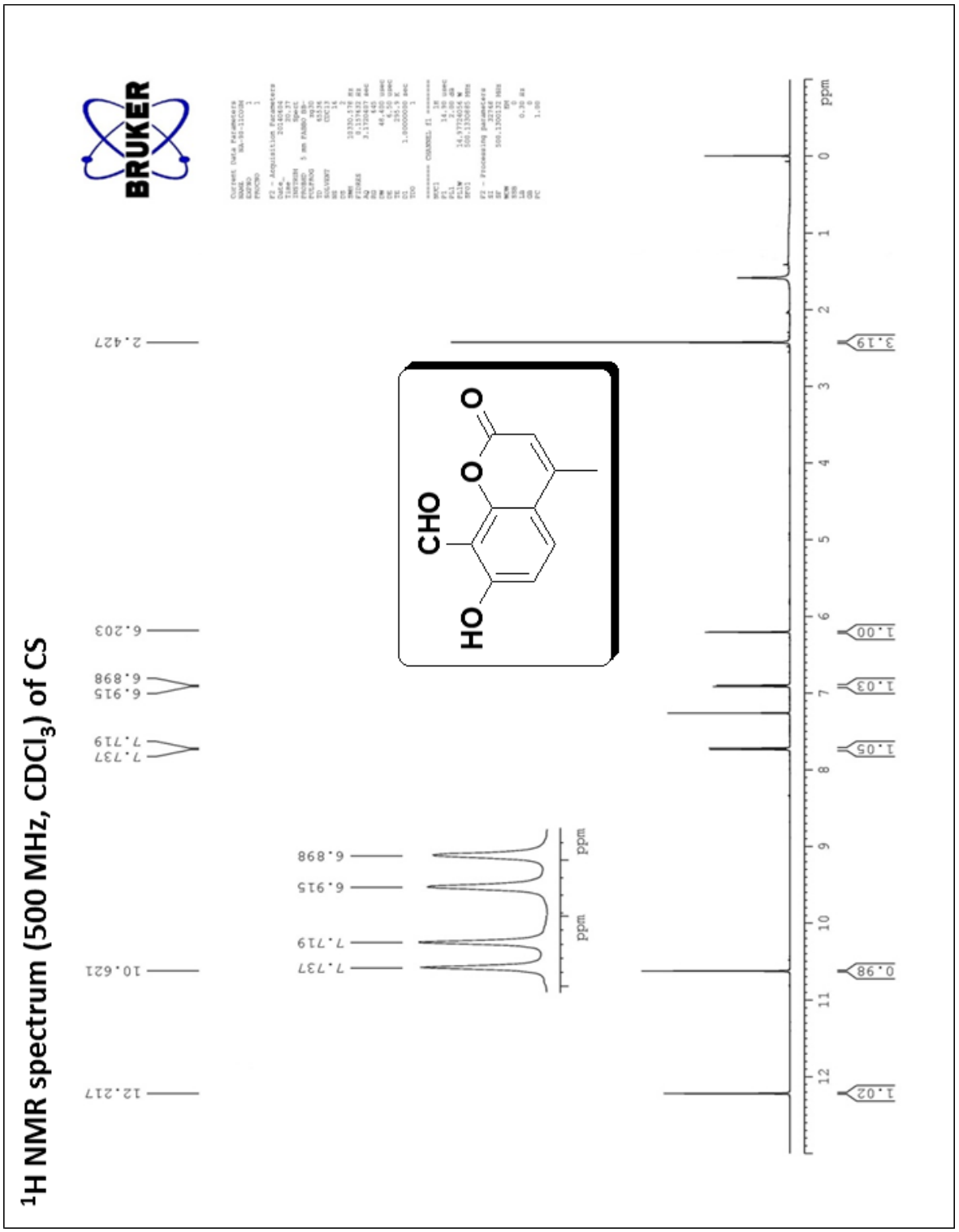
$^1$H NMR spectrum (500 MHz, $CDCl_3$) of CS
BRUKER
CHO
O
O
HO
ppm
12.217
10.621
7.737
7.719
6.915
6.898
6.203
2.427
1.02
0.98
1.05
1.03
1.00
3.19

## HRMS spectrum of CS

**Acquisition Parameter**

| | | | | | |
|---|---|---|---|---|---|
| Source Type | ESI | Ion Polarity | Positive | Set Nebulizer | 0.4 Bar |
| Focus | Not active | Set Capillary | 4500 V | Set Dry Heater | 180 °C |
| Scan Begin | 50 m/z | Set End Plate Offset | -500 V | Set Dry Gas | 4.0 l/min |
| Scan End | 3000 m/z | Set Collision Cell RF | 150.0 Vpp | Set Divert Valve | Source |

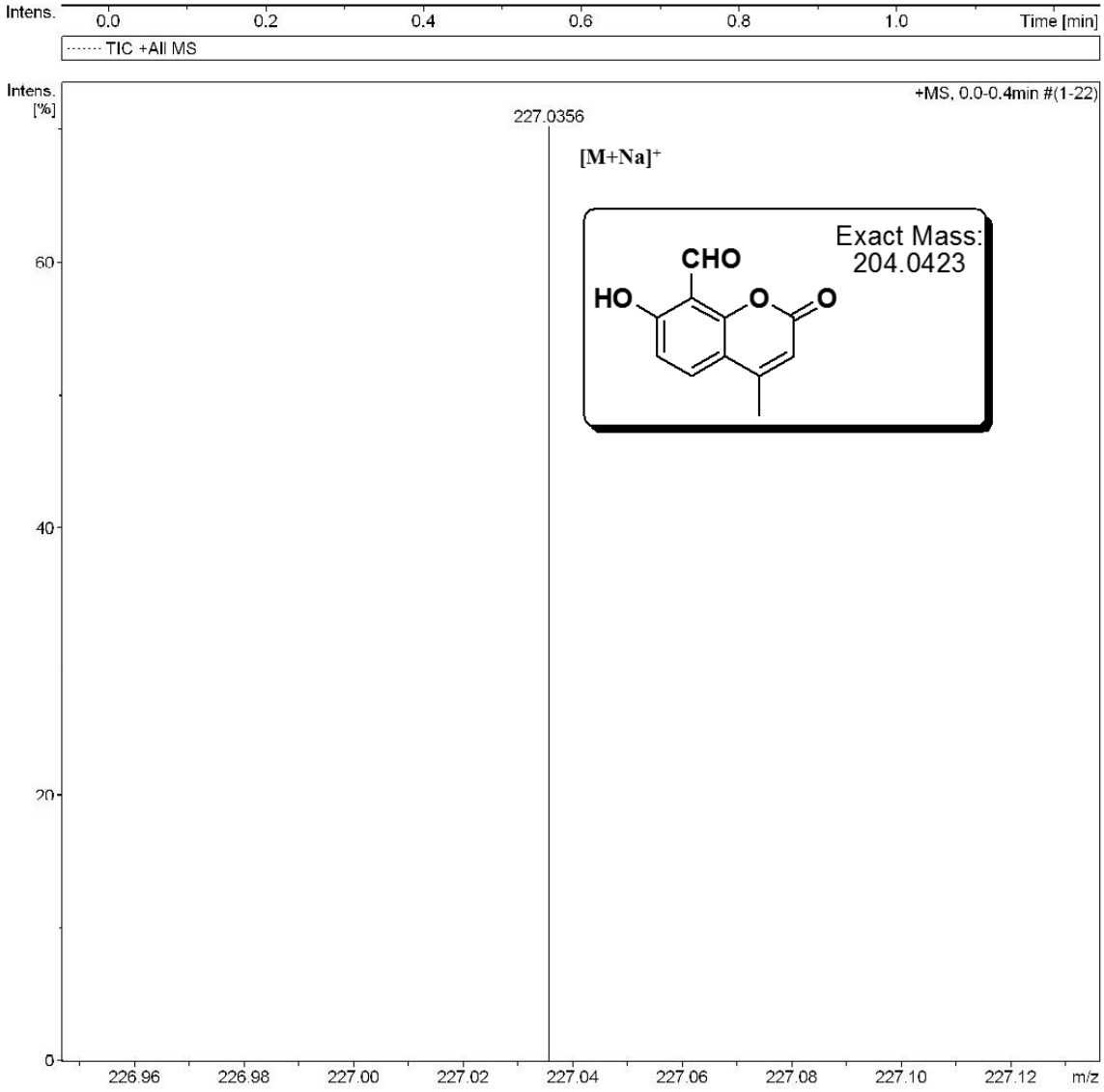

**References**


1. R.D. Grubbs, M.E. Maguire, Magnesium as a regulatory cation: Criteria and evaluation, *Magnesium*, 1987, **6**, 113–127.
2. R. Bogoroch, L.F. Belanger, Skeletal effects of magnesium deficiency in normal, ovariectomized, and estrogen-treated rats, *Anat. Rec.*, 1975, **183**, 437–447.
3. H.O. Trowbridge, J.L. Seltzer, Formation of dentin and bone matrix in magnesium-deficient rats, *J. Periodontal Res.*, 967, **2**, 147–153.
4. M.E. Maguire, J.A. Cowan, Magnesium chemistry and biochemistry, *Biometals*, 2002, **15**, 203–210.
5. R. Swaminathan, Magnesium metabolism and its disorders, *Clin. Biochem. Rev.*, 2003, **24**, 47–66.
6. W. Jahnen-Dechent, M. Ketteler, Magnesium basics, *Clin. Kidney J.*, 2012, **5**, i3–i14.
7. L. Fabbrizzi, A. Poggi, Sensors and switches from supramolecular chemistry, *Chem. Soc. Rev.*, 1995, **24**, 197–202.
8. B. Valeur, I. Leray, Design principles of fluorescent molecular sensors for cation recognition, *Coord. Chem. Rev.*, 2000, **205**, 3–40.
9. S.L. Wiskur, H. Ait-Haddou, J.J. Lavigne, E.V. Anslyn, Teaching old indicators new tricks, *Acc. Chem. Res.*, 2001, **34**, 963–972.
10. K. Rurack, U. Resch-Genger, Rigidization, preorientation and electronic decoupling-the 'magic triangle' for the design of highly efficient fluorescent sensors and switches, *Chem. Soc. Rev.*, 2002, **31**, 116–127.
11. G.W. Gokel, W.M. Leevy, M.E. Weber, Crown ethers: Sensors for ions and molecular scaffolds for materials and biological models, *Chem. Rev.*, 2004, **104**, 2723–2750.
12. A.P. de Silva, H.Q.N. Gunaratne, T. Gunnlaugsson, A.J.M. Huxley, C.P. McCoy, J.T. Rademacher, T.E. Rice, Signaling recognition events with fluorescent sensors and switches, *Chem. Rev.*, 1997, **97**, 1515–1566.
13. V.K. Gupta, A.K. Singh, L.K. Kumawat, Thiazole schiff base turn-on fluorescent chemosensor for $Al^{3+}$ ion, *Sens. Actuators B*, 2014, **195**, 98–108.
14. V.K. Gupta, A.K. Singh, N. Mergu, Antipyrine based schiff bases as turn-on fluorescent sensors for Al(III) ion, *Electrochim. Acta*, 2014, **117**, 405–412.
15. V.K. Gupta, N. Mergu, A.K. Singh, Fluorescent chemosensors for $Zn^{2+}$ ions based on flavonol derivatives, *Sens. Actuators B*, 2014, **202**, 674–682.
16. D. Kand, A.M. Kalle, S.J. Varma, P. Talukdar, A chromenoquinoline-based fluorescent off–on thiol probe for Bioimaging, *Chem. Commun.*, 2012, **48**, 2722–2724.

17. G. Zhang, Y. Wen, C. Guo, J. Xu, B. Lu, X. Duan, H. He, J. Yang, A cost-effective and practical polybenzanthrone-based fluorescent sensor for efficient determination of palladium (II) ion and its application in agricultural crops and environment, *Anal. Chim. Acta*, 2013, **805**, 87–94.
18. G. Farruggia, S. Iotti, L. Prodi, M. Montalti, N. Zaccheroni, P.B. Savage, V. Trapani, P. Sale, F.I. Wolf, 8-hydroxyquinoline derivatives as fluorescent sensors for magnesium in living Cells, *J. Am. Chem. Soc.*, 2006, **128**, 344–350.
19. H. Hama, T. Morozumi, H. Nakamura, Novel $Mg^{2+}$-responsive fluorescent chemosensor based on benzo-15-crown-5 possessing 1-naphthaleneacetamide moiety, *Tetrahedron Lett.*, 2007, **48**, 1859–1861.
20. K.C. Song, M.G. Choi, D.H. Ryu, K.N. Kim, S.K. Chang, Ratiometric chemosensing of $Mg^{2+}$ ions by a calix[4]arene diamide derivative, *Tetrahedron Lett.*, 2007, **48**, 5397–5400.
21. H. M. Kim, P.R. Yang, M.S. Seo, J.S. Yi, J.H. Hong, S.J. Jeon, Y.G. Ko, K.J. Lee, B.R. Cho, Magnesium Ion Selective Two-Photon Fluorescent Probe Based on a Benzo[h]chromene Derivative for in Vivo Imaging, *J. Org. Chem.*, 2007, **27**, 2088–2096.
22. Y. Liu, Z.Y. Duan, H.Y. Zhang, X.L. Jiang, J.R. Han, Selective binding and inverse fluorescent behavior of magnesium ion by podand possessing plural imidazo[4,5-f]-1,10-phenanthroline groups and its Ru(II) complex, *J. Org. Chem.*, 2005, **70**, 1450–1455.
23. H. Pechmann, C. Duisberg, Über die Verbindungen der phenole mit acetessigäther, *Ber. Dtsch. Chem. Ges.*, 1883, **16**, 2119−2128.
24. A.D. Patel, M.S. Sharma, J.J. Vora, J.D. Joshi, Synthesis, characterization and antimicrobial activities of binary and ternary complexes of $UO_2^{II}$ and $Th^{IV}$ complexes with 5-hydroxymethyl-8-quinolinol and 8-formyl-7-hydroxy-4-methyl-2H-1-benzopyran-2-one with aniline, *J. Indian Chem. Soc.*, 1997, **74**, 287−288.
25. H.A. Benesi, J.H. Hildebrand, A spectrophotometric investigation of the interaction of iodine with aromatic hydrocarbons, *J. Am. Chem. Soc.*, 1949, **71**, 2703−2707.
26. J.L. Bredas, R. Silbey, D.S. Boudreux, R.R. Chance, Chain-length dependence of electronic and electrochemical properties of conjugated systems: polyacetylene, polyphenylene, polythiophene, and polypyrrole, *J. Am. Chem. Soc.*, 1983, **105**, 6555−6559.

# CHAPTER 6
# Rhodamine Based Chemosensors

## 6.1. Fluorescent Reversible Chemosensors for $Al^{3+}$ Ion

### 6.1.1. Introduction

Over the past few years, high sensitive and selective fluorescent chemosensors towards various transition and other toxic metal ions are particularly attractive to current researchers due to its potential applications in the medicinal, clinical and environmental research areas [1–3]. Most of the metal ions play very important roles in living system and affect human health. Aluminum is the most widely used metal and third most abundant element in the earth's crust [4]. Excess aluminum may cause damage to certain human tissues and cells, which may lead to Parkinson's disease and Alzheimer's disease [5, 6]. Recent experiments shown that the high dosage of deposition of aluminum in bone and the nervous system in human body can cause neurotoxicity [7]. Hence, the World Health Organization (WHO) warned that the excess aluminum as one of the food pollutants and restricted it to 200 μg $L^{-1}$ in drinking water [8]. Aluminum in higher concentration may affect the growth of root and seed in plants [9, 10].

Nowadays, the recognition of various biologically, industrially and environmentally important anions such as acetate and fluoride has also attracted significant interest [11–13]. Acetate ion is of great concern due to it play a crucial role in numerous metabolic processes [14, 15]. The rate of production and oxidation of acetate has been frequently used in marine sediments as an indicator of organic decomposition [16]. Among the biologically important anions, fluoride draws considerable attention due to its critical role in dental care and osteoporosis [17, 18]. Due to the valuable effects of fluoride for human health, the addition of fluoride in drinking water (0.5–1.0 ppm) and toothpastes (1000–1500 ppm) has turned into extensive. However, overexposure to fluoride can lead to fluorosis [19, 20], acute gastric and kidney problems [21]. Fluoride is also associated with diseases like Alzheimer's disease [22].

At present, many techniques are available for qualitative and quantitative analysis of metal ions and found their applications in various food, biological, geological and industrial effluents such as atomic absorption spectroscopy [23], inductively coupled plasma-mass spectroscopy [24], inductively coupled plasma emission spectrometry [25], neutron activation analysis [26], chromatography [27] and voltammetry [28]. Nevertheless, most of these methods involve tedious sample preparation procedures, sophisticated instruments and high maintenance expenditure. On the other hand, optical (colorimetric and fluorescent) chemosensors have drawn attention and offer considerable advantages over other techniques

*via* their simplicity, convenience, low-cost, sensitivity, immediate response, and naked-eye visualization [29–31].

To date, numerous chemosensors have been reported on individual ionic species such as $Al^{3+}$ [32–34], $AcO^{-}$ [35, 36] and $F^{-}$ [37–39]. On the other hand, the enlargement of chemosensor capable of sequential recognition both of metal ion and anion is still one of the most challenging tasks [40, 41]. Nowadays, metal-based receptors have been focussed in the field of anion recognition [42, 43], since they show a greater response to anion than purely organic receptors. A very few sensors have been reported on rhodamine based chemosensor metal complex which exhibited sensing for anion. Here, anion interact directly with metal ion and destroy the chemosensor metal complex via the displacement method [44–47]. However, to the best of our knowledge, there is no report of a rhodamine-derived receptor which could detect $Al^{3+}$ as well as $AcO^{-}$ and $F^{-}$.

In this section, we described the synthesis of a series of rhodamine derivatives **L1–L4**. The sensing property of these ionophores was tested with a series of alkali, alkaline earth and transition metal ions in methanolic media. The formation of **L**–$Al^{3+}$ complexes is fully reversible in the presence of acetate and fluoride anions and it could also be used as an efficient sensor for $AcO^{-}$ and $F^{-}$ under the same conditions. The response time is found to be 10 sec and the all spectroscopic measurements are carried out at room temperature only.

### 6.1.2. Experimental

*6.1.2.1. Reagents and apparatus*

Rhodamine B, metal salts and other commercially available chemicals were purchased from Merck and Aldrich and used without further purification. The melting point was measured using SRS OptiMelt Automated melting point system. The IR spectra were recorded on a PerkinElmer FT-IR spectrometer (USA) in the range 4000–400 $cm^{-1}$ with KBr. The NMR spectra were carried out using a Bruker 500 MHz (USA), TMS as an internal standard, $CDCl_3$ DMSO-d6 and CD3OD are taken as solvents. The mass spectra were obtained on a Bruker-micrOTOF II (USA). The UV-Vis absorption spectra were recorded on a Shimadzu UV-2450 spectrophotometer (Japan) and the Fluorescent spectra were recorded by using Horiba FluoroMax-4 spectrofluorophotometer (Japan). Differential Pulse Voltammetric experiments were performed using a CHI760E electrochemical workstation (USA) with a conventional three-electrode configuration consisting of a glassy carbon working electrode, a platinum wire counter electrode, and a calomel reference electrode.

*6.1.2.2. Synthesis and characterization*

The synthetic route to chemosensors (**L1–L4**) were outlined in Scheme 6.1. They were prepared by following the literature method [48] and the structure was characterised by FT-IR, $^{1}$H NMR, $^{13}$C NMR and ESI-MS spectra.

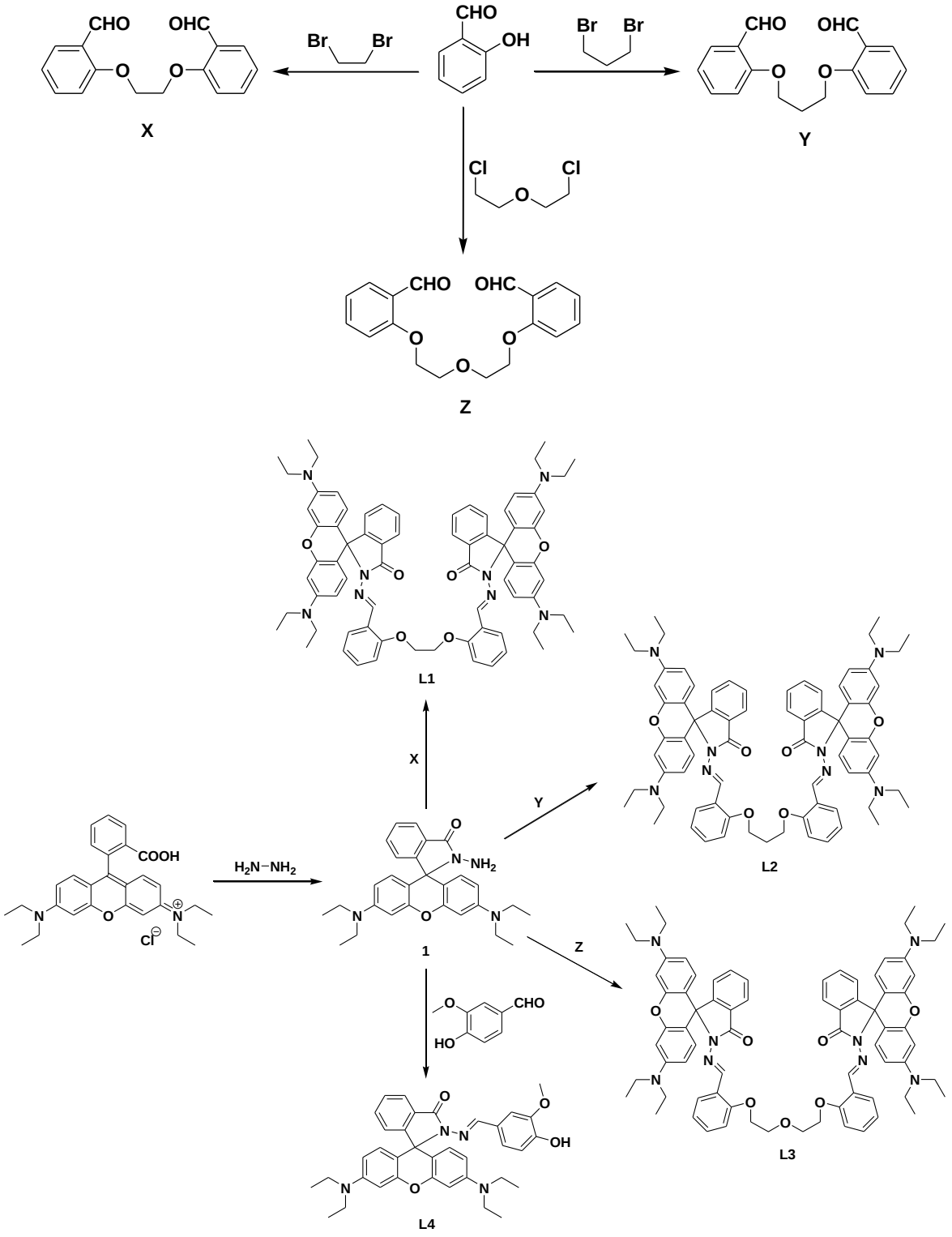


**Scheme 6.1.** Synthetic Pathways of **L1–L4**.

**Compounds X and Y:**

The DMF (20 mL) solution containing the mixture of salicylaldehyde (50 mmol), dibromoalkane (25 mmol) and $K_2CO_3$ (50 mmol) was refluxed at 155 °C in the presence of nitrogen gas about 5−6 hours, then added the crushed ice in to this mixture, the precipitated was filtered and washed with distilled water. It was then dried and recrystallized from EtOH.

**Ethylene-2-2'-(dioxydibenzaldehyde) (X):** Yield: 4.5 g; Color: brown; Mp. 110−112 °C; FT-IR (KBr), ν, $cm^{-1}$: 3074, 2937, 2869 (C−H), 1683 (C=O), 1594, 1450 (C=C), 1243, 1058 (C−O); $^1$H NMR ($CHCl_3$), δ, ppm (*J*, Hz): 4.54 (s, 4H), 7.08 (q, *J*=7.5, 4H), 7.58 (dt, *J*=2.0, 7.5, 2H), 7.85 (dd, *J*=2, 7.5, 2H), 10.44 (s, 2H).

**Propylene-2-2'-(dioxydibenzaldehyde) (Y):** Yield: 3.2 g; Color: light brown; Mp. 70−72 °C; FT-IR (KBr), ν, $cm^{-1}$: 3075, 2949, 2883 (C−H), 1682 (C=O), 1596, 1458 (C=C), 1242, 1052 (C−O); $^1$H NMR ($CDCl_3$, 500 MHz), δ (ppm): 2.43 (qn, *J*= 6.0, 2H), 4.33 (t, *J*=6.0, 4H), 7.03 (q, *J* = 8.5, 4H), 7.55 (dt, *J* = 2.0, 7.5, 2H), 7.83 (dd, *J* = 2.0, 7.5, 2H), 10.50 (s, 2H).

**Compound Z:**

The aza crown ethers were synthesized according to Scheme 6.1, salicylaldehyde was reacted with 2,2′-dichloro ethyl ether in dimethyl sulfoxide under nitrogen to give 1,7-Bis(2′-formylphenyl)-1,4,7-trioxa heptanes (**Z**). Mp. 74 °C; $^1$H NMR ($CDCl_3$, 500 MHz), δ (ppm): 4.00 (t, *J* = 4.5, 4H); 4.28 (t, *J* = 4.5, 4H); 7.00 (d, *J* = 8.5, 2H); 7.05 (t, *J* = 7.5, 2H); 7.52 (dt, *J* = 2.0, 7.5, 2H); 7.83 (dd, *J* = 2.0, 8.0, 2H); 10.50 (2H, s).

**Compound 1:**

Rhodamine B (2.0 g) was dissolved in 50 mL ethanol. Hydrazine hydrate (2.5 ml) was then added drop wise with vigorous stirring at room temperature. After the addition, the stirred solution was allowed to reflux about 6–8 h. The solution changed from dark pink to light orange. Then the mixture was cooled and solvent was removed under reduced pressure. 1 M HCl (about 50 mL) was added to the mixture in the flask to generate a clear red solution. After that, 1 M NaOH was added slowly with stirring until the pH of the solution reached 9–10. The resulting precipitate was filtered and washed 4–5 times with 15 mL water. After drying under reduced pressure, the reaction yielded 1.8 g **1** (95%) as pink solid. Mp: 176–178 °C; FT-IR (KBr), *ν*, $cm^{-1}$: 1614 (C=O), 1379, 1118 (C−N), 1224, 1015 (C−O); $^1$H NMR ($CDCl_3$, 500 MHz), *δ* (ppm): 1.16 (12H, t, *J* = 6.5 Hz), 3.34 (8H, d, *J* = 6.5 Hz), 3.62 (2H, s), 6.29 (2H, d, *J* = 7.5 Hz), 6.42–6.47 (4H, m), 7.11 (1H, s), 7.45 (2H, s), 7.93 (1H, s); $^{13}$C

NMR ($CDCl_3$, 500 MHz), $\delta$ (ppm): 12.6, 44.4, 65.9, 98.0, 104.6, 108.1, 123.0, 123.8, 128.1, 130.0, 132.5, 148.9, 151.5, 153.8, 166.1. ESI-MS *m/z*: Calcd for $C_{28}H_{32}N_4O_2$ $(M+H)^+$: 457.2604, found: 457.2500.

**Compounds L1–L3:**

Rhodamine hydrazide (**1**, 0.23 g, 0.5 mmol) and dialdehyde (**X**, **Y** and **Z**) (0.25 mmol) were dissolved in 20 mL absolute ethanol and the reaction mixture was refluxed overnight. Obtained solid was filtered and washed 3 times with 10 mL ethanol. The product was dried in vacuum, affording a pink solid of **L1**–**L3**, respectively.

**Compound L1:** Yield: 0.14 g (48%); Mp: 187–189 °C; FT-IR (KBr), *v*, $cm^{-1}$: 1616 (C=O), 1309, 1116 (C−N), 1226 (C−O); $^1$H NMR ($CDCl_3$, 500 MHz), $\delta$ (ppm): 1.04 (24H, t, *J* = 6.5 Hz), 3.20 (16H, s), 4.18 (4H, s), 6.22 (4H, d, *J* = 8.5 Hz), 6.39 (4H, s), 6.54 (4H, d, *J* = 8.5 Hz), 6.95 (2H, t, *J* = 7.5 Hz), 7.00 (2H, d, *J* = 8.5 Hz), 7.07 (2H, d, *J* = 6.5 Hz), 7.31 (2H, t, *J* = 7.5 Hz), 7.46 (4H, qn, *J* = 7.0 Hz), 8.01 (4H, d, *J* = 7.0 Hz), 8.69 (2H, s); $^{13}$C NMR ($CDCl_3$, 500 MHz), $\delta$ (ppm): 12.5, 44.2, 65.5, 66.2, 97.8, 105.6, 108.1, 112.3, 121.2, 123.4, 123.7, 124.2, 126.4, 128.1, 128.2, 128.6, 130.8, 133.3, 141.4, 148.9, 152.5, 152.8, 157.0, 165.1. ESI-MS *m/z*: Calcd for $C_{72}H_{74}N_8O_6$ $(M+Na)^+$: 1169.5629, found: 1169.5682.

**Compound L2:** Yield: 0.17 g (58%); Mp: 156–158 °C; FT-IR (KBr), *v*, $cm^{-1}$: 1614 (C=O), 1306, 1112 (C−N), 1227 (C−O); $^1$H NMR ($CDCl_3$, 500 MHz), $\delta$ (ppm): 1.09 (24H, t, *J* = 6.5 Hz), 2.05 (2H, s), 3.25 (16H, d, *J* = 7.0 Hz), 3.99 (4H, s), 6.23 (4H, d, *J* = 8.0 Hz), 6.41 (4H, s), 6.56 (4H, d, *J* = 8.0 Hz), 6.86 (4H, d, *J* = 8.0 Hz), 7.07 (2H, d, *J* = 7.0 Hz), 7.21 (2H, t, *J* = 7.0 Hz), 7.44 (4H, t, *J* = 7.0 Hz), 7.93 (2H, d, *J* = 7.5 Hz), 7.99 (2H, d, *J* = 6.5 Hz), 8.80 (2H, s); $^{13}$C NMR ($CDCl_3$, 500 MHz), $\delta$ (ppm): 12.6, 29.5, 44.2, 64.8, 65.6, 98.0, 106.0, 108.1, 112.0, 120.6, 123.4, 123.6, 124.0, 126.5, 127.8, 128.1, 128.6, 130.7, 133.2, 142.6, 148.9, 152.4, 152.8, 157.5, 165.2. ESI-MS *m/z*: Calcd for $C_{73}H_{76}N_8O_6Na^+$ $(M+Na)^+$: 1183.5786, found: 1183.5770.

**Compound L3:** Yield: 0.18 g (60%); Mp: 224–226 °C; FT-IR (KBr), *v*, $cm^{-1}$: 1614 (C=O), 1303, 1115 (C−N), 1227 (C−O); $^1$H NMR ($CDCl_3$, 500 MHz), $\delta$ (ppm): 1.12 (24H, t, *J* = 6.5 Hz), 3.28 (16H, d, *J* = 7.0 Hz), 3.83 (4H, s), 4.01 (4H, s), 6.22 (4H, d, *J* = 8.5 Hz), 6.43 (4H, s), 6.54 (4H, d, *J* = 9.0 Hz), 6.77 (2H, d, *J* = 8.0 Hz), 6.85 (2H, d, *J* = 7.5 Hz), 7.10–7.16 (4H, m), 7.46 (4H, qn, *J* = 7.5 Hz), 7.84 (2H, d, *J* = 7.5 Hz), 7.97 (2H, d, *J* = 7.0 Hz), 9.06 (2H, s); $^{13}$C NMR ($CDCl_3$, 500 MHz), $\delta$ (ppm): 12.6, 44.3, 65.9, 68.3, 69.7, 98.0, 106.3, 108.0, 113.0, 121.0, 123.3, 123.8, 124.5, 126.3, 127.9, 128.1, 129.4, 130.8, 133.1, 143.8,

148.8, 151.9, 153.2, 157.4, 164.8. ESI-MS *m/z*: Calcd for $C_{74}H_{78}N_8O_7$ $(M+Na)^+$: 1213.5891, found: 1213.5852.

**Compound L4:**

Compound **1** (0.23 g, 0.5 mmol) and vanillin (0.5 mmol) was dissolved in 20 mL absolute ethanol. The reaction mixture was stirred and refluxed overnight. Obtained solid was filtered and washed 3 times with 10 mL ethanol. After drying under reduced pressure, the reaction yielded 0.15 g **L4** (51%) as pink solid. Mp: 222–224 °C; FT-IR (KBr), *v*, $cm^{-1}$: 1563 (C=O), 1417, 1117 (C−N), 1224, 1022 (C−O); $^1$H NMR ($CDCl_3$, 500 MHz), $\delta$ (ppm): 1.15 (12H, t, *J* = 7.0 Hz), 3.32 (8H, q, *J* = 6.5 Hz), 3.90 (3H, s), 6.24 (2H, d, *J* = 8.0 Hz), 6.42 (2H, s), 6.52 (2H, d, *J* = 9.0 Hz), 6.79 (2H, q, *J* = 8.0 Hz), 7.13 (1H, d, *J* = 6.5 Hz), 7.35 (1H, s), 7.48 (2H, qn, *J* = 7.0 Hz), 7.98 (1H, d, *J* = 6.5 Hz), 8.52 (1H, s); $^{13}$C NMR ($CDCl_3$, 500 MHz), $\delta$ (ppm): 12.6, 44.3, 55.9, 66.1, 97.8, 106.2, 107.6, 108.0, 113.7, 123.2, 123.3, 123.8, 128.0, 128.2, 128.3, 129.6, 133.2, 146.7, 147.1, 147.5, 148.9, 151.6, 153.2, 164.7. ESI-MS *m/z*: Calcd for $C_{36}H_{38}N_4O_4$ $(M+H)^+$: 591.2971, found: 591.2987.

*6.1.2.3. UV-Vis and fluorescence spectra measurements*

Stock solutions of $1 \times 10^{-3}$ M various metal ions and receptors were prepared in methanol and MeOH−DMSO (99:1 v/v), respectively. The solutions were then diluted to $1 \times 10^{-4}$ M with MeOH solvent. All absorption and emission spectra were performed in a quartz optical cell of 1 cm optical path length at room temperature. During experiments with metal ions, the concentration of each component inside the cuvette is maintained at 50 μM. In titration experiments with an increasing amount of $Al^{3+}$, each time the solution of probes was maintained at 50 μM. All fluorescence measurements were carried out using excitation at 520 nm, and emission was recorded from 535 to 700 nm. Both excitation and emission slit widths were 0.5 nm.

**6.1.3. Results and discussion**

The selectivity, sensitivity and binding mode of chemosensor toward $Al^{3+}$ were examined through visual inspection, absorption, emission, ESI-MS, electrochemical (DPV), $^1$H NMR, FT-IR and DFT experiments.

*6.1.3.1. UV-Vis spectroscopic studies*

The interaction of the probes with various guest species such as $Al^{3+}$, $Ba^{2+}$, $Ca^{2+}$, $Cd^{2+}$, $Co^{2+}$, $Cr^{3+}$, $Cs^+$, $Cu^{2+}$, $Fe^{2+}$, $Fe^{3+}$, $Gd^{3+}$, $Hg^{2+}$, $K^+$, $Li^+$, $Mg^{2+}$, $Mn^{2+}$, $Na^+$, $Nd^{3+}$, $Ni^{2+}$, $Pb^{2+}$, $Sr^{2+}$ and $Zn^{2+}$ was established by UV-Vis absorption spectroscopic analysis. As

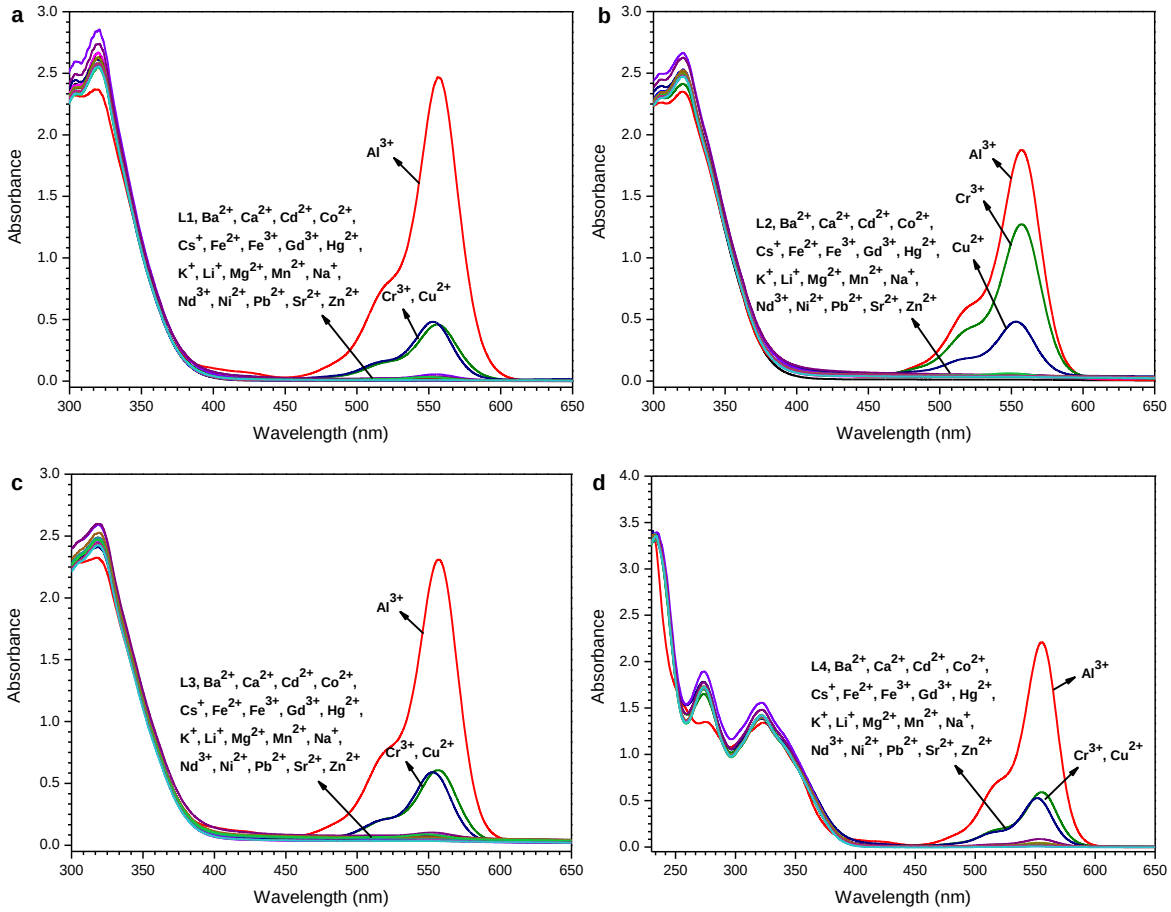


**Figure 6.1.** Absorbance spectra of **L1** (a), **L2** (b), **L3** (c) and **L4** (d) (50 µM) in presence of various metal ions (50 µM) in MeOH−DMSO (99:1 v/v).

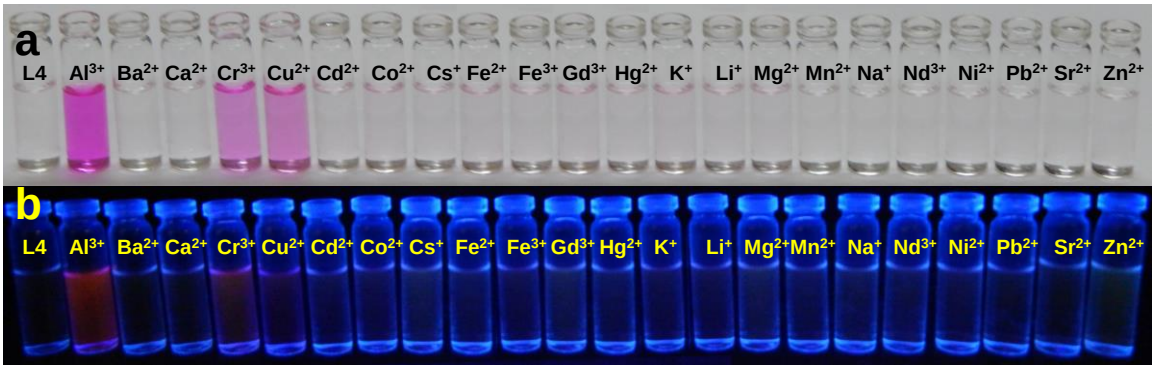


**Figure 6.2.** Photographs of **L4** (50 µM) upon addition of 1 equiv. of various metal ions in MeOH−DMSO (99:1 v/v) taken in room light (a) and under UV light (b).

observed in Figure 6.1, the UV-Vis spectrum of receptors in methanolic solvent show main bands in the range 250–400 nm. The $Al^{3+}$ addition products of probes in the same solvent exhibited a strong absorption band at ~555 nm with a shoulder at ~517 nm was appeared. On the other hand, a weak absorption band at 555 nm was noticed with $Cr^{3+}$ and $Cu^{2+}$, while no peak appeared at this region with other metal ions even in excess. The instant color change

was observed upon addition of metal ions tested were photographed and shown in Figure 6.2a. The development of the observable naked-eye detection of the pink color in the probe due to spirolactam ring opening induced by strong binding of the metal ions [49].

Upon an increase in the concentration of $Al^{3+}$ (0–2 equiv.), an increase in the absorbance band centered at 555 nm with a shoulder at ~517 nm was observed (Figure 6.3), implicating the formation of an **L**-$Al^{3+}$ ensembles. Simultaneously, the bands centered at 273 and 322 nm of free ligand (**L4**) decreased, while bands centered at 254 and 296 nm gradually increased with the concentration of $Al^{3+}$. The 1 : 1 stoichiometry of the **L4**-$Al^{3+}$ complex was established from the measurements of absorbance as a function of $Al^{3+}$ concentration (Figure 6.3, inset), where a clear bend of the curve can be observed when $Al^{3+}$ was 1 equivalent (50 µM).

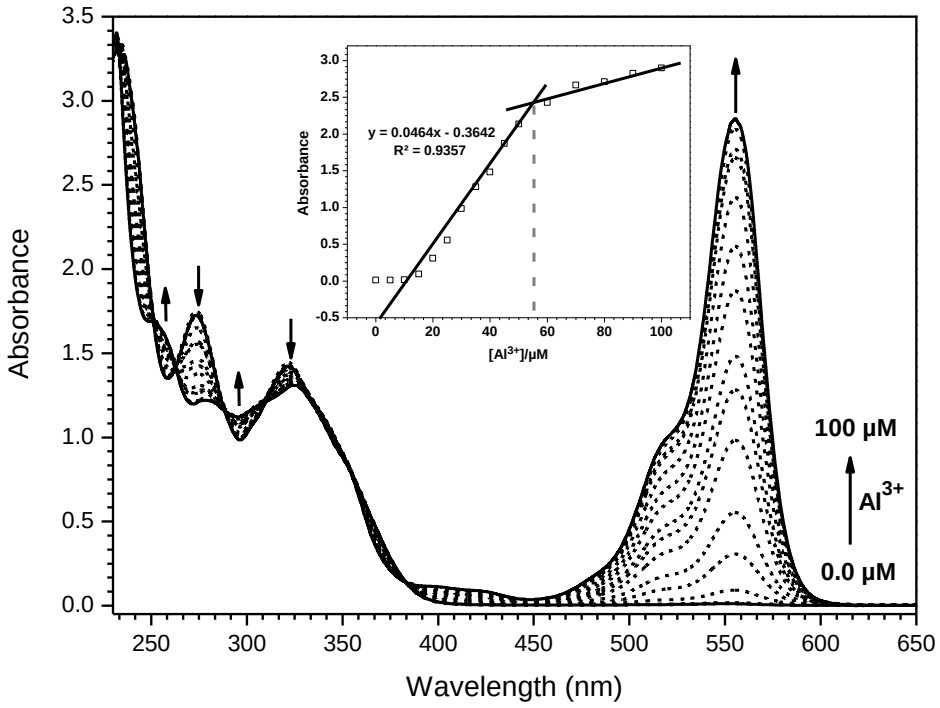


**Figure 6.3.** UV-Visible absorbance spectrum changes of sensor **L4** (50 µM) at increasing concentration of $Al^{3+}$ (0, 5, 10, 15, 20, 25, 30, 35, 40, 45, 50, 60, 70, 80, 90, 100 µM). Inset: The plot of absorbance of **L4** at $\lambda_{max}$ of 555 nm as a function of concentration of $Al^{3+}$ added.

*6.1.3.2. Fluorescence spectroscopic studies*

The emission spectra of probes were recorded in the absence and presence of various metal ions, as mentioned for UV-Vis spectroscopic studies, upon excitation of 520 nm. Initially, sensor did not show any emission band, indicating that the spirocyclic form was retained in the solution. However, addition of $Al^{3+}$ to this solution induced a significant increase in the fluorescence response (Figure 6.4). A strong new emission band at 587 nm

was formed, and up to about 15–20-fold enhancement in the fluorescence intensity was noted, indicating that the $Al^{3+}$ ions induced the formation of the strongly fluorescent, ring-opened **L**–$Al^{3+}$ complex. The spectral change is also accompanied by a visual color change from colorless to fluorescent pink (Figure 6.2b). Other cations did not cause any significant change under the same conditions, except for $Cr^{3+}$ and $Cu^{2+}$, which resulted in small fluorescence intensity changes.

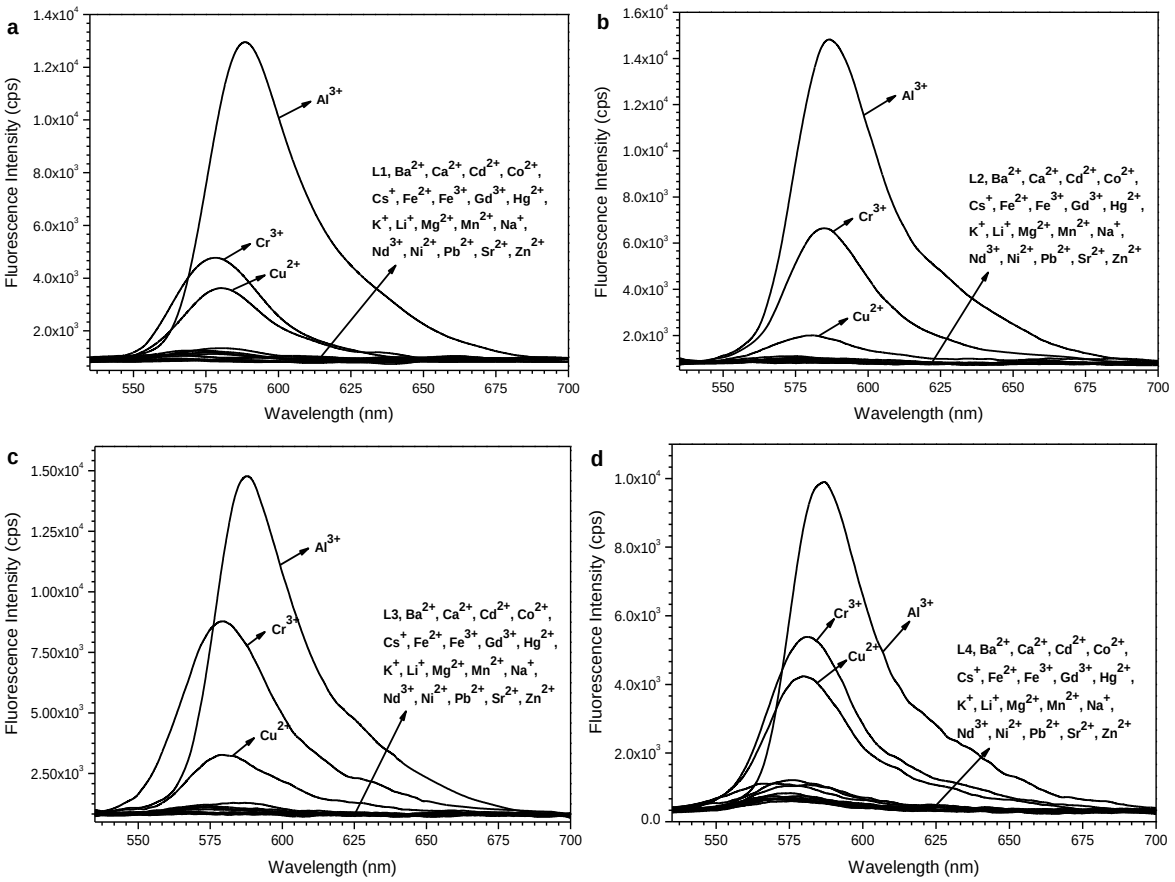


**Figure 6.4.** Fluorescence spectra ($\lambda_{ex}$ = 520 nm) of **L1** (a), **L2** (b), **L3** (c) and **L4** (d) (50 μM) in presence of various metal ions (50 μM) in MeOH−DMSO (99:1 v/v).

To gain an insight into the sensing properties of ligands as a receptor for $Al^{3+}$, a titration experiment was carried out with the gradual addition of $Al^{3+}$ to the solutions of free ligand. As shown in Figure 6.5, a gradual fluorescence enhancement associated with a red shift at 587 nm of sensor was observed upon progressive addition of $Al^{3+}$ ion. The sensor showed a nice linear relationship between the fluorescence intensity at 587 nm and the concentration of $Al^{3+}$ from 0.0 to 50 μM (Figure 6.5, bottom inset), suggests that the proposed sensors are potentially applicable for quantitative analysis of $Al^{3+}$ with a large dynamic range. No further significant changes in the emission intensity of the system were observed at above 50 μM (1 equiv.) of $Al^{3+}$ ion. Binding constant indicates the strength of

complex of metal to ligand. For this, the binding constant (Ka) for the formation of the $Al^{3+}$ complexes with **L1–L4** was estimated on account of the change in the fluorescence intensity at 587 nm by considering a 1 : 1 binding stoichiometry and found to be $5.7\times10^3$ $M^{-1}$, $1.6\times10^4$ $M^{-1}$, $1.9\times10^4$ $M^{-1}$ and $1.0 \times 10^4$ $M^{-1}$ using Benesi-Hildebrand equation (Figure 6.5, top inset). Also, the detection limit of $Al^{3+}$ ion was determined from the fluorescence titration profile as $6.0\times10^{-7}$ M (for **L1**), $5.8\times10^{-7}$ M (for **L2**), $5.0\times10^{-7}$ M (for **L3**) and $1.4 \times 10^{-7}$ M (for **L4**) based on 3σ/slope.

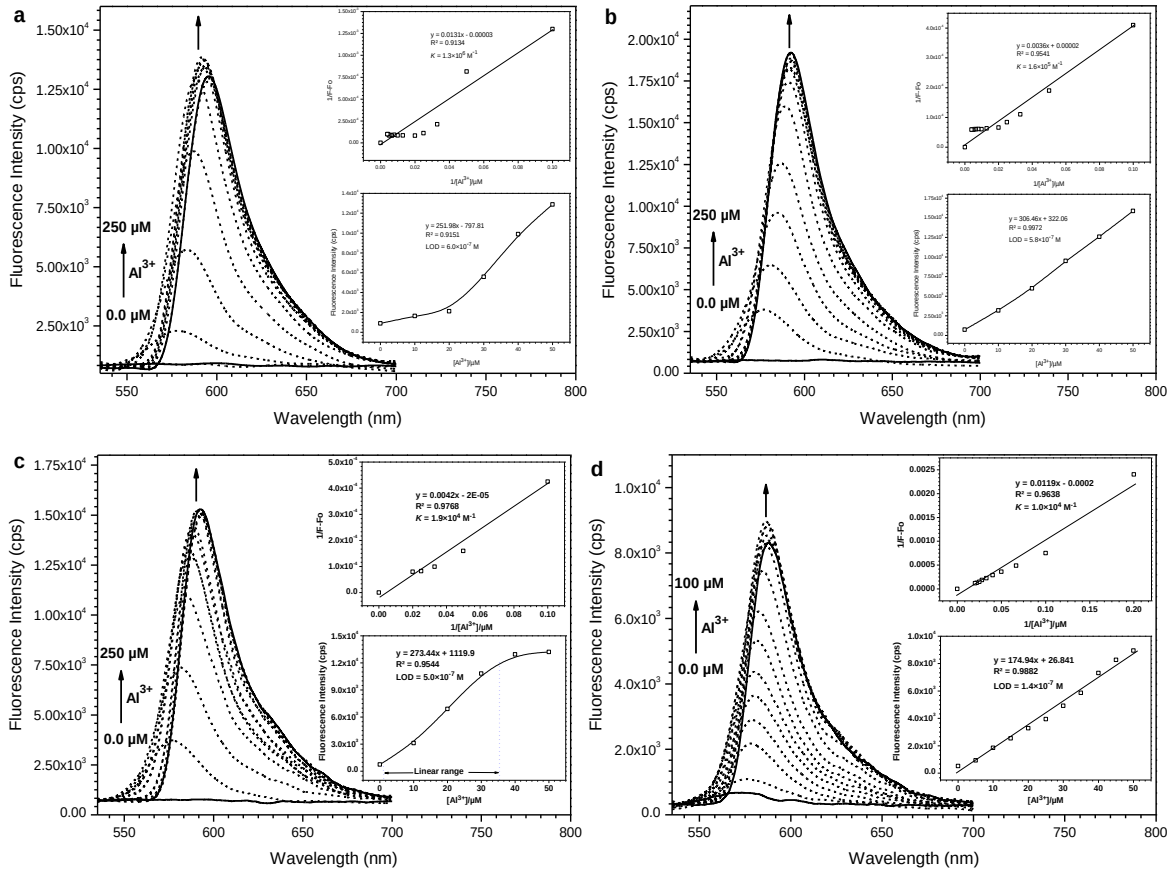


**Figure 6.5.** The fluorescence emission spectral pattern of **L1** (a), **L2** (b), **L3** (c) and **L4** (d) in the presence of increasing concentrations of $Al^{3+}$. Inset: Linear regression plot of fluorescence intensity change $1/(F\text{-}F_0)$ as a function of concentration $1/[Al^{3+}]$ (top), fluorescence enhancement change at $\lambda_{max}$ of 587 nm as a function of concentration of Al(III) added (bottom).

*6.1.3.3. Stoichiometry determination*

The binding stoichiometry of probes towards $Al^{3+}$ was achieved from the Job's method on the basis of absorbance and fluorescence. In which, Job's plot was produced by continuously varying the mole fraction of $Al^{3+}$ from 0 to 1 in a solution of [**L**] + $[Al^{3+}]$ with a total concentration of 50 μM. The Job's plot analysis revealed that the mole fraction of $Al^{3+}$ is around 0.5, which indicates a 1 : 1 stoichiometry for the probe–$Al^{3+}$ complex (Figure

6.6). To better understand the binding mode of probes with $Al^{3+}$, ESI mass spectra was performed (Figure 6.7). Observed mass peak at *m*/*z* 1173.5524, 1187.5739, 1217.5821 and 741.2480 corresponding to [**L1** + Al]$^+$ , [**L2** + Al]$^+$, [**L3** + Al]$^+$ and [**L4** + $Al^{3+}$ + $2NO_3$]$^+$, respectively. The mass data therefore confirmed the binding of $Al^{3+}$ to probe with 1 : 1 stoichiometry.

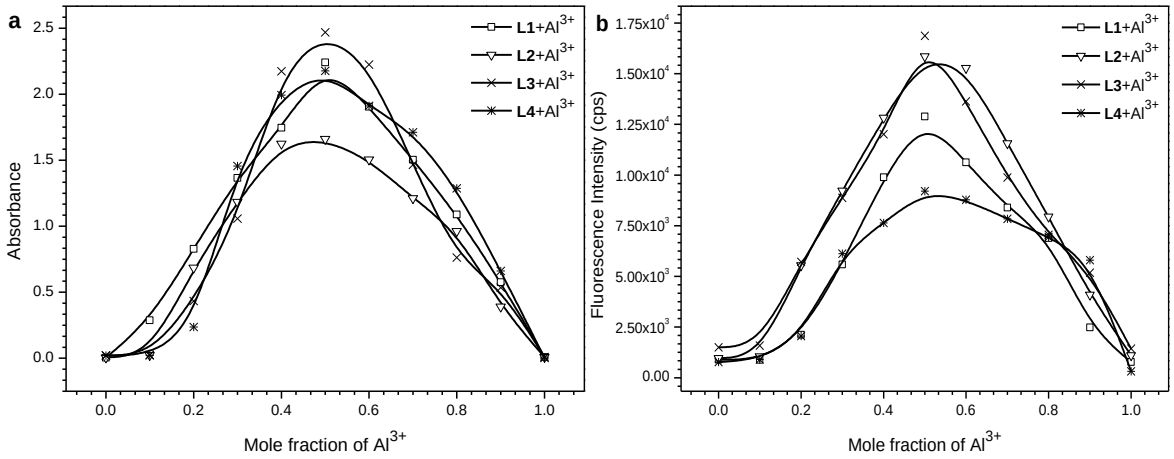


**Figure 6.6.** Job plots for the binding of $Al^{3+}$ with **L**, where absorbance (a) and fluorescence (b) intensities at $\lambda_{max}$ of 555 nm and 575 nm, respectively were plotted against the mole fraction of $Al^{3+}$.

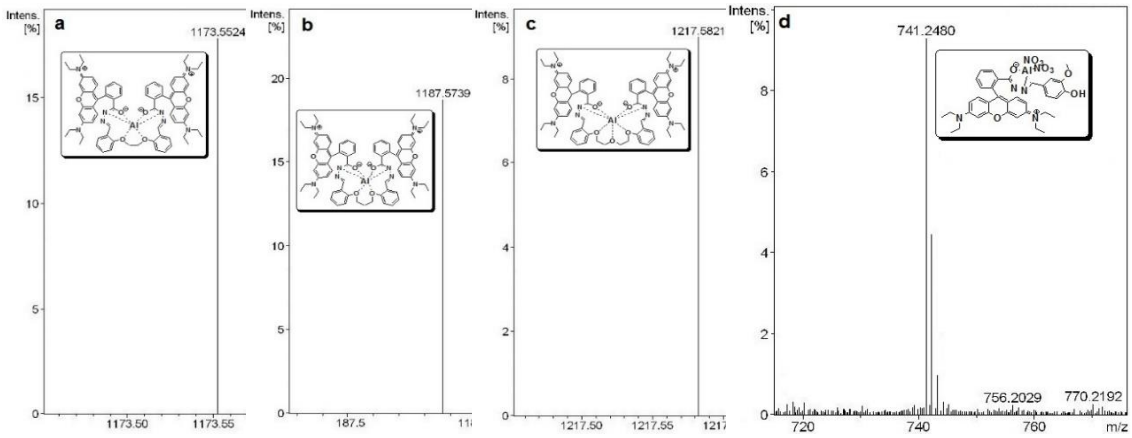


**Figure 6.7.** ESI-MS of probes upon addition of $Al(NO_3)_3.9H_2O$ (1.0 equiv.) in MeOH.

*6.1.3.4. pH effect*

The effect of pH on the absorbance and emission response of $Al^{3+}$ complexes was investigated in MeOH. The absorbance (at 555 nm) and fluorescence (at 587 nm) intensities of probes in the presence and absence of $Al^{3+}$ at different pH values (2.0–10.0) were recorded (Figure 6.8). Probes and its $Al^{3+}$ complex did not produce any distinct and characteristic absorbance and fluorescence in basic pH range, which indicated that the spirolactam form

of probe was the predominant species. When the pH was adjusted to acidic (2.0–5.0), obvious enhancement in the absorbance and fluorescence was observed due to the ring-opening process of the spirocyclic moiety of rhodamine B. This indicated that the complex was dissociated at acidic conditions and converted in its metal free fluorescent open-ring form. So these conditions are not suitable for $Al^{3+}$ detection. The absorbance and emission of probes and the corresponding $Al^{3+}$ complex were varied at neutral pH of methanol. Also, the color changes at different pH could easily be detected by the naked-eye (Figure 6.9).

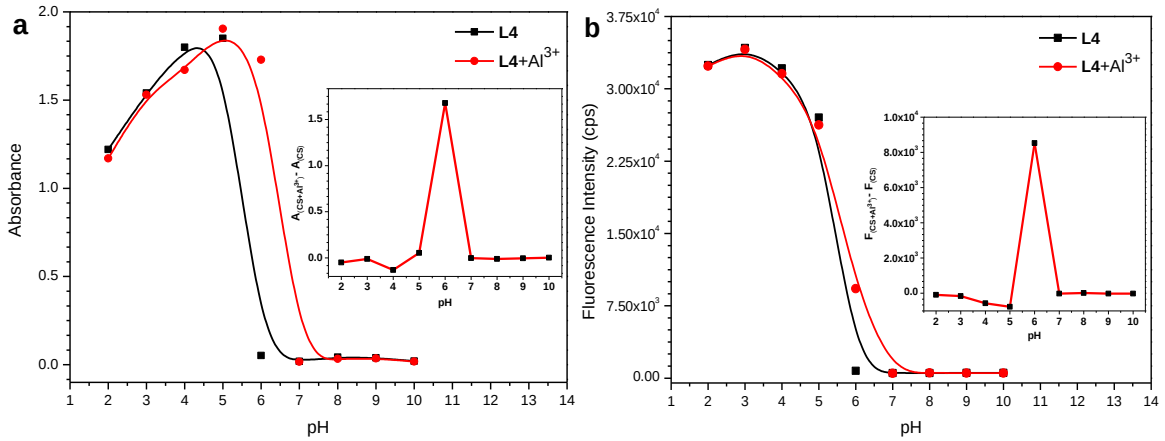


**Figure 6.8.** UV-Vis absorbance (at $\lambda_{max}$ = 555 nm) and fluorescence emission (at $\lambda_{max}$ = 587 nm) spectral changes of **L4** and **L4**–$Al^{3+}$ complex with pH variations.

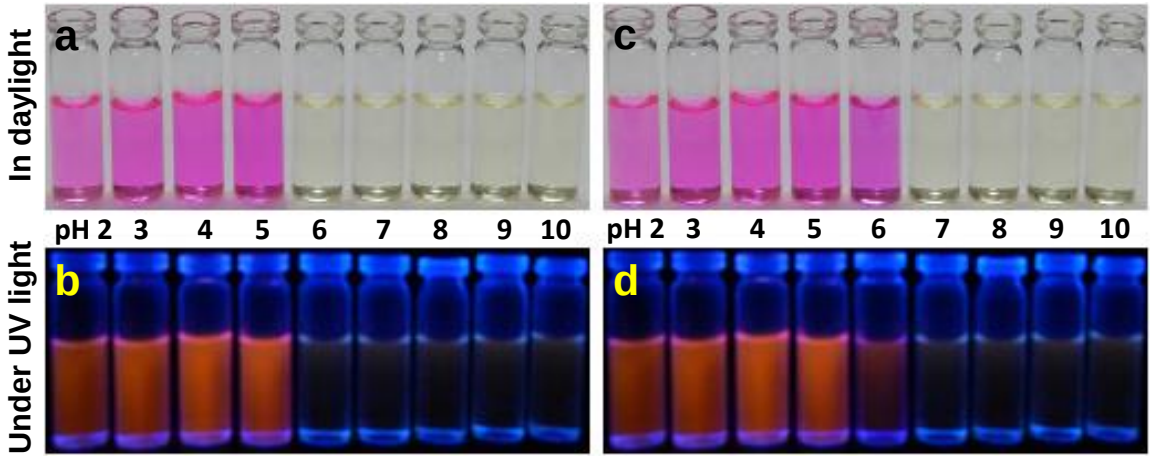


**Figure 6.9.** Photographs of **L4** in the absence (a, b) and presence (c, d) of $Al^{3+}$ in different pH conditions under daylight and UV light.

*6.1.3.5. Competitive selectivity over other metal ions*

To further estimate the selectivity of sensors for $Al^{3+}$, the competitive experiment in the presence of other metal ions including $Ba^{2+}$, $Ca^{2+}$, $Cd^{2+}$, $Co^{2+}$, $Cr^{3+}$, $Cs^{+}$, $Cu^{2+}$, $Fe^{2+}$, $Fe^{3+}$, $Gd^{3+}$, $Hg^{2+}$, $K^{+}$, $Li^{+}$, $Mg^{2+}$, $Mn^{2+}$, $Na^{+}$, $Nd^{3+}$, $Ni^{2+}$, $Pb^{2+}$, $Sr^{2+}$ and $Zn^{2+}$ under the same

conditions was conducted (Figure 6.10). It is noticeable that the competitive metal ions (except $Cr^{3+}$ and $Cu^{2+}$) did not lead to any significant changes in the fluorescence intensities of the **L**–$Al^{3+}$ complex when compared with the results obtained in the presence or absence of other metal ions, while $Cr^{3+}$ and $Cu^{2+}$ affect the Al(III)-induced fluorescence response. The distinct selectivity for $Al^{3+}$ ions is probably due to a combination of several factors, such as the suitable coordination geometry conformation of ligand and the ionic radius of the aluminum. This experiment established that the presence of other metal ions does not interfere with the detection of $Al^{3+}$ and it could be used as a selective chemosensor for $Al^{3+}$.

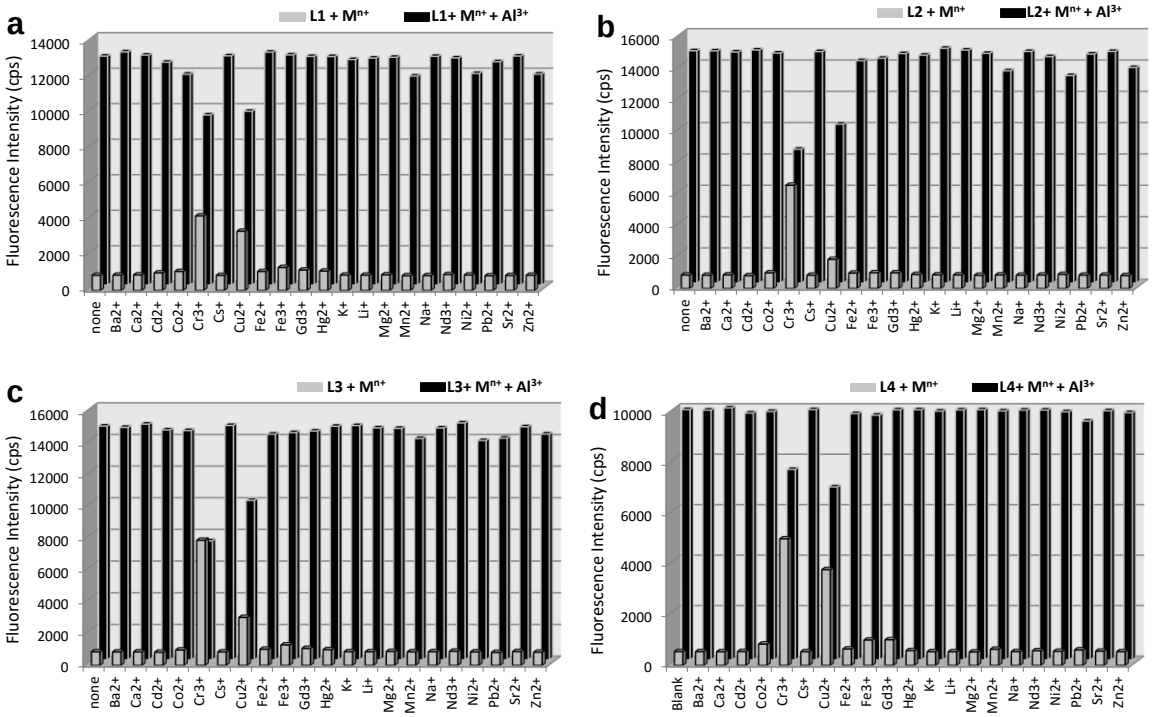


**Figure 6.10.** Competitive selectivity of probes **L1** (a), **L2** (b), **L3** (c) and **L4** (d) toward various metal ions (1.0 equiv.) in the absence (grey) and presence (black) of $Al^{3+}$ (1.0 equiv.) with an excitation of 520 nm.

*6.1.3.6. $^1$H NMR titration*

Furthermore, to better understand the interaction between probe **L3** and $Al^{3+}$, proton NMR titration experiment was performed in the presence of various amounts of $Al^{3+}$ in a DMSO-d6+$CD_3OD$ solvent (Figure 6.11). Upon complexation with $Al^{3+}$ ion, the signal of imine proton ($H_h$) of Schiff base moiety at 8.82 ppm steadily disappeared. Both doublet and triplet of $H_j$ and $H_l$, respectively, were shifted upfield then they were combined with each other and gave a simple multiplet at about 6.8 ppm, while a combine signal of $H_b$, $H_d$ and $H_i$ was splitted into two signals of $H_i$ and a combine signal of $H_b$ and $H_d$. The distance between

two signals of $H_c$ and $H_k$ of fluoroionophore **L3** is also varied upon addition of $Al^{3+}$. Similarly the signals of aryl-protons $H_e$, $H_f$ and $H_g$ of rhodamine moiety were come together then gave a typical complex signal. Other aryl-proton ($H_a$) of rhodamine moiety was also shifted slightly downfield because the strong coordination between **L3** and $Al^{3+}$ ion.

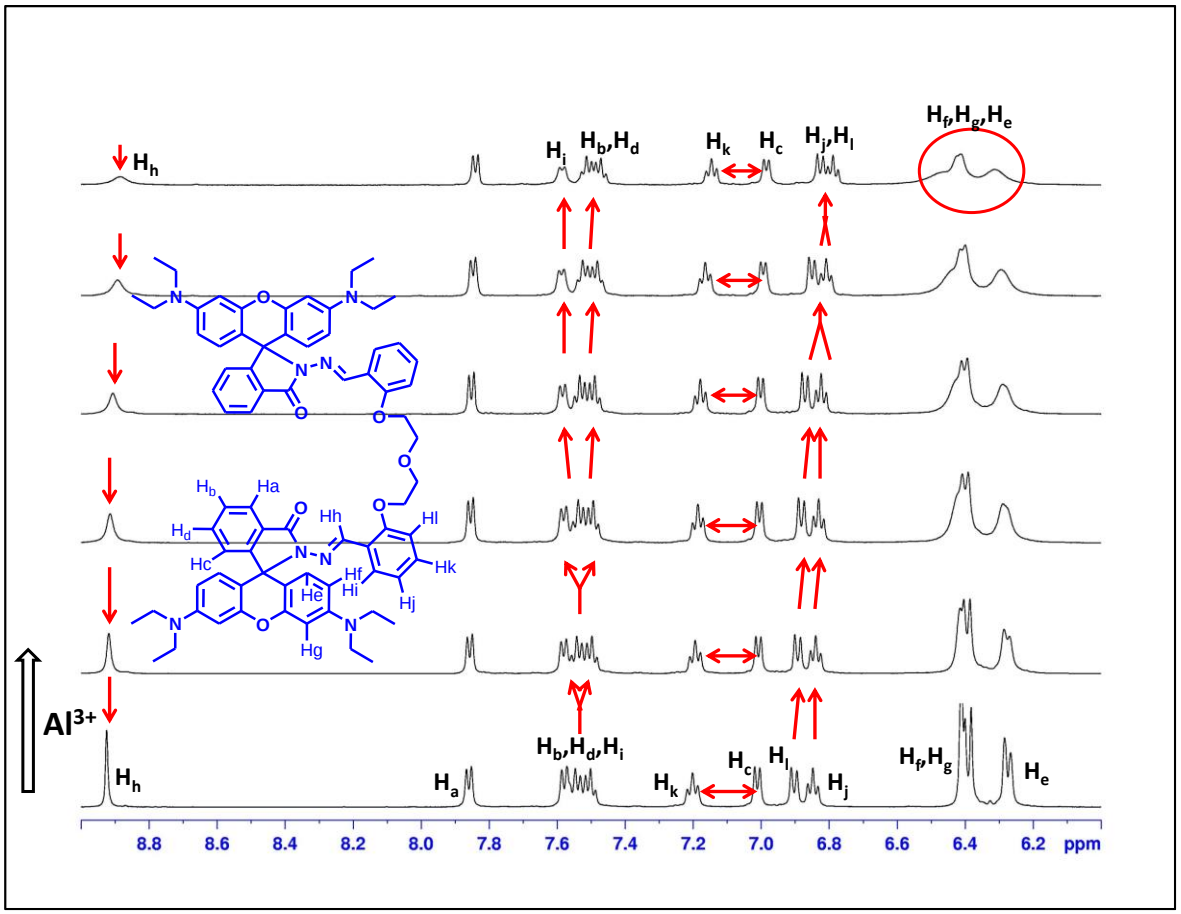


**Figure 6.11.** $^1$H NMR titration of **L3** with $Al^{3+}$ in DMSO-d6+$CD_3OD$.

*6.1.3.7. FT-IR spectral behavior*

FT-IR spectra of probe and its complex with metal ion is recorded to further examine the binding site (Figure 6.12). In complex, the newly formed band at 829 $cm^{-1}$ is ascribed to in-plane bending vibration of the $NO_3^-$ ion. The C–N stretching frequency at 1415 $cm^{-1}$ diminished and a new broad band is generated at this region. The band located at 1558 $cm^{-1}$ is attributed to C=O is completely disappeared in the metal complex. The peak at 1118 $cm^{-1}$ (C–N stretching) is neither disappeared nor shifted but the intensity was largely decreased. All the above discussed changes in the FT-IR spectra upon addition of $Al^{3+}$ metal ion confirmed the involvement of sensor in interaction with $Al^{3+}$ ion.

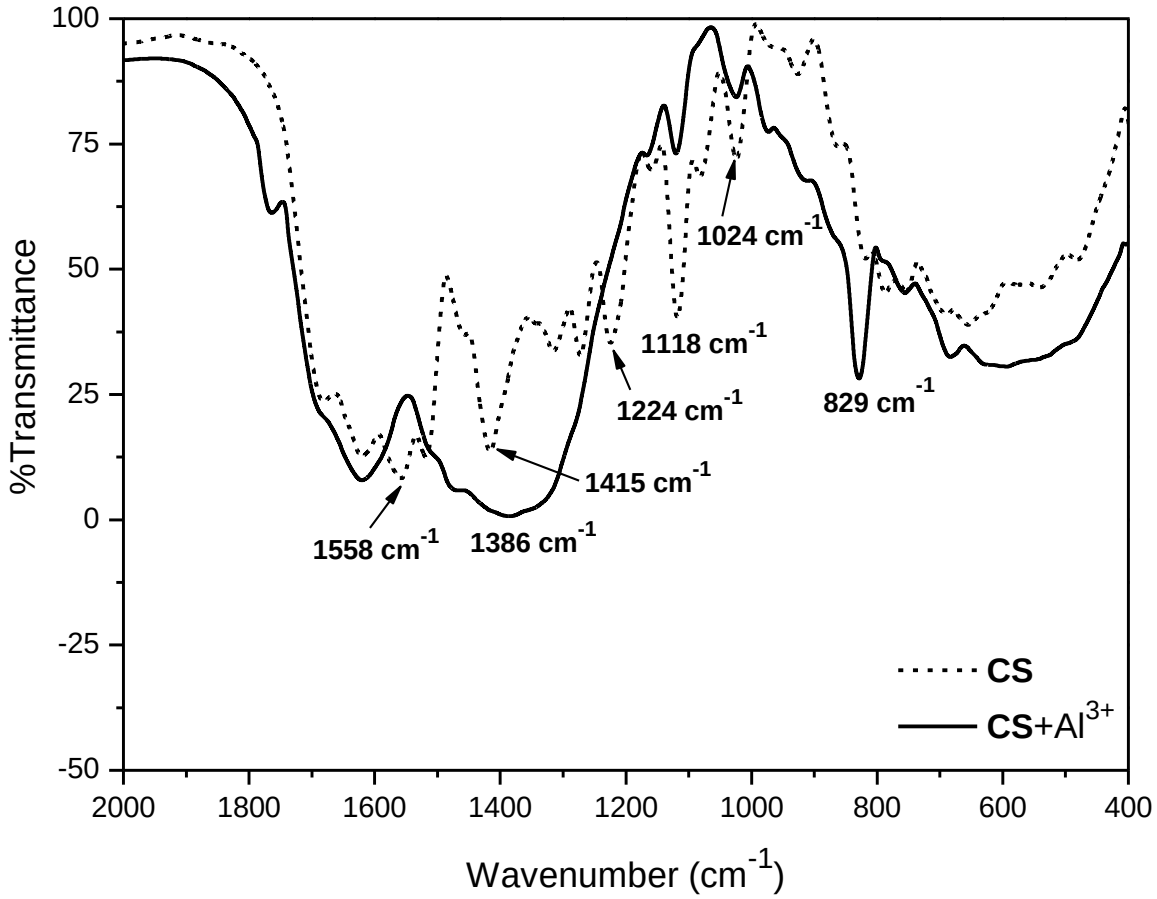


**Figure 6.12.** FT-IR spectra of **L4** in the absence and presence of $Al^{3+}$.

*6.1.3.8. Density functional theory (DFT) calculations*

To better understand the nature of the coordination of $Al^{3+}$ with **L4**, energy-optimized structures of **L4** and **L4**–$Al^{3+}$ (Figure 6.13) were obtained on density functional theory (DFT) calculations at the B3LYP level using 6-31G** basis set for simple receptor (**L4**) and LANL2DZ basis set for metal complex using the Gaussian 09 program [50]. The spatial distributions and orbital energies of the highest occupied molecular orbital (HOMO) and the lowest unoccupied molecular orbital (LUMO) of **L4** and corresponding $Al^{3+}$ complex were also generated using this calculations (Figure 6.13). As results shown, the HOMO is spread over the whole molecule, whereas LUMO is distributed on the substituted spirolactam ring in **L4**. As result revealed, the spirocyclic C–N bond breaks to facilitate the binding of $Al^{3+}$ ion with the carbonyl oxygen atom of ligand. In **L4**–$Al^{3+}$ complex, the π electrons of HOMO are mainly located on the xanthene portion and the LUMO is mostly spread over the spirolactam ring. The energy gaps between the HOMO and LUMO of the probe and corresponding $Al^{3+}$ complex were found to be 3.802 eV and 0.831 eV, respectively. The results exhibited that the binding of $Al^{3+}$ to probe lowered the HOMO−LUMO energy gap and reduction in the energy gap can explain the red-shift of the

emission spectra of the $Al^{3+}$ complex over **L4**. Thus, they show a favourable complexation according to proposed coordination.

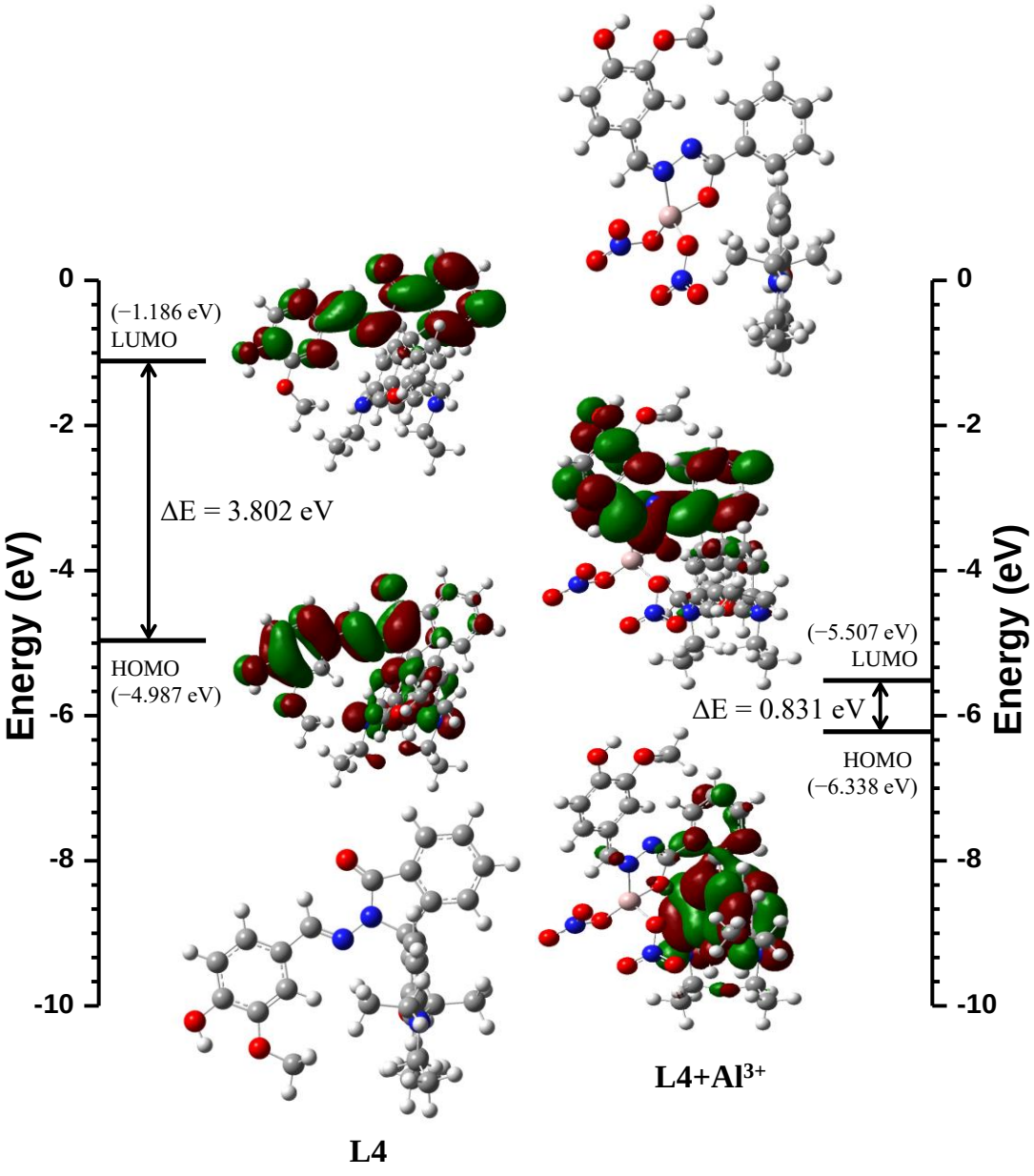


**Figure 6.13.** Optimized proposed structures and HOMO-LUMO orbital energy diagram of **L4** and its corresponding $Al^{3+}$ complex calculated at the DFT level using a B3LYP/6-31G** basis set.

*6.1.3.9. Reversibility of complexation*

To examine the reversibility of complexation of probe towards Al(III) ion, EDTA titration experiments were performed. Upon addition of EDTA to the solution containing probe (**L3**) and Al(III) diminishes the fluorescence significantly, whereas readdition of Al(III) ion could recover the fluorescence emission signal (Figure 6.14). As results show, it could provide as experimental evidence to support the reversibility of spiro ring-opening and

closing mechanism. The proposed binding mechanism of probe (**L1–L3**) with Al(III) in the presence and absence of EDTA was shown in the Scheme 6.2.

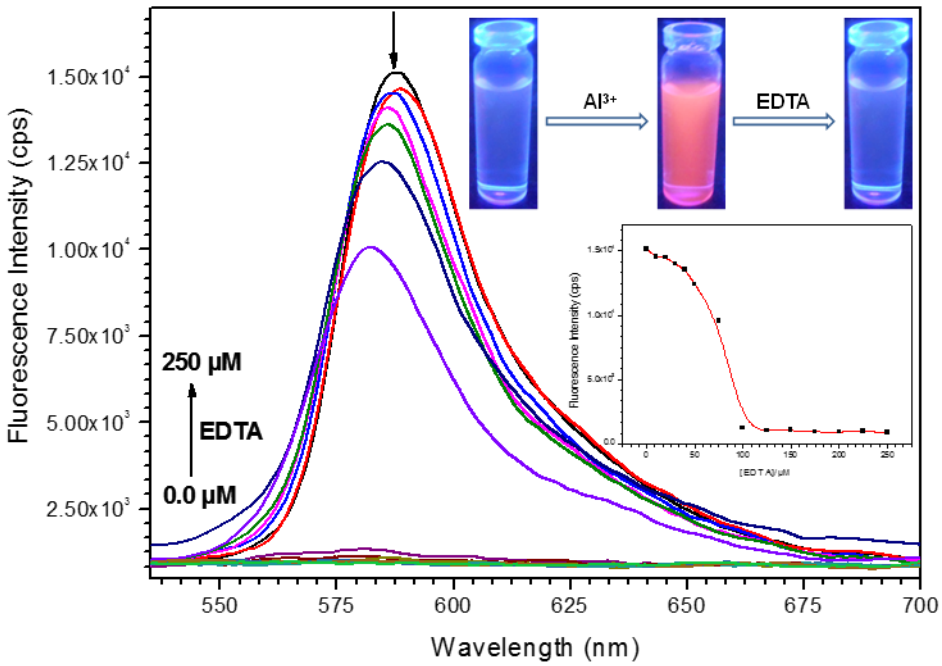


**Figure 6.14.** The fluorescence spectra of **L3**+$Al^{3+}$ upon addition of EDTA. Inset: Color changes of probe upon addition of $Al^{3+}$ and then EDTA (1.0 equiv.) (top), fluorescence spectral changes at 587 nm as a function of the amount of EDTA (bottom).

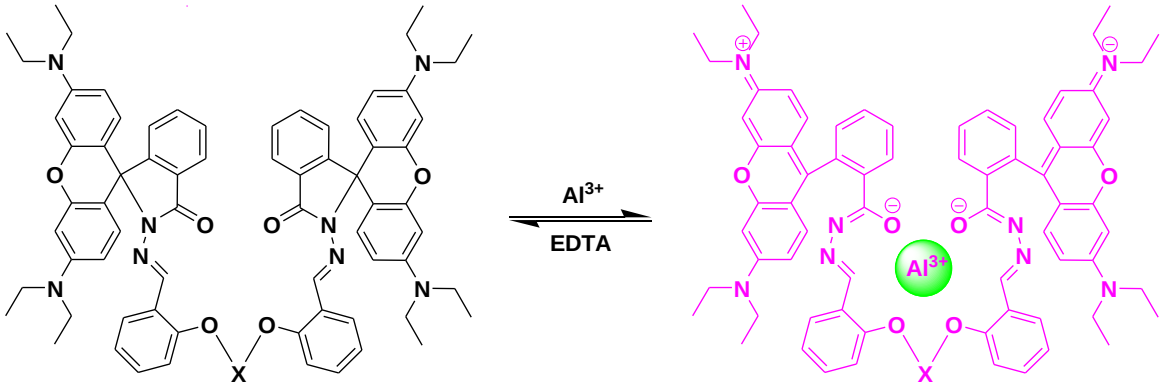


**L1 : X = -$CH_2$-$CH_2$-**

**L2 : X = -$CH_2$-$CH_2$-$CH_2$-**

**L3 : X = -$CH_2$-$CH_2$-O-$CH_2$-$CH_2$-**

**Scheme 6.2.** Proposed binding mechanism of complex in the presence and absence of EDTA.

*6.1.3.10. Detection of $AcO^-$ and $F^-$*

Further, we studied the influence of different anions on the dissociation of the **L4**–$Al^{3+}$ complex to regenerate **L4**. Absorbance and emission spectroscopic studies of the **L4**–

$Al^{3+}$ complex were performed in the presence of sodium salts of various physiological and environmental important anions including $Br^{-}$, $Cl^{-}$, $I^{-}$, $NO_3^{-}$, $SCN^{-}$, $SO_4^{2-}$ and $PO_4^{3-}$. As depicted in Figure 6.15, the significant changes were observed after the addition of 5 equiv. of $AcO^{-}/F^{-}$ to the solution containing the **L4**–Al(III) complex, while other competitive anion species induced negligible spectral changes under the same conditions. Meanwhile, the pink color of **L4**–$Al^{3+}$ solution returned to colorless upon addition of $AcO^{-}/F^{-}$, indicating that **L4**–$Al^{3+}$ ensemble can serve as a 'naked-eye' indicator for $AcO^{-}$ and $F^{-}$ anions (Figure 6.16).

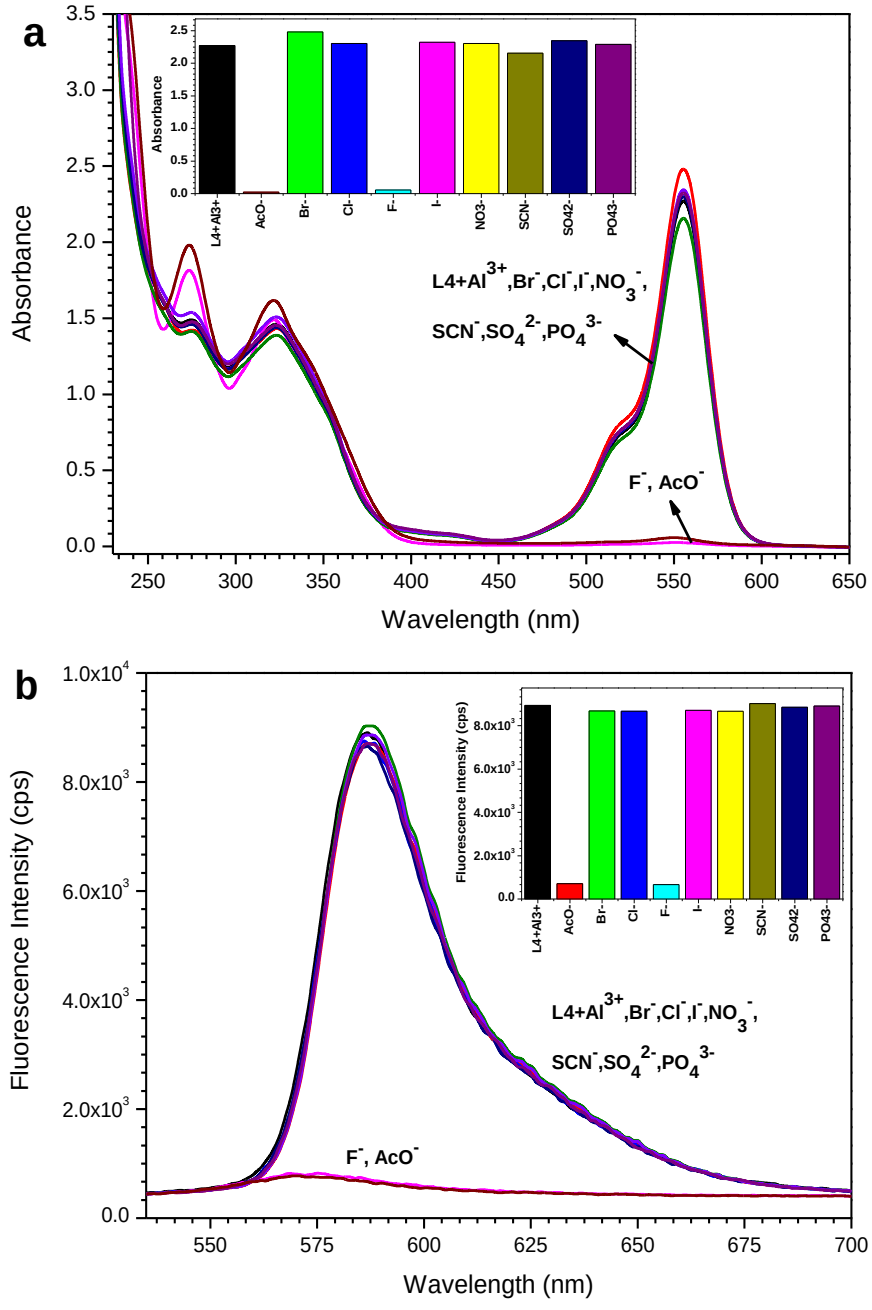


**Figure 6.15.** UV-Vis (a) and fluorescence (b) response of **L4**–$Al^{3+}$ (50 μM) in the presence of various analytes (5 equiv.), such as $AcO^{-}$, $Br^{-}$, $Cl^{-}$, $F^{-}$, $I^{-}$, $NO_3^{-}$, $SCN^{-}$, $SO_4^{2-}$ and $PO_4^{3-}$ in MeOH. Inset: The intensities were recorded at 587 nm.

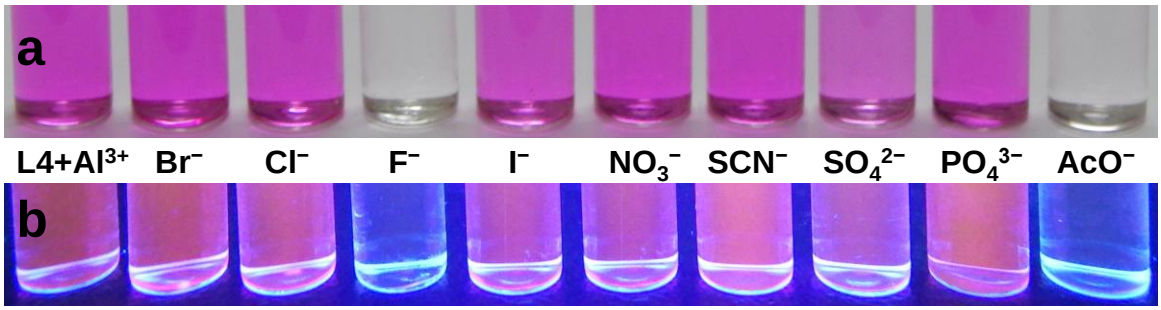


**Figure 6.16.** Photographs of **L4**–$Al^{3+}$ (50 μM) in the presence of various analytes (5 equiv.) were taken in daylight (a) and under UV light (b).

To better understand the property of the **L4**–$Al^{3+}$ complex in the presence of the interfering anions, a solution of **L4** containing 1 equiv. of $Al^{3+}$ was titrated with the gradual amount of anions ($AcO^-$ and $F^-$). The UV-Vis spectral pattern of the titration experiments (Figure 6.17) displayed a reverse trend to the titration curve obtained with $Al^{3+}$ (Figure 6.5d), which may offer evidence of the regeneration of **L4** from the complex in the presence of $AcO^-/F^-$. The fluorescence 'on-off' switching property of **L4**–$Al^{3+}$ ensemble was further examined by fluorescence titration experiments. As shown in Figure 6.17, upon incremental addition of $AcO^-/F^-$, the fluorescence of **L4**–$Al^{3+}$ at 587 nm was gradually recovered and the intensity remains unchanged when 2 equiv. of anion ($AcO^-$ and $F^-$) was added. Thus, the results indicated that probe **L4** was restored during the detection procedure of $AcO^-/F^-$. The relative absorbance and emission intensities of **L4**–$Al^{3+}$ (50 μM) are linearly proportional to the concentration of $AcO^-/F^-$ in the range 0–100 μM. From the fluorescence titration spectral pattern, the detection limit of $AcO^-$ and $F^-$ was found to be $4.3 \times 10^{-7}$ M and $4.36 \times 10^{-7}$ M, respectively based on 3σ/slope (Figure 6.17, inset).

Reversibility and regeneration of sensing probe are important factors in practical applications. As shown in Figure 6.18, the alternate additions of a constant amount of $Al^{3+}$ and $AcO^-/F^-$ to the solution of **L4** gives rise to a switchable change in the fluorescence intensity at 587 nm. Such a reversible fluorescence behavior of **L4** can be repeated several times by the modulation of metal/anion addition, this phenomena exhibited that the anions do not interact directly with the chemosensor. Here, anions bind to metal ions through break the complex to ligand and metal ion. Thus, the sensor **L4** could be used as a reversible fluorescence 'off-on-off' chemosensor for $Al^{3+}$ and $AcO^-/F^-$. These significant changes could be negligible when $Al^{3+}$ is in excess. Their corresponding fluorescence color changes are also shown in Figure 6.18 inset.

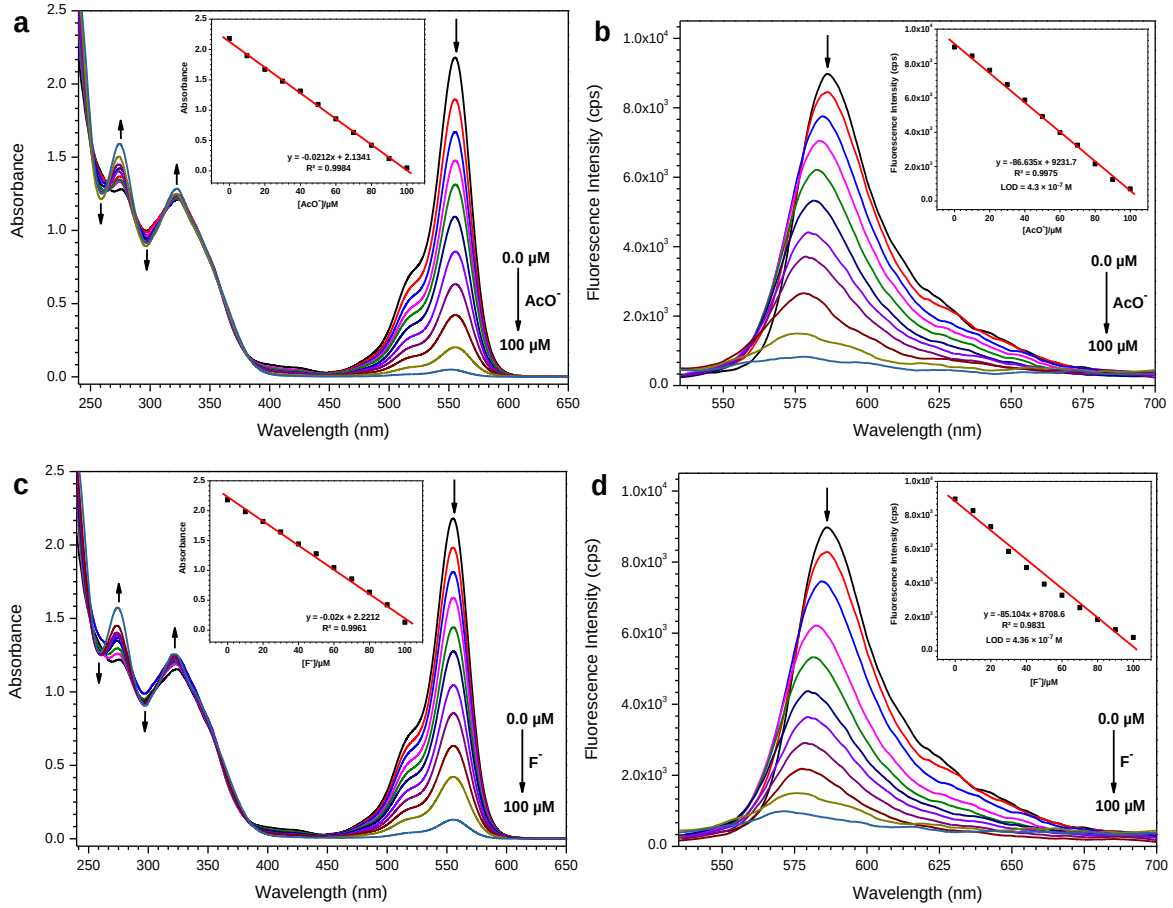


**Figure 6.17.** UV-Vis (a, c) and fluorescence (b, d) titration spectra of **L4** (50 μM) with 1 equiv. of $Al^{3+}$ upon gradual addition (0–100 μM) of sodium acetate (a, b) and sodium fluoride (c, d). Inset: Absorbance and fluorescence intensity changes of **L4**–$Al^{3+}$ complex at 555 nm and 587 nm, respectively as a function of concentration of $AcO^{-}$/$F^{-}$.

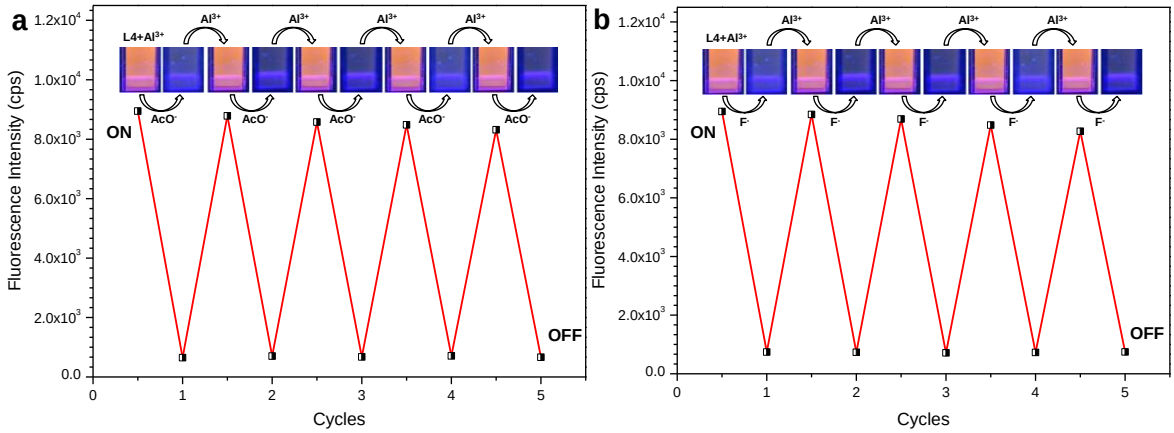


**Figure 6.18.** Fluorescence intensity of **L4** (50 μM) at 587 nm upon alternate addition of a constant amount of $Al^{3+}$ (1 equiv.) and $AcO^{-}$/$F^{-}$ (2 equiv.). Inset: Images of fluorescence reversibility.

### *6.1.3.11. Sensing studies with paper strips*

To investigate the practical application of chemosensors, paper test strips were prepared for rapid on-site detection of $Al^{3+}$, $Cr^{3+}$ and $Cu^{2+}$ ions. For this purpose, filter papers

(Whatman filter paper No. 1) were immersed in a 1 mM methanolic solution of **L4** for about 5 min and then dried in air. The test strips containing **L4** were then dipped in the corresponding metal ion solutions (100 μM) in MeOH−$H_2O$ (50:50 v/v). A significant visible color change was noticed immediately upon dipping the test strips in the metal ion solutions (Figure 6.19). The colorless strips were converted to pink, which was also observed under UV light. These pink colored test strips containing **L4**–$Al^{3+}$ were then dipped into a solution of $AcO^-/F^-$. The red color of the test strips disappeared and shown their original color (colorless) due to restoration of **L4**. This makes the sensor quite useful for rapid on-site detection of metal ions.

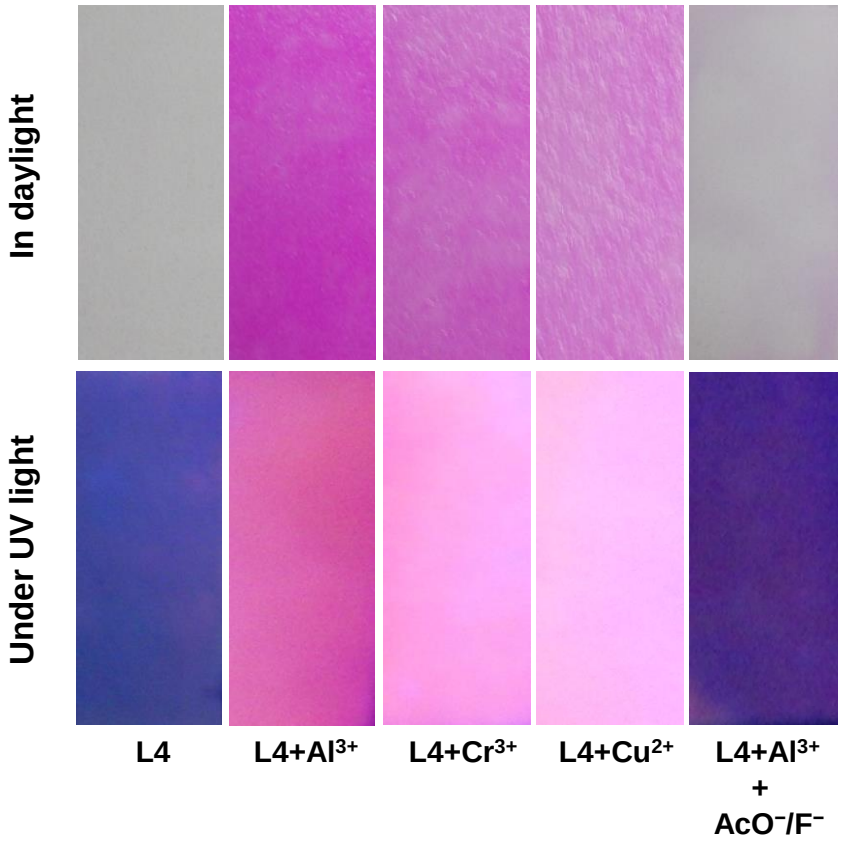


**Figure 6.19.** Photographs of the test strips of **L4** for the detection of $Al^{3+}$, $Cr^{3+}$ and $Cu^{2+}$ in MeOH−$H_2O$ (50:50 v/v). A solution of **L4** with a concentration of 1 mM was used to develop the strip.

### 6.1.4. Conclusion

The newly synthesized fluoroionophores **L1–L4** based on rhodamine derivatives exhibit a good selective and sensitive toward $Al^{3+}$ ion over a wide variation of cations in MeOH−DMSO (99:1 v/v). In all the cases, the spectral changes were observed due to reversible spirolactam ring opening. The 1 : 1 coordination mode was proposed based on a

Job's plot, which was further confirmed by ESI-MS. Further studies of **L4**–$Al^{3+}$ complex revealed that it could be selectively dissociated in the presence of $AcO^{-}/F^{-}$, which makes the **L4**–$Al^{3+}$ complex an efficient sensor for $AcO^{-}/F^{-}$ with a detection limit of 0.4 μM. Further, the DFT experiment suggested that the binding of $Al^{3+}$ to **L4** lowered the HOMO-LUMO band gap, which is evidence for the red-shift in fluorescence spectra of **L4**–$Al^{3+}$ complex. Paper strips were also used for the detection of $Al^{3+}$ and $AcO^{-}/F^{-}$ by colorimetric method.

## 6.2. Colorimetric and Off-On Fluorescent Chemosensors for $Cr^{3+}$ Ion

### 6.2.1. Introduction

Trivalent chromium, Cr(III), is a necessary metal ion of a balanced human and animal diet. Chromium is used in metal finishing, electroplating, chromate preparation and leather tanning processes. Chromium is a famous environmental contaminant that accumulates because of industrial and agricultural activities [51], and causes epigastric pain, hemorrhage, severe diarrhea and carcinogen effect [52]. Also its deficiency can increase the risk factors related with cardiovascular and diabetes diseases including elevated circulating insulin, triglycerides, total cholesterol, lipid metabolism and glucose levels [53, 54].

Thus, selective detection of such harmful metal ions at the sub-milli and micromolar level for environmental, clinical and biological purposes is highly attractive and essential. Even though various analytical methods, such as inductively coupled plasma mass spectroscopy, atomic absorption and emission spectrometry, chromatography, neutron activation analysis, X-ray fluorescence spectrophotometry and anodic stripping voltammetry [25, 27, 55–60], *etc.*, have been played a role to detect these metal ions.

Among several detection methods for metal ions, the colorimetric and fluorometric methods have become more useful and popular in medicine, biology and environmental chemistry due to its non-destructive, high selective and sensitive, quick and naked eye detection [61–65]. The rhodamine moiety to construct OFF-ON fluorescent chemosensors is a reliable method due to their structure change from non-fluorescent spirolactam to highly fluorescent ring-opened amide induced by specific chemical species at room temperature [2, 66]. Rhodamine derivatives are used widely as a fluorescent signal transducer due to their tremendous photophysical properties like as extended absorption and emission wavelengths, high fluorescence quantum yield and large absorption coefficient. In fact, a longer wavelength emission (~550 nm) was often preferred to serve as a sensing signal to avoid the background fluorescence influence (below 500 nm) [67, 68]. Recently, several rhodamine-based probes as fluorescent chemosensors for metal ions have been developed [69–76].

Herein, we described the synthesis of two novel rhodamine derivatives **RS1** and **RS2**, which show a reversible, selective and sensitive fluorescence enhancement response to Cr(III) in alcoholic media.

### 6.2.2. Experimental

*6.2.2.1. Reagents and apparatus*

Rhodamine B, metal salts and other commercially obtainable chemicals were purchased from Merck and Aldrich and used without further purification. The melting point was measured on a SRS OptiMelt Automated melting point system. The IR spectra were recorded on a PerkinElmer FT-IR spectrometer (USA) in the range 4000–400 $cm^{-1}$ with KBr. The NMR spectra were measured by using Bruker 500 MHz (USA), TMS as an internal standard, $CDCl_3$, DMSO-d6 and $CD_3OD$ are taken as solvents. The mass spectra were recorded on a Bruker-micrOTOF II (USA). The UV-Vis absorption spectra were obtained on a Shimadzu UV-2450 spectrophotometer (Japan) and the Fluorescent spectra were recorded by using Shimadzu RF-5301PC spectrofluorophotometer (Japan). Differential Pulse Voltammetric experiments were performed using a CHI760E electrochemical workstation (USA) with a conventional three-electrode configuration consisting of a glassy carbon working electrode, a platinum wire counter electrode, and an aqueous $Ag/AgNO_3$ reference electrode. The pH was measured with a Eutech CyberScan pH 510 (Singapore).

*6.2.2.2. Synthesis and characterization*

The synthetic route for Chemosensors (**RS1** and **RS2**) was outlined in Scheme 6.3. Chemosensors were prepared by following the literature method [48] and the structures were characterised by FT-IR, $^1H$ NMR, $^{13}C$ NMR and ESI-MS.

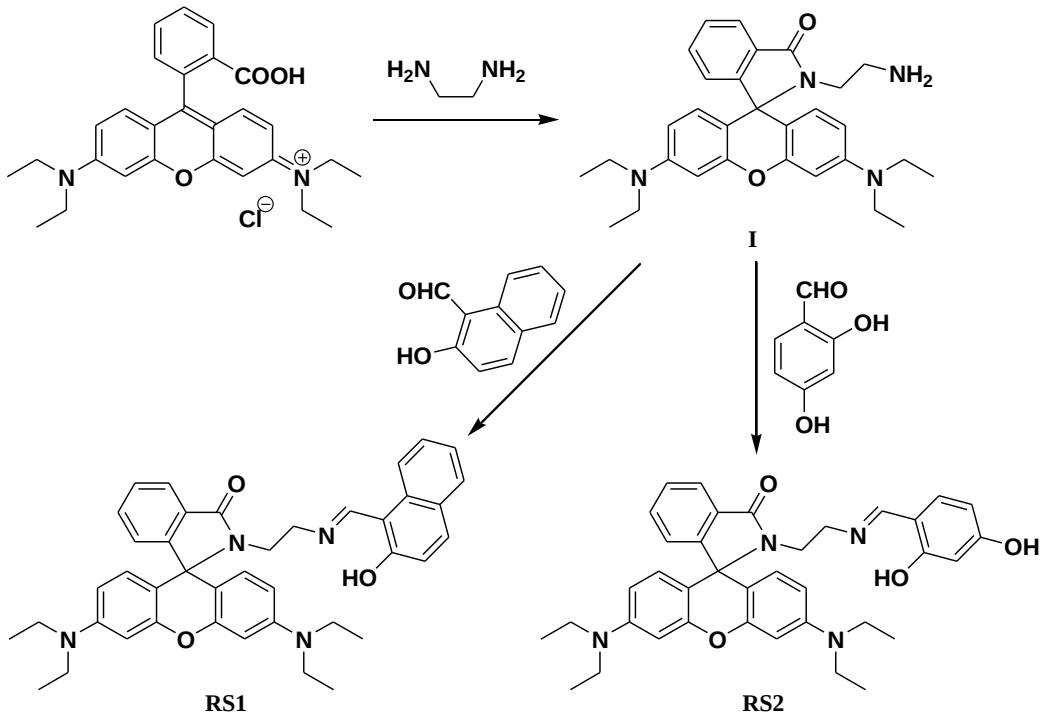


**Scheme 6.3.** Synthetic Pathways of **RS1** and **RS2**.

**Compound I:**

Ethylenediamine (2.5 ml) was added drop wise to the ethanolic solution of rhodamine B (2.0 g) with vigorous stirring at room temperature. On completion of addition, the stirred solution was allowed to reflux about 6–8 h. The color of mixture changed from dark pink to light orange. Then the mixture was cooled and solvent was removed under reduced pressure. 1 M HCl (about 50 mL) was added to the reaction mixture to produce a clear red solution. Later than, 1 M NaOH in water was added gradually with constant stirring until the pH of the solution reached 9–10. The resulting precipitate was filtered and washed 4–5 times with 15 mL water. After drying under reduced pressure, the reaction yielded 1.8 g **I** (90%) as pink solid. Mp: 215–217 °C; FT-IR (KBr), *v*, $cm^{-1}$: 1620 (C=O), 1385, 1121 (C−N), 1224, 1021 (C−O); $^{1}H$ NMR ($CDCl_3$, 500 MHz), $\delta$ (ppm): 1.16 (12H, t, *J* = 7.0 Hz), 2.42 (2H, t, *J* = 6.0 Hz), 3.19 (2H, t, *J* = 6.0 Hz), 3.33 (8H, q, *J* = 7.0 Hz), 6.27 (2H, d, *J* = 8.5 Hz), 6.37 (2H, s), 6.43 (2H, d, *J* = 8.5 Hz), 7.09 (1H, s), 7.44 (2H, s), 7.90 (1H, s); $^{13}C$ NMR ($CDCl_3$, 500 MHz), $\delta$ (ppm): 12.6, 40.8, 43.8, 44.3, 65.0, 97.7, 105.7, 108.2, 122.7, 123.8, 128.0, 128.7, 131.2, 132.4, 148.8, 153.3, 153.5, 168.6. ESI-MS *m/z*: Calcd for $C_{30}H_{36}N_4O_2$ $(M+H)^+$: 485.2917, found: 485.2762.

**Compound RS1 and RS2:**

Compound **I** (0.24 g, 0.5 mmol) and aldehyde (0.5 mmol) were dissolved in 20 mL absolute ethanol. The reaction mixture was stirred for 6 h at room temperature. Obtained solid was filtered and washed 3 times with 10 mL ethanol. After drying under reduced pressure, the reaction afforded 0.26 g **RS1** (82%) as yellow solid and 0.22 g **RS2** (73%) as white solid, respectively.

**Compound RS1:** Mp: 167–169 °C; FT-IR (KBr), *v*, $cm^{-1}$: 1620 (C=O), 1365, 1121 (C−N), 1227, 1012 (C−O); $^{1}H$ NMR ($CDCl_3$, 500 MHz), $\delta$ (ppm): 1.16 (12H, t, *J* = 7.0 Hz), 3.31 (8H, q, *J* = 6.5 Hz), 3.39–3.45 (4H, m), 6.24 (2H, d, *J* = 8.5 Hz), 6.41–6.44 (4H, m), 6.84 (1H, d, *J* = 9.0 Hz), 7.10 (1H, s), 7.19 (1H, t, *J* = 7.5 Hz), 7.39 (1H, t, *J* = 7.5 Hz), 7.45 (2H, s), 7.55 (1H, d, *J* = 7.5 Hz), 7.61 (1H, d, *J* = 9.0 Hz), 7.78 (1H, d, *J* = 8.0 Hz), 7.93 (1H, s), 8.50 (1H, s), 13.99 (1H, s); $^{13}C$ NMR ($CDCl_3$, 500 MHz), $\delta$ (ppm): 12.6, 40.9, 44.3, 50.6, 65.1, 97.8, 105.1, 106.8, 108.2, 118.0, 122.6, 122.9, 123.9, 124.9, 126.2, 127.8, 128.2, 128.7, 129.1, 130.9, 132.6, 133.9, 137.1, 148.9, 153.4, 158.5, 168.4, 176.3. ESI-MS *m/z*: Calcd for $C_{41}H_{42}N_4O_3$ $(M+H)^+$: 639.3335, found: 639.3147.

**Compound RS2:** Mp: 205–207 °C; FT-IR (KBr), *ν*, $cm^{-1}$: 1626 (C=O), 1397, 1115 (C−N), 1218 (C−O); $^{1}H$ NMR ($CDCl_3$, 500 MHz), *δ* (ppm): 1.16 (12H, t, *J* = 6.0 Hz), 3.21 (2H, t, *J* = 6.5 Hz), 3.32 (8H, d, *J* = 6.5 Hz), 3.42 (2H, t, *J* = 6.0 Hz), 6.25–6.31 (3H, m), 6.39–6.42 (5H, m), 6.82 (1H, d, *J* = 8.0 Hz), 7.08 (1H, d, *J* = 5.0 Hz), 7.43 (2H, s), 7.75 (1H, s), 7.90 (1H, s); $^{13}C$ NMR ($CDCl_3$, 500 MHz), *δ* (ppm): 12.6, 40.9, 44.3, 54.5, 65.3, 97.8, 103.8, 105.1, 107.1, 108.2, 111.7, 123.0, 123.8, 128.2, 128.8, 130.8, 132.6, 133.4, 148.9, 153.3, 153.5, 162.0, 164.8, 167.0, 168.6. ESI-MS *m/z*: Calcd for $C_{37}H_{40}N_4O_4$ $(M+Na)^+$: 627.2947, found: 627.2942.

*6.2.2.3. UV-Vis and fluorescent studies*

Stock solutions of $1 \times 10^{-3}$ M various metal ions and receptor were prepared in methanol and MeOH−DMSO (99:1 v/v), respectively. The solutions were then diluted to $1 \times 10^{-4}$ M using same solvents. All measurements of UV-Vis absorption and fluorescence emission spectra were carried out in 1.0 cm path length quartz cuvettes at room temperature. Absorption and emission spectra of the chemosensor in the presence of various metal ions were measured in the concentration of 50 μM. Stoichiometry, binding constant of sensing probe–$Cr^{3+}$ complex, limit of detection of $Cr^{3+}$ and quantum yield were calculated by using spectrofluorophotometer. For all the fluorescence emission measurements, excitation wavelength was 520 nm, and both the excitation and emission slit widths were 1.5 and 3 nm, respectively.

**6.2.3. Results and discussion**

The binding ability and mode of chemosensors toward $Cr^{3+}$ were investigated through absorption, emission, electrochemical, ESI-MS, DFT calculation and $^{1}H$ NMR experiments.

*6.2.3.1. Absorption spectroscopic studies*

The binding ability of probe (50 μM) against different metal ions (50 μM) such as $Cd^{2+}$, $Co^{2+}$, $Cr^{3+}$, $Cu^{2+}$, $Fe^{2+}$, $Fe^{3+}$, $Gd^{3+}$, $Hg^{2+}$, $Mn^{2+}$, $Nd^{3+}$, $Ni^{2+}$,$Pb^{2+}$ and $Zn^{2+}$ were carried out by UV-Vis absorption studies. As observed, the UV-Vis spectra of **RS1** and **RS2** exhibited an absorption band in the 350–450 nm region, on addition of $Cr^{3+}$ ion (1:1, v/v) lead to form of a strong absorption transition at ~555 nm with a shoulder at ~518 nm (Figure 6.20). The noticeable naked eye recognition of the pink color development in these probes (Figure 6.20, inset) upon Cr(III) addition implies a metal-induced delactonization of rhodamine, while the rest of the metal ions induced an insignificant absorption change even

when added in excess. On complexation, initial spirolactam form of probe is converted into its ring opened amide conformation [77].

The plot of absorbance at 555 nm of **RS1** and **RS2** as a function of mole fraction of $Cr^{3+}$ ions (Jobs plot) exposes that these probes bind to the chromium metal ion in 1:1 stoichiometry (Figure 6.21).

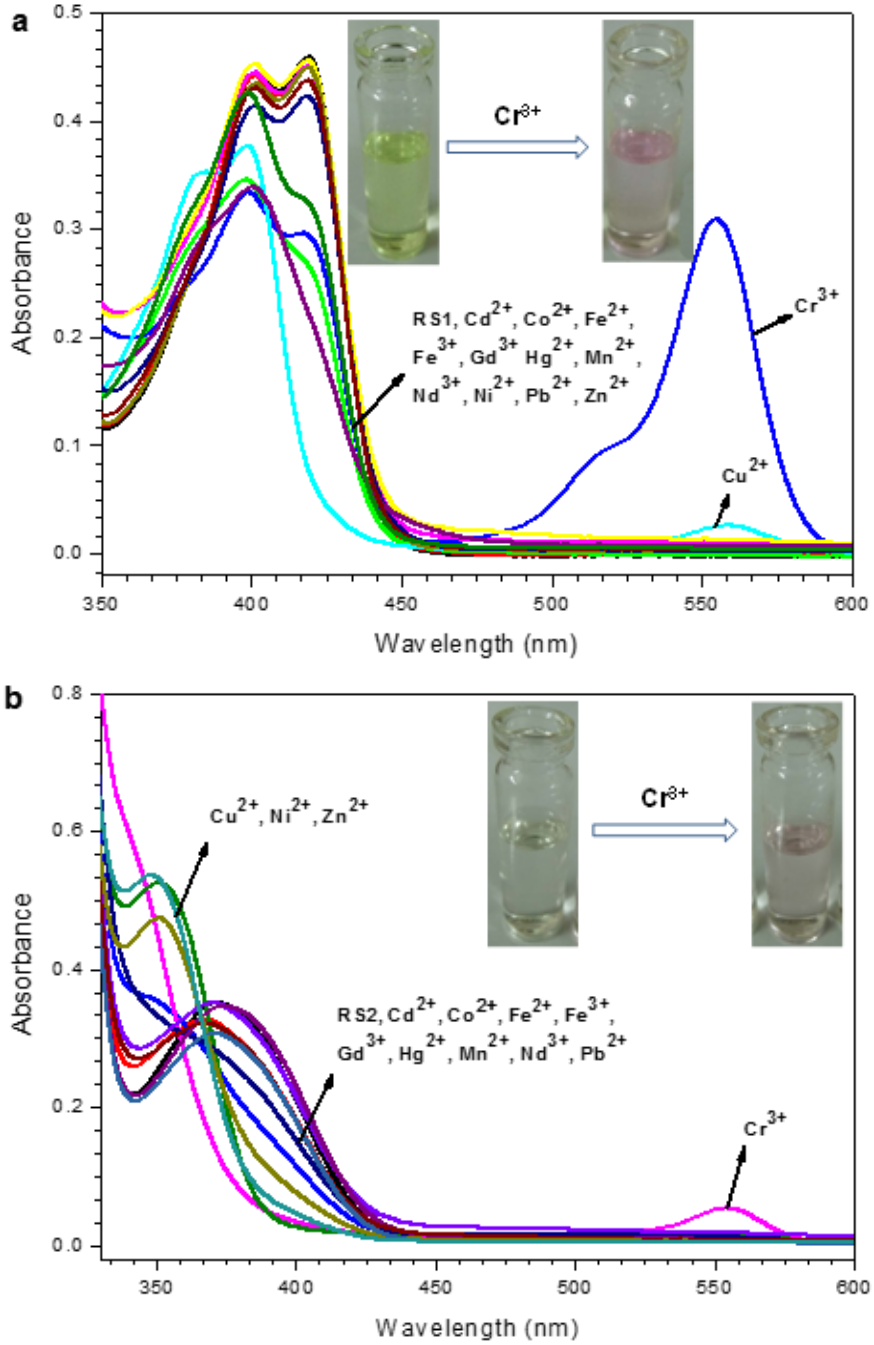


**Figure 6.20.** Absorbance spectra of **RS1** (a) and **RS2** (b) (50 μM) in presence of various metal ions (50 μM) in MeOH−DMSO (99:1 v/v). Inset: Color change of probe in the presence of $Cr^{3+}$.

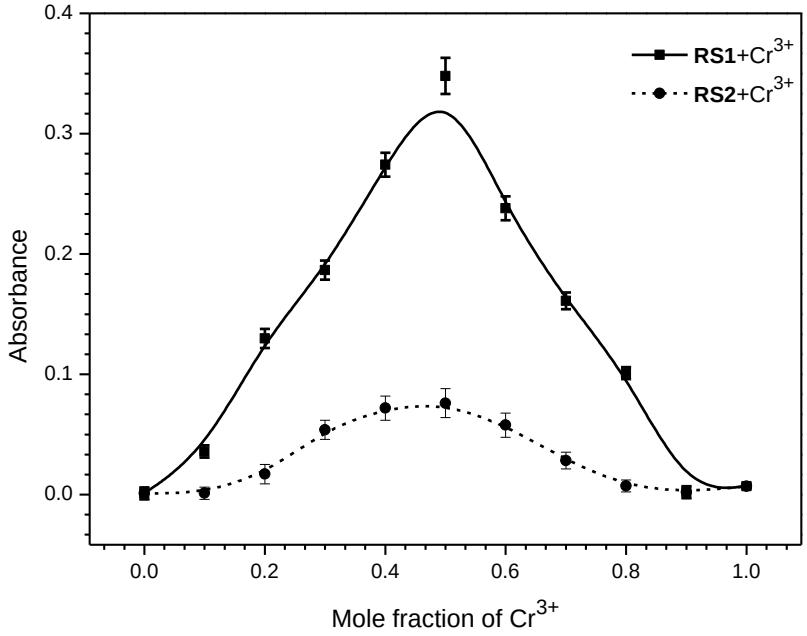


**Figure 6.21.** Job's plot for **RS1** and **RS2** with $Cr^{3+}$, absorbance intensity at 555 nm was plotted as a function of the molar ratio.

*6.2.3.2. Fluorescence emission studies*

The fluorescence spectral pattern (Figure 6.22) of **RS1** and **RS2** when excited at 520 nm in the presence of different metal ions exhibited that their non-fluorescent behaviour becomes highly fluorescent upon metal addition (OFF-ON). Under a UV lamp, showed a fabulous color change from colorless to brick red in the solution of probes upon the addition of $Cr^{3+}$, which could simply be identified by the naked-eye (Figure 6.22, inset). This implies a delactonization process, of the non-fluorescent spirocyclic form to its highly fluorescent ring opened form of rhodamine which is induced by metal ion coordination. The degree of chelation-enhanced fluorescence effects depend on the character of the ligands and interacting metal ions. The binding ability depends on size, charge and electron configuration of the metal ion and ligand. Those characters of metal ion and ligand are very suitable for each other to form metal complex. Amongst all the metal ions examined, these probes displayed high fluorescence enhancement at $\lambda_{em}$ = ~575 nm in the presence of Cr(III) ion. Probe **RS1** exhibited maximum Cr(III)-induced fluorescence enhancement (114-fold) than **RS2** (38-fold), showing its higher affinity towards Cr(III) with a good response time (<5 seconds) in comparison to other probe (**RS2**).

The emission spectral pattern of **RS1** and **RS2 (**50 µM) upon addition of increasing concentration (0, 5, 10, 15, 20, 25, 30, 35, 40, 45, 50, 60, 70, 80, 90, 100 µM) of $Cr^{3+}$ ion, a new emission band peaked at ~575 nm appeared with increasing intensity (Figure 6.23). The complex stability constants (*K*) through Benesi-Hildebrand method for Cr(III) with **RS1** and

**RS2** were found to be $2.7\times10^4$ $M^{-1}$ and $4.5\times10^3$ $M^{-1}$, respectively (Figure 6.23, inset). The observable brick red color development in these probes due to a highly delocalized π-conjugated system of probes was formed. The detection limit of Cr(III) was calculated based on the fluorescence titration profile as $4.9\times10^{-8}$ M (for **RS1**) and $2.4\times10^{-7}$ M (for **RS2**) based on S/N = 3 (Figure 6.23, inset).

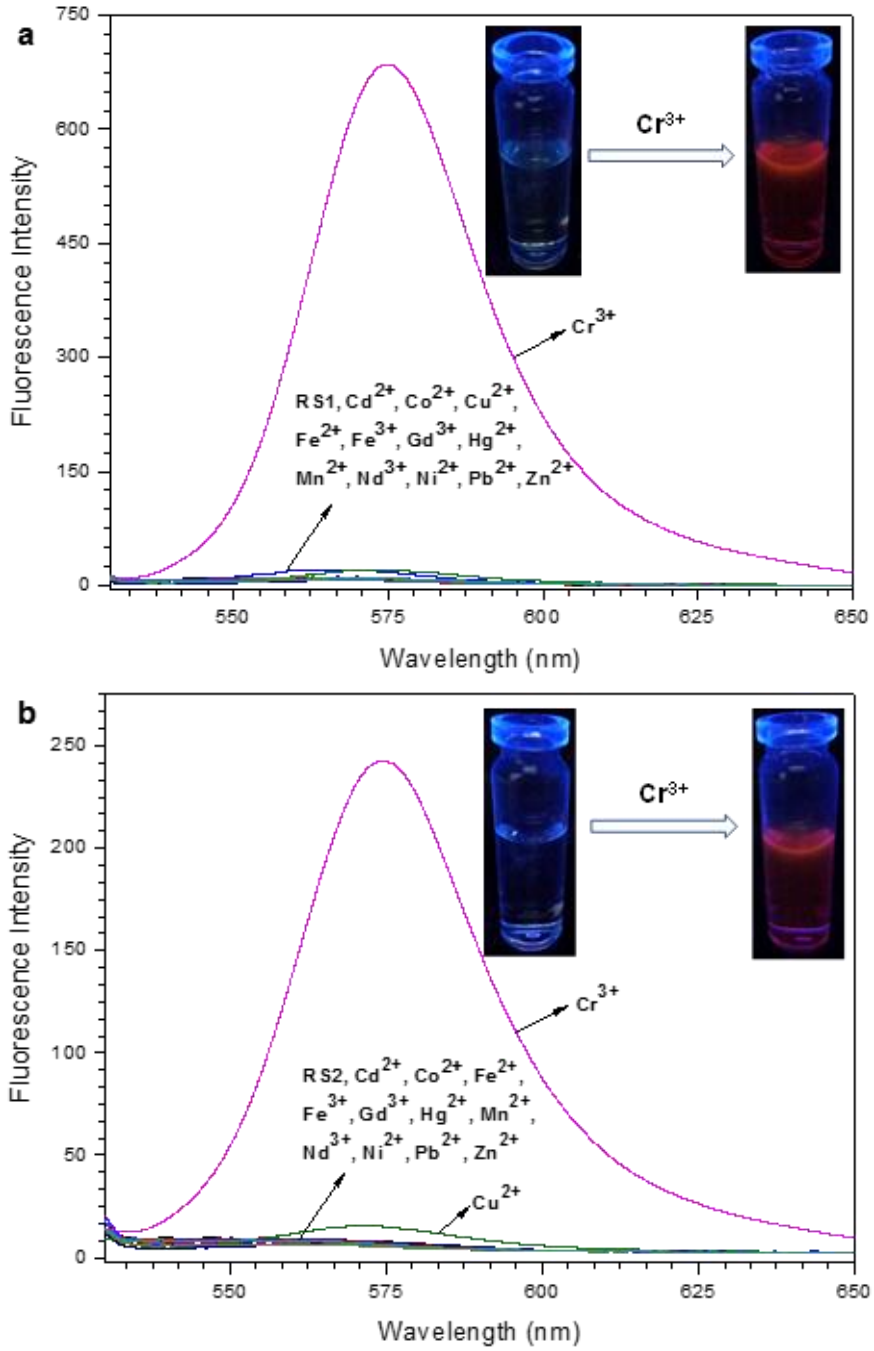


**Figure 6.22.** Fluorescence spectra ($\lambda_{ex}$ = 520 nm) of **RS1** (a) and **RS2** (b) (50 μM) in presence of various metal ions (50 μM) in MeOH−DMSO (99:1 v/v). Inset: Color change of probe in the presence of $Cr^{3+}$.

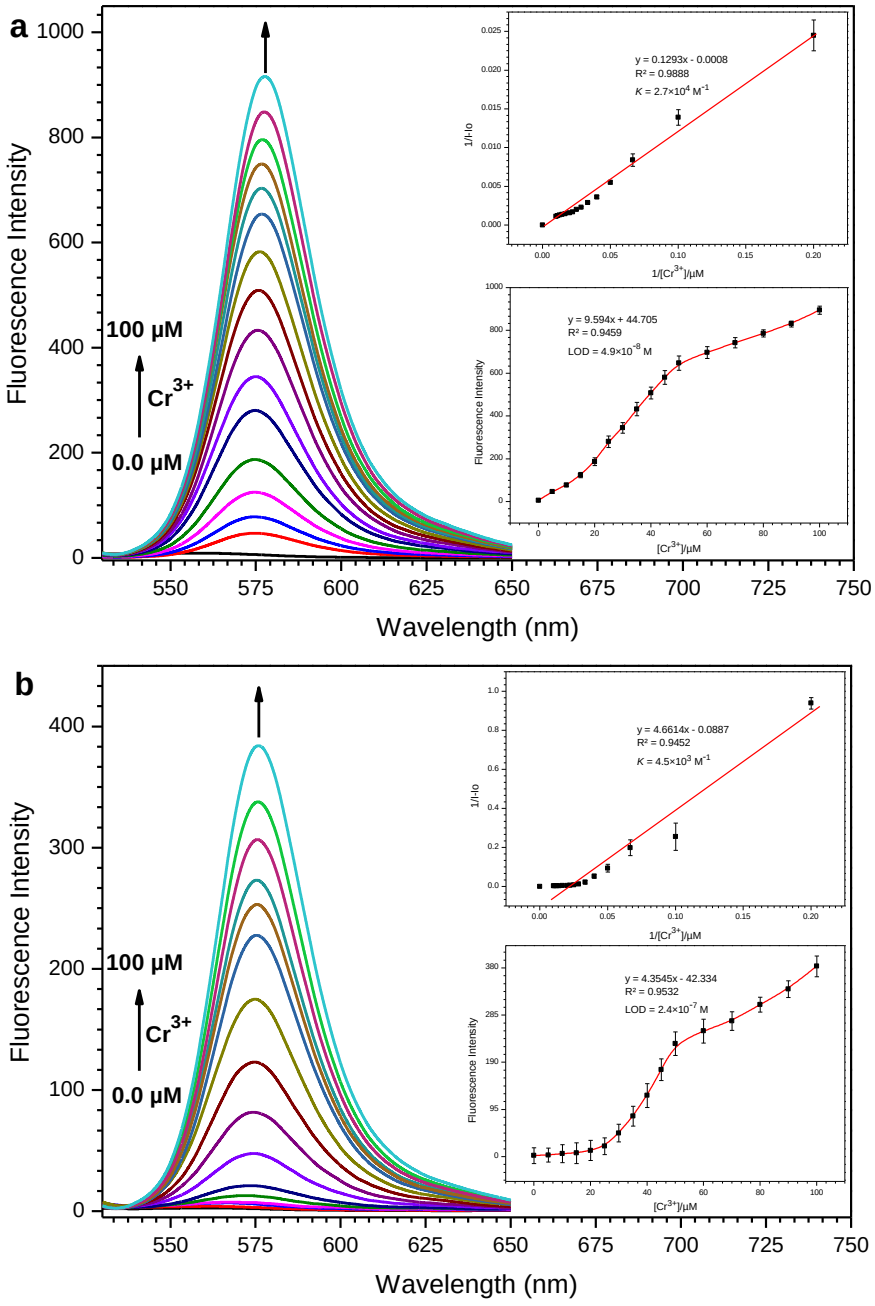


**Figure 6.23.** The variation in fluorescence emission spectra of **RS1** (a) and **RS2** (b) in the presence of increasing concentrations of $Cr^{3+}$ (0, 5, 10, 15, 20, 25, 30, 35, 40, 45, 50, 60, 70, 80, 90, 100 μM). Inset: Linear regression plot of fluorescence intensity change $1/(I-I_0)$ as a function of concentration $1/[Cr^{3+}]$ (top), fluorescence enhancement change as a function of concentration of Cr(III) added (bottom).

Furthermore, to determine the stoichiometry of probe–$Cr^{3+}$ complex, continuous variation (Job's) method was conducted (Figure 6.24). As supposed, the results show the formation of a 1:1 stoichiometry complex between $Cr^{3+}$ and probe, and stoichiometric ratio was further confirmed by ESI-MS analysis (Figure 6.25). Observed mass peak at *m*/*z*

742.2372 and 708.2255 corresponding to [**RS1** + Cr + Cl + $H_2O$ − H]$^+$ and [**RS2** + Cr + Cl + $H_2O$ − H]$^+$ respectively, which are solid evidence for the formation of a 1:1 complex.

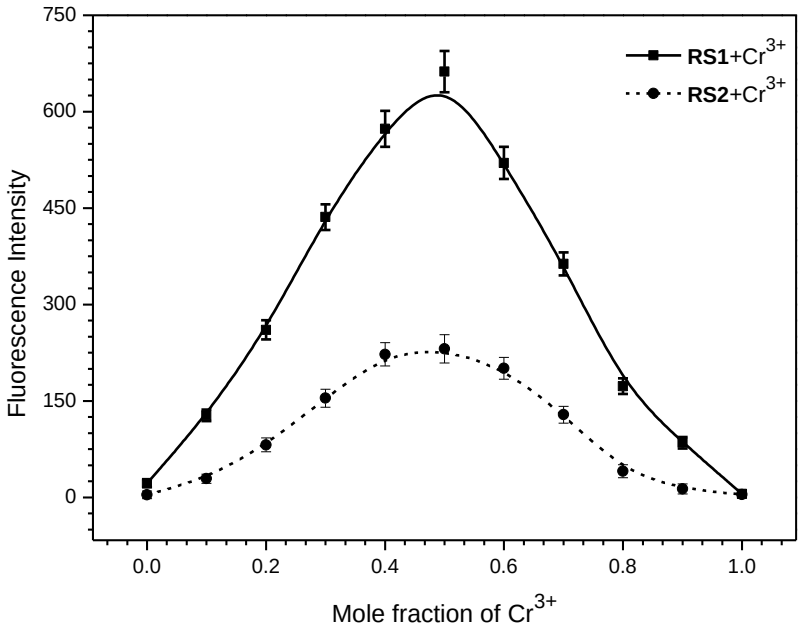


**Figure 6.24.** Job's plot for **RS1** and **RS2** with $Cr^{3+}$, fluorescence intensity at 575 nm was plotted as a function of the molar ratio.

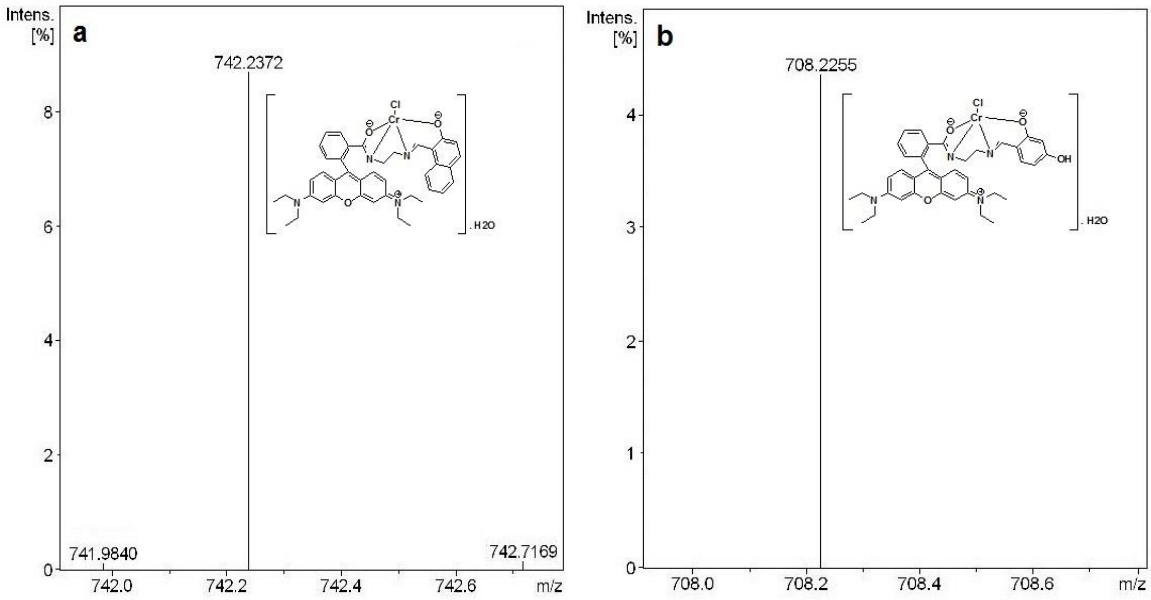


**Figure 6.25.** ESI-MS spectrum of **RS1** (a) and **RS2** (b) upon addition of $CrCl_3.6H_2O$ (1.0 equiv.) in MeOH.

In addition, to verify the selectivity of these ligands towards Cr(III) ions over various competitive metal ions. The emission intensity changes of **RS1** and **RS2** (50 μM) upon addition of other metal ions (50 μM) and Cr(III) along with other metal ions were evaluated

(Figure 6.26). The results exposed that Cr(III)-induced fluorescence response was unaffected in the presence of other interfering ions used. This experiment establishes the significant feature of high selectivity of these probes towards Cr(III) over other competitive metal ions.

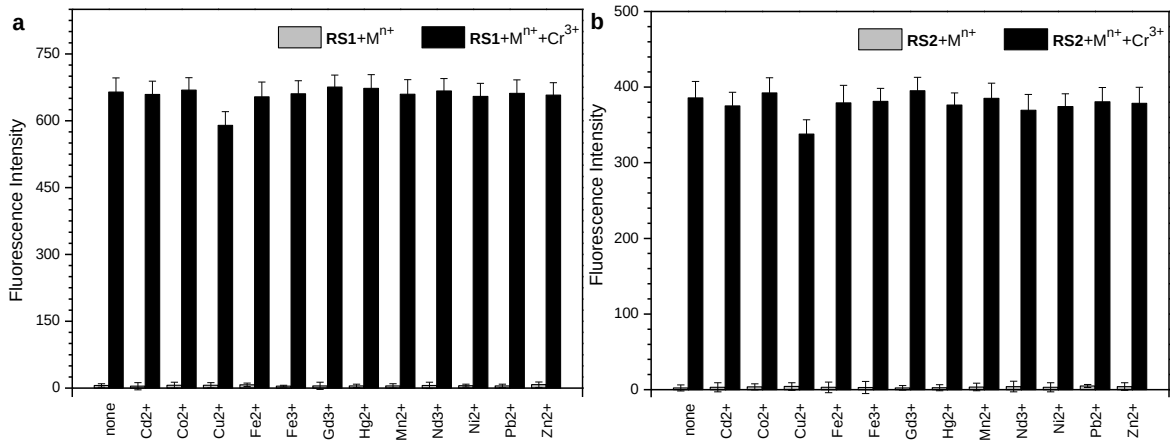


**Figure 6.26.** Competitive selectivity of probes **RS1** (a) and **RS2** (b) toward various metal ions (1.0 equiv.) in the absence (black bars) and presence (red bars) of $Cr^{3+}$ (1.0 equiv.) with an excitation of 520 nm.

In acidic media, the spirolactam ring of the rhodamine and its derivatives is open and then shows the absorbance and fluorescence characteristics of rhodamine. The absorbance and fluorescence responses of probes in the presence of Cr(III) in different pH value were estimated (Figure 6.27). The absorbance spectra of probe–Cr(III) is gradually increased from pH 2 to 4 and reached a $\lambda_{max}$ at pH 4. From pH 4 to 6, the absorbance maxima moved downward. A rapid fluorescence enhancement accompanied by a red shift was observed with pH variation from 2 to 4. The fluorescence quenching accompanied by a blue shift was started while changing in the pH from 4 to 6. Absorbance (at 555 nm) and fluorescence emission (at 575 nm) of probe–Cr(III) disappeared in basic conditions (≥7). The same spectral changes were observed for probe (**RS1** and **RS2**) alone in various pH conditions. The chemosensors **(RS1** and **RS2**) in the presence of Cr(III) exhibited a dramatic color changes in the different pH media, which could simply be identified by the naked-eye (Figure 6.27, inset). Absorbance and Emission enhancement factor, and corresponding quantum yields of **RS1** and **RS2** with pH variation in the absence and presence of Cr(III) are collected in Table 6.1.

To examine the reversibility of complexation of probe towards Cr(III) ion, EDTA titration experiments were conducted. Upon addition of EDTA to the solution containing probe (**RS1** and **RS2**) and Cr(III) weaken the fluorescence intensity significantly, whereas readdition of excess Cr(III) ion could recover the fluorescence emission signal (Figure 6.28).

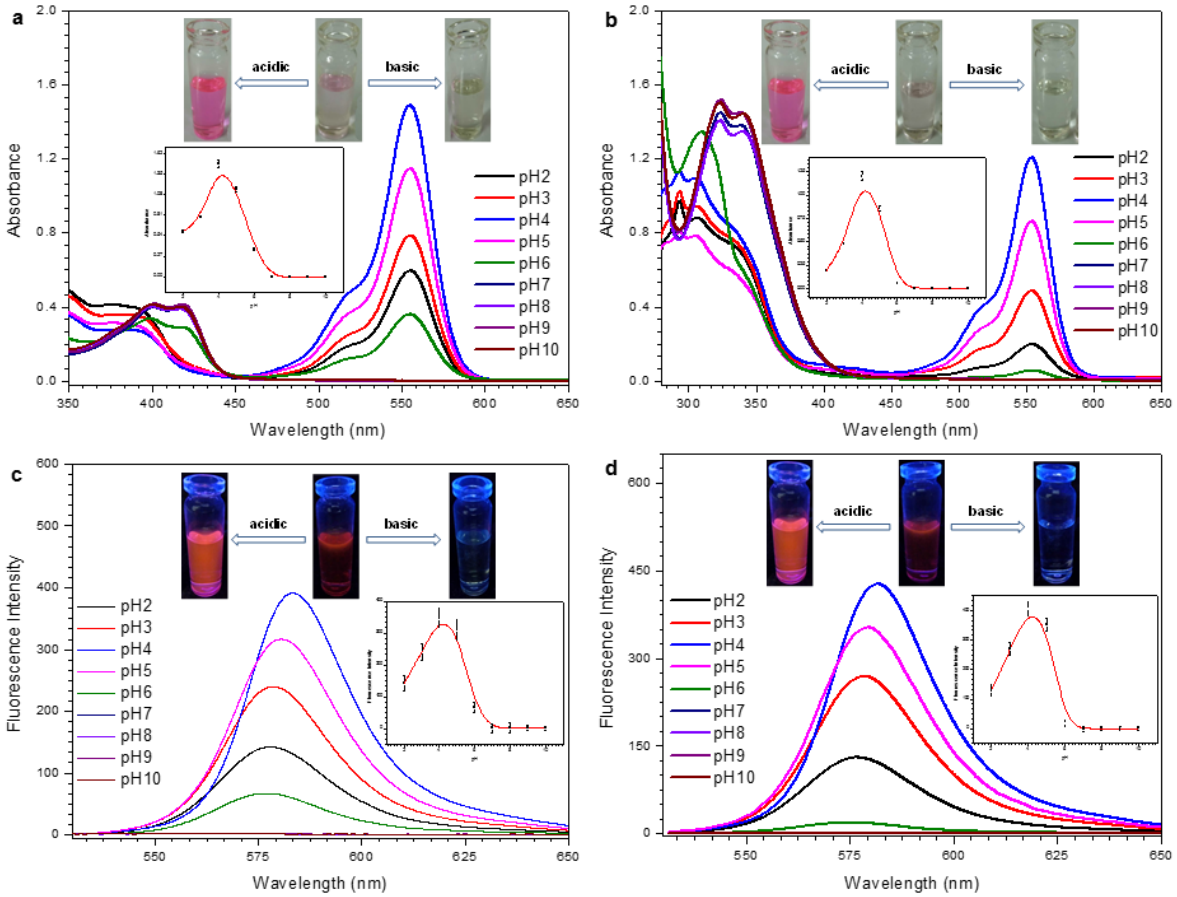


**Figure 6.27.** UV-Vis absorbance spectral changes of **RS1** (a) and **RS2** (b)**,** Fluorescence emission intensities (both excitation and emission slit widths were 1.5 nm) of **RS1** (c) and **RS2** (d) with $Cr^{3+}$ as a function of pH. Inset: Color changes of **RS1**+$Cr^{3+}$ and **RS2**+$Cr^{3+}$ in different pH media under a normal (a, b) and fluorescent (c, d) light (top), absorbance (a and b, at 555 nm) and emission (c and d, at 575 nm) intensities of **RS1** and **RS2** in the presence of $Cr^{3+}$ with pH variation (bottom).

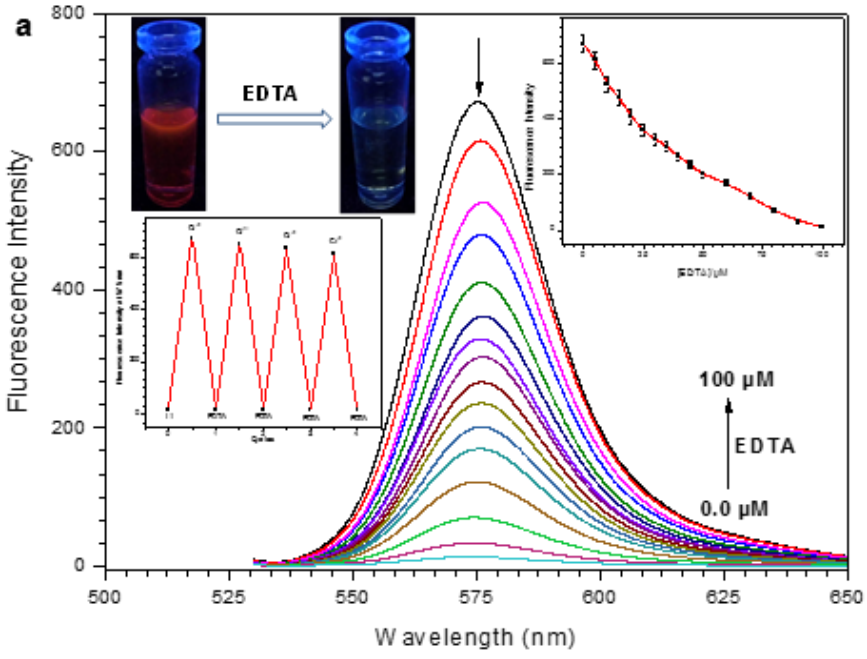

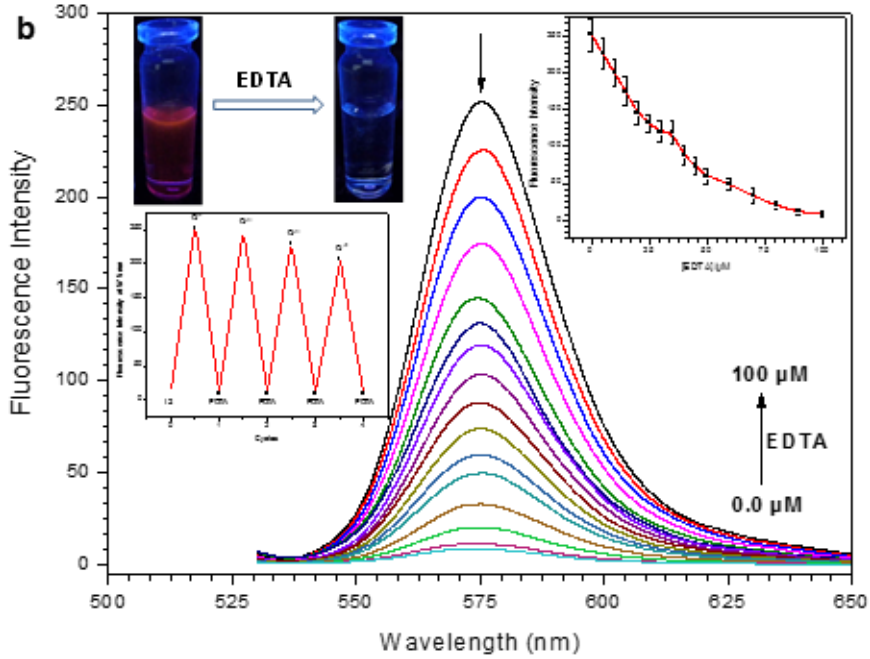


**Figure 6.28.** The variation in fluorescence emission spectra of **RS1**+$Cr^{3+}$ (a) and **RS2**+$Cr^{3+}$ (b) upon addition of EDTA (0, 10, 15, 20, 25, 30, 35, 40, 45, 50, 60, 70, 80, 90, 100 μM). Inset: Color changes of probe+$Cr^{3+}$ upon addition of EDTA (2 equiv.) (Top left), fluorescence spectral changes at 575 nm as a function of the amount of EDTA (right) and recovery of the molecular fluorescence at 575 nm of the sensor (50 μM) after addition of $Cr^{3+}$ (1 equiv.) after each addition of 2 equiv. of EDTA (Bottom left).

**Table 6.1.** Absorbance and emission enhancement factor, and corresponding quantum yields of **RS1** and **RS2** in the presence of Cr(III)

| System | pH | Absorbance EF (*A*/*Ao**) | Emission EF (*I*/*Io**) | Quantum yield (*Φ*) |
|---|---|---|---|---|
| **RS1** | 4.0 | 497 | 263 | 0.47 |
| **RS1**+$Cr^{3+}$ | 4.0 | 500 | 261 | 0.44 |
| **RS1** | 6.5 | 1 | 1 | < 0.001 |
| **RS1**+$Cr^{3+}$ | 6.5 | 103 | 114 | 0.14 |
| **RS1** | > 7.0 | ~1 | ~1 | < 0.001 |
| **RS1**+$Cr^{3+}$ | > 7.0 | ~1 | ~1 | < 0.001 |
| **RS2** | 4.0 | 397 | 286 | 0.51 |
| **RS2**+$Cr^{3+}$ | 4.0 | 402 | 285 | 0.57 |
| **RS2** | 6.5 | 1 | 1 | < 0.001 |
| **RS2**+$Cr^{3+}$ | 6.5 | 18 | 38 | 0.1 |
| **RS2** | > 7.0 | ~1 | ~1 | < 0.001 |
| **RS2**+$Cr^{3+}$ | > 7.0 | ~1 | ~1 | < 0.001 |

* *Ao* = Absorbance of probe at neutral pH at 555 nm,

**Io* = Emission intensity of probe at neutral pH at 575 nm

As results show, it could provide as experimental evidence to support the reversibility of spiro ring-opening and closing mechanism. The proposed binding mechanism of probe (**RS1** and **RS2**) with Cr(III) in the presence and absence of EDTA was shown in the Scheme 6.4.

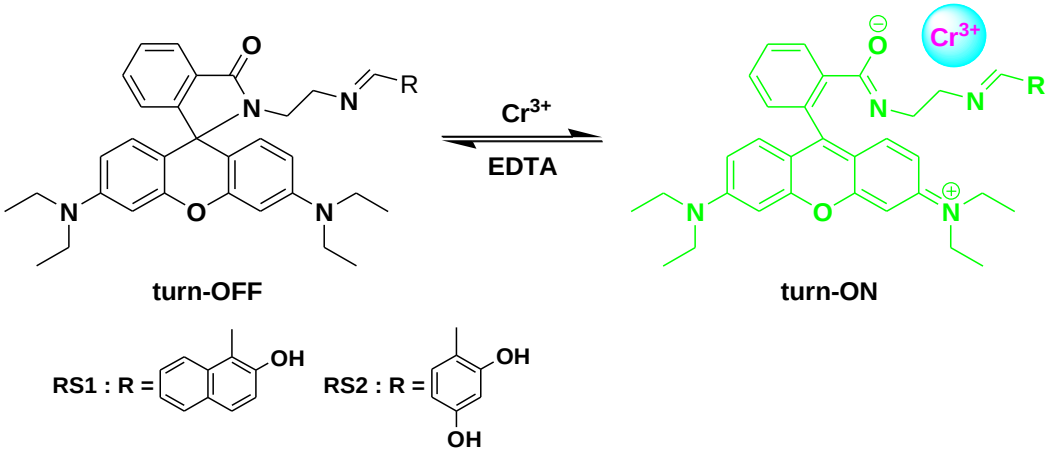


**Scheme 6.4.** Proposed binding mechanism of Cr(III) with probes in the presence and absence of EDTA.

Both UV-Vis and fluorescence emission results indicate that probes show a good selectivity and sensitivity toward Cr(III) over other metal ions.

*6.2.3.3. Electrochemical measurements*

As shown in Figure 6.29, the band gap energy related wavelength for probes is obtained from the cross point of absorption onset line and corrected base line [78]. The corresponding wavelengths are 444 and 424 nm, and are equal to 2.79 and 2.92 eV energy band gap for **RS1** and **RS2,** respectively. The corresponding wavelength to the band gap

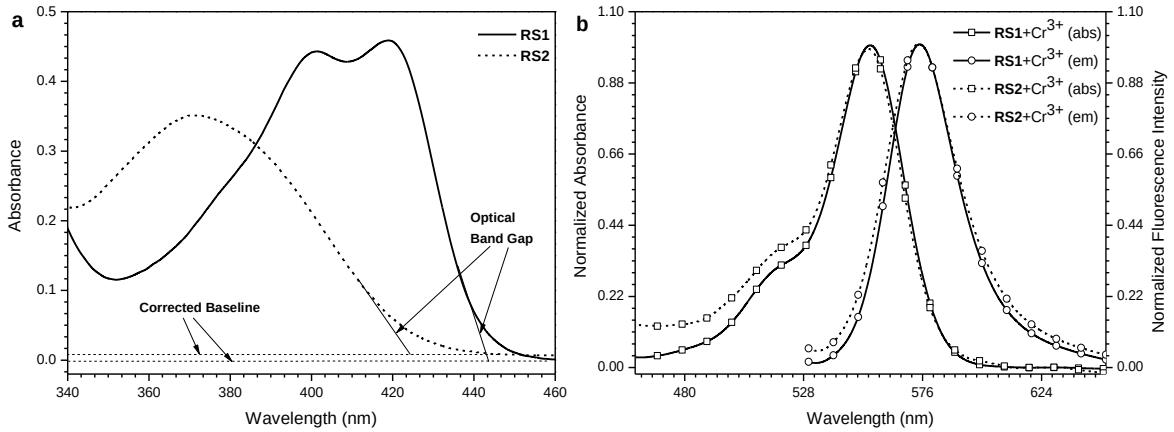


**Figure 6.29.** (a) Absorption spectra and optical band gaps of probes **RS1** and **RS2**, (b) UV-Vis absorption and fluorescence emission spectra of ligands and the corresponding $Cr^{3+}$ addition products in MeOH−DMSO (99:1 v/v).

energy for probes with Cr(III) can be determined from the cross point of absorption and emission onset lines (Figure 6.29). The corresponding wavelengths are 565 and 564 nm which are equal to 2.19 and 2.20 eV energy band gap for **RS1**+Cr(III) and **RS2**+Cr(III), respectively.

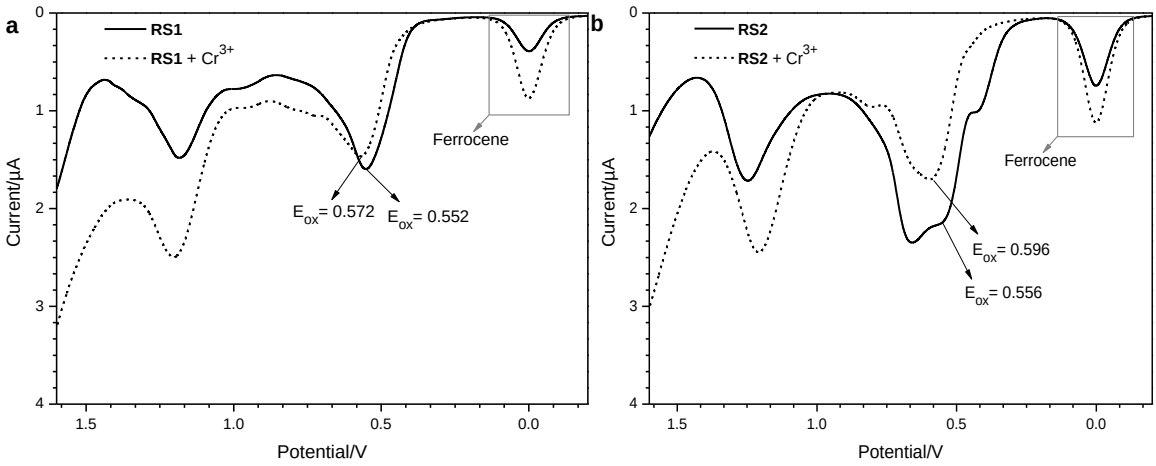


**Figure 6.30.** Differential pulse voltammograms recorded for **RS1** (a) and RS**2** (b), and the corresponding $Cr^{3+}$ addition products in MeOH−DMSO (99:1 v/v).

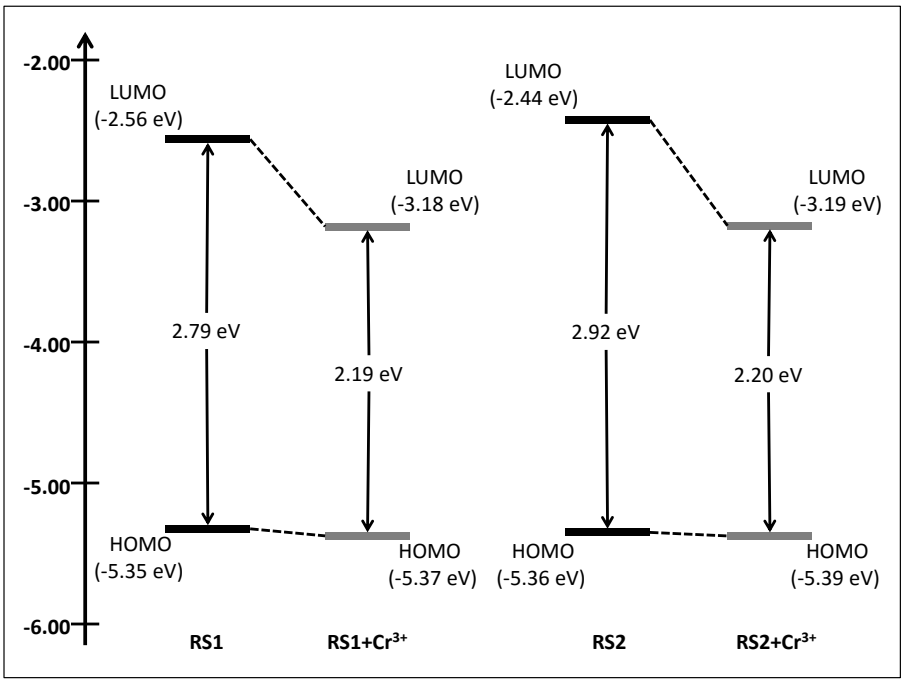


**Figure 6.31.** Energy level diagram of the probes and the corresponding $Cr^{3+}$ addition products.

The current-voltage curve for probes (**RS1** and **RS2**) in the absence and presence of Cr(III) regarding to Differential Pulse Voltammetric experiments are shown in Figure 6.30. Based on results, **RS1** and **RS2** alone show $E_{ox}$= 0.552 and 0.556 V which are equal to $E_{HOMO}$= −5.35 and −5.36 eV, respectively. The probes in the presence of Cr(III) ions show

$E_{ox}$= 0.572 and 0.596 V which are equal to $E_{HOMO}$= −5.37 (for **RS1**+$Cr^{3+}$) and −5.39 eV (for **RS2**+$Cr^{3+}$). By addition of Cr(III) ion changes are occurred in the oxidation potentials of probes, due to decrease in electron releasing nature of probe-$Cr^{3+}$ complexes. LUMO energy levels (for **RS1**, **RS2**, **RS1**+$Cr^{3+}$ and **RS2**+$Cr^{3+}$ are −2.56, −2.44, −3.18 and −3.19 eV, respectively) were estimated from HOMO and band gap energies.

This experiment proves that, increase in oxidation potential and decrease in band gap due to strong interactions between probes (**RS1** and **RS2**) and chromium ion. Figure 6.31 shows the energy diagram with HOMO/LUMO levels of probes alone and in the presence of Cr(III).

*6.2.3.4. Density functional theory (DFT) calculations*

To better understand the nature of the coordination of $Cr^{3+}$ with **RS1** and **RS2**, energy-optimized structures of **RS1**, **RS2** and its corresponding $Cr^{3+}$ complexes (Figure 6.32) were obtained on density functional theory (DFT) calculations at the B3LYP level using 6-31G** basis set for simple ionophores (**RS1** and **RS2**) and LANL2DZ basis set for metal complexes using the Gaussian 09 program [50].

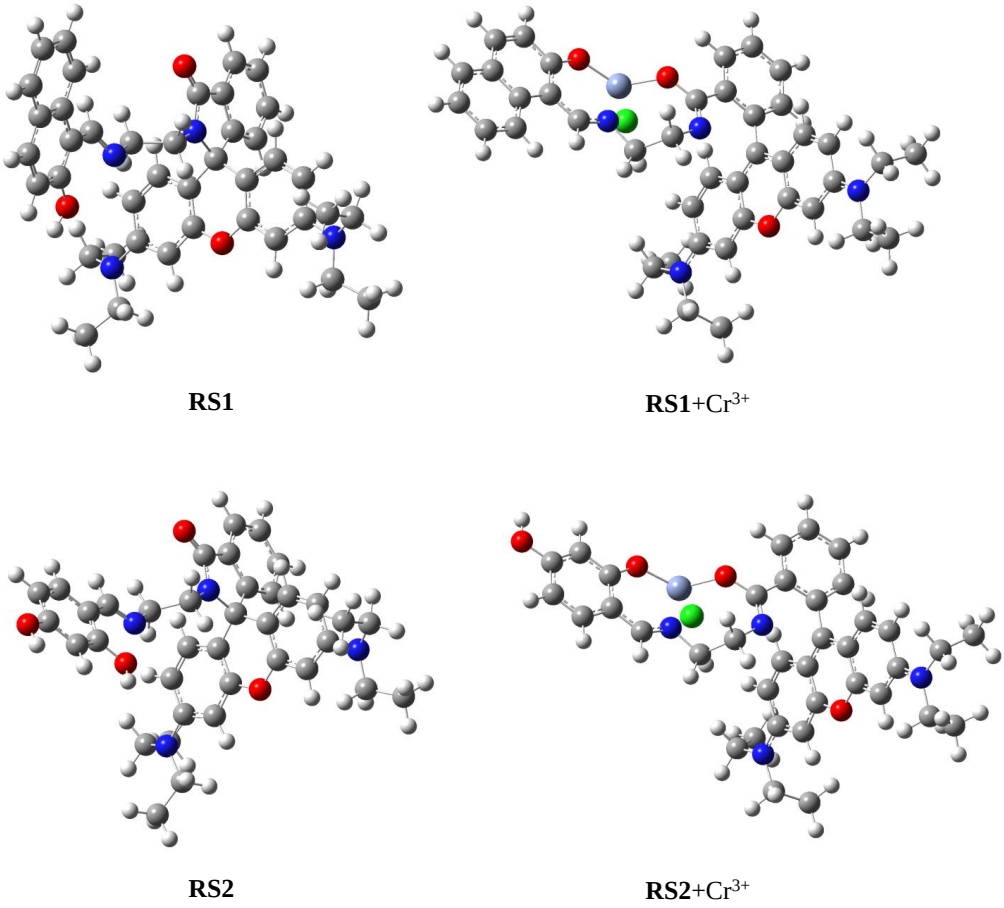


**Figure 6.32.** Optimized structures of **RS1** and **RS2** and the corresponding $Cr^{3+}$ addition products.

The spatial distributions and orbital energies of the highest occupied molecular orbital (HOMO) and the lowest unoccupied molecular orbital (LUMO) of **RS1**, **RS2** and its corresponding $Cr^{3+}$ complexes were also generated using this calculations (Figure 6.33). As results indicated, the HOMO is distributed over the xanthene moiety, while LUMO is spread on the naphthol part (in **RS1)** and phenylene part (in **RS2**). As result shown, the spirocyclic C–N bond breaks to facilitate the binding of $Cr^{3+}$ ion with the carbonyl oxygen atom of ligand. The sensors have also the capability to bind metal ion through phenolic –OH. The π electrons of HOMO orbitals of **RS1**–$Cr^{3+}$ and **RS2**–$Cr^{3+}$ are mainly located on the naphthol and phenylene moiety, respectively and the LUMO is mostly spread around the metal ion. The energy gaps between the HOMO and LUMO of the probes (**RS1** and **RS2**) and its corresponding $Cr^{3+}$ complexes were calculated as 3.906 eV, 4.433 eV, 2.727 eV and 2.719 eV, respectively. The results exhibited that the binding of $Cr^{3+}$ to probe lowered the HOMO−LUMO energy gap and stabilized the system. Thus, they show a favourable complexation according to proposed coordination.

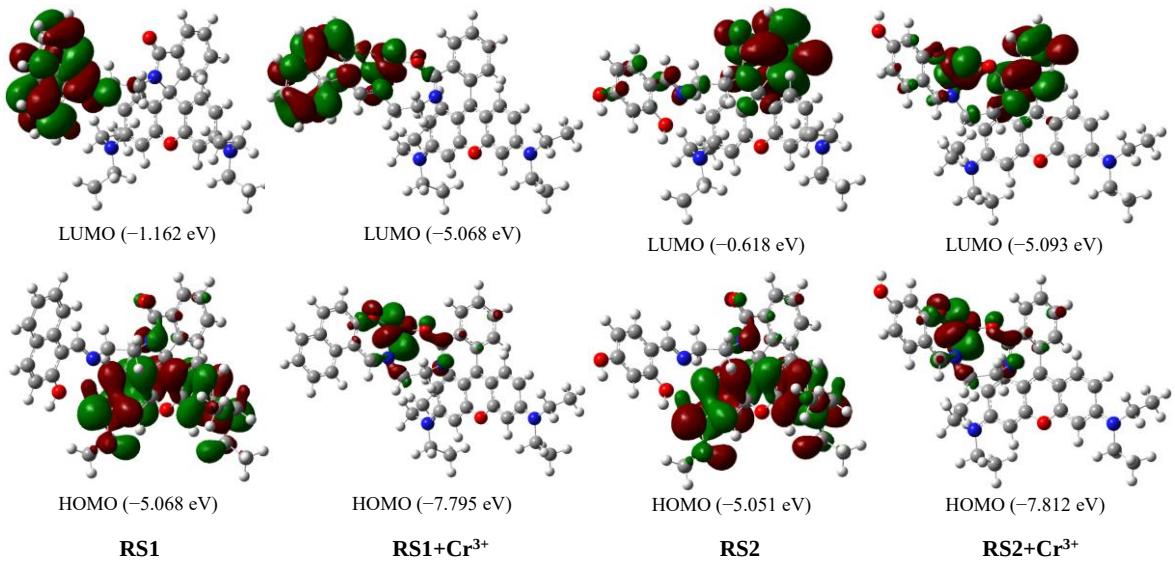


**Figure 6.33.** HOMO and LUMO orbitals of probes (**RS1** and **RS2**) and its corresponding $Cr^{3+}$ complexes.

*6.2.3.5. $^1H$ NMR titration*

Furthermore, to better understand the interaction between probe **RS1** and $Cr^{3+}$, proton NMR titration experiment was performed in the presence of various amounts of $Cr^{3+}$ in a DMSO-d6+$CD_3OD$ solvent (Figure 6.34). Upon complexation with $Cr^{3+}$ ion, the signals of imine proton ($H_g$) and an aryl proton ($H_a$) of 2-naphthol downfield shifted from 8.68 ppm to 8.79 ppm and 6.67 ppm to 6.82 ppm, respectively. The signals of protons $H_b$ and $H_c$ of 2-

naphthol were combined with each other and gave a single peak at 7.8 ppm. Similarly the signals of aryl-protons $H_i$, $H_j$ of rhodamine moiety and $H_e$ of 2-naphthol were come together then gave a typical complex signal. Upon addition of $Cr^{3+}$ ions, a combine signal of aryl-protons ($H_m$, $H_n$) of rhodamine moiety was splitted into two signals of $H_m$ and $H_n$. The distance between two signals of $H_d$ and $H_k$ of 2-naphthol and rhodamine moiety, respectively, is also varied upon addition of $Cr^{3+}$. Other signals of aryl-protons ($H_f$, $H_h$) of 2-naphthol and rhodamine moiety also downfield shifted because the strong coordination between **RS1** and $Cr^{3+}$ ion.

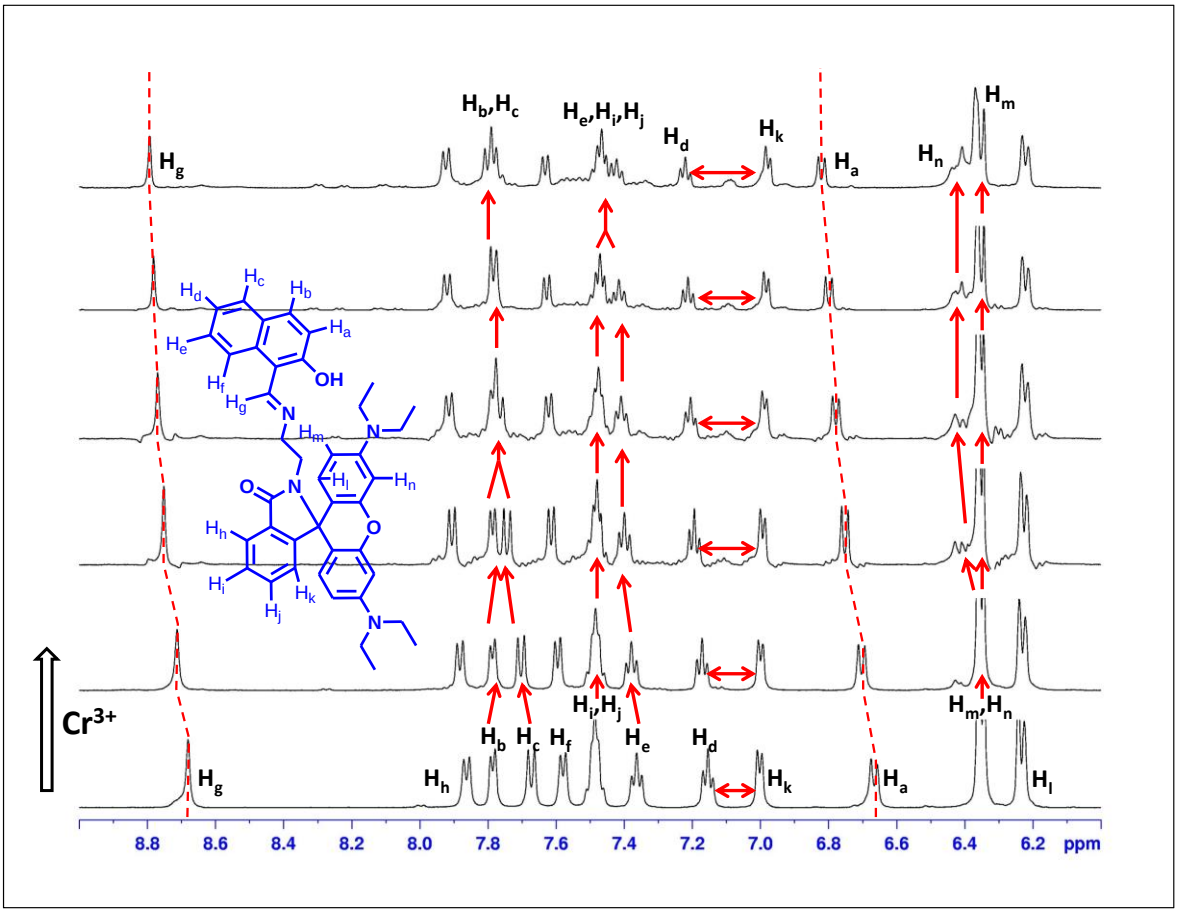


**Figure 6.34.** $^1H$ NMR titration of **RS1** with $Cr^{3+}$ in DMSO-d6+$CD_3OD$.

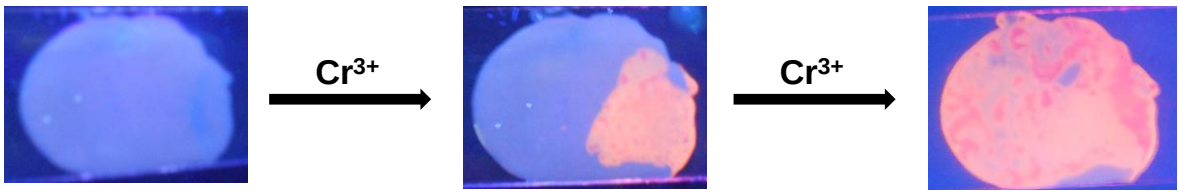


**Figure 6.35.** Fluorescence image of PVC polymeric thin film doped with ligand. The polymeric film on the glass slide was irradiated with a UV lamp.

To investigate the practical application of chemosensor (**RS1** and **RS2**), polymeric thin films were prepared [79]. Polyvinyl chloride (PVC) (100 mg), Bis(2-ethylhexyl)sebacate (as plasticizer) (200 mg) and probe were dissolved in THF (5 ml). The homogeneous mixture obtained after completion of dissolution of all ingredients was concentrated by evaporation of THF at room temperature. This homogeneous mixture was poured onto a clean glass surface. The solvent was allowed to evaporate and obtained non-fluorescent polymeric membrane sensor was used for $Cr^{3+}$ detection. A solution containing $Cr^{3+}$ in methanol (1 mM) was sprayed onto the film, on the solvent evaporation a strong fluorescent image appeared on the $Cr^{3+}$ exposed regions (Figure 6.35).

### 6.2.4. Conclusion

The newly synthesized rhodamine based fluoroionophores **RS1** and **RS2** exhibit a good selective and sensitive toward $Cr^{3+}$ ion over other tested metal ions in MeOH−DMSO (99:1 v/v). The binding ability and mode of chemosensors toward $Cr^{3+}$ were investigated through absorption, emission, electrochemical, ESI-MS and $^{1}H$ NMR experiments. The reported fluoroionophores exhibited a reversible absorption and fluorescence enhancement response to Cr(III) via a 1:1 binding mode at neutral pH. A polymeric thin film can be obtained by doping PVC with chemosensor **RS1** and **RS2**. Such a thin film can be used as a sensor to detect $Cr^{3+}$ with high selectivity.

## 6.3. Multifunctional Probe for $Cu^{2+}$, $Al^{3+}$ and $Fe^{3+}$ Ions

### 6.3.1. Introduction

In the last few years, the development of colorimetric and fluorescent chemosensors with high sensitivity and selectivity towards various transition and other metal ions are particularly attractive to current researchers due to its potential applications in the field of medicinal, clinical and environmental research [1–3]. Most of the metal ions play very important roles in living system and affect human health. $Cu^{2+}$, $Fe^{3+}$ and $Al^{3+}$ are essential nutrients for life, and both their deficiency and excesses are associated to various disorders [80–82].

Copper is the third most abundant metal in the human body [83] and an essential trace element in biological systems and its importance may be attributed to its redox nature [84]. Extreme ingestion of copper is harmful due to its ability to generate reactive oxygen species and it can interfere in cellular metabolism [85]. In addition, its deficiency is also related to various neurodegenerative disorders including Wilson's disease [86], Alzheimer's disease [87], Parkinson's disease [88] and Menkes syndrome [89]. Among many biologically important metals, Fe(III) is one of the most essential metals and play a crucial role in physiological processes, such as oxygen uptake [90], oxygen metabolism [91] and electron transfer [92]. Deficiency of $Fe^{3+}$ will lead to low oxygen delivery, which is related to low blood pressure, anaemia and decreased immunity [93, 94]. In contrast, excess iron can generate reactive oxygen species, which can cause damage to lipids, proteins and nucleic acids [95, 96]. Aluminum is the widespread metal and third most abundant element in the earth's crust [4]. Excess aluminum may cause damage to certain human tissues and cells, which lead to serious health problems like as Parkinson's disease and Alzheimer's disease [6].

Recently, anion recognition and sensing have become an area of huge research interest due to anions play an important roles in chemical, biological, industrial and environmental fields [11–13]. Among various anions, acetate and fluoride are of great concern due to their importance in numerous metabolic processes [15, 97], marine sediments [98], treatment of osteoporosis and the prevention of dental caries [18, 99, 100], and energy storage in biological systems [101].

Currently, many techniques are available for quantitative analysis of metal ions such as atomic absorption spectroscopy [23], inductively coupled plasma-mass spectroscopy [24], inductively coupled plasma emission spectrometry [25], neutron activation analysis [26], chromatography [27] and voltammetry [28]. Those techniques are found in various sources

such as food, biological, geological and industrial effluent. However, most of these methods require tedious sample preparation procedures, sophisticated instruments and high maintenance cost. On the other hand, colorimetric and fluorescent chemosensors have attracted great attention and provide considerable advantages over other techniques *via* their simplicity, low-cost, convenience, sensitivity, real-time monitoring and bared-eye visualization [29–31]. From the recent literature it is apparent that significant efforts have been made to develop selective and sensitive chemosensors of $Cu^{2+}$ [102–104], $Fe^{3+}$ [105, 106], $Al^{3+}$ [32–34], $AcO^{-}$ [35, 36] and $F^{-}$ [37–39]. On the other hand, the development of optical chemosensor capable of sequential recognition both of metal ion and anion is still one of the most challenging tasks [40, 41]. Recently, metal-based receptors have attracted much attention in the field of anion sensing [42, 43]. However, probes which can indicate $Cu^{2+}$, $Fe^{3+}$, $Al^{3+}$, $AcO^{-}$ and $F^{-}$ at the same time *via* a single molecular species have not been reported, and the colorimetric and fluorometric detection of these analytes in aqueous/mixed aqueous media is still rare.

In this section, we report the synthesis and characterisation of a new Rhodamine B-derived chemosensor based on a salicylaldehyde moiety, named **RH**. The sensing property of this ionophore was tested with a series of alkali, alkaline earth and transition metal ions in semi aqueous media, and it can differentiate $Cu^{2+}$, $Fe^{3+}$ and $Al^{3+}$ from other metal ions.

### 6.3.2. Experimental

*6.3.2.1. Reagents and apparatus*

Rhodamine B, metal salts and other commercially available chemicals were purchased from Merck and Aldrich and used without further purification. The melting point was measured using SRS OptiMelt Automated melting point system. The IR spectra were recorded on a PerkinElmer FT-IR spectrometer (USA) in the range 4000–400 $cm^{-1}$ with KBr. The NMR spectra were performed using a Bruker 500 MHz (USA), TMS as an internal standard, $CDCl_3$ is taken as solvent. The mass spectra were obtained on a Bruker-micrOTOF II (USA). The UV-Vis absorption and the Fluorescence emission spectra were recorded by using Shimadzu UV-2450 spectrophotometer (Japan) and Horiba FluoroMax-4 spectrofluorophotometer (Japan), respectively.

*6.3.2.2. Synthesis and characterization*

The synthetic route to Chemosensor (**RH**) was outlined in Scheme 6.5. It was prepared according to the literature method [48] and the structure was characterised by FT-IR, $^{1}H$ NMR, $^{13}C$ NMR and ESI mass.

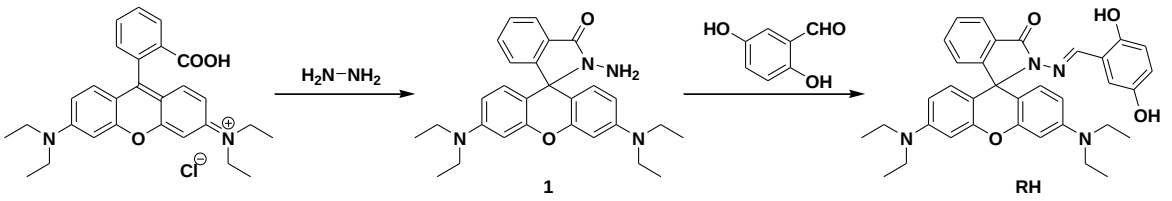


**Scheme 6.5.** Synthetic Pathways of **RH**.

**Compound 1:** Rhodamine B (2.0 g) was dissolved in 50 mL ethanol. Hydrazine hydrate (2.5 ml) was then added drop wise with vigorous stirring at room temperature. After the addition, the stirred solution was allowed to reflux about 6–8 h. The solution changed from dark pink to light orange. Then the mixture was cooled and solvent was removed under reduced pressure. 1 M HCl (about 50 mL) was added to the mixture in the flask to generate a clear red solution. After that, 1 M NaOH was added slowly with stirring until the pH of the solution reached 9–10. The resulting precipitate was filtered and washed 4–5 times with 15 mL water. After drying under reduced pressure, the reaction yielded 1.8 g **1** (95%) as pink solid. Mp: 176–178 °C; FT-IR (KBr), *v*, $cm^{-1}$: 1614 (C=O), 1379, 1118 (C−N), 1224, 1015 (C−O); $^{1}H$ NMR ($CDCl_3$, 500 MHz), $\delta$ (ppm): 1.16 (12H, t, $J$ = 6.5 Hz), 3.34 (8H, d, $J$ = 6.5 Hz), 3.62 (2H, s), 6.29 (2H, d, $J$ = 7.5 Hz), 6.42–6.47 (4H, m), 7.11 (1H, s), 7.45 (2H, s), 7.93 (1H, s); $^{13}C$ NMR ($CDCl_3$, 500 MHz), $\delta$ (ppm): 12.6, 44.4, 65.9, 98.0, 104.6, 108.1, 123.0, 123.8, 128.1, 130.0, 132.5, 148.9, 151.5, 153.8, 166.1. ESI-MS *m/z*: Calcd for $C_{28}H_{32}N_4O_2$ $(M+H)^+$: 457.2604, found: 457.2500.

**Compound RH:** Compound **1** (0.23 g, 0.5 mmol) and aldehyde (0.5 mmol) was dissolved in 20 mL absolute ethanol. The reaction mixture was stirred and refluxed overnight. Obtained solid was filtered and washed 3 times with 10 mL ethanol. After drying under reduced pressure, the reaction yielded 0.2 g **RH** (69%) as light pink color solid. Mp: 275–277 °C; FT-IR (KBr), *v*, $cm^{-1}$: 1622 (C=O), 1414, 1117 (C−N), 1221, 1019 (C−O); $^{1}H$ NMR ($CDCl_3$, 500 MHz), $\delta$ (ppm): 1.15 (12H, t, $J$ = 7.0 Hz), 3.31 (8H, q, $J$ = 7.0 Hz), 6.26 (1H, d, $J$ = 2.0 Hz), 6.28 (1H, d, $J$ = 2.0 Hz), 6.31 (1H, d, $J$ = 2.0 Hz), 6.35 (1H, s), 6.46 (2H, d, $J$ = 2.0 Hz), 6.48 (1H, s), 6.50 (1H, s), 6.94 (1H, d, $J$ = 8.5 Hz), 7.17 (1H, d, $J$ = 7.5 Hz), 7.51 (2H, qn, $J$ = 7.5 Hz), 7.96 (1H, d, $J$ = 7.5 Hz), 9.17 (1H, s), 11.00 (1H, s); $^{13}C$ NMR ($CDCl_3$, 500 MHz), $\delta$ (ppm): 12.6, 44.4, 66.7, 98.1, 103.5, 105.5, 107.2, 108.2, 112.2, 123.2, 124.1, 128.1, 128.6, 130.2, 133.1, 133.3, 149.1, 150.6, 153.6, 154.1, 159.2, 160.6, 164.1. ESI-MS *m/z*: Calcd for $C_{35}H_{36}N_4O_4$ $(M+H)^+$: 577.2815, found: 577.2664.

*6.3.2.3. UV-Vis and fluorescence spectra measurements*

Stock solutions of various metal ions/anions ($1 \times 10^{-3}$ M) were prepared in MeOH-$H_2O$ (50:50 v/v) solvent. A stock solution of **RH** ($1 \times 10^{-3}$ M) was prepared in MeOH−DMSO (99:1 v/v). The all solutions were then diluted to $2 \times 10^{-5}$ M with MeOH-$H_2O$ (50:50 v/v) solvent. All absorption and emission spectra were performed in a quartz optical cell of 1 cm optical path length at room temperature. During experiments with metal ions/anions, the concentration of each component inside the cuvette is maintained at 10 µM. In titration experiments with an increasing amount of metal ion ($Cu^{2+}$, $Fe^{3+}$ and $Al^{3+}$) or anion ($AcO^-$ and $F^-$), each time the solution of **RH** was maintained at 10 µM. Fluorescence measurements were carried out using excitation at 520 nm, and emission was recorded from 535 to 700 nm. Both excitation and emission slit widths were 1.0 nm.

### 6.3.3. Results and discussion

The selectivity, sensitivity and binding mode of chemosensor toward $Cu^{2+}$, $Fe^{3+}$ and $Al^{3+}$ were examined through visual inspection, absorption, emission, ESI-MS and DFT experiments.

*6.3.3.1. UV-Vis spectroscopic studies of **RH** with metal ions*

The interaction of **RH** with various metal ions such as $Ag^+$, $Al^{3+}$, $Ba^{2+}$, $Ca^{2+}$, $Cd^{2+}$, $Co^{2+}$, $Cr^{3+}$, $Cs^+$, $Cu^{2+}$, $Fe^{2+}$, $Fe^{3+}$, $Gd^{3+}$, $Hg^{2+}$, $K^+$, $Li^+$, $Mg^{2+}$, $Mn^{2+}$, $Na^+$, $Nd^{3+}$, $Ni^{2+}$, $Pb^{2+}$, $Sr^{2+}$ and $Zn^{2+}$ was carried out by UV-Vis absorption spectroscopic analysis. As observed in Figure 6.36a, the UV-Vis spectrum of probe **RH** in semi aqueous solvent (MeOH-$H_2O$; 50:50 v/v) exhibits two main bands centered at 275 and 324 nm. Upon addition of metal ions, a strong band appears at 555 nm for both $Cu^{2+}$ and $Al^{3+}$, while no significant changes were observed in 200–450 nm wavelength regions. On the other hand, a weak absorption band at 555 nm was noticed with $Fe^{3+}$. The other metal ions tested did not exhibit formation of any new band even in excess amount. The binding ability depends on size, charge and electron configuration of the metal ion and ligand, which are very suitable for the $Cu^{2+}$ and $Al^{3+}$ with probe **RH** to form a complex. The probe sense to $Fe^{3+}$ due to some of the coexistence properties. The observed color changes upon addition of metal ions tested were photographed and shown in Figure 6.36b. The development of the noticeable naked-eye detection of the magenta color in the probe upon metal addition involves a metal-induced delactonization of rhodamine. Upon complexation, colorless spirolactam form is converted into its colored ring-opened amide form [77].

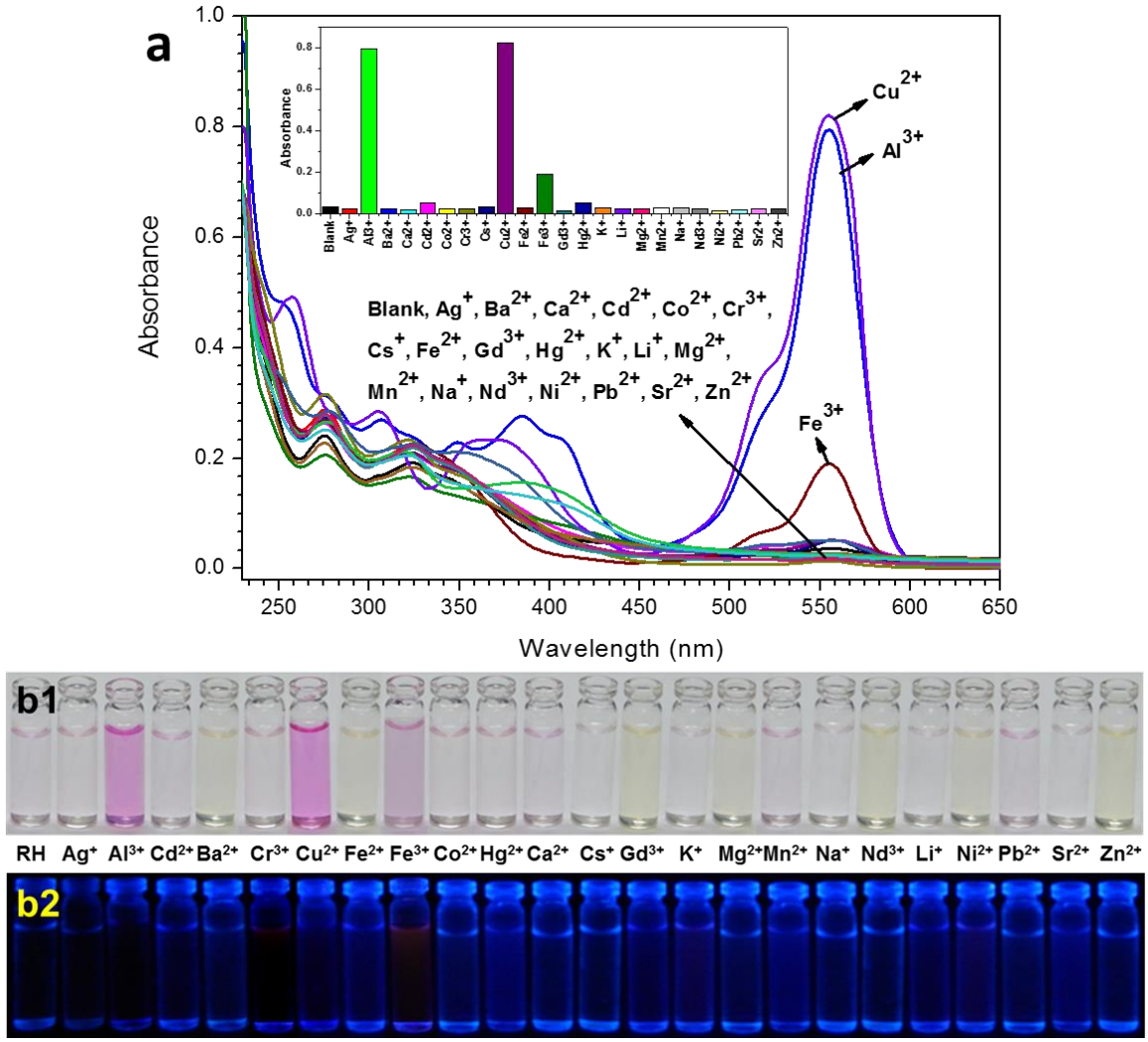


**Figure 6.36.** (a) UV-Vis spectrum of **RH** (10 µM) in the presence of various metal ions (above mentioned, 10 µM) in MeOH-$H_2O$ (50:50 v/v). Inset: A bar diagram showing the change in the absorbance of **RH** at $\lambda_{max}$ = 555 nm. (b) Photographs taken in room light (b1) and under UV light (b2).

To gain an insight into the sensing properties of **RH** as a receptor, a titration experiment was carried out with the gradual addition (0, 1, 2, 3, 4, 5, 6, 7, 8, 9, 10, 12, 14, 16, 18 and 20 µM) of metal ions ($Cu^{2+}$ and $Al^{3+}$) to the **RH** solution. As shown in Figure 6.37, an increase in the absorbance band centered at 555 nm with a shoulder at ~520 nm was observed upon progressive addition of metal ions, implicating the formation of a metal complex with **RH**. Simultaneously, a new band centered at 370 (for $Cu^{2+}$) and 385 nm (for $Al^{3+}$) gradually increased with the concentration of metal ion. The sensor showed a nice linear relationship between the absorbance at 555 nm and the concentration of metal ions ($Cu^{2+}$ and $Al^{3+}$) from 0.0 to 10 µM (Figure 6.37, right inset), suggests that sensor **RH** is potentially applicable for quantitative analysis of $Cu^{2+}$ and $Al^{3+}$ with a large dynamic range.

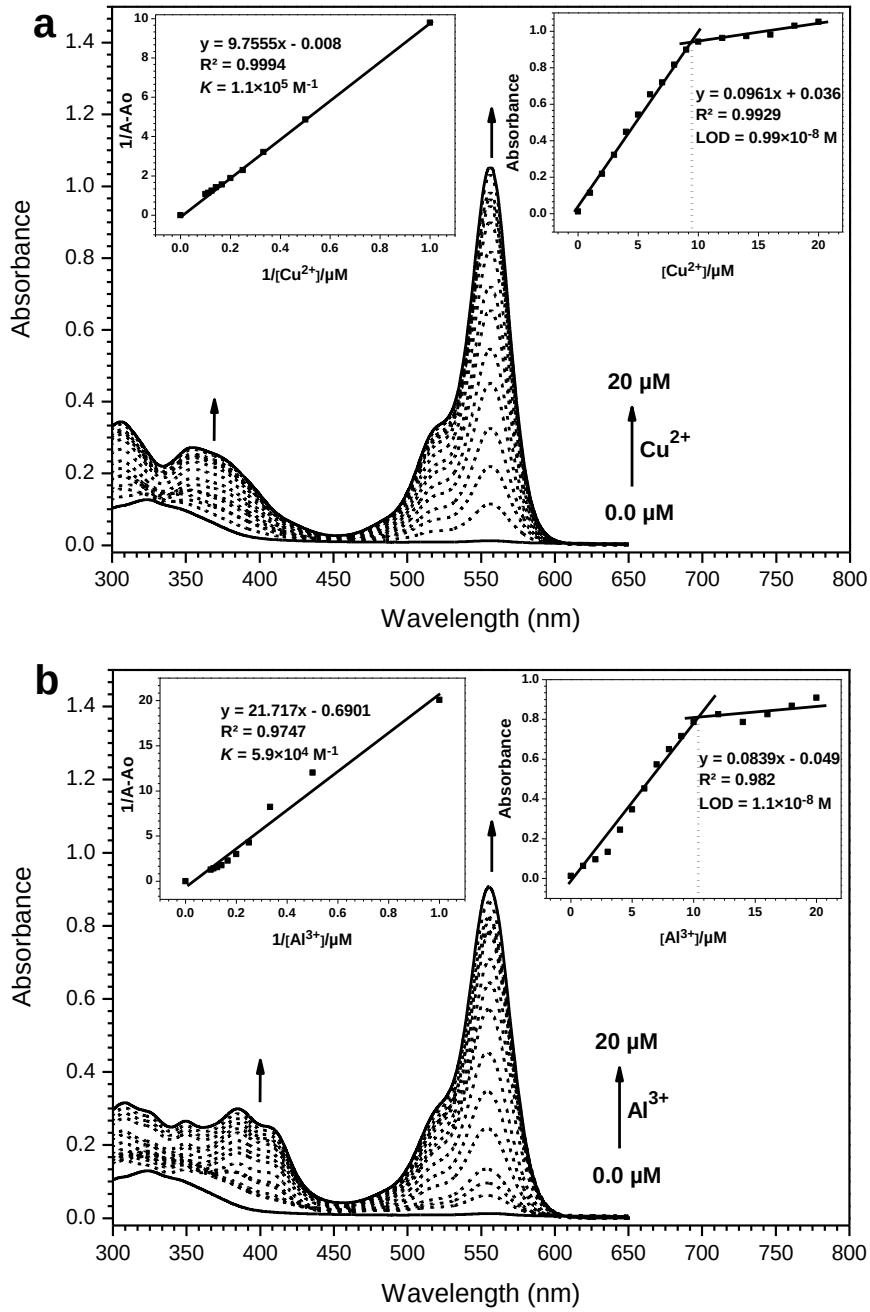


**Figure 6.37.** UV-Visible absorbance spectrum changes of sensor **RH** (10 μM) at increasing concentration of $Cu^{2+}$ (a) and $Al^{3+}$ (b) ion (0, 1, 2, 3, 4, 5, 6, 7, 8, 9, 10, 12, 14, 16, 18, 20 μM). Inset: Variation of $1/(A\text{-}A_0)$ as a function of 1/[M] (left) and the plot of absorbance of **RH** at $\lambda_{max}$ of 555 nm as a function of concentration of metal ion added (right).

No further significant changes in the absorbance of the system were observed at above 10 μM (1 equiv.) of metal ions. The binding constant for the formation of the metal complex was estimated on account of the change in the absorbance at 555 nm by considering a 1 : 1 binding stoichiometry and found to be $1.1 \times 10^6$ $M^{-1}$ and $5.9 \times 10^4$ $M^{-1}$ for **RH**–$Cu^{2+}$ and **RH**–$Al^{3+}$, respectively using Benesi-Hildebrand equation (Figure 6.37, left inset). Also, the

detection limit of $Cu^{2+}$ and $Al^{3+}$ ions was determined from the absorbance titration profile as $0.99 \times 10^{-8}$ M and $1.1 \times 10^{-8}$ M, respectively based on 3σ/slope.

The binding stoichiometry of **RH** towards $Cu^{2+}$ and $Al^{3+}$ was achieved from the Job's method on the basis of absorbance. In which, Job's plot was produced by continuously varying the mole fraction of metal ion from 0 to 1 in a solution of [**RH**] + [Metal ion] with a total concentration of 10 μM. The Job's plot analysis revealed that the maximum absorbance was observed when mole fraction of metal ion is around 0.5, which indicates a 1 : 1 stoichiometry for both **RH**–$Cu^{2+}$ and **RH**–$Al^{3+}$ complexes (Figure 6.38).

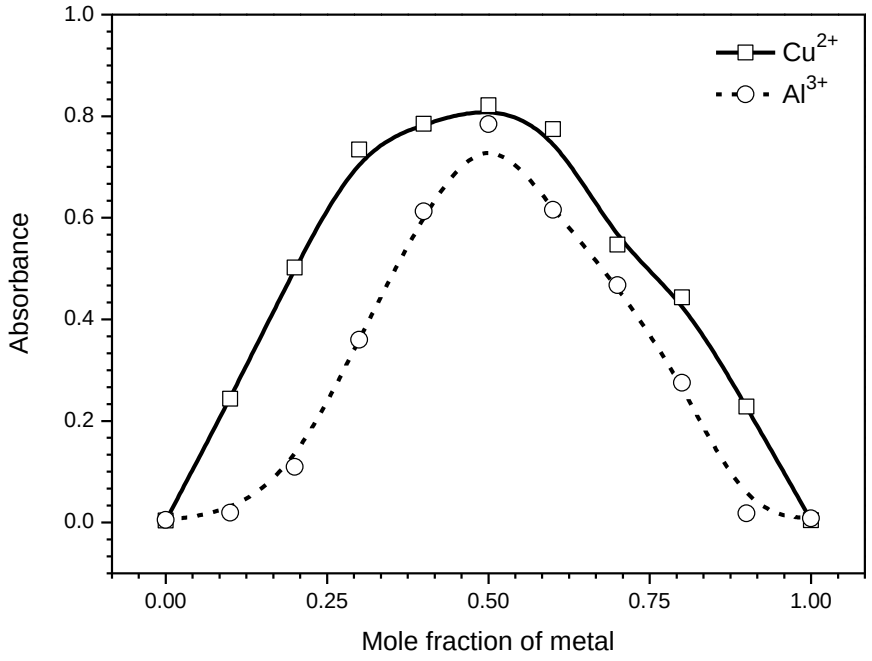


**Figure 6.38.** Job plots for the binding of $Cu^{2+}$ and $Al^{3+}$ with **RH**, where absorbance at $\lambda_{max}$ of 555 nm was plotted against the mole fraction of metal ion.

The effect of pH on the absorbance of sensor **RH** and its metal complexes was investigated in MeOH-$H_2O$ (50:50 v/v). The absorbance (at 555 nm) of **RH** in the presence and absence of metal ion ($Cu^{2+}$ and $Al^{3+}$) at different pH values (2–10) were recorded (Figure 39a). When the pH of **RH** and its $Al^{3+}$ complex was adjusted to acidic (2–5), obvious enhancement in the absorbance was observed, demonstrating that the probe **RH** is a sensitive acid-responsive probe and the large fluorescence enhancement is due to the $H^+$-induced spirocyclic ring opening [107]. **RH**–$Cu^{2+}$ did not show any significant spectral changes in acidic conditions. **RH** and its $Al^{3+}$ complex did not produce any distinct and characteristic absorbance in basic pH range (7–10), which indicated that the spirolactam form of **RH** was the predominant species. **RH**–$Cu^{2+}$ is the non-destructive species in basic conditions. The absorbance of **RH** and the corresponding metal complexes were varied at pH 2–10 (for $Cu^{2+}$)

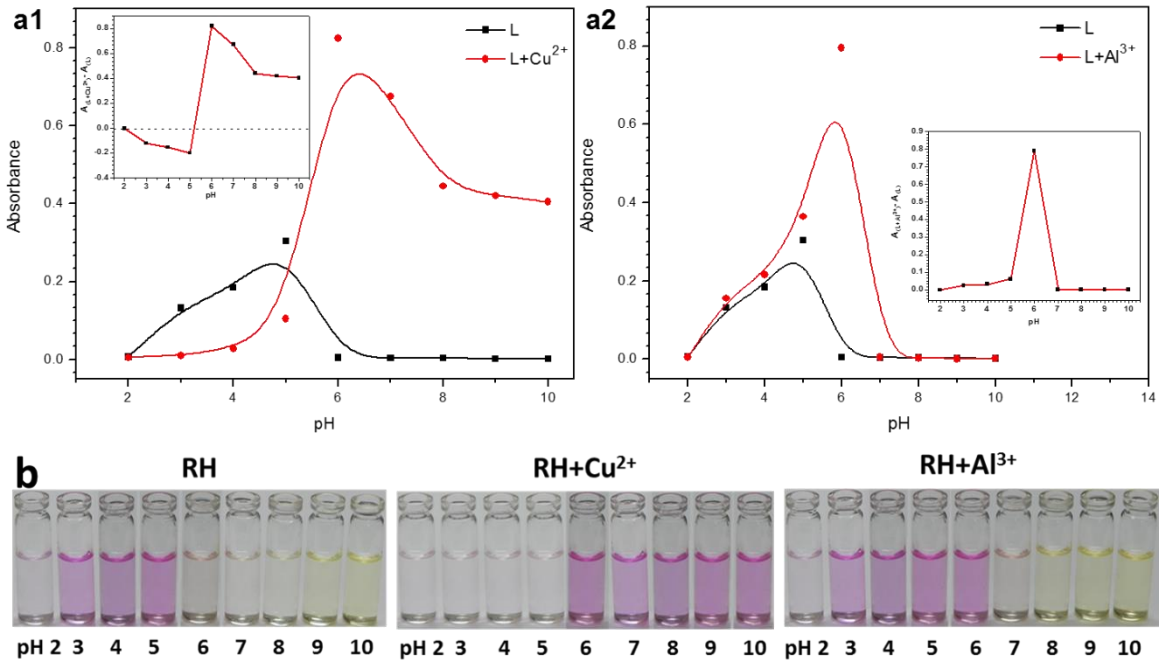


**Figure 6.39.** (a) UV-Vis absorbance (at $\lambda_{max}$ = 555 nm) spectral changes of **RH** and its corresponding $Cu^{2+}$ and $Al^{3+}$ complexes with pH variations. (b) Photographs of **RH** and its corresponding metal complexes at different pH conditions in daylight.

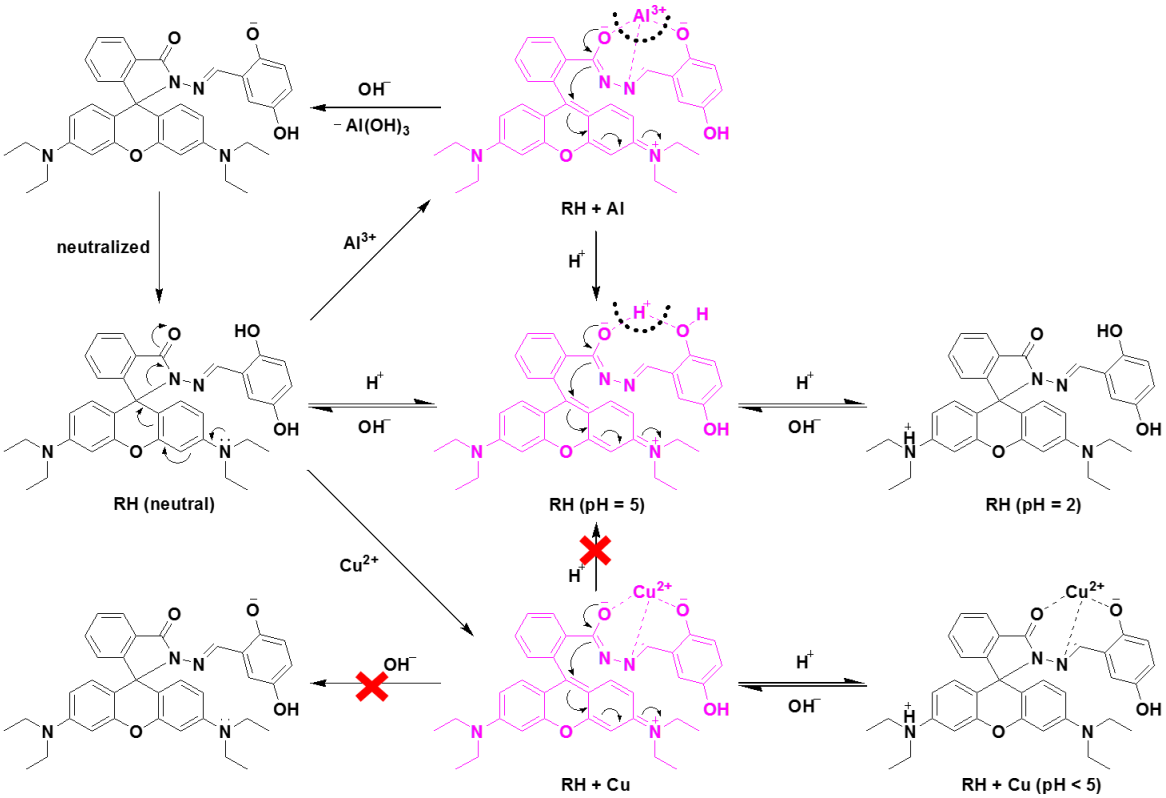


**Scheme 6.6**. Spirolactam ring-opening and closing mechanism of **RH** and its corresponding $Cu^{2+}$ and $Al^{3+}$ complexes upon pH variation.

and neutral (for $Al^{3+}$). Also, the color changes at different pH could easily be detected by the naked-eye (Figure 6.39b). All these are mainly due to the weaker coordination ability and stronger hydration ability of $Al^{3+}$ ions compared to $Cu^{2+}$ ions [108, 109], and $Al^{3+}$ is hard-acid and it can easily be effected in the basic environment [110]. Thus, it does not favour in forming complex in basic range than $Cu^{2+}$. $Cu^{2+}$ has a specific high thermodynamic affinity for typical N-donor ligands and fast metal-to ligand binding kinetics [111]. As Shown in Scheme 6.6, the probe is colorless at neutral pH. Probe **RH** produce color in the presence of $Cu^{2+}$ and $Al^{3+}$ due to conversion of spirolactam form to metal induced ring-opened amide form. When pH of the probe and its corresponding $Al^{3+}$ complex was decreased to 5, the colored $H^+$-induced spirocyclic ring opening form was generated. Furthermore at strong acidic conditions (pH = 2), the H-bonding interaction was effectively quenched by the increasing of $H^+$. The diethylamino group was possibly protonated and the electron deficient nature of the xanthene moiety was also favorable for the nucleophilic attraction of the amide moiety, thus inducing the ring-closed reaction to give the colorless protonated form [112]. At basic range, the $Al^{3+}$ complex of probe is converted into its initial colorless spirolactam form due to dissociation of complex. $Cu^{2+}$ complex shows quite opposite to $Al^{3+}$ complex, it forms non-destructive complex with **RH** in a wide pH range (2–10), but it shows color only in neutral and basic conditions due to $Cu^{2+}$-induced opening of the rhodamine ring. On the other hand, the colorless predominant complex is formed in acidic conditions due to the protonated form of complex.

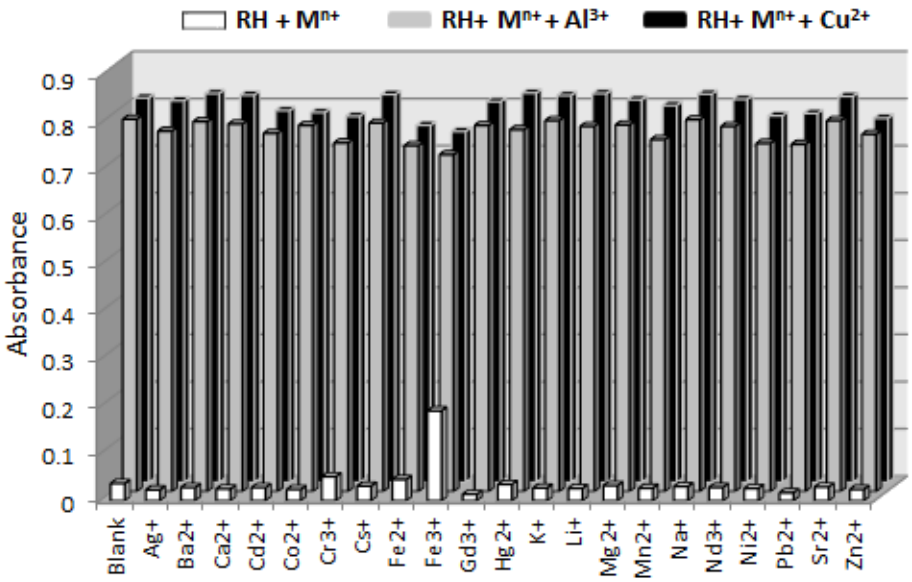


**Figure 6.40.** UV-Vis absorbance (at $\lambda_{max}$ = 555 nm) of the probe to various metal ions in the absence and presence of $Cu^{2+}/Al^{3+}$.

To further estimate the selectivity of **RH** for $Cu^{2+}$ and $Al^{3+}$, the competitive experiment in the presence of other metal ions including $Ag^{+}$, $Ba^{2+}$, $Ca^{2+}$, $Cd^{2+}$, $Co^{2+}$, $Cr^{3+}$, $Cs^{+}$, $Fe^{2+}$, $Fe^{3+}$, $Gd^{3+}$, $Hg^{2+}$, $K^{+}$, $Li^{+}$, $Mg^{2+}$, $Mn^{2+}$, $Na^{+}$, $Nd^{3+}$, $Ni^{2+}$, $Pb^{2+}$, $Sr^{2+}$ and $Zn^{2+}$ under the same conditions was conducted (Figure 6.40). It is noticeable that the competitive metal ions did not lead to any significant changes in the absorbance of the **RH**–$Cu^{2+}$ and **RH**–$Al^{3+}$ complexes when compared with the results obtained in the presence or absence of other metal ions (above mentioned). The distinct selectivity for $Cu^{2+}$ and $Al^{3+}$ ions is probably due to a combination of several factors, such as the suitable coordination geometry conformation of ligand and the ionic radius of the metal ion. This experiment established that the presence of other metal ions does not interfere with the detection of $Cu^{2+}$ and $Al^{3+}$, and it could be used as a selective chemosensor for $Cu^{2+}$ and $Al^{3+}$.

*6.3.3.2. Fluorescence spectroscopic studies of **RH** with metal ions*

The emission spectra of **RH** were recorded in the absence and presence of various metal ions as mentioned in UV-Vis spectroscopic studies, upon excitation of 520 nm. Firstly, sensor **RH** did not show any emission band, indicating that the spirocyclic form was retained in the solution. However, addition of $Fe^{3+}$ to this solution induced a significant increase in the fluorescence response (Figure 6.41). A strong new emission band at 587 nm was formed,

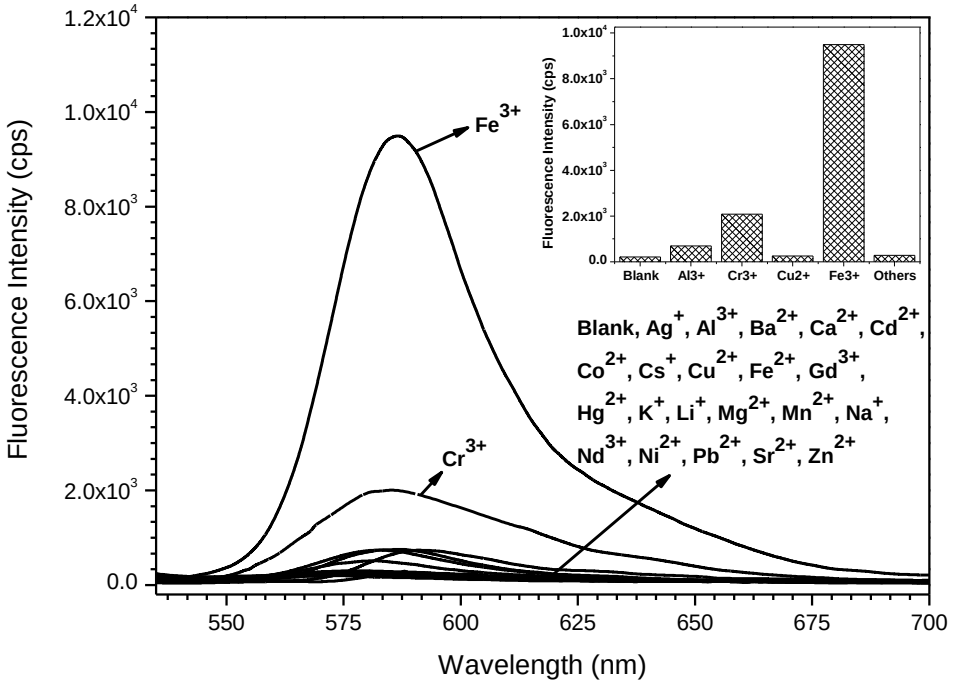


**Figure 6.41.** Emission spectra for the probe **RH** (10 μM) in the absence and presence of 1 equiv. of various metal ions in MeOH-$H_2O$ (50:50 v/v). Inset: Fluorescence response of **RH** to the above mentioned metal ions, the intensity was monitored at 587 nm.

and up to about 43-fold enhancement in the fluorescence intensity was noted, indicating that the $Fe^{3+}$ ions induced the formation of the strongly fluorescent, ring-opened **RH**–$Fe^{3+}$ complex. The fluorescence spectra showed that $Cr^{3+}$ also induced a noticeable fluorescence enhancement. Because, $Fe^{3+}$ and $Cr^{3+}$ show similar electron configuration as $Fe^{3+}$ contains half-filled $t_{2g}$ and $e_g$, $Cr^{3+}$ contains half-filled $e_g$ orbitals. No significant fluorescence response of **RH** occurred in the presence of other metal ions, except for $Fe^{2+}$ and $Hg^{2+}$, which displayed a weak response. The spectral change is also accompanied by a visual color change from colorless to fluorescent pink (Figure 6.36b).

A fluorescence titration experiments were carried out to attain a clear knowledge about sensing nature of **RH** with the continuing addition of $Fe^{3+}$ (0, 1, 2, 3, 4, 5, 6, 7, 8, 9, 10, 12, 14, 16, 18 and 20 μM). Upon progressive addition of $Fe^{3+}$ ion, a gradual increment in the fluorescence at 587 nm was observed (Figure 6.42). **RH** showed a fine linear relationship ($R^2 = 0.98$) between the emission intensity at 587 nm and the $Fe^{3+}$ concentration from 0.0 to 10 μM (Figure 6.42, bottom inset), no considerable changes in the fluorescence emission intensity of receptor were observed upon further addition of $Fe^{3+}$ ion at above 10 μM. By considering a 1 : 1 binding stoichiometry between **RH** and $Fe^{3+}$ ion and using Benesi-Hildebrand equation, the binding constant of this complex was estimated on account of the change in the fluorescence intensity at 587 nm and found to be $5.0 \times 10^4\ M^{-1}$ (Figure 6.42, top inset). Based on 3σ/slope, the detection limit of $Fe^{3+}$ ion was determined from the fluorescence titration profile as $1.9 \times 10^{-8}$ M (Figure 6.42, bottom inset). The binding stoichiometry of **RH** towards $Fe^{3+}$ was achieved from the Job's method on the basis of fluorescence and the results revealed that the maximum emission was observed when mole fraction of $Fe^{3+}$ is around 0.5, which indicates a 1 : 1 stoichiometry for **RH**–$Fe^{3+}$ complex (Figure 6.43).

The investigation of pH effect on the sensing behavior of RH towards $Fe^{3+}$ was carried out in MeOH-$H_2O$ (50:50 v/v). The fluorescence intensity (at 587 nm) of RH in the presence and absence of $Fe^{3+}$ at various pH (2.0–10.0) were recorded (Figure 6.44a). When the pH was adjusted to acidic (2–5), a gradual enhancement in the fluorescence was observed due to the activation of the ring-opening process of the spirocyclic moiety. **RH** and its $Fe^{3+}$ complex did not produce any distinct and characteristic fluorescence in basic pH range (7–10) because of its "ring-closed" form. Thus, **RH**–$Fe^{3+}$ complex did not produce any significant spectral changes with **RH** in acidic and basic conditions. The fluorescence intensity of **RH** and the corresponding $Fe^{3+}$ complex was varied at pH ~6. Also, the color changes at different pH could easily be detected by the naked-eye (Figure 6.44b).

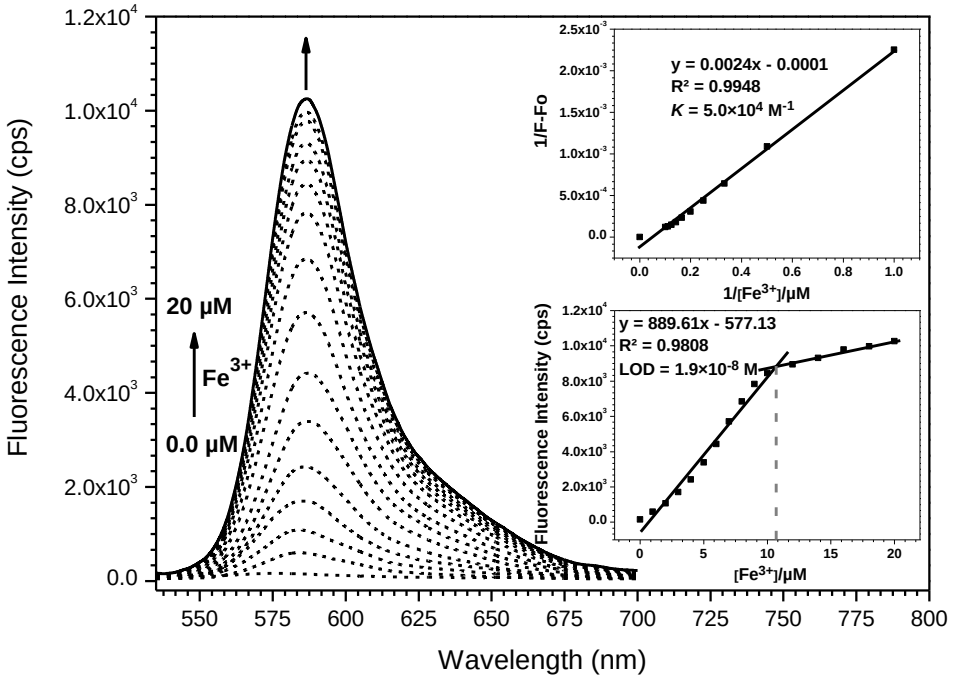


**Figure 6.42.** Fluorescence spectrum changes of sensor **RH** (10 μM) at increasing concentration of $Fe^{3+}$ (0, 1, 2, 3, 4, 5, 6, 7, 8, 9, 10, 12, 14, 16, 18, 20 μM) with 520 nm excitation. Inset: Variation of $1/(F\text{-}F_0)$ as a function of $1/[Fe^{3+}]$ (top) and fluorescence enhancement change at $\lambda_{max}$ of 587 nm as a function of concentration of $Fe^{3+}$ (bottom).

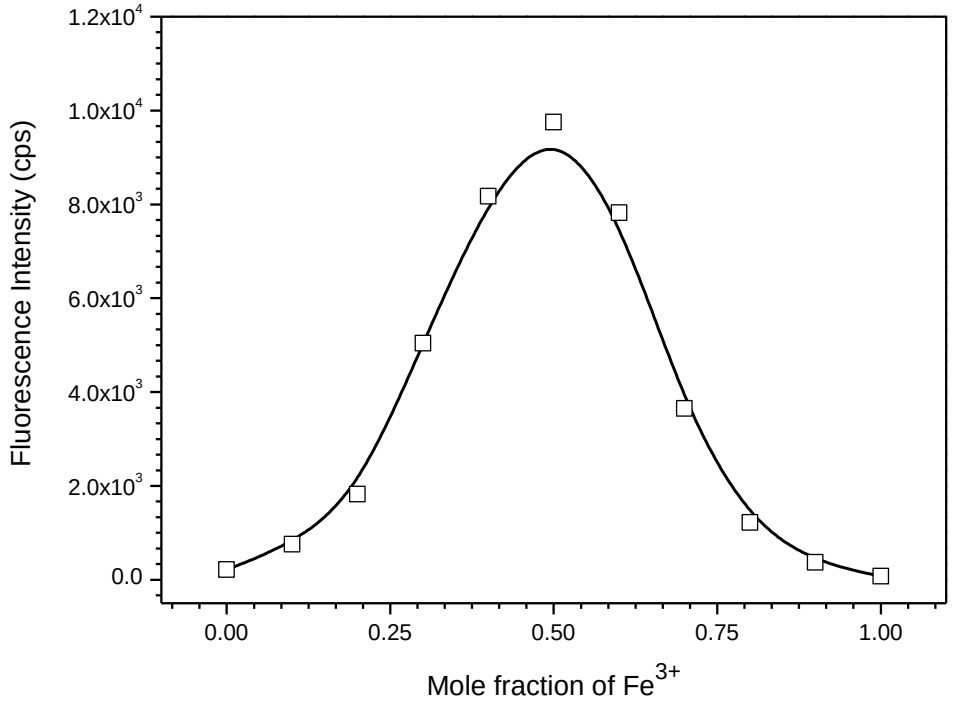


**Figure 6.43.** Job plot for the binding of $Fe^{3+}$ with **RH**, where fluorescence intensity at 587 nm was plotted against the mole fraction of $Fe^{3+}$.

To further estimate the selectivity of **RH** for $Fe^{3+}$, the competitive experiment in the presence of other metal ions (above mentioned) under the same conditions was conducted. It is noticeable that the competitive metal ions (except $Cu^{2+}$ and $Al^{3+}$) did not lead to any significant changes in the fluorescence of the **RH**–$Fe^{3+}$ complexes when compared with the results obtained in the presence or absence of other metal ions, while $Cu^{2+}$ and $Al^{3+}$ can interfere the Fe(III)-induced fluorescence response (Figure 6.45).

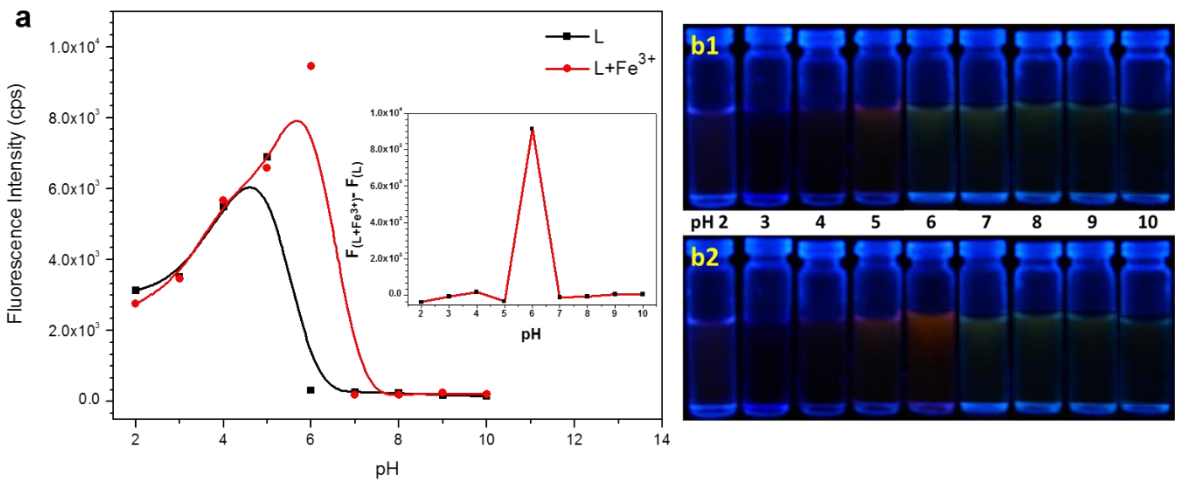


**Figure 6.44.** (a) Fluorescence emission (at $\lambda_{max}$ = 587 nm) spectral changes of **RH** and its corresponding $Fe^{3+}$ complex with pH variations. Photographs of **RH** in the absence (b1) and presence (b2) of $Fe^{3+}$ at different pH conditions under UV light.

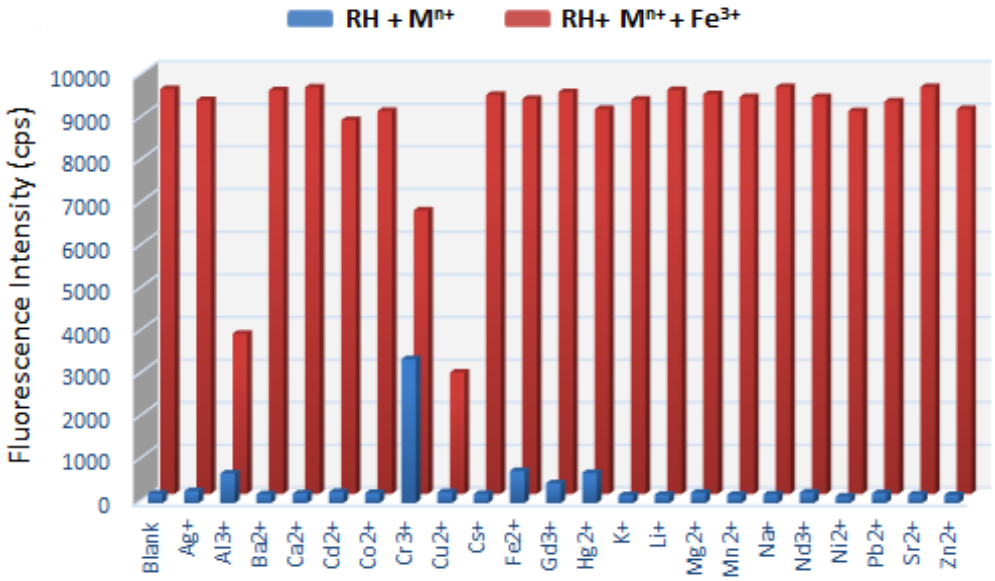


**Figure 6.45.** Fluorescence emission (at $\lambda_{max}$ = 587 nm) response of the probe to various metal ions in the absence and presence of $Fe^{3+}$.

*6.3.3.3. ESI mass analysis*

To better understand the binding mode of **RH** towards $Cu^{2+}$, $Al^{3+}$ and $Fe^{3+}$, ESI mass spectra of probe in the presence of metal ion was performed (Figure 6.46). The observed mass peak at *m/z* 638.2003, 664.2340 and 693.1902 corresponding to [**RH** + Cu − H]$^+$ (calculated: 638.1954), [**RH** + Al + $NO_3$ − H]$^+$ (calculated: 664.2352) and [**RH** + Fe + $NO_3$ − H]$^+$ (calculated: 693.188), respectively. The mass data therefore confirmed the binding of metal ion ($Cu^{2+}$, $Al^{3+}$ and $Fe^{3+}$) to **RH** with 1 : 1 stoichiometry.

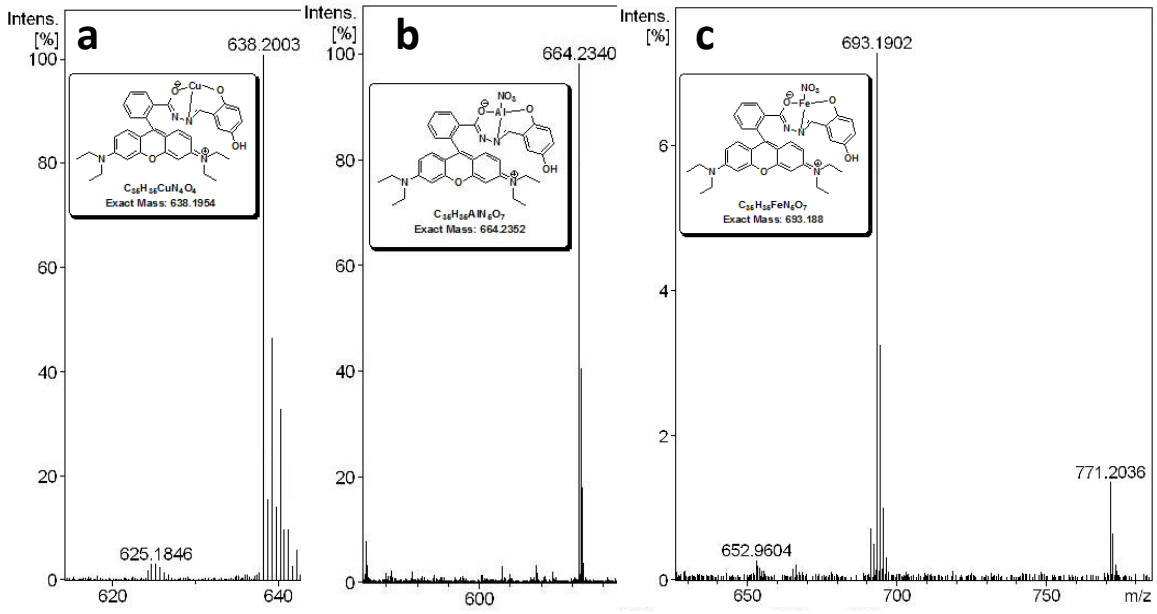


**Figure 6.46.** ESI-MS of **RH** upon addition of $CuCl_2.2H_2O$, $Al(NO_3)_3.9H_2O$ and $Fe(NO_3)_3.9H_2O$ in MeOH.

*6.3.3.4. Density functional theory (DFT) calculations*

To better understand the nature of the coordination of $Cu^{2+}$, $Al^{3+}$ and $Fe^{3+}$ with **RH**, energy-optimized structures of **RH** and its corresponding metal complexes (Figure 6.47) were obtained on density functional theory (DFT) calculations at the B3LYP level using 6-31G** basis set for simple receptor (**RH**) and LANL2DZ basis set for metal complex using the Gaussian 09 program [50]. The spatial distributions and orbital energies of the highest occupied molecular orbital (HOMO) and the lowest unoccupied molecular orbital (LUMO) of **RH** and corresponding metal complexes were also generated using this calculations. As shown in Figure 6.47, the HOMO is spread over the whole molecule, whereas LUMO is distributed on the substituted spirolactam ring in **RH**. As result shown, the spirocyclic C–N bond breaks to facilitate the binding of metal ion with the carbonyl oxygen atom of ionophore. The π electrons of HOMO orbitals of **RH**–$Cu^{2+}$ and **R**H–$Al^{3+}$ are mainly located

over the whole molecule and xanthene moiety respectively, while the π electrons are spread around the metal ion in **RH**–$Fe^{3+}$. The LUMO is distributed on the xanthene moiety in **RH**–$Cu^{2+}$ and **RH**–$Fe^{3+}$, whereas they are spread over the substituted spirolactam ring in **RH**–$Al^{3+}$. The energy gaps between the HOMO and LUMO of the free ligand and its corresponding metal complexes of $Cu^{2+}$, $Al^{3+}$ and $Fe^{3+}$ were found to be 3.782 eV, 2.363 eV, 0.89 eV and 2.731 eV, respectively. The results exhibited that the binding of $Fe^{3+}$ to probe lowered the HOMO-LUMO energy gap and reduction in the energy gap can explain the red-shift of the emission spectra of the $Fe^{3+}$ complex over **RH**. Thus, they show a favourable complexation according to proposed coordination.

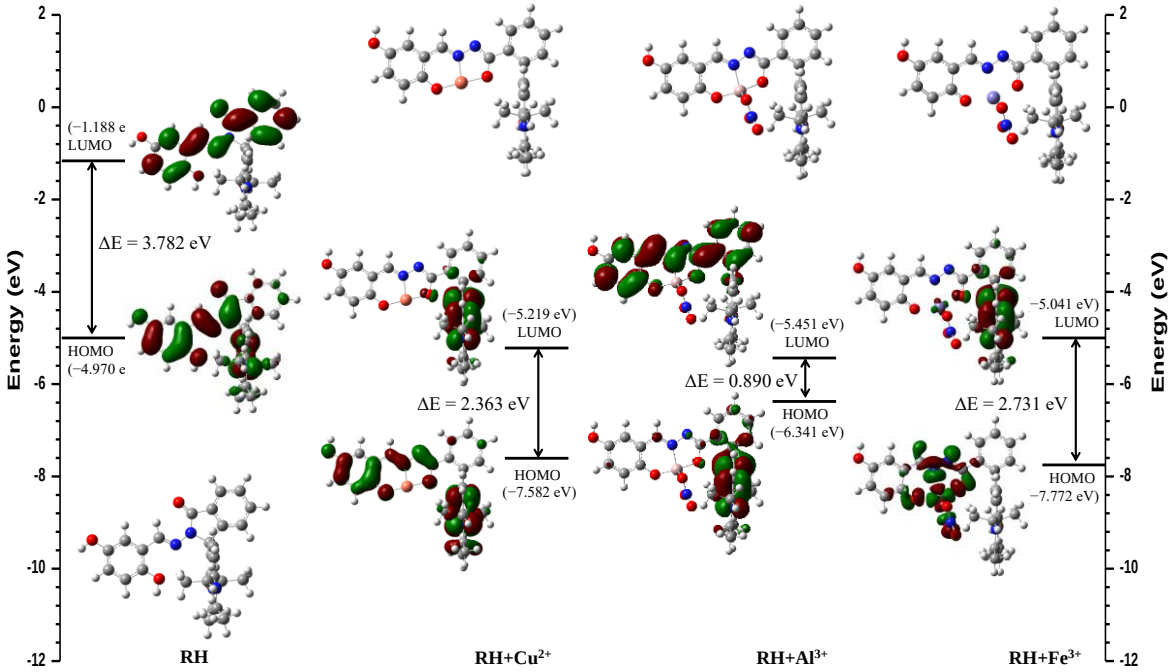


**Figure 6.47.** Energy diagram of HOMO and LUMO orbitals of **RH** and its corresponding metal complexes calculated at the DFT level using a B3LYP/6-31G** basis set.

The energy levels of HOMO and LUMO of receptor and fluorophore in the chemosensor play an important role in this mechanism. The simple molecule is non-fluorescent that may due to the receptor unit acts as the electron donating unit and the PET process is activated via the electron transfer from fulfilled HOMO of the receptor unit to the semi vacant ground state orbital of the fluorophore. This process blocks the usual relaxation pathway of excited fluorophore and quenches emission. When it bind with $Al^{3+}$ or $Cu^{2+}$, there may not be major changes in the energy levels. That is why the complex is non-fluorescent. On the other hand, the fluorescent nature of the $Fe^{3+}$ complex could be due to the donor orbital of receptor unit can be controlled or somehow stabilized.

*6.3.3.5. UV-Vis and fluorescence spectroscopic studies of **RH**–$Al^{3+}$ towards various anions*

Further, we studied the influence of different anions on the dissociation of the **RH**–$Al^{3+}$ complex to regenerate free **RH**. Absorbance spectroscopic experiments were carried out with **RH**–$Al^{3+}$ complex in the presence of sodium salts of various physiological and environmental important anions such as $Br^-$, $Cl^-$, $I^-$, $NO_3^-$, $SCN^-$, $SO_4^{2-}$ and $PO_4^{3-}$. As shown in Figure 6.48, the noticeable changes were observed after the addition of 5 equiv. of $AcO^-$/$F^-$ to the solution containing the **RH**–Al(III) complex, while other competitive anion species induced negligible spectral changes under the same conditions. Meanwhile, the pink color of **RH**–$Al^{3+}$ solution returned to colorless upon addition of $AcO^-$/$F^-$, indicating that **RH**–$Al^{3+}$ ensemble can serve as a 'naked-eye' indicator for $AcO^-$ and $F^-$ anions (Figure 6.48).

To better understand the nature of the **RH**–$Al^{3+}$ complex in the presence of the interfering anions, a solution of **RH** containing 1 equiv. of $Al^{3+}$ was titrated with the gradual amount of anions ($AcO^-$ and $F^-$). The UV-Vis spectral pattern of the titration experiments (Figure 6.49) displayed a reverse trend to the titration curve obtained with $Al^{3+}$ (Figure 6.37), which may offer evidence of the regeneration of **RH** from its complex with $Al^{3+}$ in the

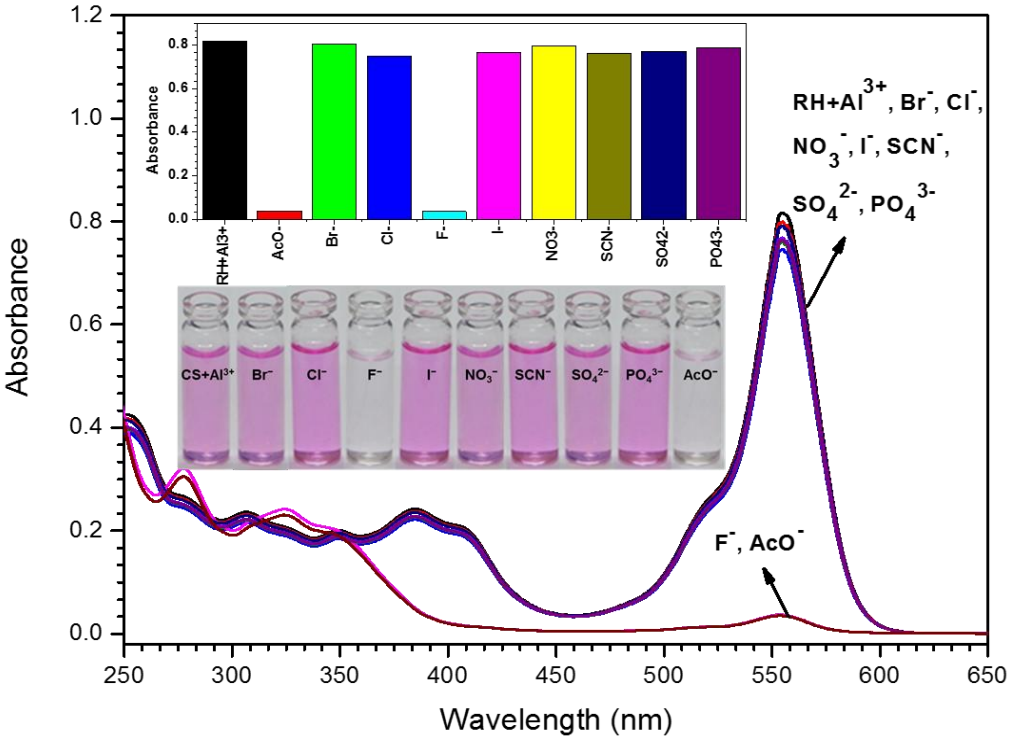


**Figure 6.48.** UV-Vis spectral behavior of **RH**–$Al^{3+}$ (10 µM) in the presence of various analytes (5 equiv.), such as $AcO^-$, $Br^-$, $Cl^-$, $F^-$, $I^-$, $NO_3^-$, $SCN^-$, $SO_4^{2-}$ and $PO_4^{3-}$ in MeOH-$H_2O$ (50:50 v/v). Inset: The absorbance was recorded at 587 nm (top) and the photographs of **RH**–$Al^{3+}$ in the presence of various analytes were taken in daylight (bottom).

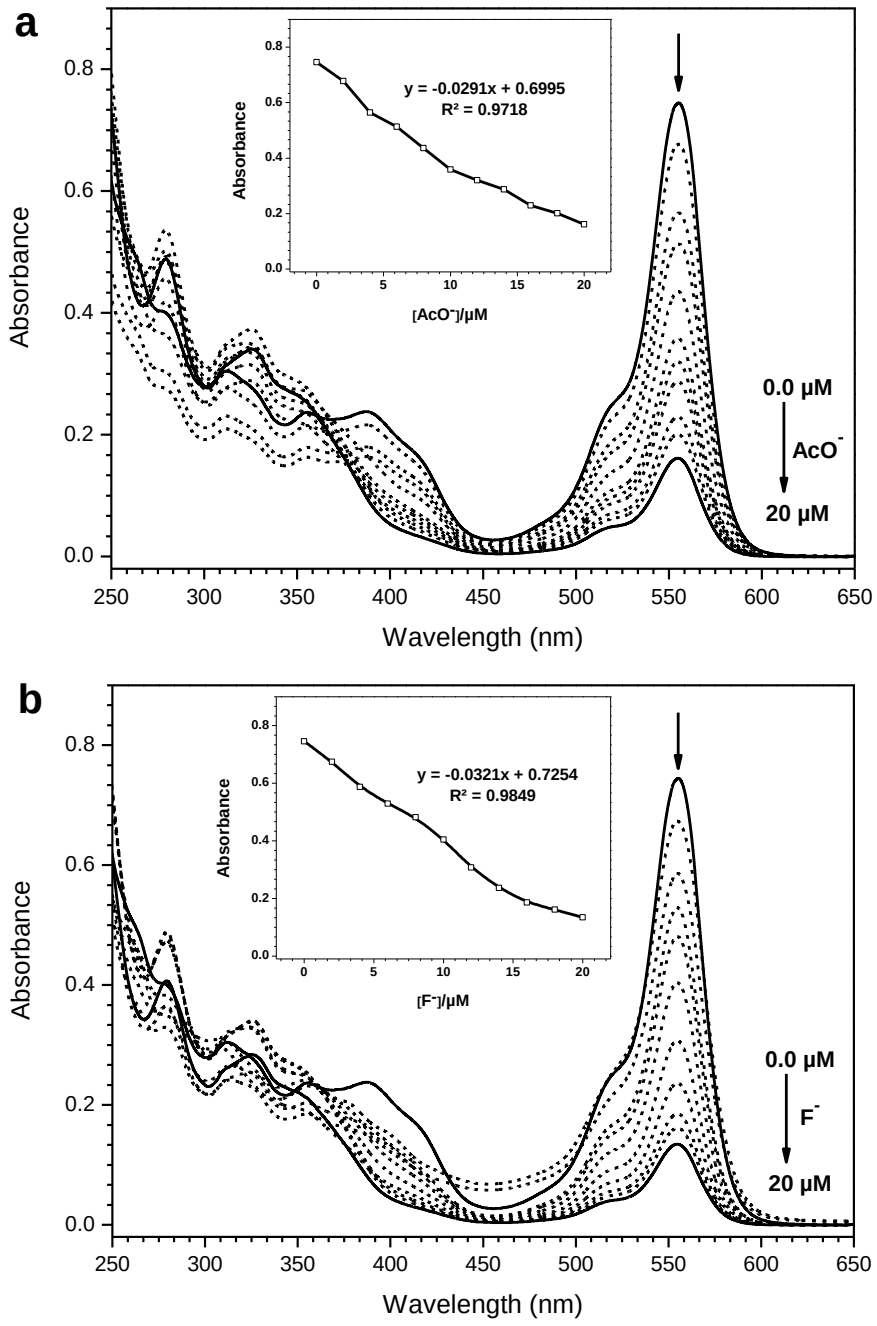


**Figure 6.49.** UV-Vis absorbance titration spectra of **RH** (10 μM) with 1 equiv. of $Al^{3+}$ upon gradual addition (0–20 μM) of sodium acetate (a) and sodium fluoride (b). Inset: Changes in absorbance of **RH**–$Al^{3+}$ complex at 555 nm as a function of concentration of $AcO^-/F^-$.

presence of $AcO^-/F^-$. Thus, the results indicated that the probe **RH** was restored during the detection procedure of $AcO^-/F^-$. The relative absorbance of **RH**–$Al^{3+}$ (10 μM) are linearly proportional to the concentration of $AcO^-/F^-$ in the different concentration ranges.

Reversibility and regeneration of sensing probe are important factors in practical applications. As shown in Figure 6.50, the alternate additions of a constant amount of $Al^{3+}$ and $AcO^-/F^-$ to the solution of **RH** gives rise to a switchable change in the absorbance at

555 nm. Such a reversible absorbance spectral behavior of **RH** can be repeated several times by the modulation of metal/anion addition, indicating that the probe **RH** could be used as a reversible chemosensor for $Al^{3+}$ and $AcO^{-}/F^{-}$. Their corresponding color changes are also shown in Figure 6.50 insert.

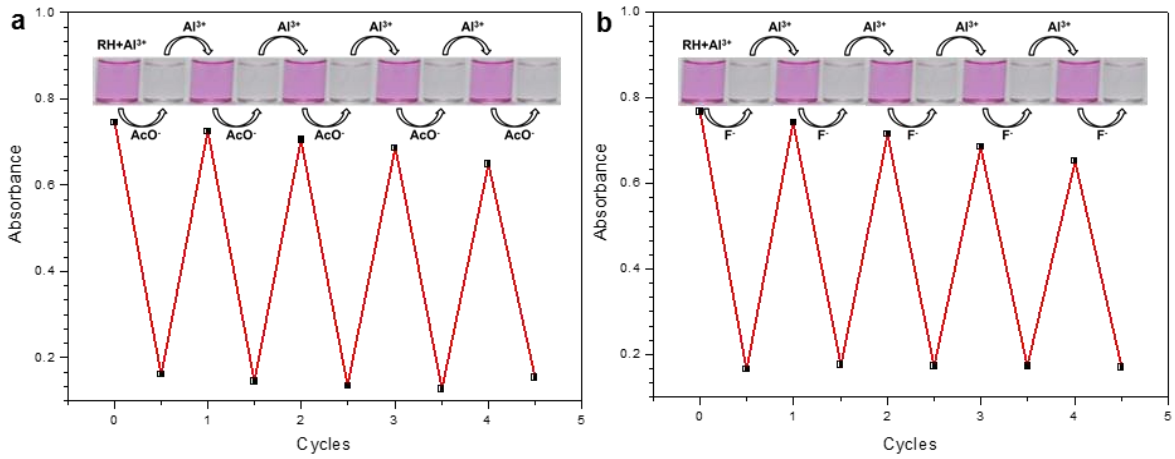


**Figure 6.50.** Changes in absorbance of **RH** (10 μM) at 555 nm upon alternate addition of a constant amount of $Al^{3+}$ (1 equiv.) and $AcO^{-}/F^{-}$ (2 equiv.). Inset: Images of proof of reversibility.

*6.3.3.6. Sensing studies with paper strips*

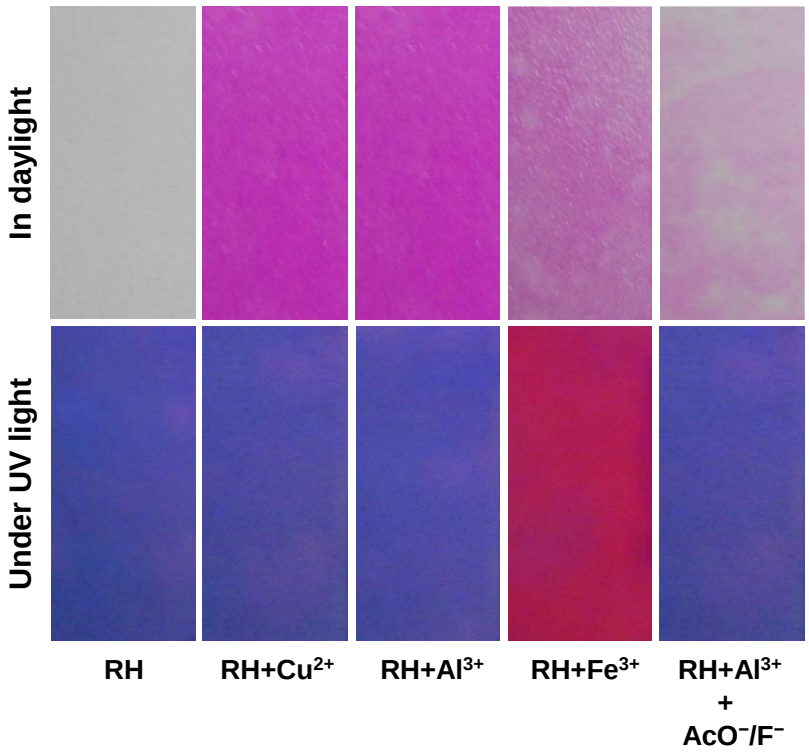


**Figure 6.51.** Photographs of the test strips of **RH** for the detection of $Cu^{2+}$, $Al^{3+}$ and $Fe^{3+}$ in MeOH−$H_2O$ (50:50 v/v). A solution of **RH** with a concentration of 1 mM was used to develop the strips.

To investigate the practical application of proposed sensor **RH**, paper test strips were prepared for rapid on-site detection of $Cu^{2+}$, $Al^{3+}$ and $Fe^{3+}$ ions. For this purpose, filter papers (Whatman filter paper No. 1) were dipped in a 1 mM alcoholic solution of **RH** for about 5 min and then dried in air. A significant visible color change was observed immediately when the test strips were sprayed with a solution containing the corresponding metal ions (100 μM) in MeOH−$H_2O$ (50:50 v/v) (Figure 6.51). The colorless strips were converted to pink, which was also observed under UV light. These pink colored test strips containing **RH**–$Al^{3+}$ were then sprayed with a solution of $AcO^-/F^-$. The pink color disappeared and is converted back into its colorless due to restoration of **RH**. This makes the sensor quite useful for rapid on-site detection of metal ions.

### 6.3.4. Conclusion

In summary, we report a new rhodamine-derived chemosensor (**RH**) for the selective determination of $Cu^{2+}$, $Al^{3+}$ and $Fe^{3+}$ in different modes in aqueous media. The sensing property of **RH** was examined by visual inspection, UV-Vis, fluorescence and ESI-MS experiments. The probe showed highly selective and sensitive colorimetric response toward $Cu^{2+}$ and $Al^{3+}$, and "off-on" fluorescence response to $Fe^{3+}$ over a wide range of metal ions. Upon addition of metal ions, the solution of **RH** shows significant enhanced absorbance and color change from colorless to pink especially for $Cu^{2+}$ and $Al^{3+}$, and shows remarkable 'off-on' fluorescence accompanied by a color change from colorless to fluorescent pink especially for $Fe^{3+}$. In all the cases, the spectral changes and the visual color changes were observed due to reversible spirolactam ring opening. The 1 : 1 stoichiometric ratio between probe and metal ions was proposed based on a Job's plot, which was further confirmed by ESI mass analysis. Moreover, the DFT experiment suggested that the binding of $Fe^{3+}$ to **RH** lowered the HOMO-LUMO band gap, which is evidence for the red-shift in fluorescence spectra of **RH**–$Fe^{3+}$ complex. Further studies of **RH**–$Al^{3+}$ complex revealed that it could be selectively dissociated in the presence of $AcO^-/F^-$, which makes the **RH**–$Al^{3+}$ ensemble an efficient sensor for $AcO^-/F^-$. Paper strips were also used for the detection of $Cu^{2+}$, $Al^{3+}$ and $Fe^{3+}$ ions.

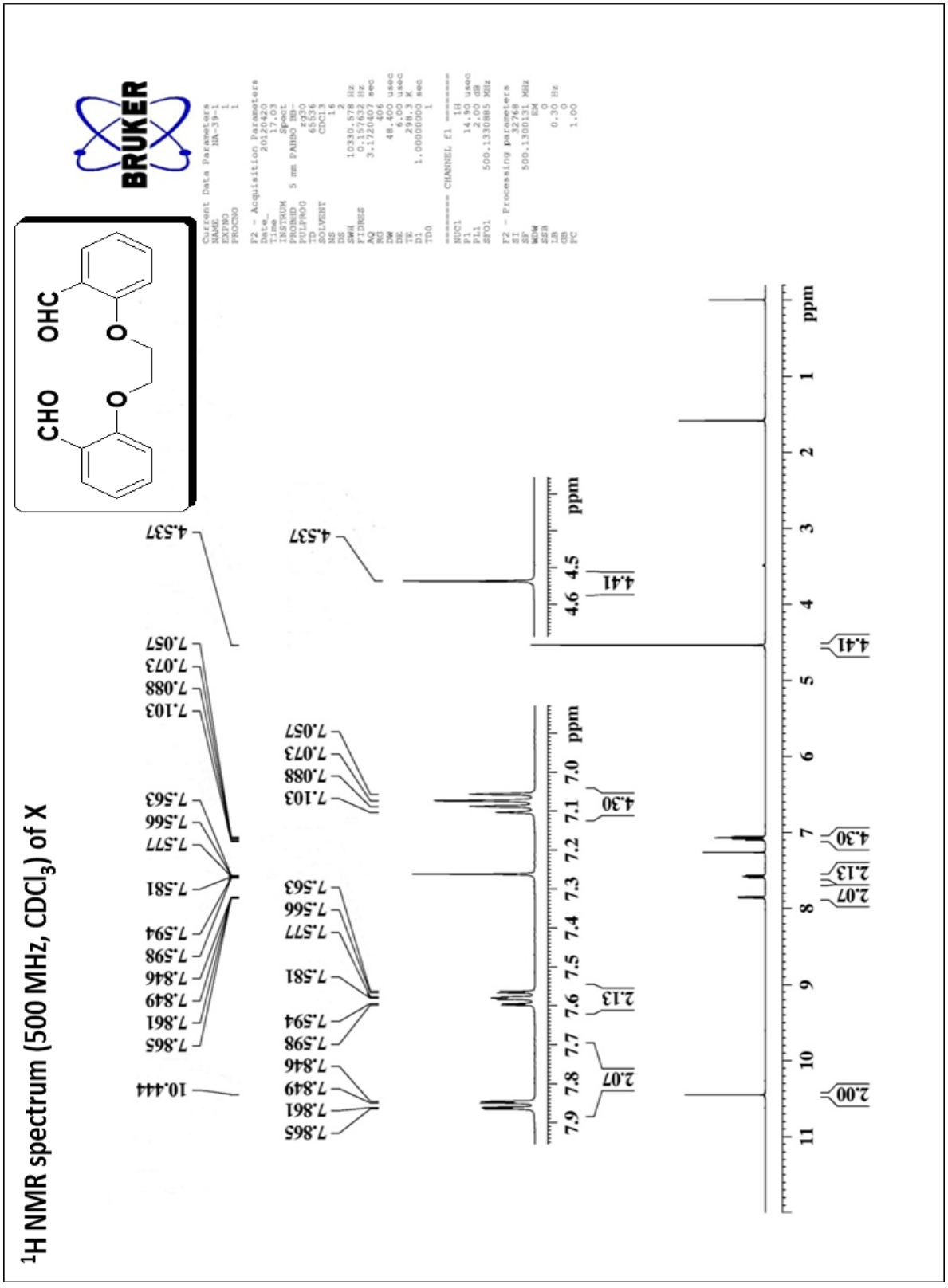
$^1$H NMR spectrum (500 MHz, $CDCl_3$) of X
OHC
CHO
O
O
BRUKER
ppm

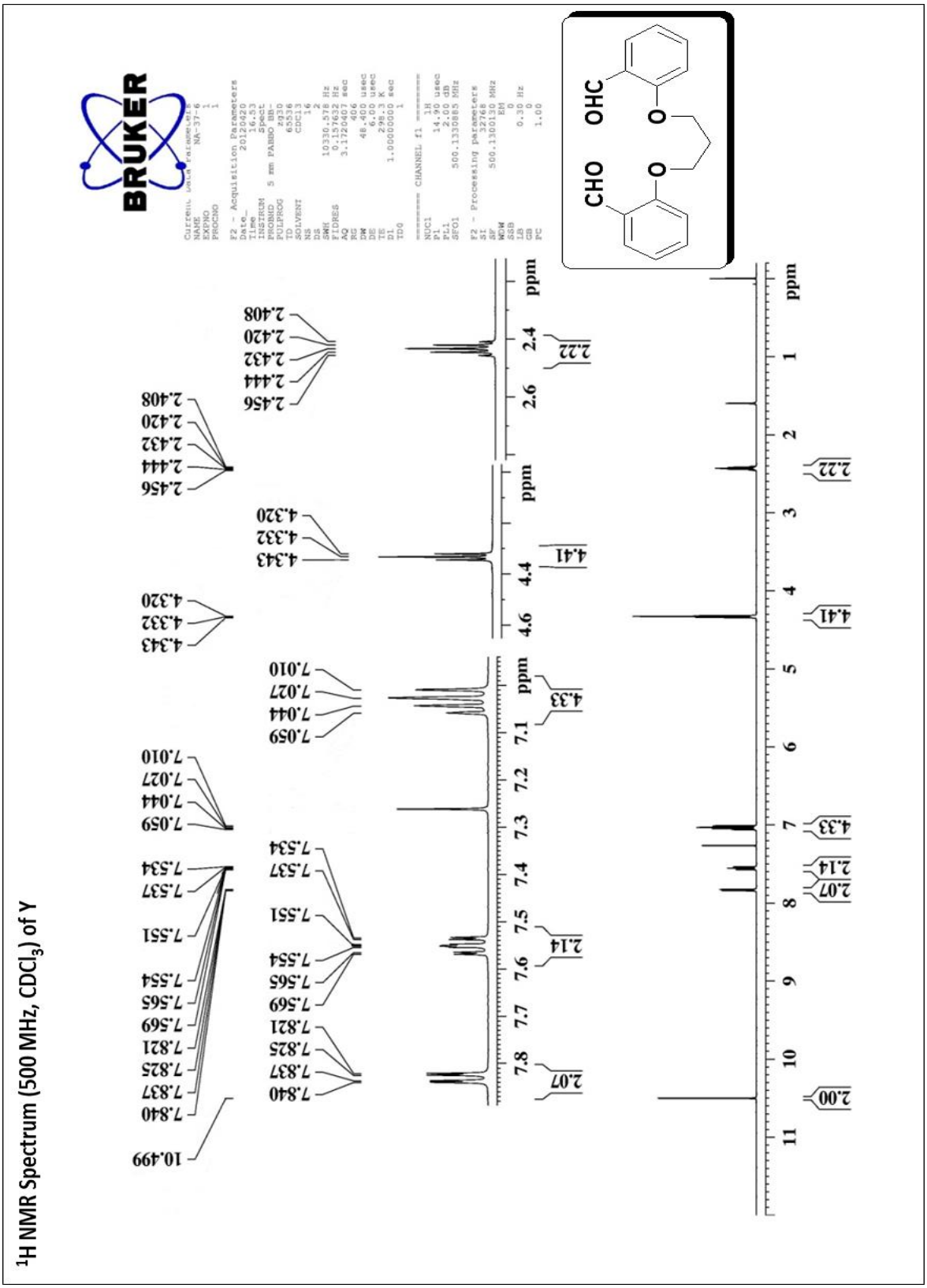


$^1$H NMR Spectrum (500 MHz, $CDCl_3$) of Y

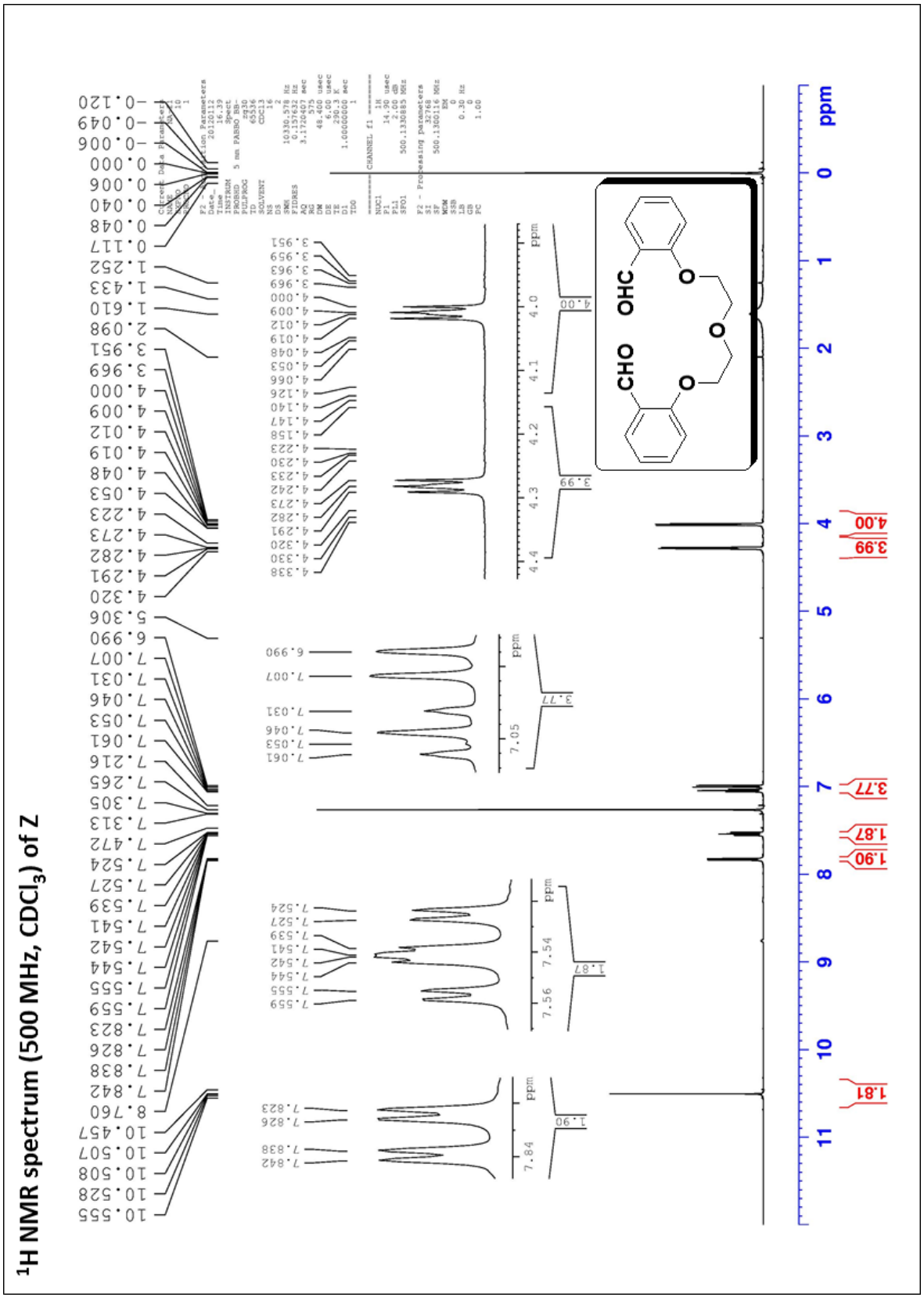
$^1$H NMR spectrum (500 MHz, $CDCl_3$) of Z
CHO
OHC
O
O
O
ppm
4.00
3.99
3.77
1.87
1.90
1.81

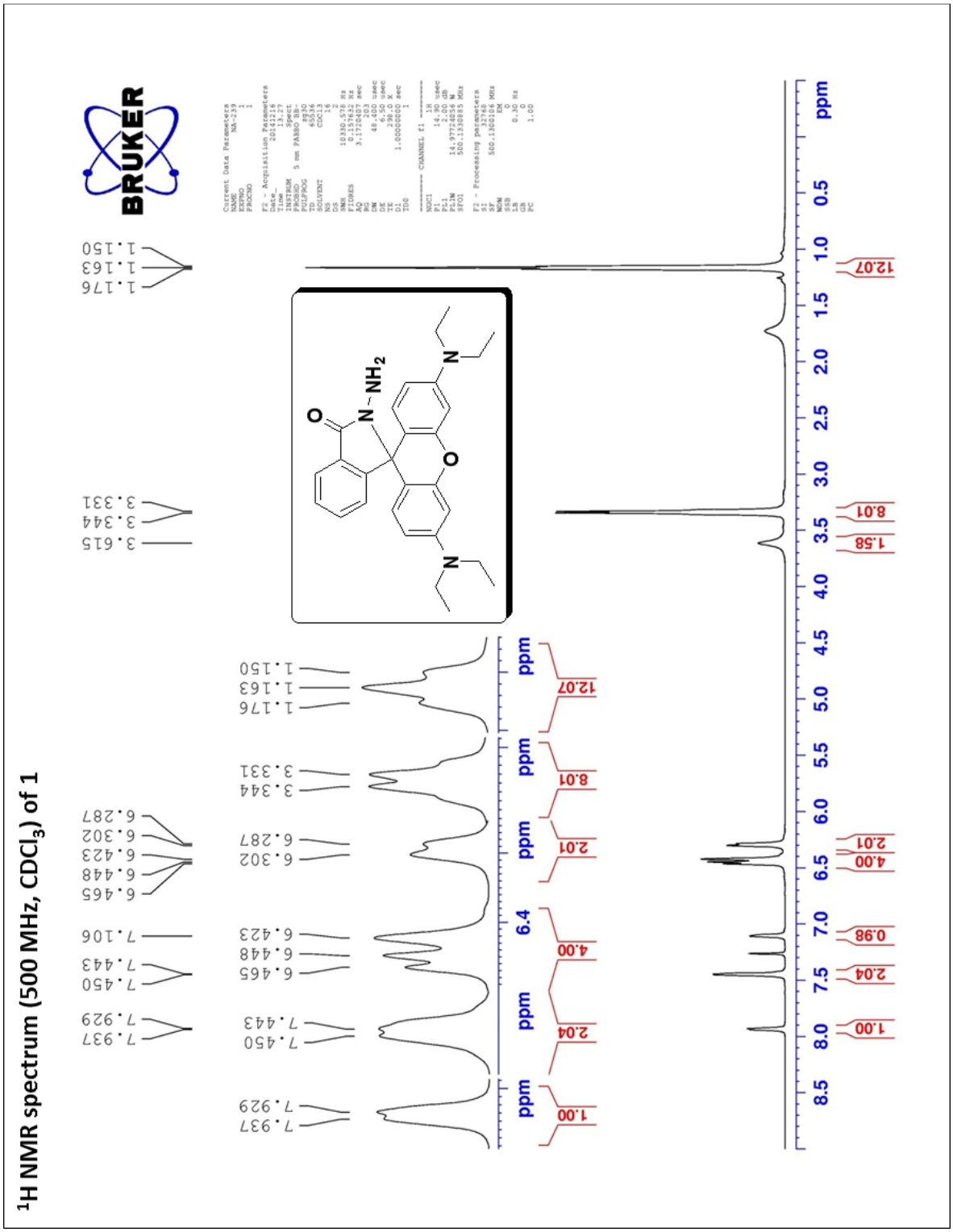
$^1$H NMR spectrum (500 MHz, $CDCl_3$) of 1
BRUKER
ppm

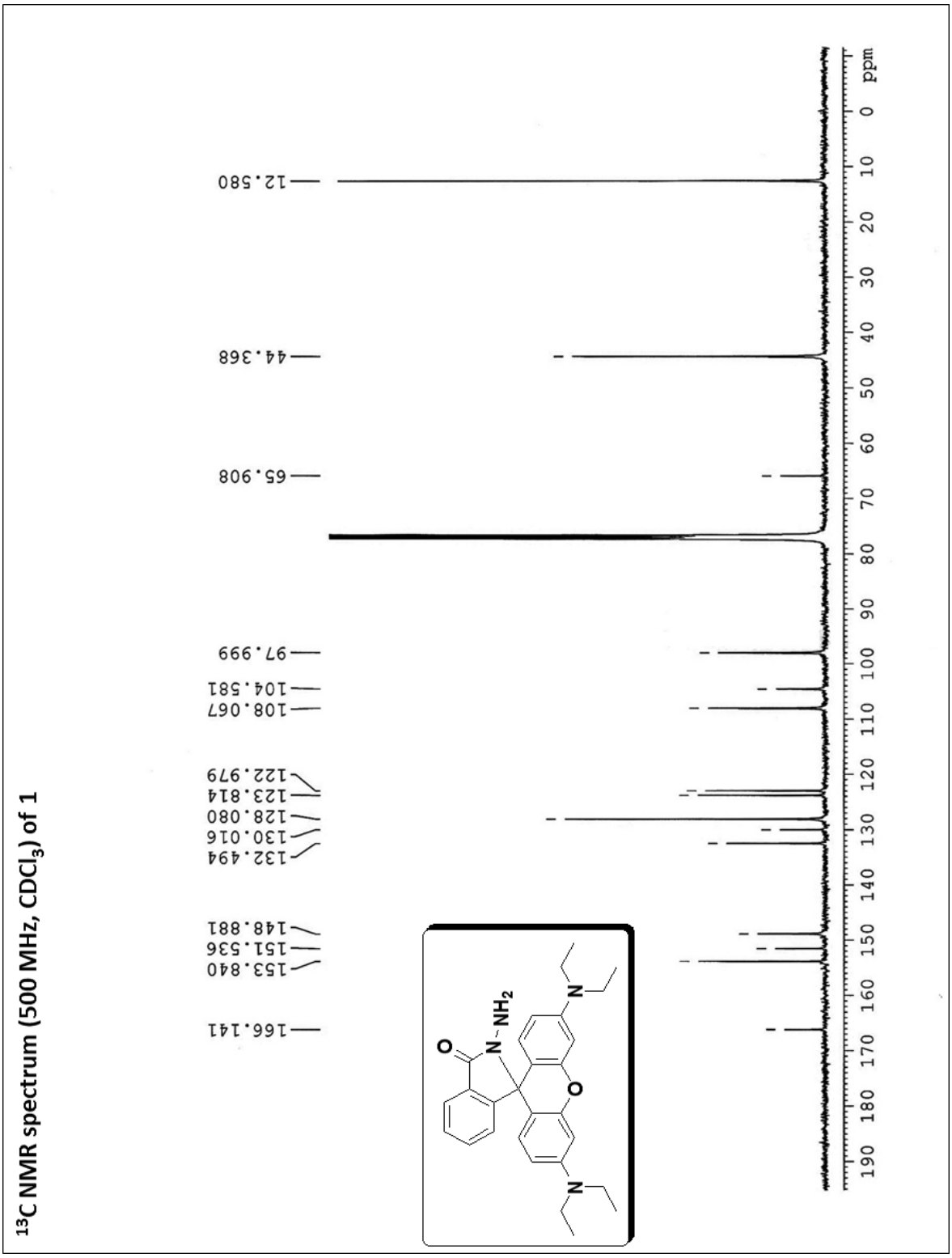


$^{13}C$ NMR spectrum (500 MHz, $CDCl_3$) of 1

## ESI-MS spectrum of 1

**Acquisition Parameter**

| | | | | | |
|---|---|---|---|---|---|
| Source Type | ESI | Ion Polarity | Positive | Set Nebulizer | 0.4 Bar |
| Focus | Not active | Set Capillary | 4500 V | Set Dry Heater | 180 °C |
| Scan Begin | 21 m/z | Set End Plate Offset | -500 V | Set Dry Gas | 4.0 l/min |
| Scan End | 3000 m/z | Set Collision Cell RF | 150.0 Vpp | Set Divert Valve | Source |

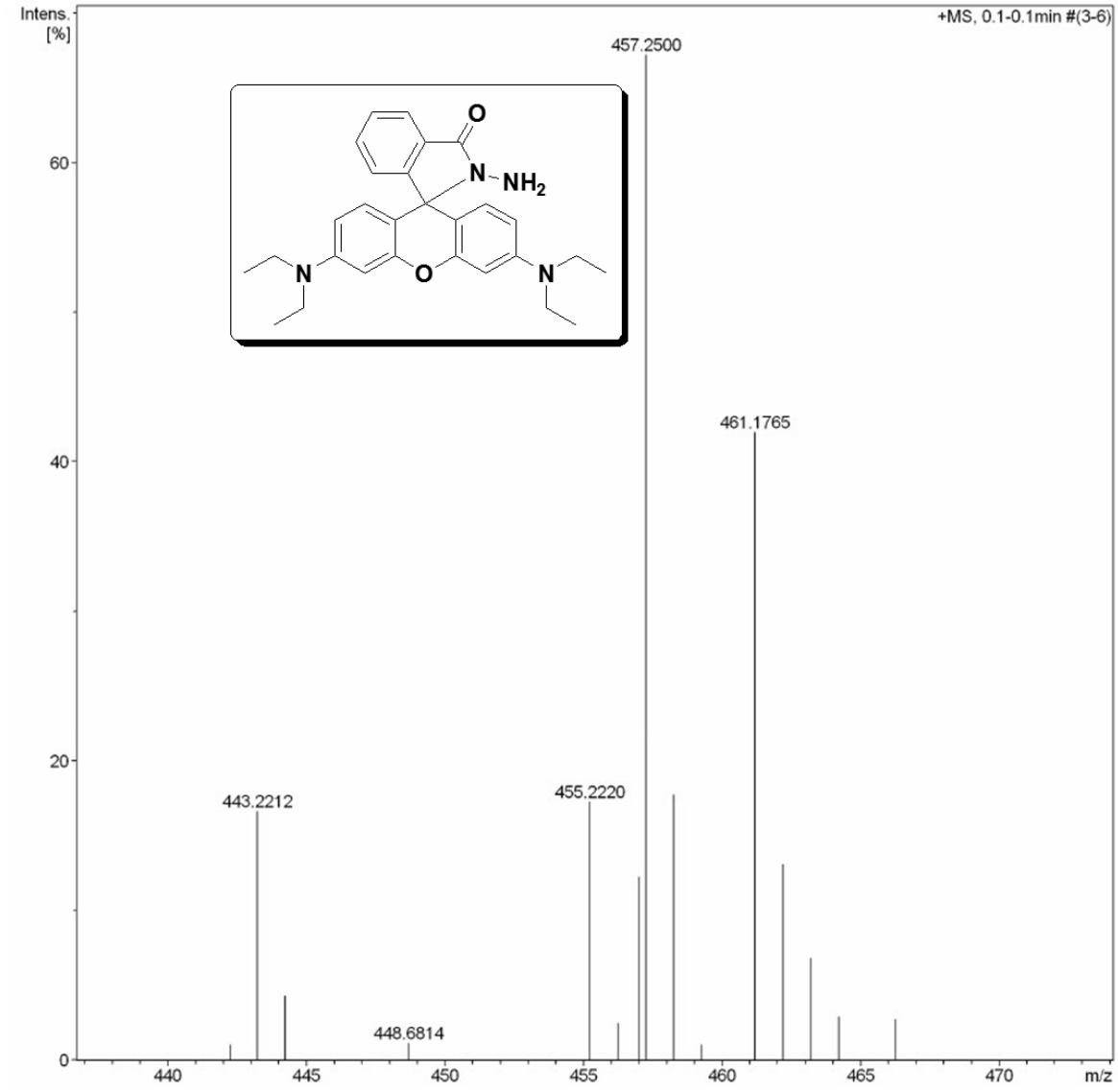

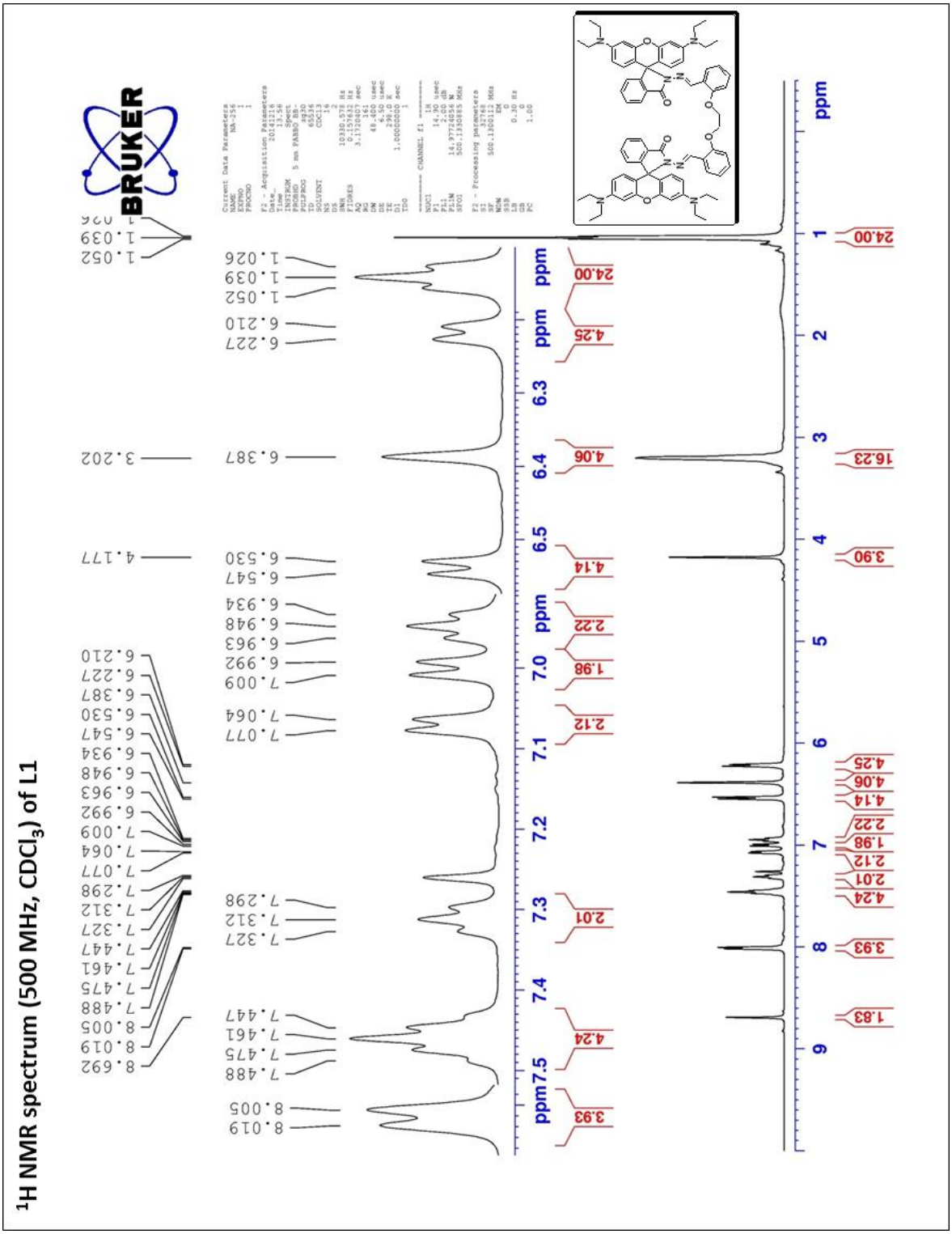


$^1$H NMR spectrum (500 MHz, $CDCl_3$) of L1

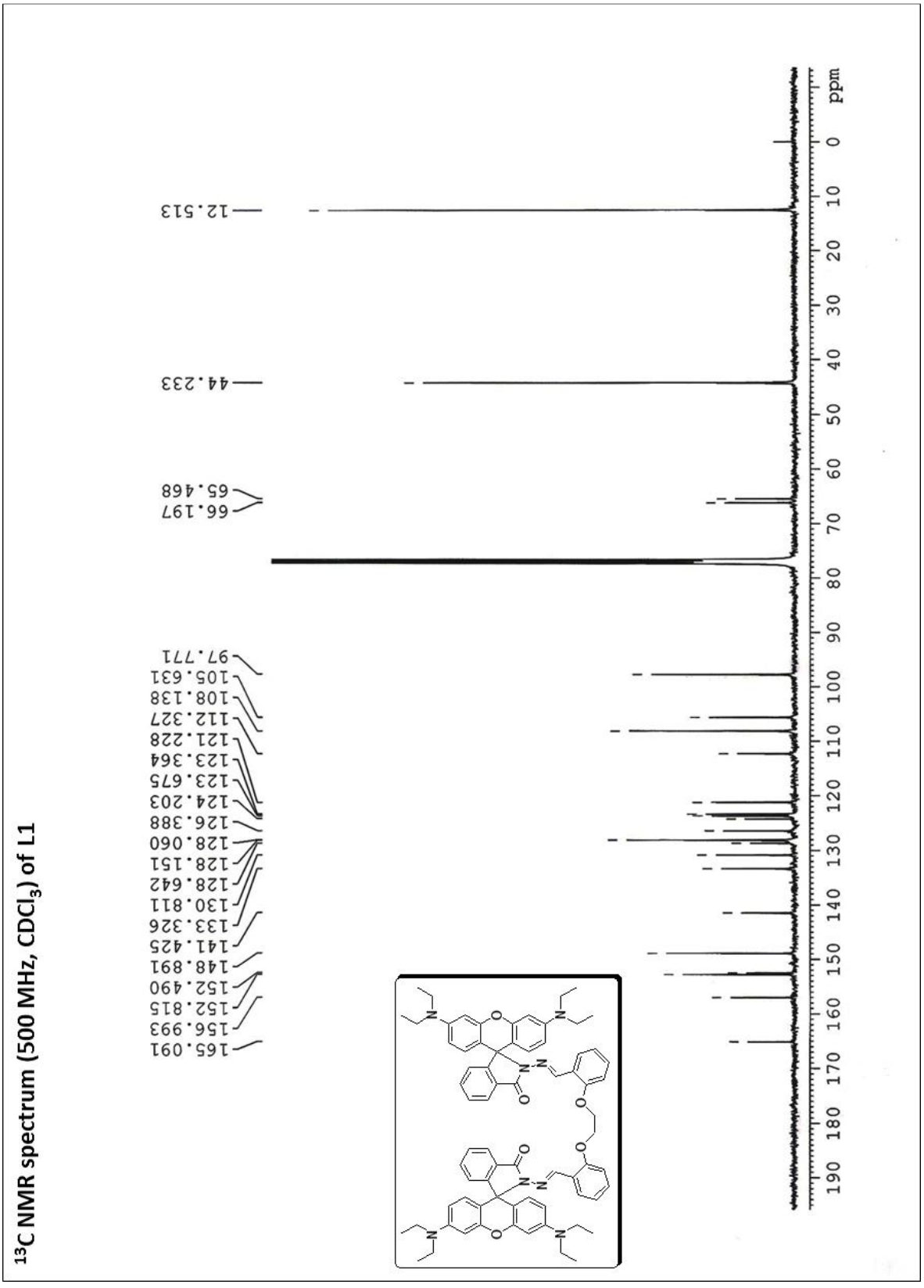


$^{13}$C NMR spectrum (500 MHz, $CDCl_3$) of L1

## ESI-MS spectrum of L1

**Acquisition Parameter**

| | | | | | |
|---|---|---|---|---|---|
| Source Type | ESI | Ion Polarity | Positive | Set Nebulizer | 0.4 Bar |
| Focus | Not active | Set Capillary | 4500 V | Set Dry Heater | 180 °C |
| Scan Begin | 50 m/z | Set End Plate Offset | -500 V | Set Dry Gas | 4.0 l/min |
| Scan End | 3000 m/z | Set Collision Cell RF | 150.0 Vpp | Set Divert Valve | Source |

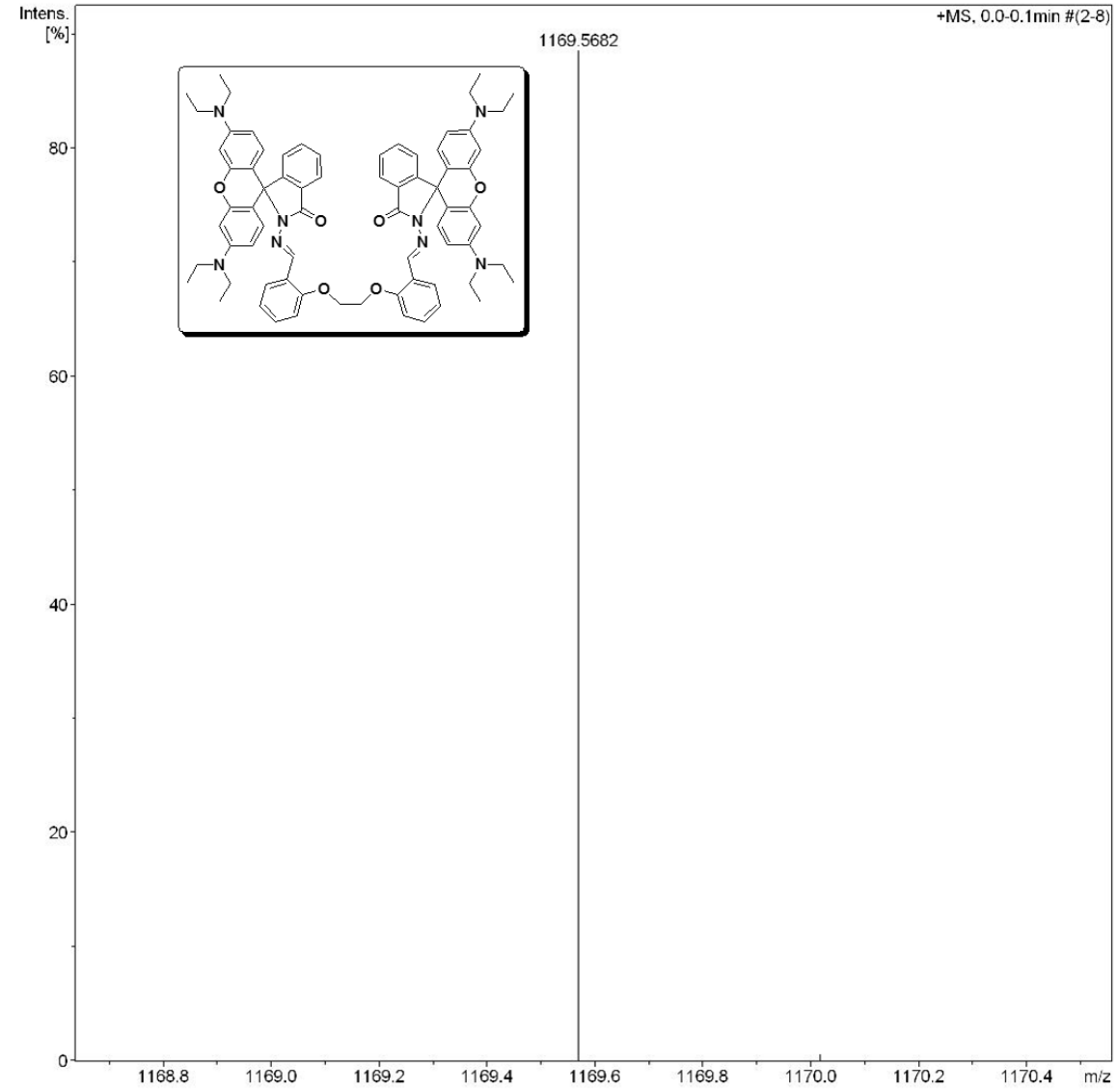

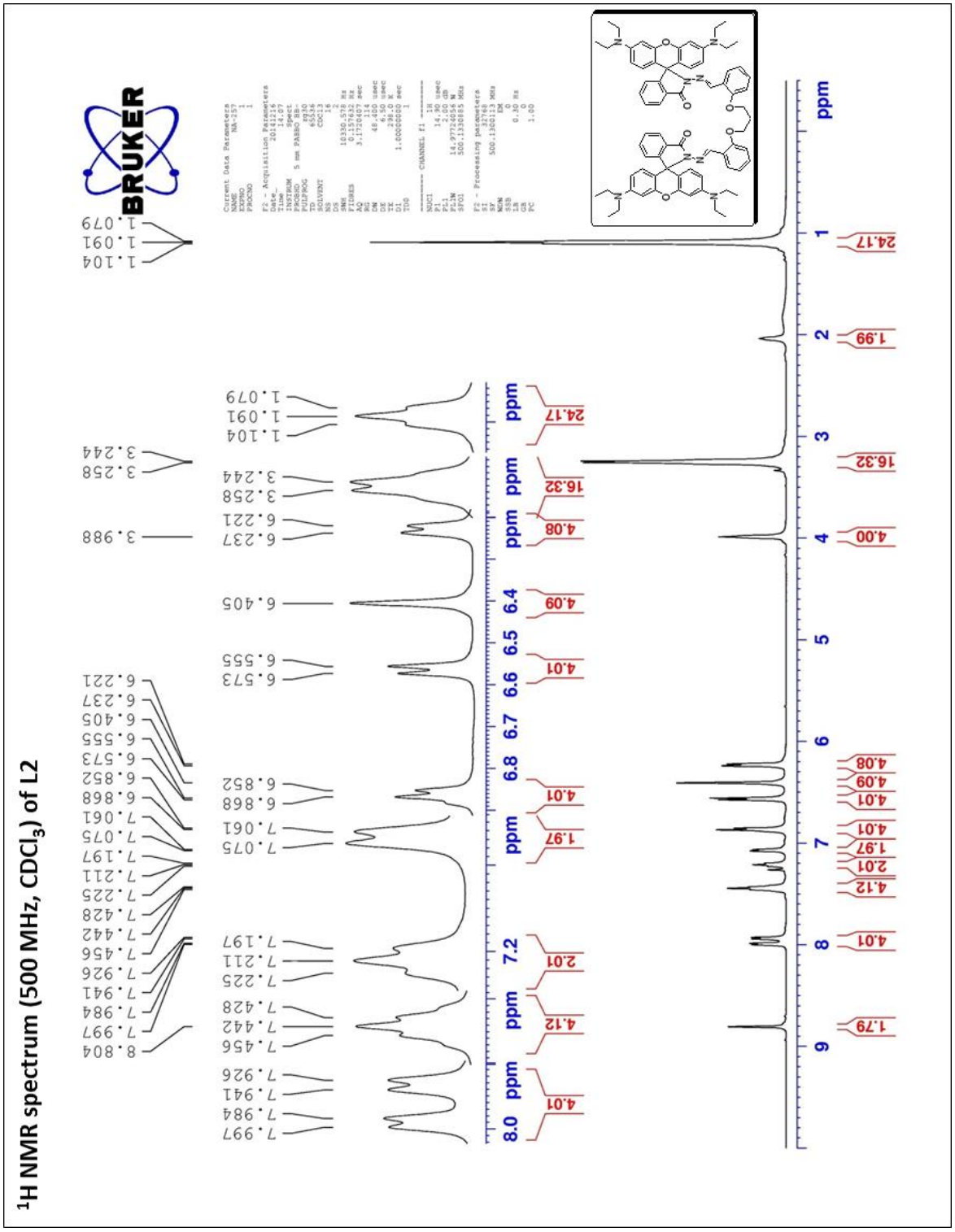


$^1$H NMR spectrum (500 MHz, $CDCl_3$) of L2

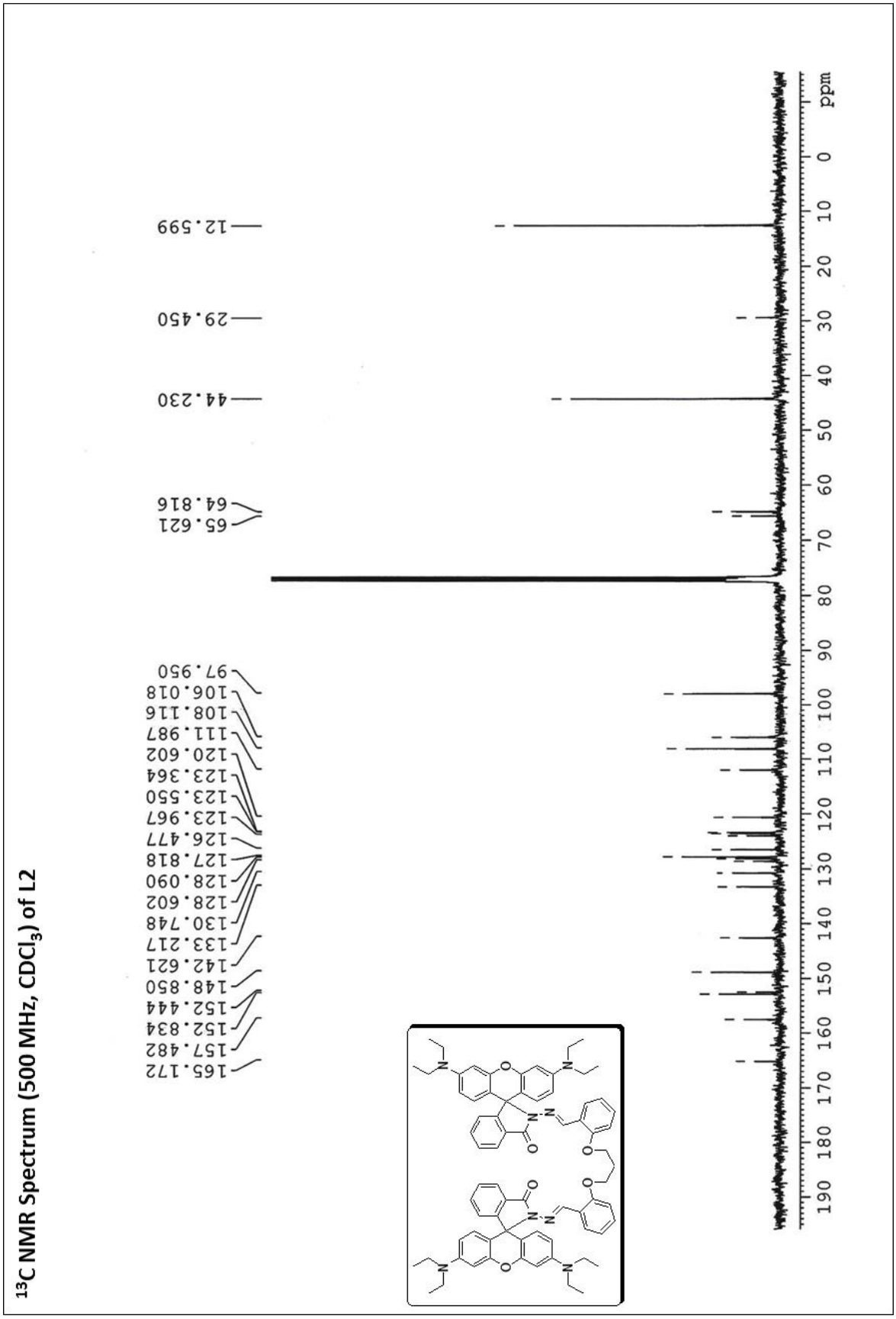


$^{13}$C NMR Spectrum (500 MHz, $CDCl_3$) of L2

## ESI-MS spectrum of L2

**Acquisition Parameter**

| | | | | | |
|---|---|---|---|---|---|
| Source Type | ESI | Ion Polarity | Positive | Set Nebulizer | 0.4 Bar |
| Focus | Not active | Set Capillary | 4500 V | Set Dry Heater | 180 °C |
| Scan Begin | 50 m/z | Set End Plate Offset | -500 V | Set Dry Gas | 4.0 l/min |
| Scan End | 3000 m/z | Set Collision Cell RF | 150.0 Vpp | Set Divert Valve | Source |

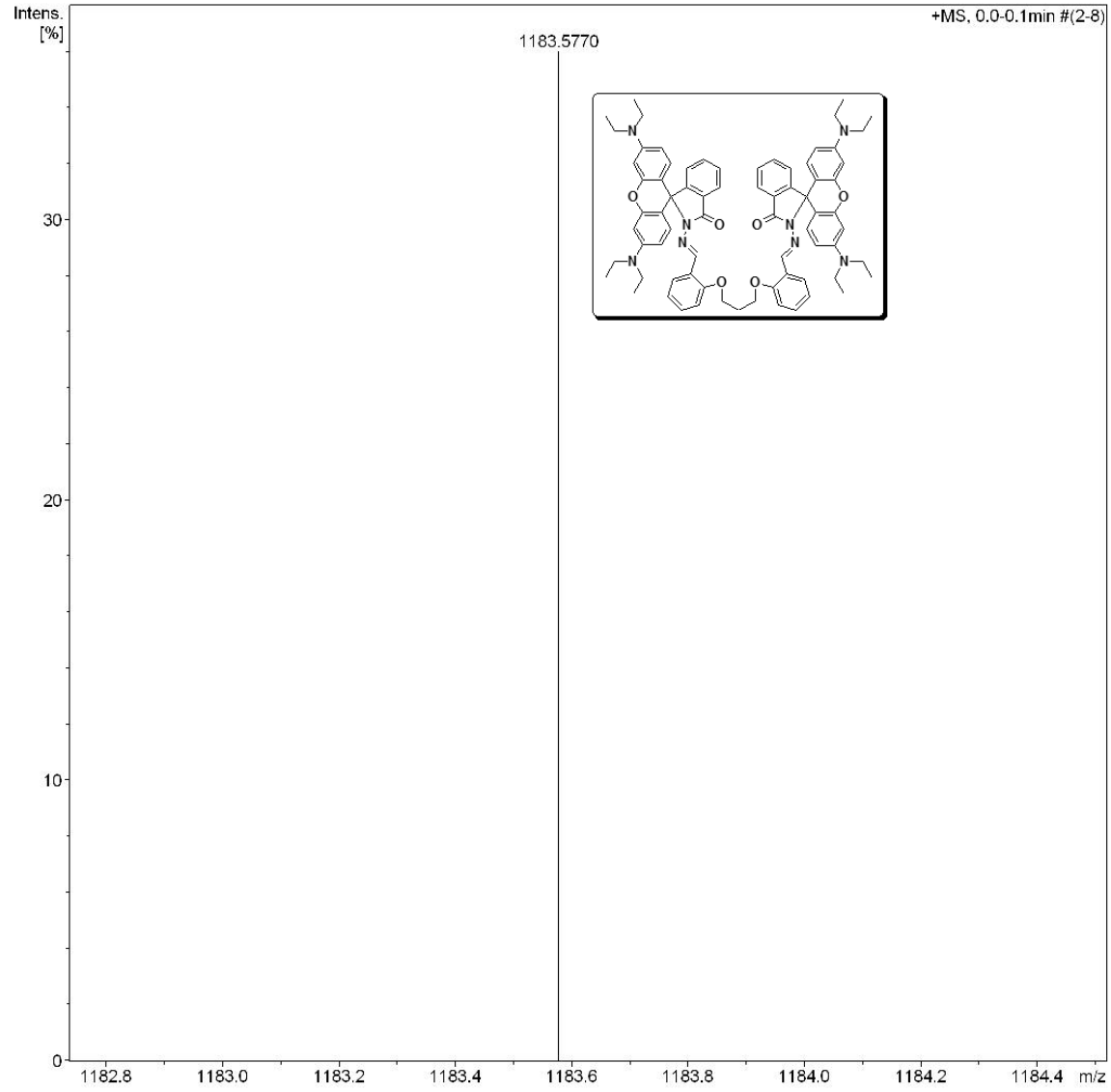

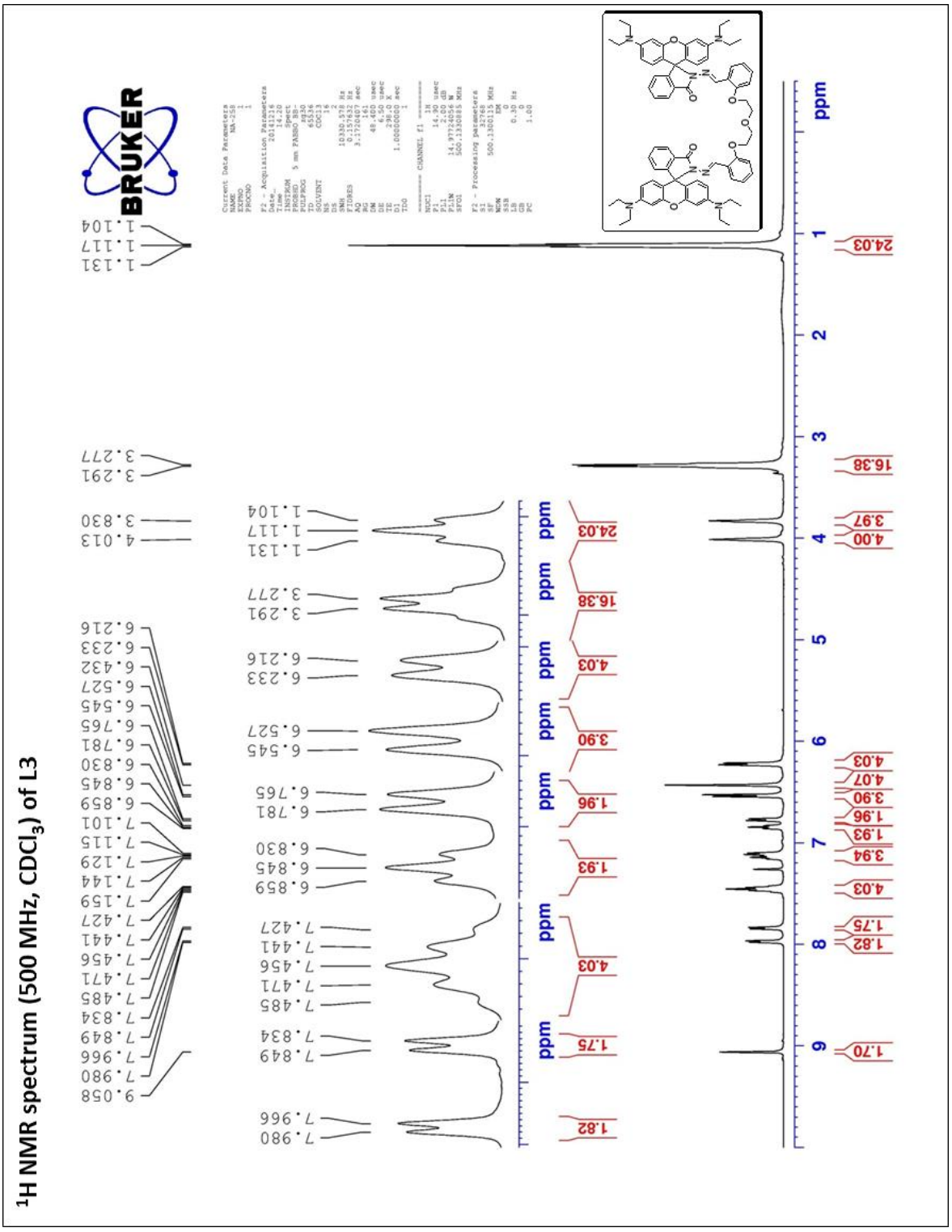
$^1$H NMR spectrum (500 MHz, $CDCl_3$) of L3
BRUKER
ppm

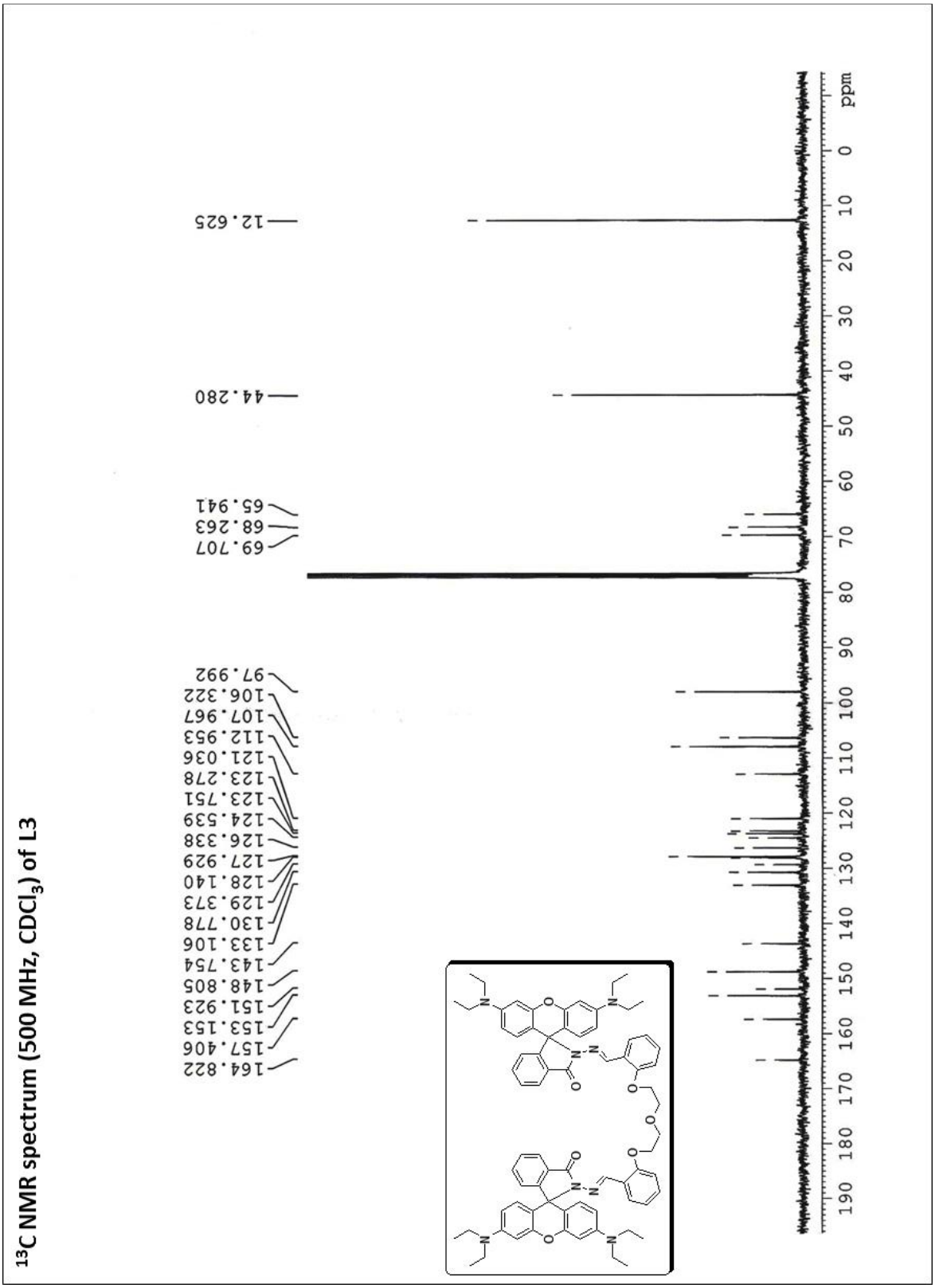
$^{13}$C NMR spectrum (500 MHz, $CDCl_3$) of L3
12.625
44.280
65.941
68.263
69.707
97.992
106.322
107.967
112.953
121.036
123.278
123.751
124.539
126.338
127.929
128.140
129.373
130.778
133.106
143.754
148.805
151.923
153.153
157.406
164.822
ppm

## ESI-MS spectrum of L3

**Acquisition Parameter**

| | | | | | |
|---|---|---|---|---|---|
| Source Type | ESI | Ion Polarity | Positive | Set Nebulizer | 0.4 Bar |
| Focus | Not active | Set Capillary | 4500 V | Set Dry Heater | 180 °C |
| Scan Begin | 50 m/z | Set End Plate Offset | -500 V | Set Dry Gas | 4.0 l/min |
| Scan End | 3000 m/z | Set Collision Cell RF | 150.0 Vpp | Set Divert Valve | Source |

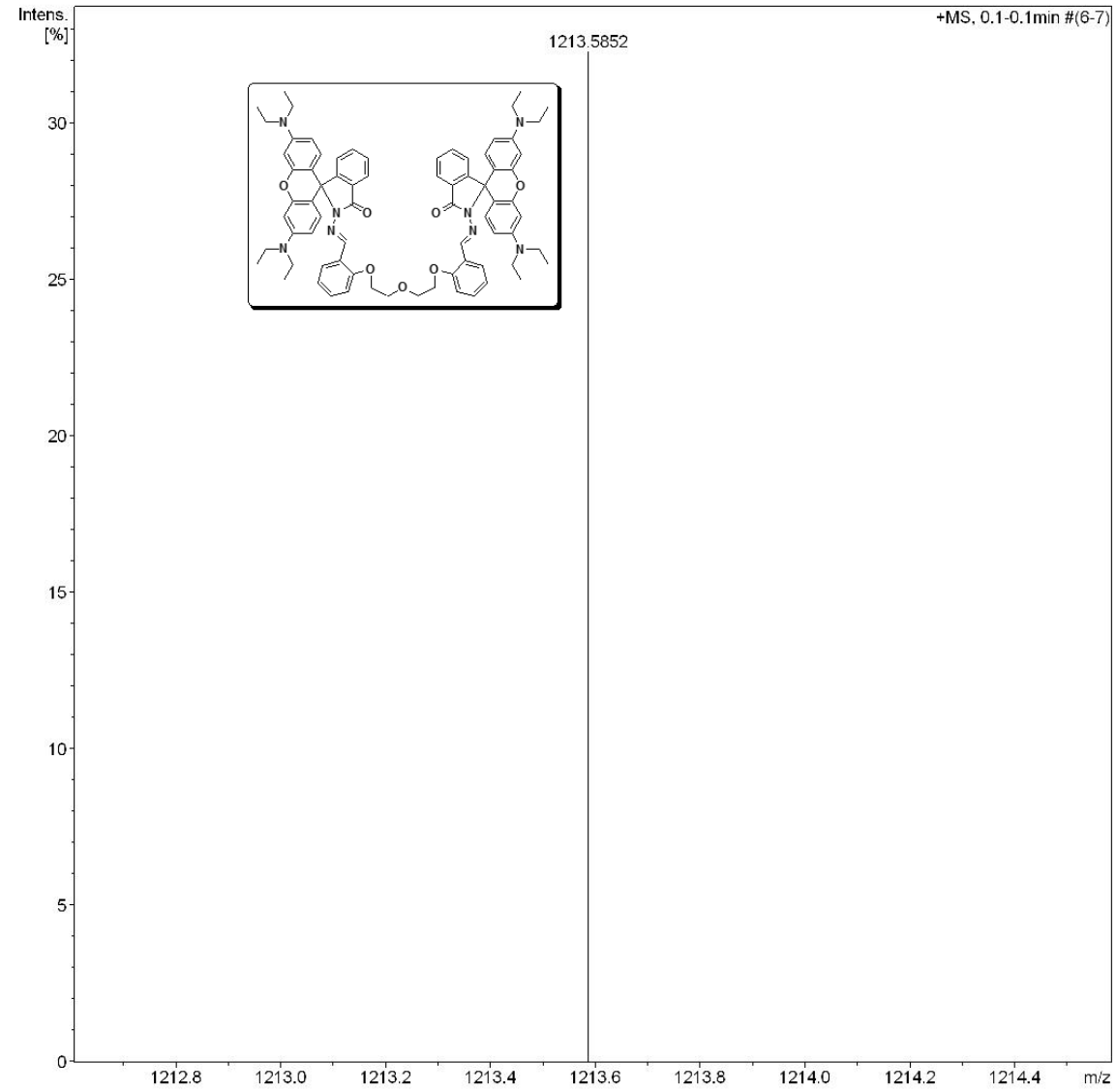

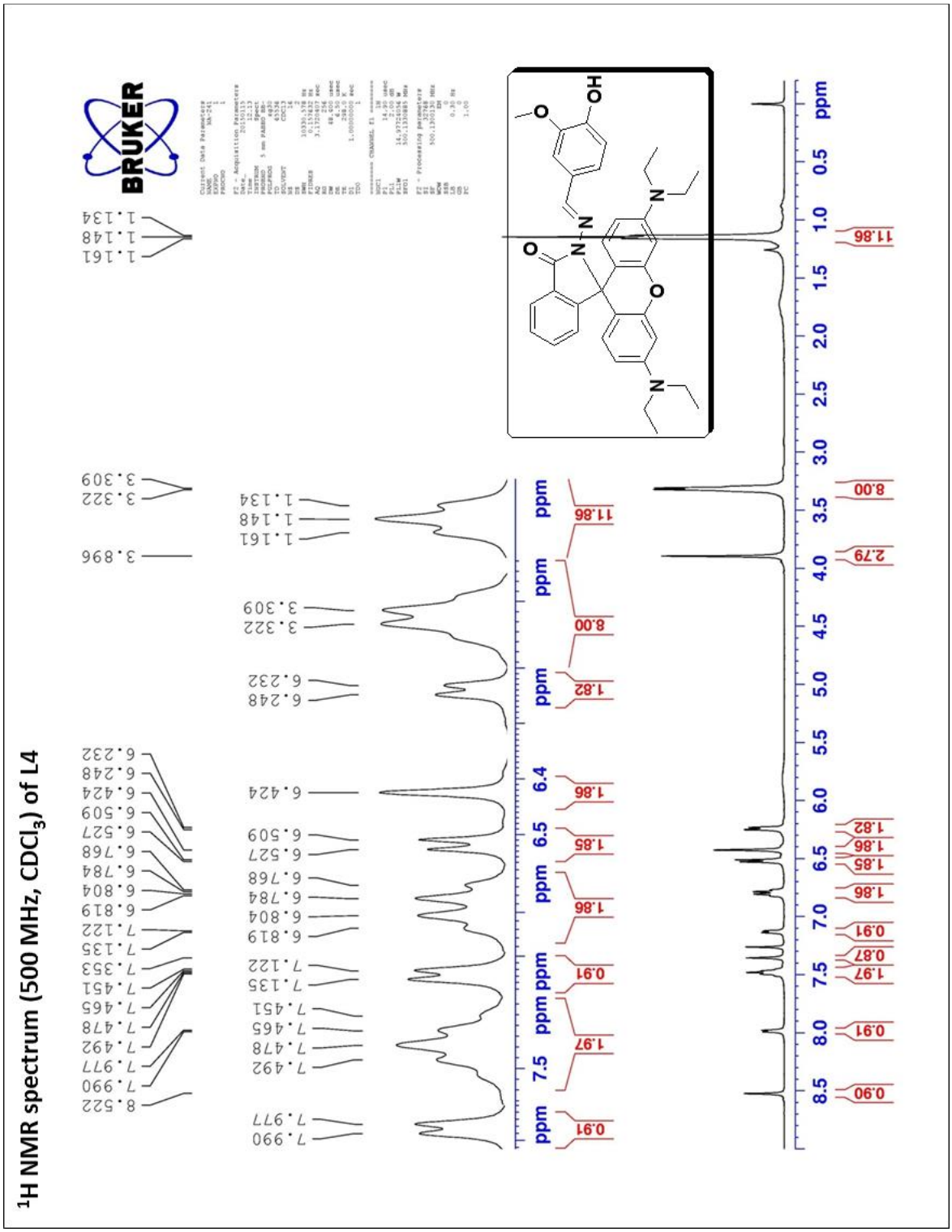
$^1$H NMR spectrum (500 MHz, $CDCl_3$) of L4
BRUKER
OH
O
N
ppm

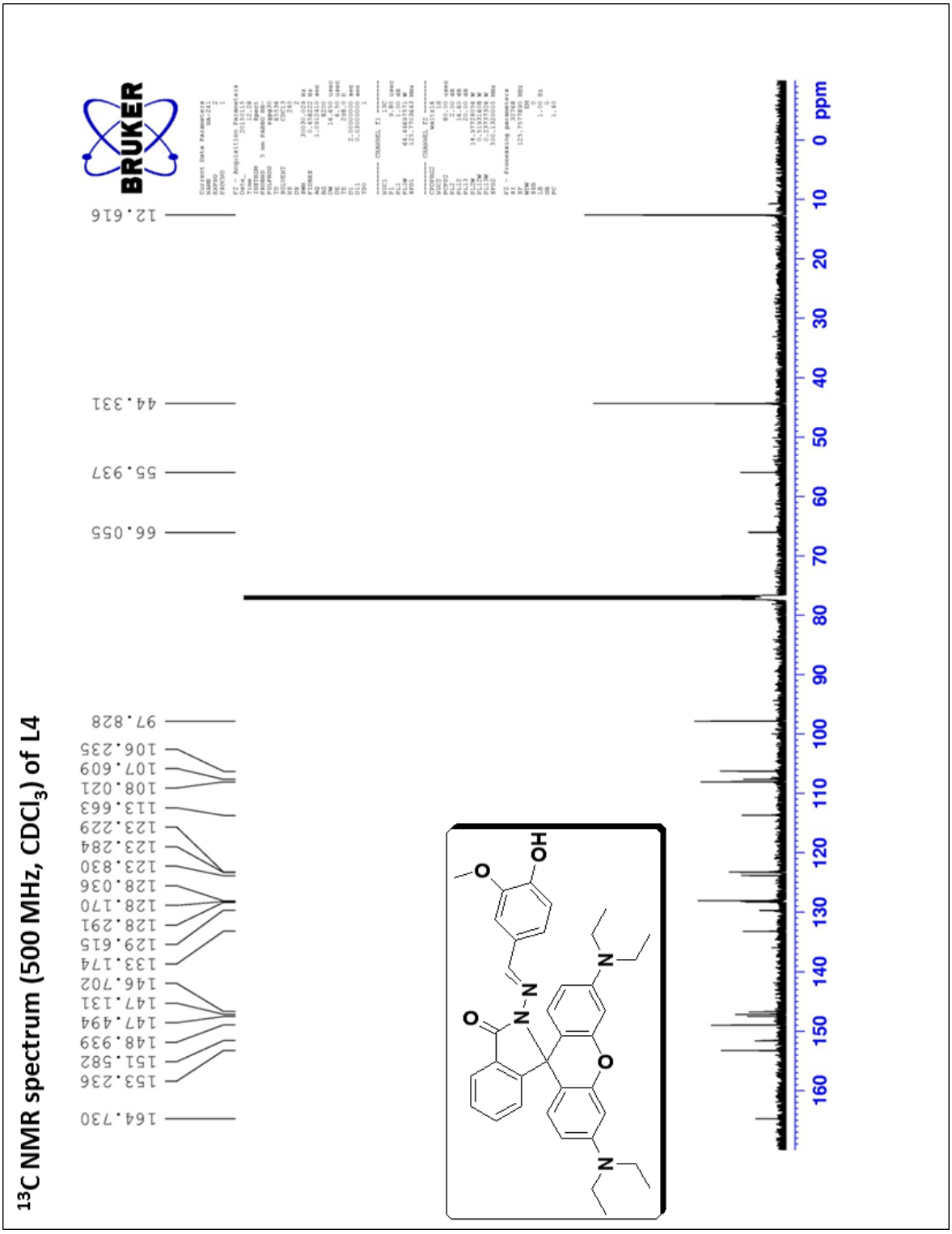
$^{13}$C NMR spectrum (500 MHz, $CDCl_3$) of L4
12.616
44.331
55.937
66.055
97.828
106.235
107.609
108.021
113.663
123.229
123.284
123.830
128.036
128.170
128.291
129.615
133.174
146.702
147.131
147.494
148.939
151.582
153.236
164.730
OH
O
N
O
N
N
O
N
0 ppm

## ESI-MS spectrum of L4

**Acquisition Parameter**

| | | | | | |
|---|---|---|---|---|---|
| Source Type | ESI | Ion Polarity | Positive | Set Nebulizer | 0.4 Bar |
| Focus | Not active | Set Capillary | 4500 V | Set Dry Heater | 180 °C |
| Scan Begin | 50 m/z | Set End Plate Offset | -500 V | Set Dry Gas | 4.0 l/min |
| Scan End | 3000 m/z | Set Collision Cell RF | 150.0 Vpp | Set Divert Valve | Source |

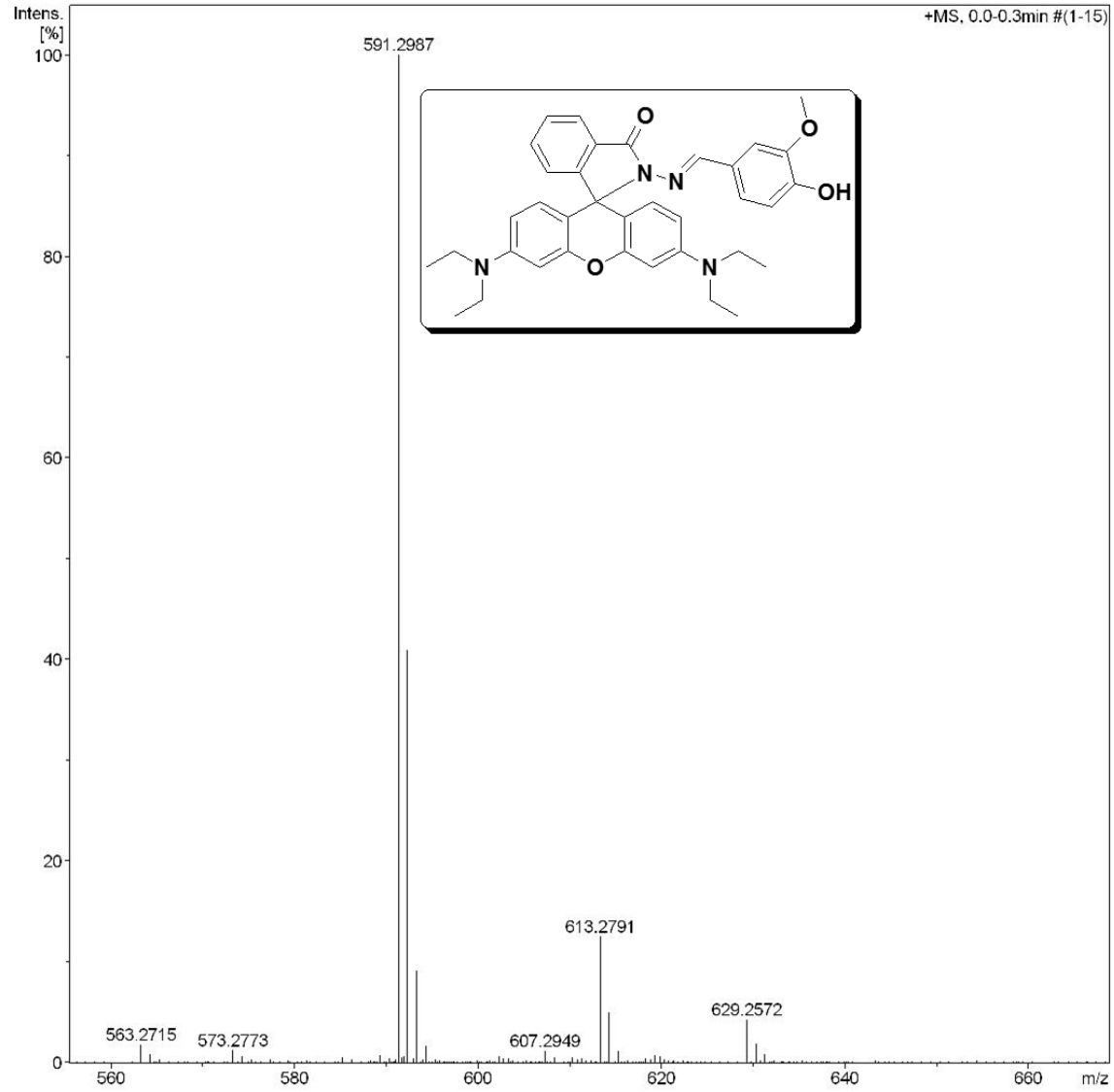

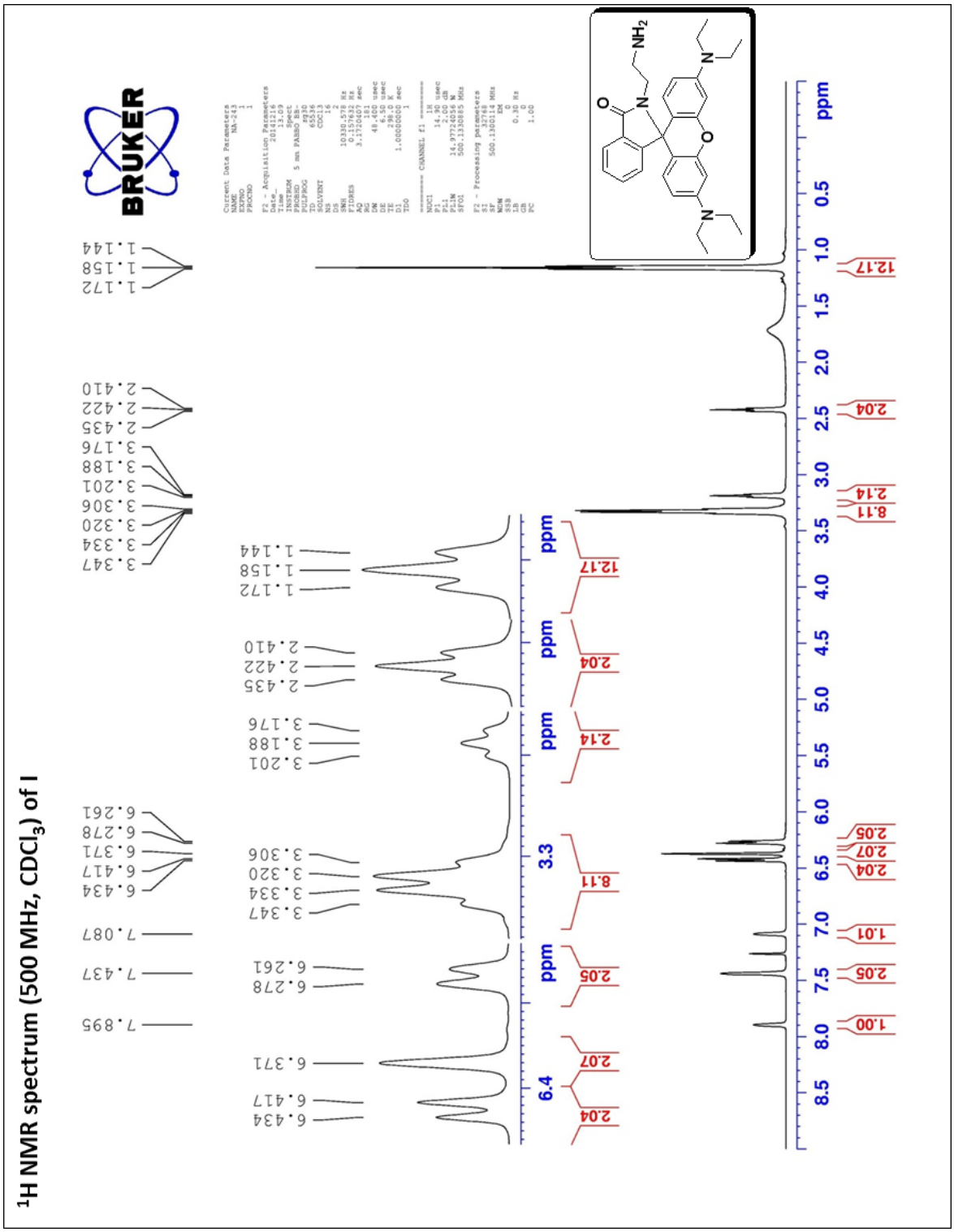
$^1$H NMR spectrum (500 MHz, $CDCl_3$) of I
BRUKER
$NH_2$
ppm

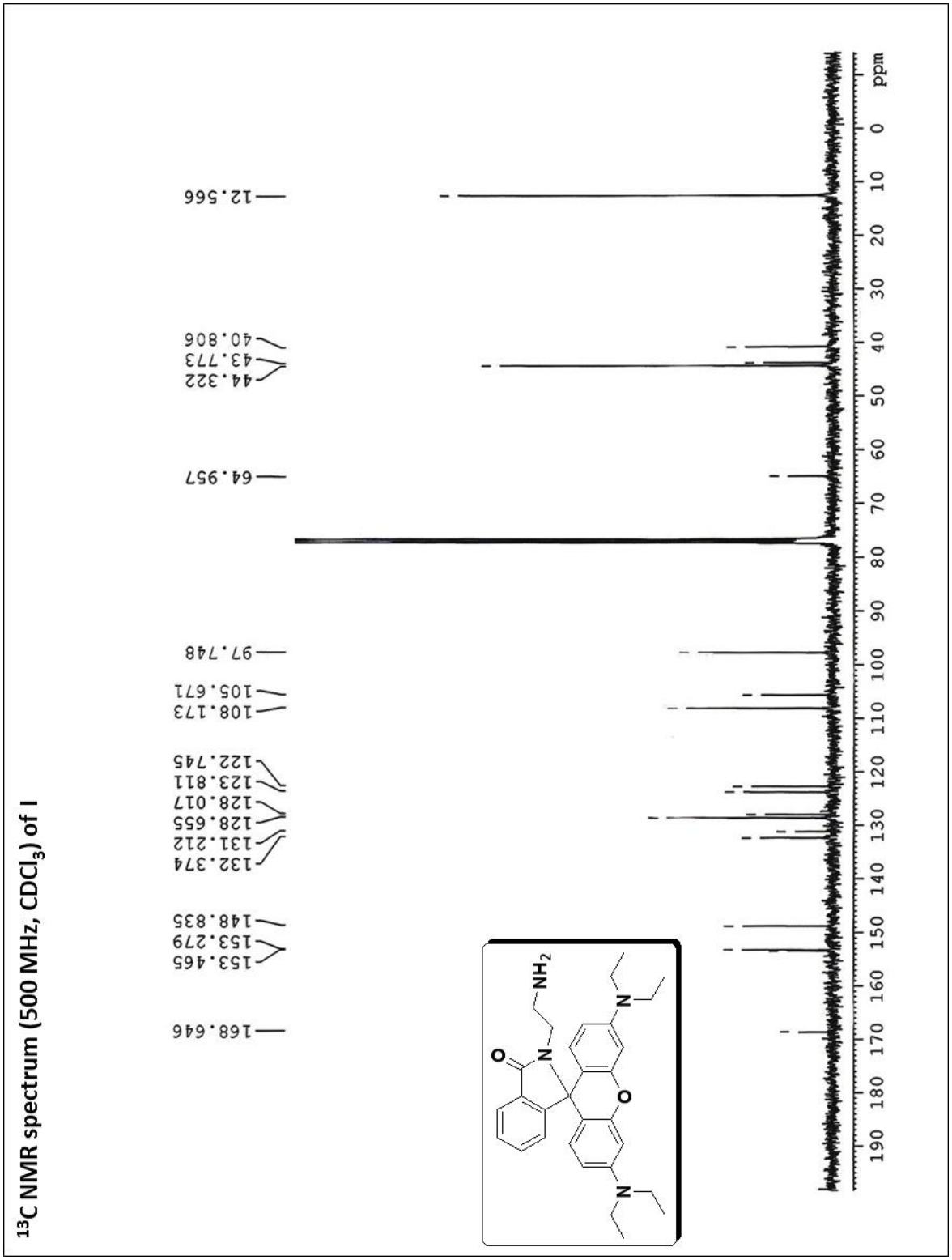


$^{13}$C NMR spectrum (500 MHz, $CDCl_3$) of I

## ESI-MS spectrum of I

**Acquisition Parameter**

| | | | | | |
|---|---|---|---|---|---|
| Source Type | ESI | Ion Polarity | Positive | Set Nebulizer | 0.4 Bar |
| Focus | Not active | Set Capillary | 4500 V | Set Dry Heater | 180 °C |
| Scan Begin | 21 m/z | Set End Plate Offset | -500 V | Set Dry Gas | 4.0 l/min |
| Scan End | 3000 m/z | Set Collision Cell RF | 150.0 Vpp | Set Divert Valve | Source |

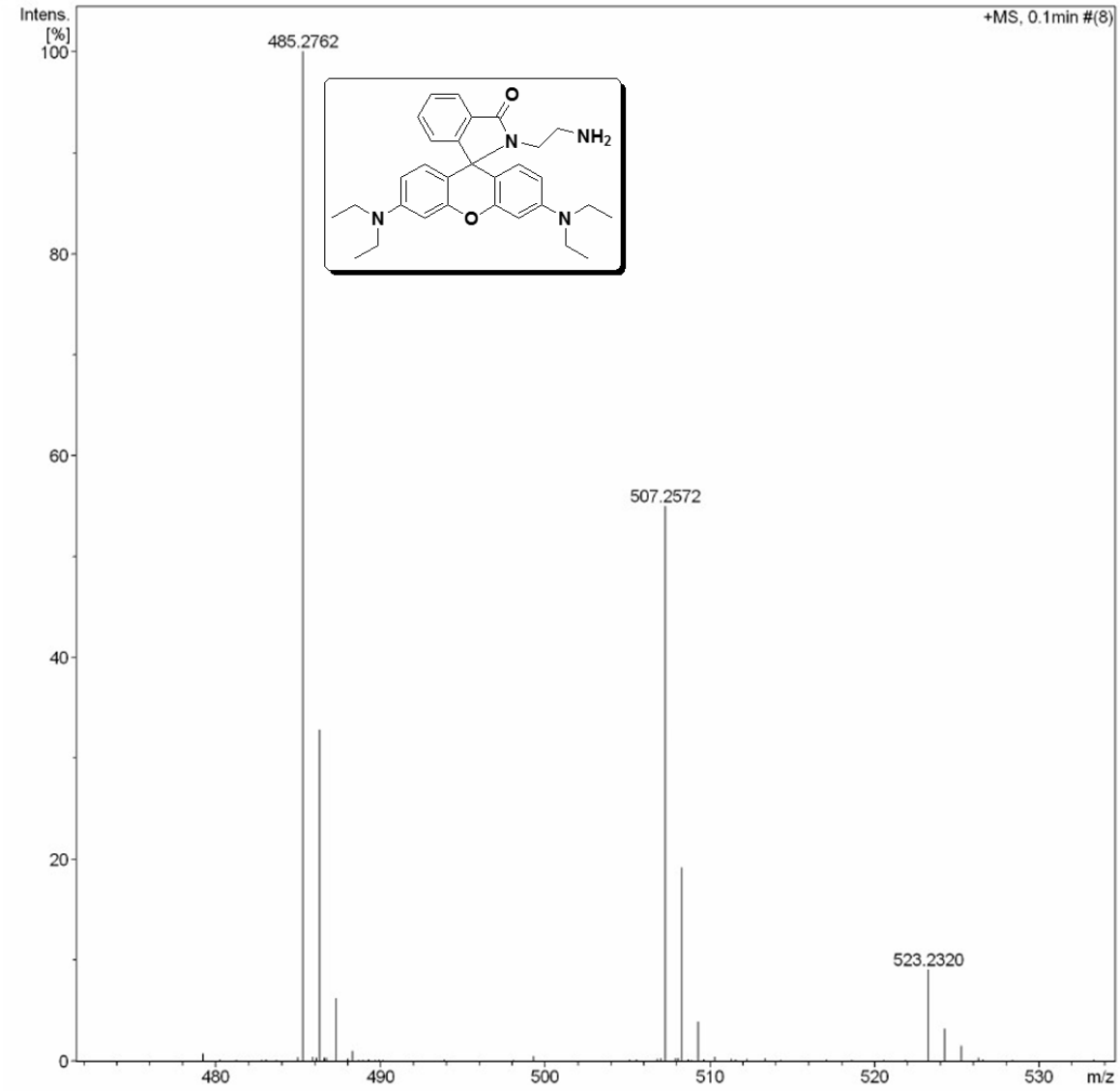

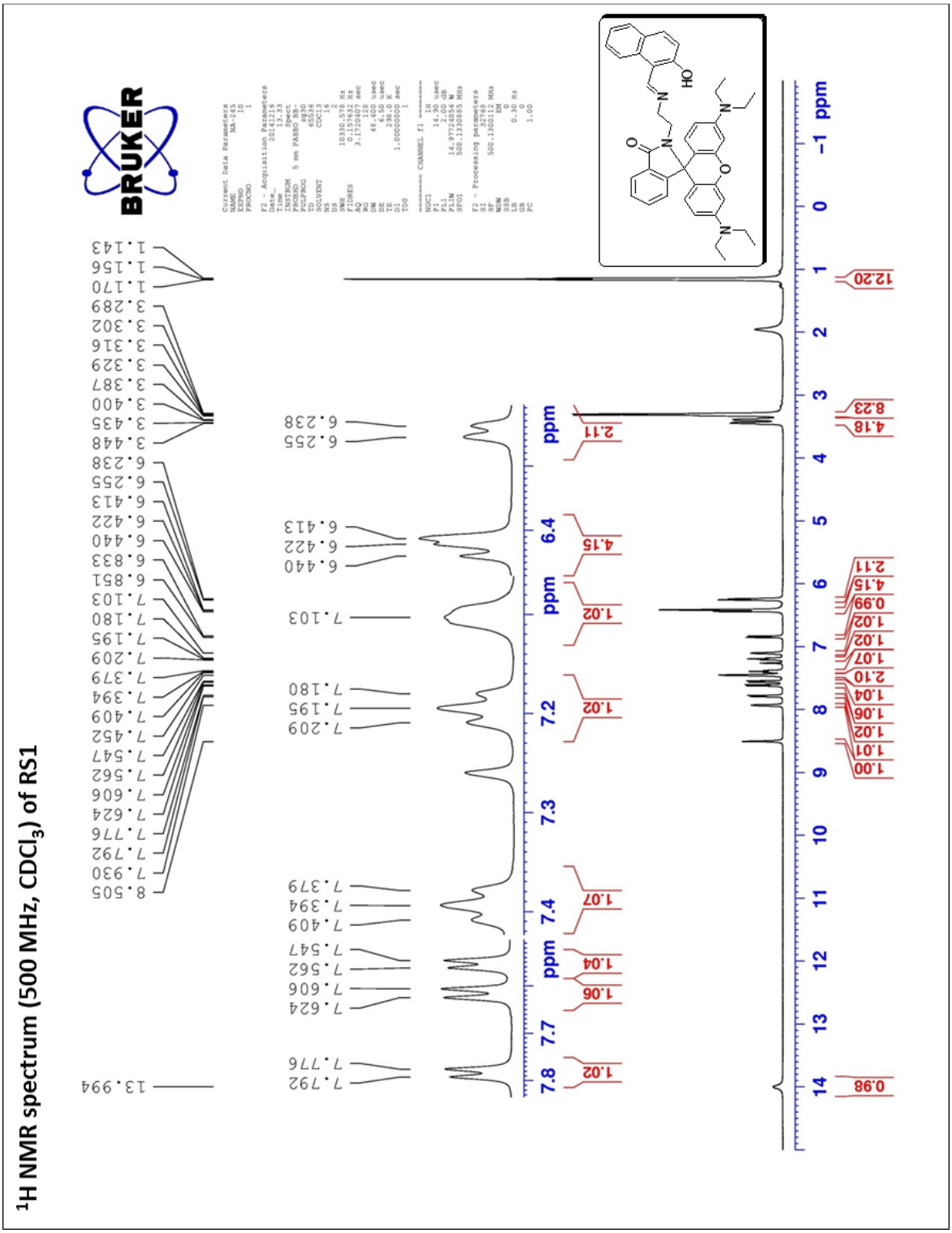
$^1$H NMR spectrum (500 MHz, $CDCl_3$) of RS1
BRUKER
HO
O
N
ppm

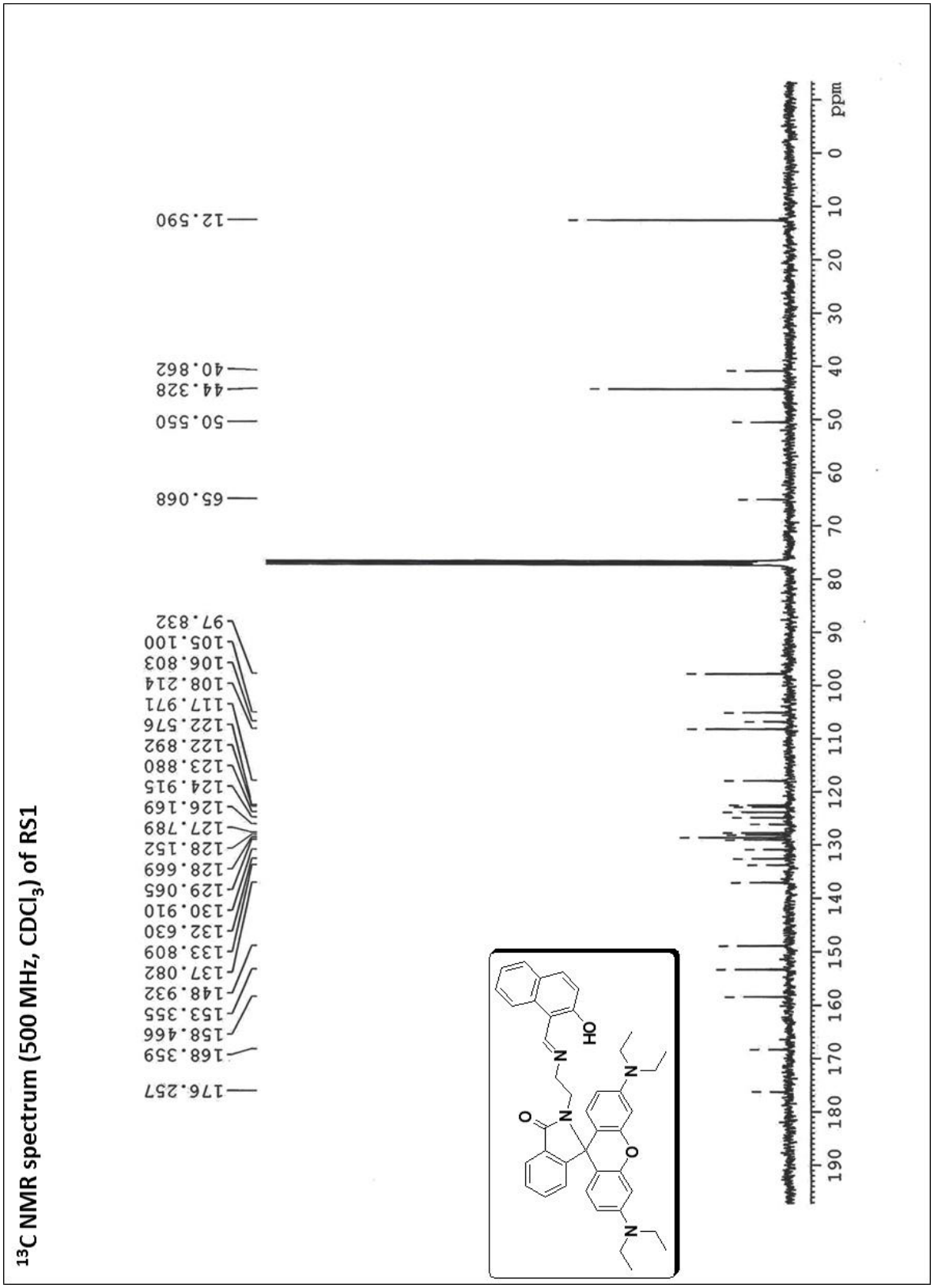


$^{13}$C NMR spectrum (500 MHz, $CDCl_3$) of RS1

## ESI-MS spectrum of RS1

**Acquisition Parameter**

| | | | | | |
|---|---|---|---|---|---|
| Source Type | ESI | Ion Polarity | Positive | Set Nebulizer | 0.4 Bar |
| Focus | Not active | Set Capillary | 4500 V | Set Dry Heater | 180 °C |
| Scan Begin | 21 m/z | Set End Plate Offset | -500 V | Set Dry Gas | 4.0 l/min |
| Scan End | 3000 m/z | Set Collision Cell RF | 150.0 Vpp | Set Divert Valve | Source |

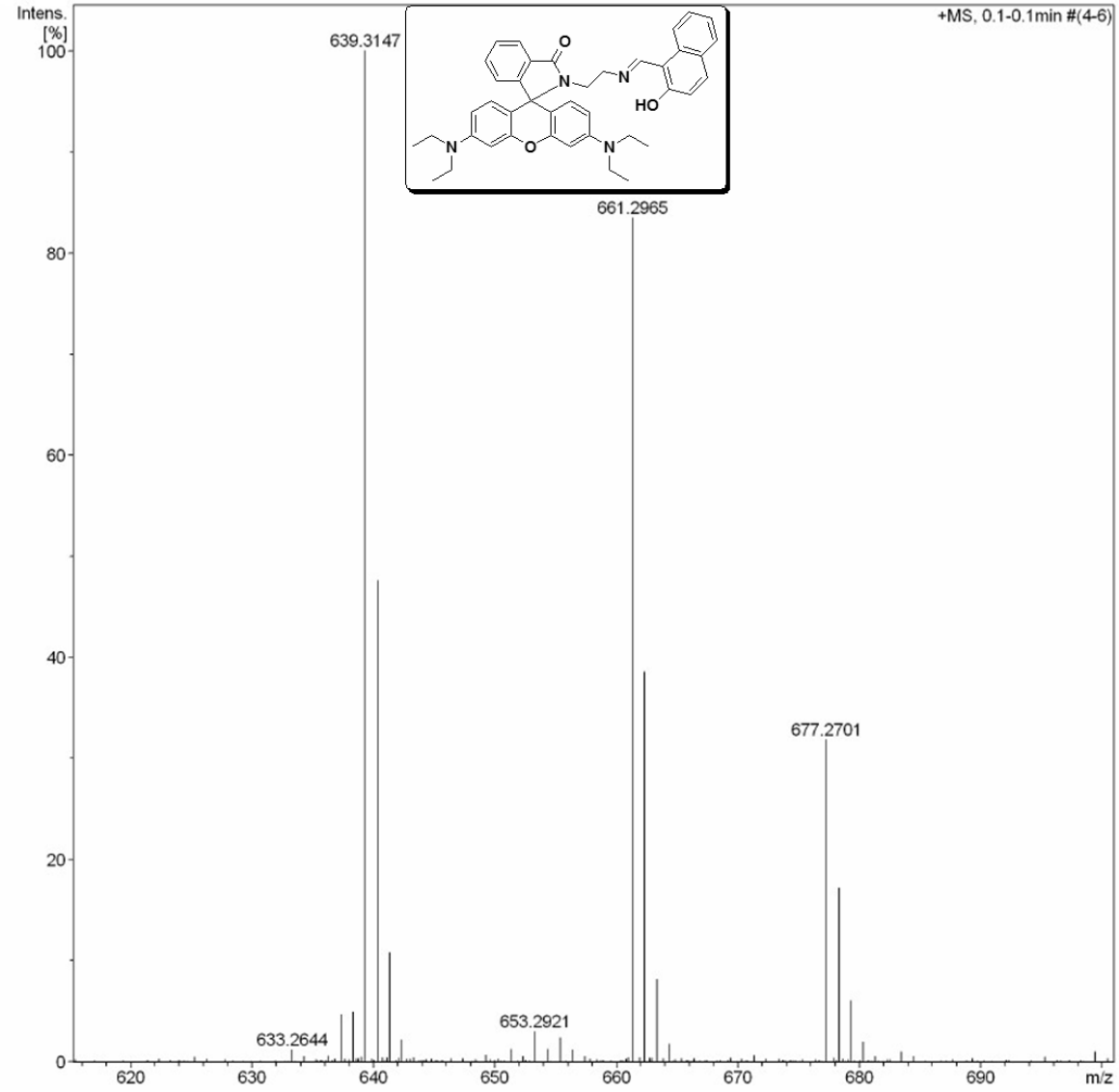

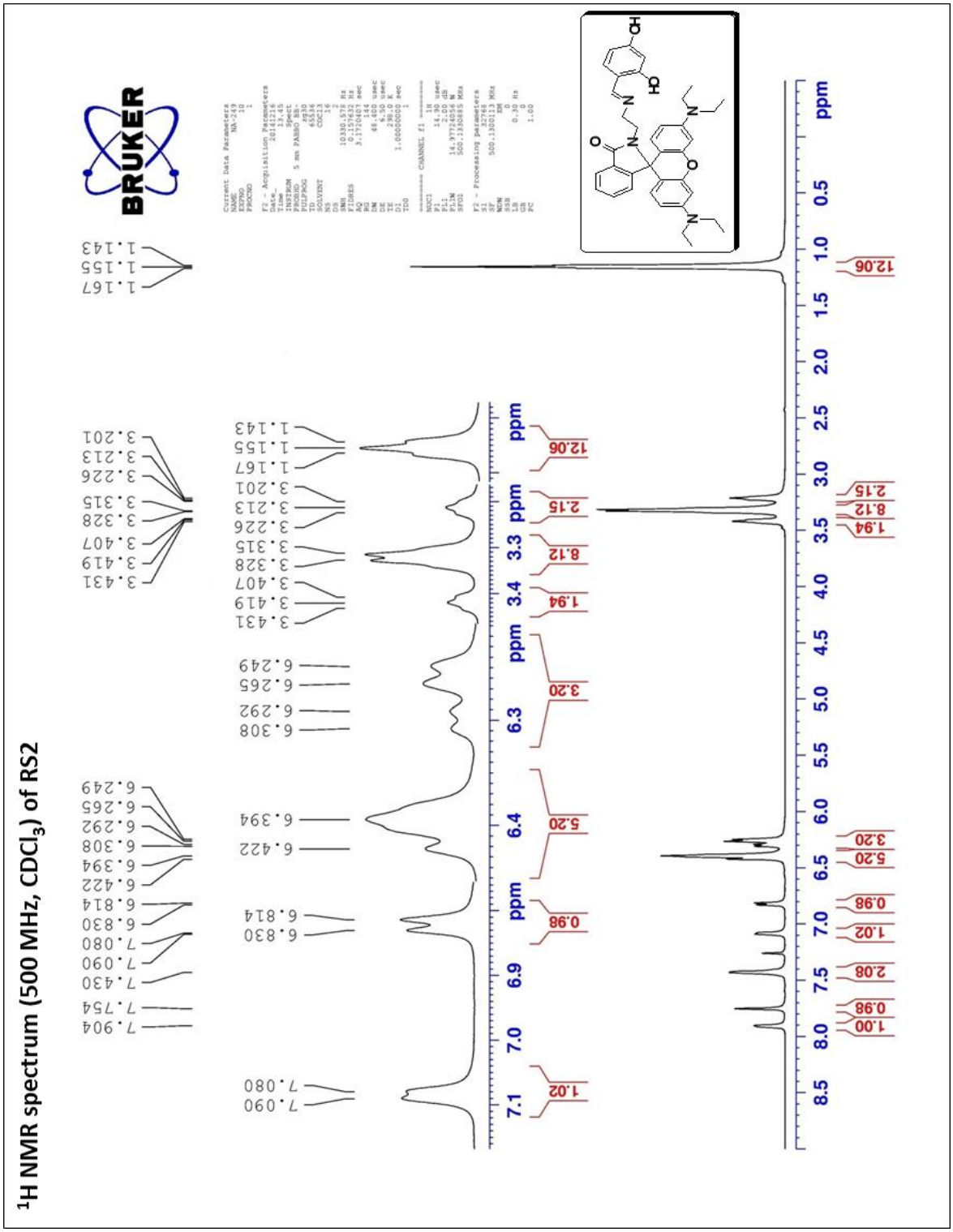


$^1$H NMR spectrum (500 MHz, $CDCl_3$) of RS2

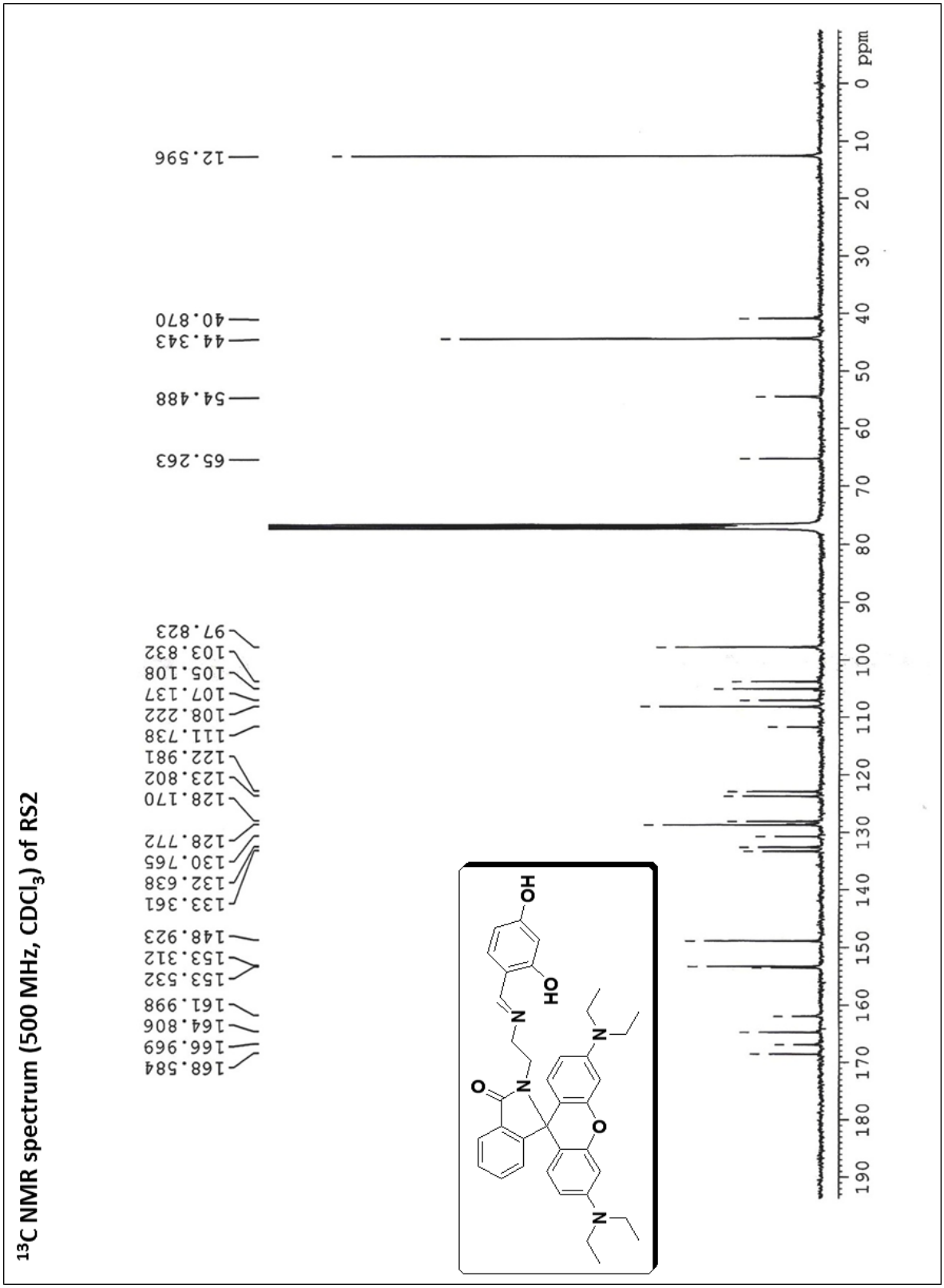


$^{13}$C NMR spectrum (500 MHz, $CDCl_3$) of RS2

## ESI-MS spectrum of RS2

**Acquisition Parameter**

| | | | | | |
|---|---|---|---|---|---|
| Source Type | ESI | Ion Polarity | Positive | Set Nebulizer | 0.4 Bar |
| Focus | Not active | Set Capillary | 4500 V | Set Dry Heater | 180 °C |
| Scan Begin | 50 m/z | Set End Plate Offset | -500 V | Set Dry Gas | 4.0 l/min |
| Scan End | 3000 m/z | Set Collision Cell RF | 650.0 Vpp | Set Divert Valve | Source |

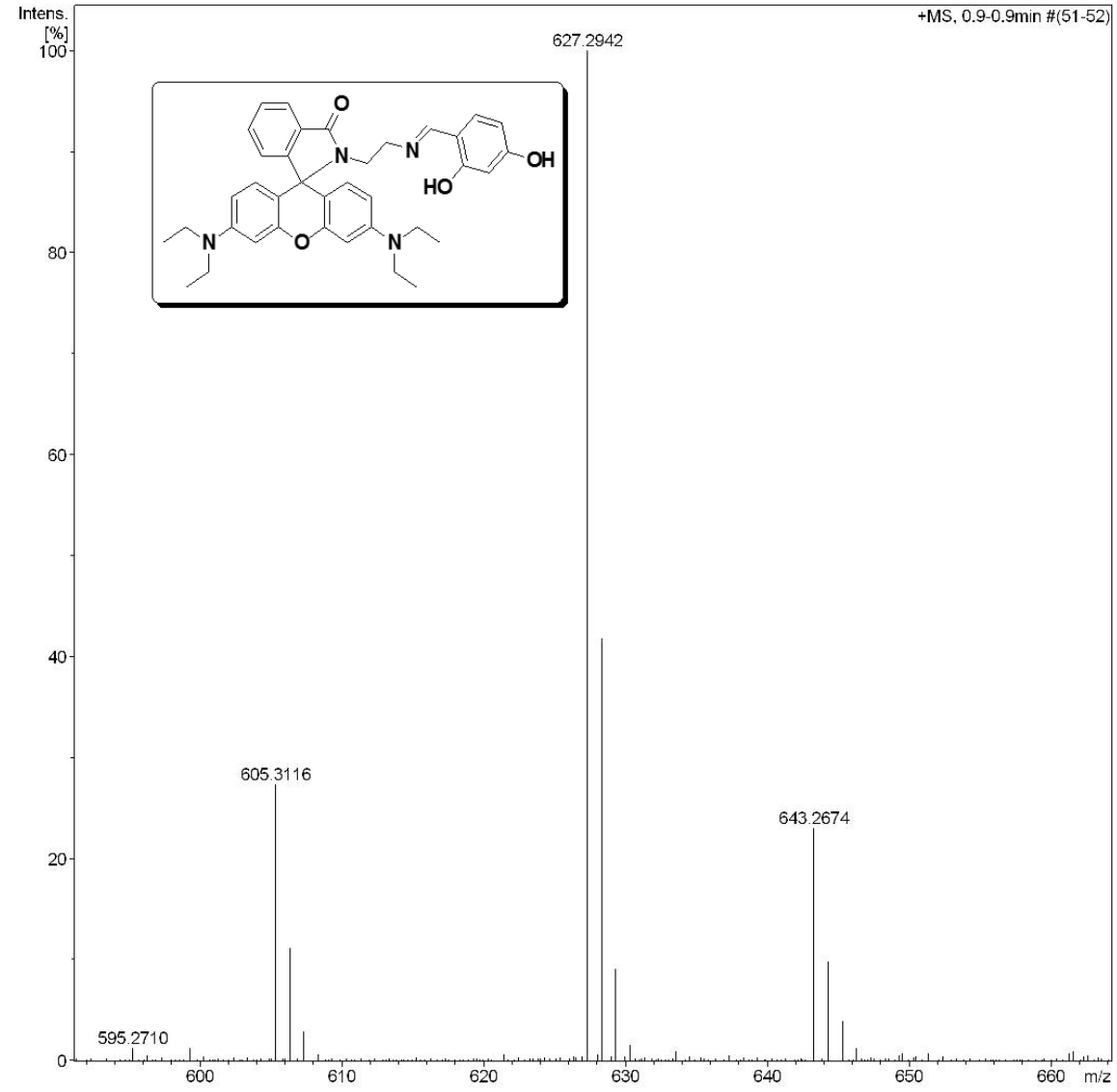

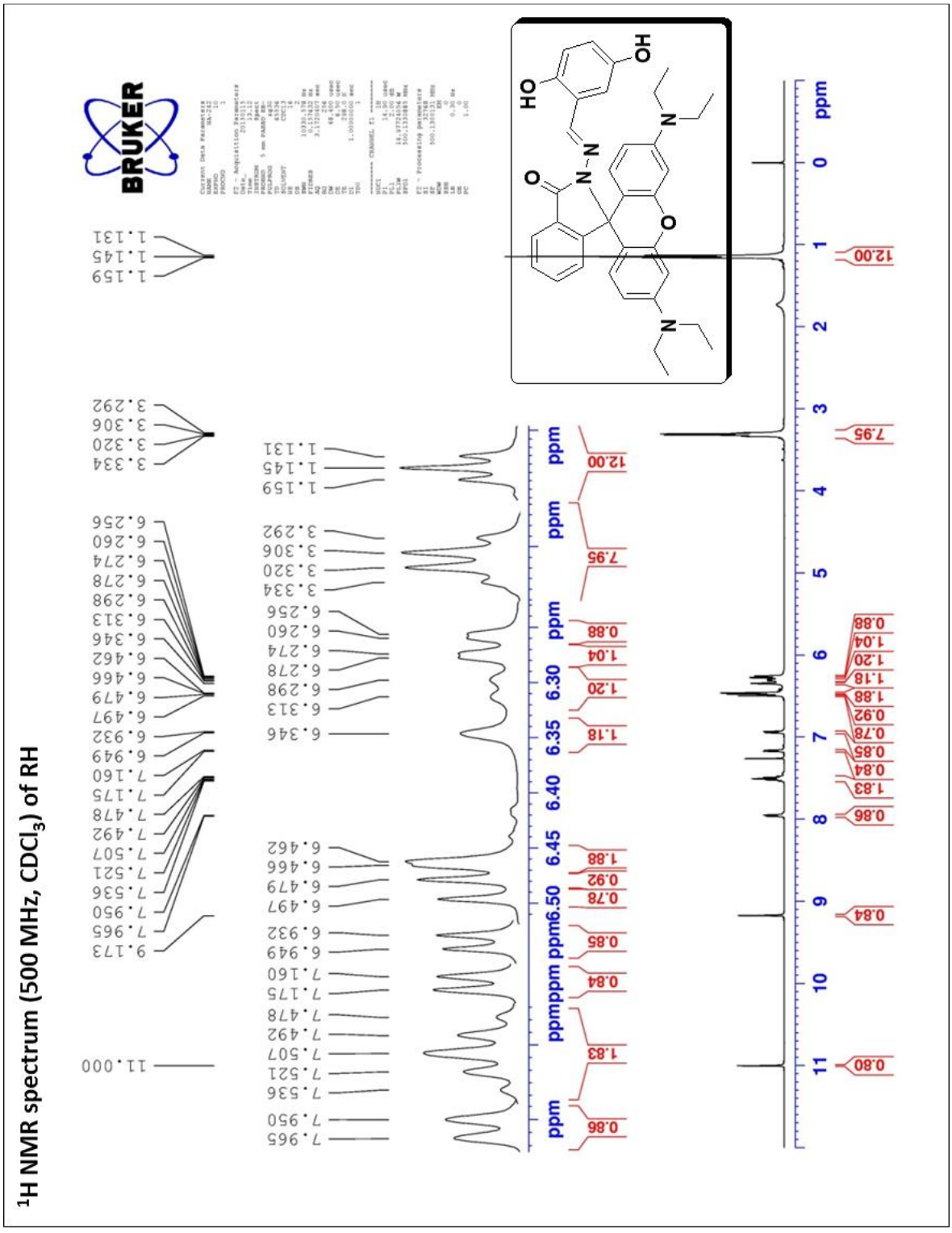
$^1$H NMR spectrum (500 MHz, $CDCl_3$) of RH
BRUKER
HO
OH
N
O
ppm

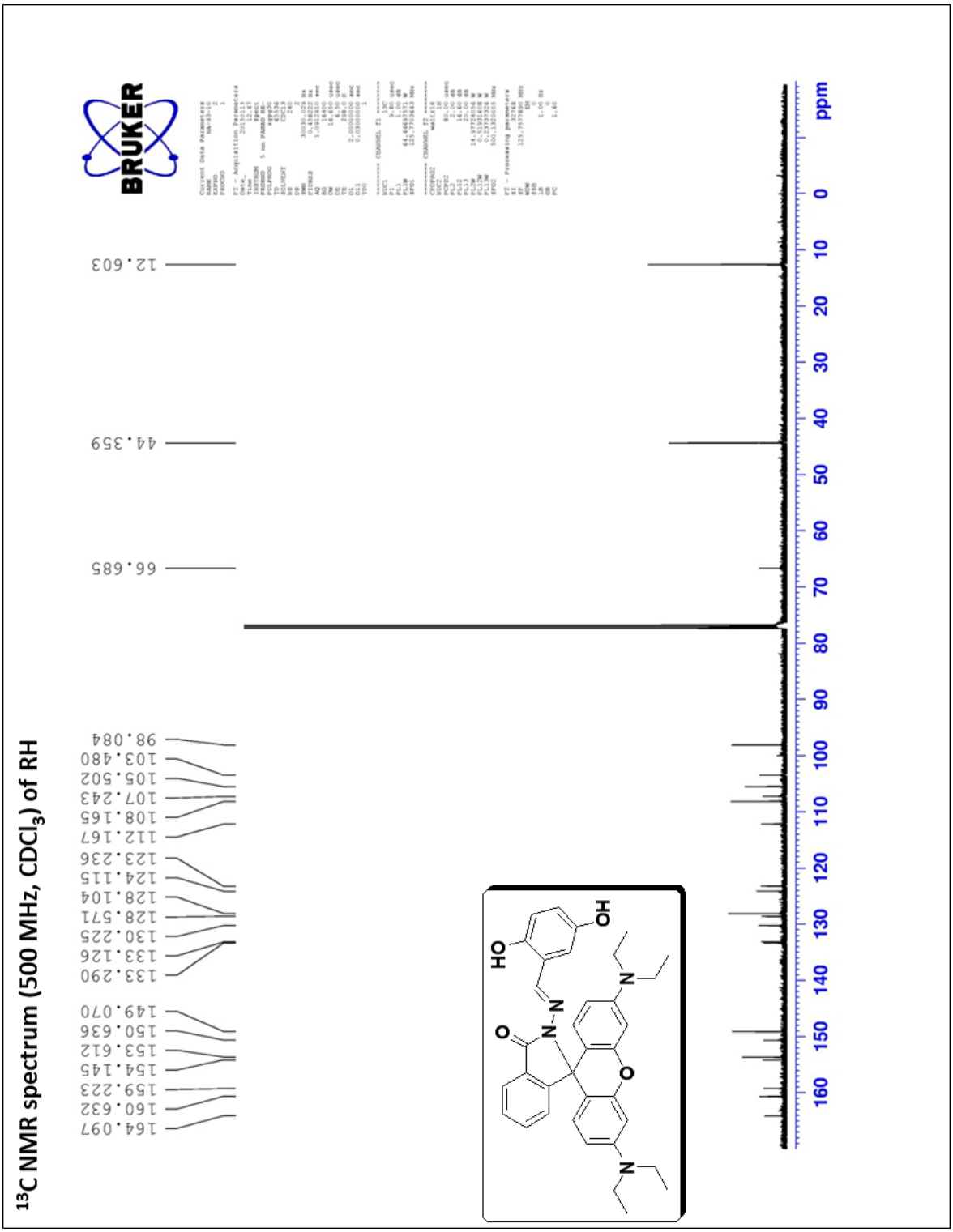
$^{13}$C NMR spectrum (500 MHz, $CDCl_3$) of RH
BRUKER
12.603
44.359
66.685
98.084
103.480
105.502
107.243
108.165
112.167
123.236
124.115
128.104
128.571
130.225
133.126
133.290
149.070
150.636
153.612
154.145
159.223
160.632
164.097
HO
OH
N
N
O
O
N
N
ppm
0
10
20
30
40
50
60
70
80
90
100
110
120
130
140
150
160

## ESI-MS spectrum of RH

**Acquisition Parameter**

| | | | | | |
|---|---|---|---|---|---|
| Source Type | ESI | Ion Polarity | Positive | Set Nebulizer | 0.4 Bar |
| Focus | Not active | Set Capillary | 4500 V | Set Dry Heater | 180 °C |
| Scan Begin | 21 m/z | Set End Plate Offset | -500 V | Set Dry Gas | 4.0 l/min |
| Scan End | 3000 m/z | Set Collision Cell RF | 150.0 Vpp | Set Divert Valve | Source |

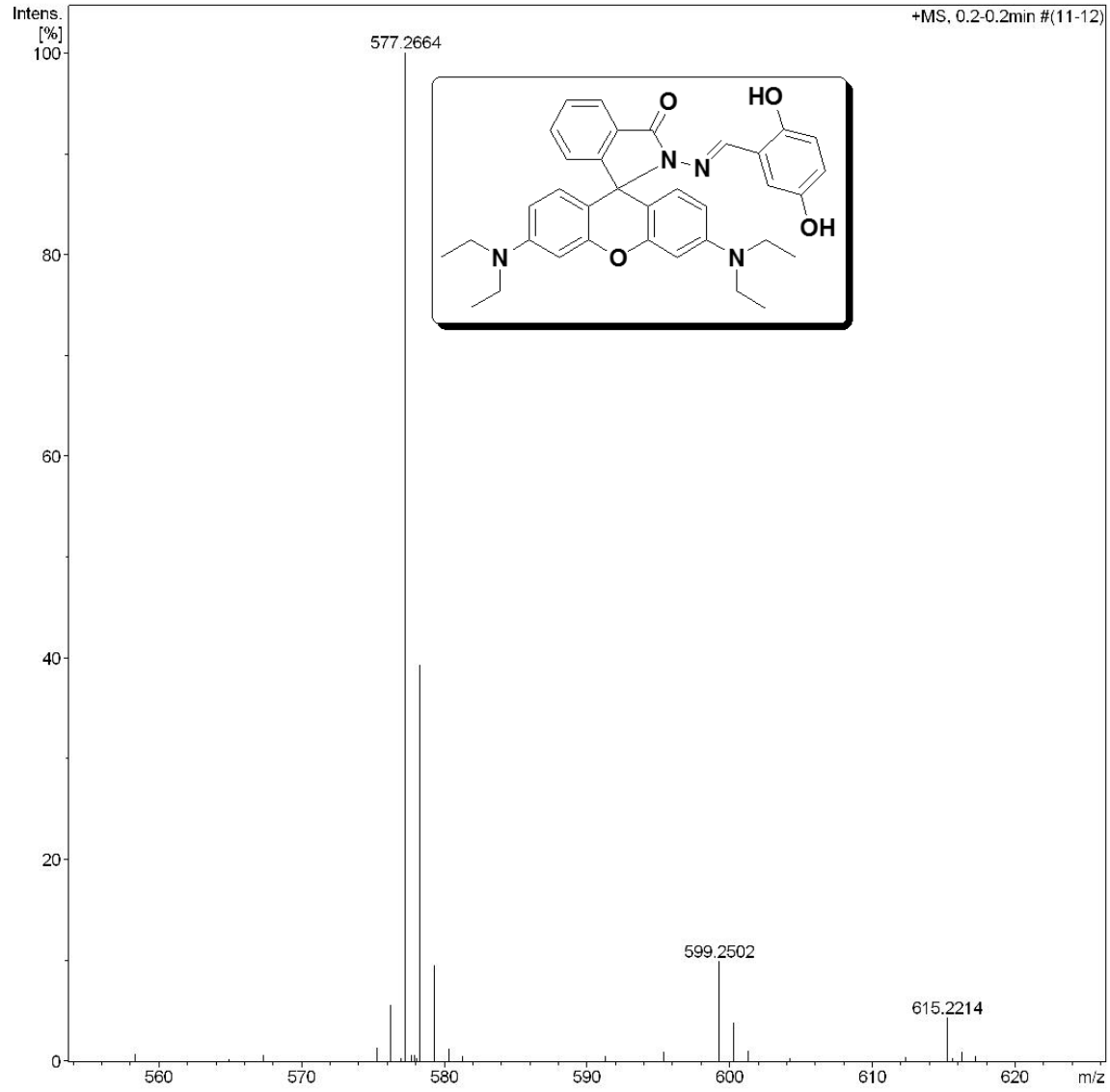

**References**


1. J.S. Kim, D.T. Quang, Calixarene-derived fluorescent probes, *Chem. Rev.*, 2007, **107**, 3780–3799.
2. H.N. Kim, M.H. Lee, H.J. Kim, J.S. Kim, J. Yoon, A new trend in rhodamine-based chemosensors: application of spirolactam ring-opening to sensing ions, *Chem. Soc. Rev.*, 2008, **37**, 1465–1472.
3. X. Chen, T. Pradhan, F. Wang, J.S. Kim, J. Yoon, Fluorescent chemosensors based on spiroring-opening of xanthenes and related derivatives, *Chem. Rev.*, 2012, **112**, 1910–1956.
4. S. Goswami, S. Paul, A. Manna, Selective "naked eye" detection of Al(III) and PPi in aqueous media on a rhodamine-isatin hybrid moiety, *RSC Adv.*, 2013, **3**, 10639–10643.
5. P.F. Good, C.W. Olanow, D.P. Perl, Neuromelanin-containing neurons of the substantia nigra accumulate iron and aluminum in parkinson's disease: a LAMMA study, *Brain Res.*, 1992, **593**, 343–346.
6. D.P. Perl, A.R. Brody, Alzheimer's disease: X-ray spectrometric evidence of aluminum accumulation in neurofibrillary tangle-bearing neurons, *Science*, 1980, **208**, 297–299.
7. W.A. Banks, A.J. Kastin, Aluminum-induced neurotoxicity: alterations in membrane function at the blood-brain barrier, *Neurosci. Biobehav. Rev.*, 1989, **13**, 47–53.
8. N.E.W. Alstad, B.M. Kjelsberg, L.A. Vollestad, E. Lydersen, A.B.S. Poleo, The significance of water ionic strength on aluminium toxicity in brown trout (Salmo trutta L.), *Environ. Pollut.*, 2005, **133,** 333–342.
9. M.N. Alvim, F.T. Ramos, D.C. Oliveira, R.M.S. Isaias, M.G.C. Franca, Aluminium localization and toxicity symptoms related to root growth inhibition in rice (Oryza sativa L.) seedlings, *J. Biosci.*, 2012, **37**, 1079–1088.
10. A.N.M. Alamgir, S. Akhter, Effects of aluminium ($Al^{3+}$) on seed germination and seedling growth of wheat (Triticum aestivum L.), *Bangladesh J. Bot.*, 2009, **38**, 1–6.
11. V. Amendola, D. Esteban-Gomez, L. Fabbrizzi, M. Licchelli, What anions do to N-H-containing receptors, *Acc. Chem. Res.*, 2006, **39**, 343–353.
12. P.D. Beer, P.A. Gale, Anion recognition and sensing: The state of the art and future perspectives, *Angew. Chem., Int. Ed.*, 2001, **40**, 486–516.
13. P.A. Gale, S.E. Garcia-Garrido, J. Garric, Anion receptors based on organic frameworks: Highlights from 2005 and 2006, *Chem. Soc. Rev.*, 2008, **37,** 151–190.

14. T. Gunnlaugsson, P.E. Kruger, P. Jensen, J. Tierney, H.D.P. Ali, G.M. Hussey, Colorimetric ‘‘naked eye’’ sensing of anions in aqueous solution, *J. Org. Chem.*, 2005, **70**, 10875–10878.
15. A. Davenport, F.J. Will, A.M. Davison, Hyperlactatemia and metabolic acidosis during haemofiltration using lactate-buffered fluids, *Nephron*, 1991, **59**, 461–465.
16. X.F. Shang, X.F. Xu, The anion recognition properties of hydrazone derivatives containing anthracene, *Biosystems*, 2009, **96**, 165–171.
17. K.L. Kirk, Biochemistry of the halogens and inorganic halides, *Plenum Press*, New York, 1991, p. 58.
18. M. Kleerekoper, The role of fluoride in the prevention of osteoporosis, *Endocrinol. Metab. Clin. North. Am.*, 1998, **27**, 441–452.
19. T. Jentsch, Chloride channels: a molecular perspective, *Curr. Opin. Neurobiol.*, 1996, **6**, 303–310.
20. J.A. Weatherall, Pharmacology of fluorides, in: Handbook of experimental pharmacology, F.A. Smith (ed.), vol. XX/2, Part 2, *Springer-Verlag, Berlin*, 1969, p. 141.
21. Y. Michigami, Y. Kuroda, K. Ueda, Y. Yamamoto, Determination of urinary fluoride by ion chromatography, *Anal. Chim. Acta*, 1993, **274**, 299–302.
22. J.A. Varner, K.F. Jensen, W. Horvath, R.L. Isaacson, Chronic administration of aluminum fluoride or sodium fluoride to rats in drinking water: alterations in neuronal and cerebrovascular integrity, *Brain Res.*, 1998, **784**, 284–298.
23. Y. Yamini, N. Alizadeh, M. Shamsipur, Solid phase extraction and determination of ultra trace amounts of mercury(II) using octadecyl silica membrane disks modified by hexathia-18-crown-6-tetraone and cold vapour atomic absorption spectrometry, *Anal. Chim. Acta*, 1997, **355**, 69–74.
24. C.F. Harrington, S.A. Merson, T.M.D. D’Silva, Method to reduce the memory effect of mercury in the analysis of fish tissue using inductively coupled plasma mass spectrometry, *Anal. Chim. Acta*, 2004, **505**, 247–254.
25. S.L.C. Ferreira, A.S. Queiroz, M.S. Fernandes, H.C. dos Santos, Application of factorial designs and Doehlert matrix in optimization of experimental variables associated with the preconcentration and determination of vanadium and copper in seawater by inductively coupled plasma optical emission spectrometry, *Spectrochim. Acta B*, 2002, **57**, 1939–1950.

26. J.C. Yu, J.M. Lo, K.M. Wai, Extraction of gold and mercury from sea water with bismuth diethyldithiocarbamate prior to neutron activation—γ-spectrometry, *Anal. Chim. Acta*, 1983, **154**, 307–312.
27. A. Ali, H. Shen, X. Yin, Simultaneous determination of trace amounts of nickel, copper and mercury by liquid chromatography coupled with flow injection online derivatization and preconcentration, *Anal. Chim. Acta*, 1998, **369**, 215–223.
28. A. Bobrowski, K. Nowak, J. Zarebski, Application of a bismuth film electrode to the Voltammetric determination of trace iron using a Fe(III)-TEA-$BrO_3^-$ catalytic system, *Anal. Bioanal. Chem.*, 2005, **382**, 1691–1697.
29. V.K. Gupta, N. Mergu, A.K. Singh, Fluorescent chemosensors for $Zn^{2+}$ ions based on flavonol derivatives, *Sens. Actuators B*, 2014, **202**, 674–682.
30. V.K. Gupta, A.K. Singh, L.K. Kumawat, A turn-on fluorescent chemosensor for $Zn^{2+}$ ions based on antipyrine schiff base, *Sens. Actuators B*, 2014, **204**, 507–514.
31. V.K. Gupta, N. Mergu, L.K. Kumawat, A.K. Singh, Selective naked-eye detection of magnesium (II) ions using a coumarin-derived fluorescent probe, *Sens. Actuators B*, 2015, **207**, 216–223.
32. V.K. Gupta, A.K. Singh, N. Mergu, Antipyrine based schiff bases as turn-on fluorescent sensors for Al(III) ion, *Electrochim. Acta*, 2014, **117**, 405–412.
33. V.K. Gupta, A.K. Singh, L.K. Kumawat, Thiazole schiff base turn-on fluorescent chemosensor for $Al^{3+}$ ion, *Sens. Actuators B*, 2014, **195**, 98–108.
34. V.K. Gupta, S.K. Shoora, L.K. Kumawat, A.K. Jain, A highly selective colorimetric and turn-on fluorescent chemosensor based on 1-(2-pyridylazo)-2-naphthol for the detection of aluminium(III) ions, *Sens. Actuators B*, 2015, **209**, 15–24.
35. W. Gong, B. Gao, S. Bao, J. Ye, G. Ning, Selective ‘‘naked-eye’’ sensing of acetate ion based on conformational flexible amide-pyridinium receptor, *J. Inclusion Phenom. Macrocyclic Chem.*, 2012, **72**, 481–486.
36. J. Shao, H. Lin, M. Yu, Z. Cai, H. Lin, Study on acetate ion recognition and sensing in aqueous media using a novel and simple colorimetric sensor and its analytical application, *Talanta*, 2008, **75**, 551–555.
37. Y. Zhou, J.F. Zhang, J. Yoon, Fluorescence and colorimetric chemosensors for fluoride-ion detection, *Chem. Rev.*, 2014, **114**, 5511−5571.
38. S. Goswami, R. Chakrabarty, An imidazole based colorimetric sensor for fluoride anion, *Eur. J. Chem.*, 2011, **2**, 410−415.

39. B. Bai, J. Ma, J. Wei, J. Song, H. Wanga, M. Li, A simple structural hydrazide-based gelator as a fluoride ion colorimetric sensor, *Org. Biomol. Chem.*, 2014, **12**, 3478–3483.
40. R. McRae, P. Bagchi, S. Sumalekshmy, C.J. Fahrni, In situ imaging of metals in cell and tissues, *Chem. Rev.*, 2009, **109**, 4780–4827.
41. E.L. Que, D.W. Domaille, C.J. Chang, Metals in neurobiology: Probing their chemistry and biology with molecular imaging, *Chem. Rev.*, 2008, **108**, 1517–1549.
42. C. Kar, S. Samanta, S. Mukherjee, B.K. Datta, A. Ramesh, G. Das, A simple and efficient fluorophoric probe for dual sensing of $Fe^{3+}$ and $F^{-}$: Application to bioimaging in native cellular iron pools and live cells, *New J. Chem.*, 2014, **38**, 2660–2669.
43. D. Ramaiah, P.P. Neelakandan, A.K. Nair, R.R. Avirah, Functional cyclophanes: Promising hosts for optical biomolecular recognition, *Chem. Soc. Rev.*, 2010, **39**, 4158–4168.
44. N. Kumar, V. Bhalla, M. Kumar, Recent developments of fluorescent probes for the detection of gasotransmitters (NO, CO and $H_2S$), *Coord. Chem. Rev.*, 2013, **257**, 2335–2347.
45. D. Guo, Z. Dong, C. Luo, W. Zan, S. Yan, X. Yao, A rhodamine B-based "turn-on" fluorescent sensor for detecting $Cu^{2+}$ and sulfur anions in aqueous media, *RSC Adv.*, 2014, **4**, 5718–5725.
46. C.R. Lohani, J.M. Kim, S.Y. Chung, J. Yoon, K.H. Lee, Colorimetric and fluorescent sensing of pyrophosphate in 100% aqueous solution by a system comprised of rhodamine B compound and $Al^{3+}$ complex, *Analyst*, 2010, **135**, 2079–2084.
47. M.G. Choi, S. Cha, H. Lee, H.L. Jeon, S.-K. Chang, Sulfide-selective chemosignaling by a $Cu^{2+}$ complex of dipicolylamine appended fluorescein, *Chem. Commun.*, 2009, 7390–7392.
48. Y. Xiang, A. Tong, P. Jin, Y. Ju, New fluorescent rhodamine hydrazone chemosensor for Cu(II) with high selectivity and sensitivity, *Org. Lett.*, 2006, **8**, 2863–2866.
49. B.N. Ahamed, P. Ghosh, An integrated system of pyrene and rhodamine-6G for selective colorimetric and fluorometric sensing of mercury (II). *Inorg. Chim. Acta*, 2011, **372**, 100–107.
50. M.J. Frisch, G.W. Trucks, H.B. Schlegel, G.E. Scuseria, M.A. Robb, J.R. Cheeseman, G. Scalmani, V. Barone, B. Mennucci, G.A. Petersson, H. Nakatsuji, M. Caricato, X. Li, H.P. Hratchian, A.F. Izmaylov, J. Bloino, G. Zheng, J.L. Sonnenberg, M. Hada, M. Ehara, K. Toyota, R. Fukuda, J. Hasegawa, M. Ishida, T. Nakajima, Y. Honda, O.

Kitao, H. Nakai, T. Vreven, J.A. Montgomery, Jr. J.E. Peralta, F. Ogliaro, M. Bearpark, J.J. Heyd, E. Brothers, K.N. Kudin, V.N. Staroverov, R. Kobayashi, J. Normand, K. Raghavachari, A. Rendell, J.C. Burant, S.S. Iyengar, J. Tomasi, M. Cossi, N. Rega, J.M. Millam, M. Klene, J.E. Knox, J.B. Cross, V. Bakken, C. Adamo, J. Jaramillo, R. Gomperts, R.E. Stratmann, O. Yazyev, A.J. Austin, R. Cammi, C. Pomelli, J.W. Ochterski, R.L. Martin, K. Morokuma, V.G. Zakrzewski, G.A. Voth, P. Salvador, J.J. Dannenberg, S. Dapprich, A.D. Daniels, O. Farkas, J.B. Foresman, J.V. Ortiz, J. Cioslowski, D.J. Fox, Gaussian 09, Revision A.02, *Gaussian Inc.*, Wallingford, CT, 2009.

51. A.J. Weerasinghe, C. Schmiesing, E.H. Sinn, Highly sensitive and selective reversible sensor for the detection of $Cr^{3+}$, *Tetrahedron Lett.*, 2009, **50**, 6407–6410.
52. D.E. Kimbrough, Y. Cohen, A.M. Winer, L. Creelman, C.A. Mabuni, A critical assessment of chromium in the environment, *Crit. Rev. Environ. Sci. Technol.*, 1999, **29**, 1–46.
53. A.K. Singh, V.K. Gupta, B.H. Gupta, Chromium(III) selective membrane sensors based on Schiff bases as chelating ionophores, *Anal. Chim. Acta*, 2007, **585**, 171–178.
54. M. Sarkar, S. Banthia, A. Samanta, A highly selective 'off–on' fluorescence chemosensor for Cr(III), *Tetrahedron Lett.*, 2006, **47**, 7575–7578.
55. M.H. Mashhadizadeh, M. Pesteh, M. Talakesh, I. Sheikhshoaie, M.M. Ardakani, M.A. Karimi, Solid phase extraction of lead(II), copper(II), cadmium(II) and nickel(II) using gallic acid-modified silica gel prior to determination by flame atomic absorption spectrometry, *Spectrochim. Acta B*, 2008, **63**, 885–888.
56. R.J. Cassella, O.I.B. Magalhaes, M.T. Couto, E.L.S. Lima, M.A.F.S. Neves, F.M.B. Coutinho, Synthesis and application of a functionalized resin for flow injection/ F AAS copper determination in waters, *Talanta*, 2005, **67**, 121–128.
57. Chung Chow Chan (Ed.), Analytical method validation and instrument performance verification, *Wiley*, New York, 2004, p. 303.
58. D. Harvey, Modern analytical chemistry, *Wiley*, New York, 2000, p. 816.
59. A. Mohadesi, M.A. Taher, Voltammetric determination of Cu(II) in natural waters and human hair at a meso-2,3-dimercaptosuccinic acid self-assembled gold electrode, *Talanta*, 2007, **72**, 95–100.
60. G.D. Christian, Analytical chemistry, *Phoenix Color Corp*, New York, 1994, p. 812.

61. M. Zhao, L. Ma, M. Zhang, W. Cao, L. Yang, L.J. Ma, Glutamine-containing "turn-on" fluorescence sensor for the highly sensitive and selective detection of chromium (III) ion in water, *Spectrochim. Acta A*, 2013, **116**, 460–465.
62. Z. Zhou, M. Yu, H. Yang, K. Huang, F. Li, T. Yi, C. Huang, FRET-based sensor for imaging chromium(III) in living cells, *Chem. Commun.*, 2008, 3387–3389.
63. Y.J. Jang, Y.H. Yeon, H.Y. Yang, J.Y. Noh, I.H. Hwang, C. Kim, A colorimetric and fluorescent chemosensor for selective detection of $Cr^{3+}$ and $Al^{3+}$, *Inorg. Chem. Commun.*, 2013, **33**, 48–51.
64. H.W. Wang, Y.Q. Feng, C. Chen, J.Q. Xue, Two novel fluorescent calix[4]arene derivatives with benzoazole units in 1,3-alternate conformation for selective recognition to $Fe^{3+}$ and $Cr^{3+}$, *Chin. Chem. Lett.*, 2009, **20**, 1271–1274.
65. X. Wang, Y. Wei, S. Wang, L. Chen, Red-to-blue colorimetric detection of chromium via Cr (III)-citrate chelating based on Tween 20 stabilized gold nanoparticles, *Colloids Surf. A*, 2015, **472**, 57–62.
66. M. Beija, C.A.M. Afonso, J.M.G. Martinho, Synthesis and applications of Rhodamine derivatives as fluorescent probes, *Chem. Soc. Rev.*, 2009, **38**, 2410–2433.
67. G. Grynkiewicz, M. Poenie, R.Y. Tsien, A new generation of $Ca^{2+}$ indicators with greatly improved fluorescence properties, *J. Biol. Chem.*, 1985, **260**, 3440–3450.
68. A. Minta, R.Y. Tsien, Fluorescent indicators for cytosolic sodium, *J. Biol. Chem.*, 1989, **264**, 19449–19457.
69. C. Yu, J. Zhang, R. Wang, L. Chen, Highly sensitive and selective colorimetric and off-on fluorescent probe for $Cu^{2+}$ based on rhodamine derivative, *Org. Biomol. Chem.*, 2010, **8**, 5277–5279.
70. C. Kaewtong, B. Wanno, Y. Uppa, N. Morakot, B. Pulpoka, T. Tuntulani, Facile synthesis of rhodamine-based highly sensitive and fast responsive colorimetric and off-on fluorescent reversible chemosensors for $Hg^{2+}$: preparation of fluorescent thin film sensor, *Dalton Trans.*, 2011, **40**, 12578–12583.
71. A. Sahana, A. Banerjee, S. Lohar, A. Banik, S.K. Mukhopadhyay, D.A. Safin, M.G. Babashkina, M. Bolte, Y. Garcia, D. Das, FRET based tri-color emissive rhodamine-pyrene conjugate as an $Al^{3+}$ selective colorimetric and fluorescence sensor for living cell imaging, *Dalton Trans.*, 2013, **42**, 13311–13314.

72. M.H. Lee, J.S. Wu, J.W. Lee, J.H. Jung, J.S. Kim, Highly sensitive and selective chemosensor for $Hg^{2+}$ based on the rhodamine fluorophore, *Org. Lett.*, 2007, **9**, 2501–2504.

73. J. Du, J. Fan, X. Peng, P. Sun, J. Wang, H. Li, S. Sun, A new fluorescent chemodosimeter for $Hg^{2+}$: selectivity, sensitivity, resistance to Cys and GSH, *Org. Lett.*, 2010, **12**, 476–479.

74. C. Yu, L. Chen, J. Zhang, J. Li, P. Liu, W. Wang, B. Yan, "Off-On" based fluorescent chemosensor for $Cu^{2+}$ in aqueous media and living cells, *Talanta*, 2011, **85**, 1627–1633.

75. C. Yu, J. Zhang, J. Li, P. Liu, P. Wei, L. Chen, Fluorescent probe for copper(II) ion based on a rhodamine spirolactame derivative, and its application to fluorescent imaging in living cells, *Microchim. Acta*, 2011, **174**, 247–255.

76. N. Mergu, A.K. Singh, V.K. Gupta, Highly sensitive and selective colorimetric and off-on fluorescent reversible chemosensors for $Al^{3+}$ based on the rhodamine fluorophore, *Sensors*, 2015, **15**, 9097–9111.

77. B. Bag, A. Pal, Rhodamine-based probes for metal ion-induced chromo-/fluorogenic dual signalling and their selectivity towards Hg(II) ion, *Org. Biomol. Chem.*, 2011, **9**, 4467–4480.

78. A. Shafiee, M.M. Salleh, M. Yahaya, Determination of HOMO and LUMO of [6,6]-phenyl C61-butyric acid 3-ethylthiophene ester and poly (3-octyl-thiophene-2, 5-diyl) through voltametry characterization, *Sains Malays.*, 2011, **40**, 173–176.

79. V.K. Gupta, A.K. Singh, N. Mergu, A new beryllium ion-selective membrane electrode based on dibenzo(perhydrotriazino)aza-14-crown-4 ether, *Anal. Chim. Acta*, 2012, **749**, 44–50.

80. X. Wu, Z. Guo, Y. Wu, S. Zhu, T.D. James, W. Zhu, Near-infrared colorimetric fluorescent $Cu^{2+}$ sensors based on indoline–benzothiadiazole derivatives via formation of radical cations, *ACS Appl. Mater. Interfaces*, 2013, **5**, 12215–12220.

81. R. Kagit, M. Yildirim, O. Ozay, S. Yesilot, H. Ozay, Phosphazene based multicentered naked-eye fluorescent sensor with high selectivity for $Fe^{3+}$ ions, *Inorg. Chem.*, 2014, **53**, 2144–2151.

82. J. Li, C. Han, W. Wu, S. Zhang, J. Guo, H. Zhou, Selective and cyclic detection of $Cr^{3+}$ using poly(methylacrylic acid) monolayer protected gold nanoparticles, *New J. Chem.*, 2014, **38**, 717–722.

83. K.P. Carter, A.M. Young, A.E. Palmer, Fluorescent sensors for measuring metal ions in living systems, *Chem. Rev.*, 2014, **114**, 4564–4601.

84. L. Zeng, E.W. Miller, A. Pralle, E.Y. Isacoff, C.J. Chang, A selective turn-on fluorescent sensor for imaging copper in living cells, *J. Am. Chem. Soc.*, 2006, **128**, 10–11.

85. L.M. Gaetke, C.K. Chow, Copper toxicity, oxidative stress, and antioxidant nutrients, *Toxicology*, 2003, **189**, 147–163.

86. E. Madsen, J.D. Gitlin, Copper and iron disorders of the brain, *Annu. Rev. Neurosci.*, 2007, **30**, 317–337.

87. Y.H. Hung, A.I. Bush, R.A. Cherny, Copper in the brain and Alzheimer's disease, *J. Biol. Inorg. Chem.*, 2010, **15**, 61–76.

88. J.C. Lee, H.B. Gray, J.R. Winkler, Copper(II) binding to α-synuclein, the Parkinson's protein, *J. Am. Chem. Soc.*, 2008, **130**, 6898–6899.

89. C. Vulpe, B. Levinson, S. Whitney, S. Packman, J. Gitschier, Isolation of a candidate gene for Menkes disease and evidence that it encodes a copper-transporting ATPase, *Nat. Genet.*, 1993, **3**, 7–13.

90. G.C. Kabat, T.E. Rohan, Does excess iron play a role in breast carcinogenesis? An unresolved hypothesis, *Cancer Causes Control*, 2007, **18**, 1047–1053.

91. P. Aisen, C. Enns, M. Wessling-Resnick, Chemistry and biology of eukaryotic iron metabolism, *Int. J. Biochem. Cell Biol.*, 2001, **33**, 940–959.

92. K.J. Hintze, E.C. Theil, DNA and mRNA elements with complementary responses to hemin, antioxidant inducers, and iron control ferritin-L expression, *Proc. Natl. Acad. Sci. U.S.A.*, 2005, **102**, 15048–15052.

93. L. Huang, F. Hou, J. Cheng, P. Xi, F. Chen, D. Bai, Z. Zeng, Selective off–on fluorescent chemosensor for detection of $Fe^{3+}$ ions in aqueous media, *Org. Biomol. Chem.*, 2012, **10**, 9634–9638.

94. H. Kim, K.B. Kim, E.J. Song, I.H. Hwang, J.Y. Noh, P.-G. Kim, K.-D. Jeong, C. Kim, Turn-on selective fluorescent probe for trivalent cations, *Inorg. Chem. Commun.*, 2013, **36**, 72–76.

95. J. Wang, D. Zhang, Y. Liu, P. Ding, C. Wang, Y. Ye, Y. Zhao, A N-stablization rhodamine-based fluorescent chemosensor for $Fe^{3+}$ in aqueous solution and its application in bioimaging, *Sens. Actuators B*, 2014, **191**, 344–350.

96. P. Xie, F. Guo, R. Xia, Y. Wang, D. Yao, G. Yang, L. Xie, A rhodamine-dansyl conjugate as a FRET based sensor for $Fe^{3+}$ in the red spectral region, *J. Lumin.*, 2014, **145**, 849–854.
97. B. Verdejo, J. Aguilar, A. Domenech, C. Miranda, P. Navarro, H.R., Jimenez, C. Soriano, E. Garcia-Espana, Binuclear $Cu^{2+}$ complex mediated discrimination between L-glutamate and L-aspartate in water, *Chem. Commun.*, 2005, 3086–3088.
98. T.Y. Joo, N. Singh, G.W. Lee, D.O. Jang, Benzimidazole-based ratiometric fluorescent receptor for selective recognition of acetate, *Tetrahedron Lett.*, 2007, **48**, 8846–8850.
99. T.S. Snowden, E.V. Anslyn, Anion recognition: Synthetic receptors for anions and their application in sensors, *Curr. Opin. Chem. Biol.*, 1999, **3**, 740–746.
100. J.M. Lehn, From supramolecular chemistry towards constitutional dynamic chemistry and adaptive chemistry, *Chem. Soc. Rev.*, 2007, **36**, 151–160.
101. B.L. Riggs, Treatment of osteoporosis with sodium fluoride: An appraisal, in: Bone and mineral research, Annual 2, W.A. Peck (ed.), *Elsevier*, Amsterdam, 1984, pp. 366–393.
102. R.K. Pathak, V.K. Hinge, P. Mondala, C.P. Rao, Ratiometric fluorescence off-on-off sensor for $Cu^{2+}$ in aqueous buffer by a lower rim triazole linked benzimidazole conjugate of calix[4]arene, *Dalton Trans.*, 2012, **41**, 10652–10660.
103. N. Mergu, V.K. Gupta, A novel colorimetric detection probe for copper(II) ions based on a Schiff base, *Sens. Actuators B*, 2015, **210**, 408–417.
104. L.K. Kumawat, N. Mergu, A.K. Singh, V.K. Gupta, A novel optical sensor for copper ions based on phthalocyanine tetrasulfonic acid, *Sens. Actuators B*, 2015, **212**, 389–394.
105. D.P. Murale, S.T. Manjare, Y.S. Lee, D.G. Churchill, Fluorescence probing of the ferric Fenton reaction via novel chelation, *Chem. Commun.*, 2014, **50**, 359–361.
106. Y. Yang, K. Yu, L. Yang, J. Liu, K. Li, S. Luo, One single molecule as a multifunctional fluorescent probe for ratiometric sensing of $Fe^{3+}$, $Cr^{3+}$ and colorimetric sensing of $Cu^{2+}$, *Sensors*, 2015, **15**, 49–58.
107. S.L. Shen, X.P. Chen, X.F. Zhang, J.Y. Miao, B.X. Zhao, A rhodamine B-based lysosomal pH probe, *J. Mater. Chem. B*, 2015, **3**, 919–925.
108. K. Soroka, R. Vithanage, D.A. Philips, B. Walker, P.K. Dasgupta, Fluorescence properties of metal complexes of 8-hydroxyquinoline-5-sulfonic acid and chromatographic applications, *Anal. Chem.*, 1987, **59**, 629–636.

109. X. Sun, Y.W. Wang, Y. Peng, A selective and ratiometric bifunctional fluorescent probe for $Al^{3+}$ ion and proton, *Org. Lett.*, 2012, **14**, 3420–3423.
110. D. Maity, T. Govindaraju, Conformationally constrained (coumarin-triazolyl-bipyridyl) click fluoroionophore as a selective $Al^{3+}$ sensor, *Inorg. Chem.*, 2010, **49**, 7229–7231.
111. H. Yu, J.Y. Lee, S. Angupillai, S. Wang, S. Feng, S. Matsumoto, Y.A. Son, A new dual fluorogenic and chromogenic ‘‘turn-on’’ chemosensor for $Cu^{2+}/F^{-}$ ions, *Spectrochim. Acta A*, 2015, **151**, 48–55.
112. H. Li, H. Guan, X. Duan, J. Hu, G. Wang, Q. Wang, An acid catalyzed reversible ring-opening/ring-closure reaction involving a cyano-rhodamine spirolactam, *Org. Biomol. Chem.*, 2013, **11**, 1805–1809.